Dissertation
submitted to the
Combined Faculties for the Natural Sciences and for Mathematics
of the Ruperto-Carola University of Heidelberg, Germany
for the degree of
Doctor of Natural Sciences

Put forward by
Dipl.-Phys. Christine Kräuter
born in Kandel

Oral examination: 4.2.2015

Visualization of air-water gas exchange

Referees:
Prof. Dr. Bernd Jähne
Prof. Dr. Werner Aeschbach-Hertig

Abstract

The mechanisms of air-sea gas transfer are studied in a large annular air-sea interaction facility, the Heidelberg *Aeolotron*. A novel visualization technique is used, in which an alkaline gas (ammonia) in ppm concentration levels is absorbed into slightly acid water (pH = 4). The concentration gradient in the aqueous mass boundary layer is transformed into a sharp pH gradient, which is made visible by a fluorescent pH indicator (Pyranine). Regulating the gas flux into the water allows controlling the thickness of the fluorescent layer. By observing the fluorescence induced by high power LEDs on a 2D surface patch ((21 ×25) cm^2) with a camera from above at 100 fps and a spatial resolution of 150 µm, the processes creating near-surface turbulence can be studied even at a wavy water surface. Results from an extensive set of experiments are presented, covering wind speeds from 0.4 - 8.6 m/s, different concentrations of a soluble surfactant, and waves with limited and unlimited fetch. The fluorescence footprints of different processes known to contribute to gas exchange, e.g. Langmuir circulations and microscale breaking, are identified. It is found that the transition of the Schmidt number exponent, which is essential for the scaling of transfer velocities of different gases, from 2/3 to 1/2 is correlated with the frequency of microscale breaking. Surfactants shift the onset of surface renewal events to higher wind speeds. Direct comparison to simultaneously captured thermal imagery shows that despite the large difference in diffusion coefficients between ammonia and heat by a factor of 100, the transport of both tracers is governed by the same mechanisms.

Zusammenfassung

Die Mechanismen des Gasaustausches zwischen Ozean und Atmosphäre wurden im großen ringförmigen Wind-Wellen Kanal in Heidelberg (*Aeolotron*) untersucht. Eine neu entwickelte Technik erlaubt die Visualisierung der Invasion eines alkalischen Gases (Ammoniak) in saurem Wasser (pH = 4). Der Konzentrationsgradient in der wasserseitigen Grenzschicht wird in einen scharfen Gradienten im pH-Wert umgewandelt, der durch den Fluoreszenzfarbstoff Pyranin sichtbar gemacht wird. Durch Regelung des Ammoniakflusses kann die Dicke der fluoreszierenden Schicht kontrolliert werden. Eine (21 × 25) cm^2 große Fläche auf dem Wasser wird durch Hochleistungs-LEDs zur Fluoreszenz angeregt und von oben mit einer Kamera mit einer Frequenz von 100 Hz und einer räumlichen Auflösung von 150 µm beobachtet. Dies ermöglicht die Untersuchung von Prozessen, die nahe einer welligen Wasseroberfläche Turbulenz erzeugen. Ergebnisse aus Messreihen bei verschiedenen Windgeschwindigkeiten (0.4 - 8.6 m/s), verschiedenen Konzentrationen von oberflächenaktiven Substanzen und verschiedenen Windwirklängen werden vorgestellt. Charakteristische fluoreszierende Strukturen auf der Wasseroberfläche werden identifiziert (z.B. Langmuir Zirkulationen und "microscale breaking"). Für die Skalierung von Transfergeschwindigkeiten verschiedener Gase ist die Kenntnis des Schmidtzahlexponenten entscheidend. Es wird gezeigt, dass dessen gradueller Übergang von 2/3 zu 1/2 mit der Frequenz des microscale breaking korreliert. Oberflächenfilme verschieben diesen Übergang zu größeren Windgeschwindigkeiten. Ein direkter Vergleich von Fluoreszenz- mit simultan gemessenen Wärmestrukturen zeigt, dass trotz des großen Unterschiedes in den Diffusionskonstanten (Faktor 100) die gleichen Prozesse den Transport beeinflussen.

Contents

1 Introduction

Transfer between ocean and atmosphere

Water surfaces cover two thirds of the earth and connect the two most climate relevant compartments of the earth: ocean and atmosphere. The chemical composition of the ocean and atmosphere, which is influenced by the cycle of the chemicals between the compartments, has direct and indirect feedbacks on earths climate (Carpenter et al. 2012). For example, the chemical composition of the atmosphere directly changes the radiative budget (Myhre et al. 2013) and the exchange of CO_2 from the atmosphere to the oceans leads to an increasing acidification of the oceans (Doney et al. 2009). These two direct effects have an indirect influence on the sea level (Donnelly et al. 2004), since higher temperatures lead to ice melting at the poles and a change in pH value due to CO_2 leads to a die off of coral reefs (Richmond and Wolanski 2011). Thus, the exchange of environmentally relevant trace gases (e.g. CO_2, N_2O and NH_3) between air and water plays a key role for understanding the past, current and future climate (IPCC 2013).

Knowledge of chemical fluxes between the ocean and atmosphere is important to get a better understanding of the cycles of these chemicals. The direct measurements of fluxes, for example by eddy covariance, is challenging (Jacobs et al. 2002). Another possibility to estimate fluxes is by measuring the concentration c of a gas in air and water (Kock et al. 2012, Quack et al. 2004). By approximating a transfer velocity k, which is a measure for the speed with which gases are transported through the air-water interface, the flux j can then be computed by $j = k\Delta c$. The estimations for the transfer velocity are commonly conducted by semi-empirical parameterizations (Nightingale et al. 2000, Wanninkhof 1992), which relate the transfer velocity to the wind speed. Different parameterizations with the wind speed exist and at a

typical wind speed of 7 m/s they vary by a factor of two (Ho et al. 2011, Johnson et al. 2011). However, especially at local or regional scales, parameterizations derived from global data sets may fail. Local effects can be significant. For example, regions of high biological activity in coastal waters are producing surface slicks, which dampen waves and reduce gas exchange (Kock et al. 2012). Local estimates of fluxes are additionally used for global simulations (Stemmler et al. 2013). Thus, errors in local flux estimates can have an impact for global modeling and hence climate predictions.

Processes controlling the transfer

Concentrations in the air and water bulk are assumed to be well mixed by turbulence. Close to the water surface turbulence is inhibited and molecular diffusion is the driving transport mechanism (Whitman 1923). The transfer of sparingly soluble gases is controlled by a 20 - 200 µm thick aqueous mass boundary layer (Jähne et al. 1989). Hence, the transfer velocity is controlled by processes disrupting this thin layer. The kinetic forcing by the wind does not directly influence the transfer velocity, but indirectly by various processes. This also explains the differences in the parameterization based on the wind speed (Ho et al. 2011). However, the wind has an impact on the near-surface turbulence, which directly influences the exchange rate of sparingly soluble gases. The energy input by the wind directly influences the tangential shear stress at the water surface and creates turbulent shear stress, which has an impact on the near-surface turbulence. Additionally, the wind stress is put into the form drag of waves and leads to a growth of the waves (Peirson 1997). The interaction of shear stress and waves produces counter rotating eddies beneath the water surface, which axis are directed in along-wind direction. These are called Langmuir circulations (Thorpe 2004) and are known to enhance the exchange at low wind speeds (Veron and Melville 2001). At medium wind speeds before waves start to break with bubble entrainment, microscale wave breaking occurs (Melville et al. 1998). These are small waves, which break and renew the water surface. It has been shown that the gas exchange in this medium wind speed range is significantly enhanced if microscale breaking occurs (Zappa et al. 2004). The energy input by the wind depends on the surface roughness. If a surface active material (surfactant) is present on the water surface, it dampens the small-scale waves and hence reduces the surface roughness. This leads to a reduction of momentum transport by the wind and to a reduced near-surface turbulence.

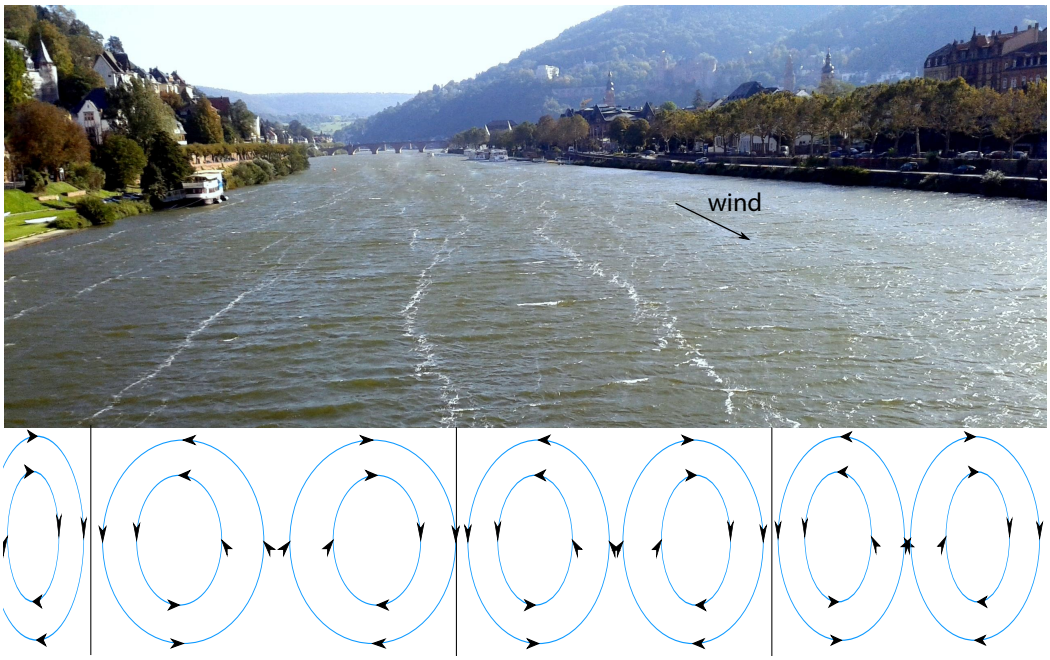

Figure 1.1.
Surface signature of Langmuir circulations on the river Neckar in Heidelberg. White foam accumulates in streaks on the water surface. The wind direction is marked by the arrow. Waves are clearly visible. The underlying Langmuir cells creating the streaks are shown schematically.

Investigating transfer processes

How is it possible to investigate the processes driving air-sea exchange? By looking at Fig. 1.1, it is clearly visible that white foam lines have accumulated aligned with the wind direction at the water surface of the river Neckar in Heidelberg. This pattern is created by surface flows caused by Langmuir circulations. The underwater flow field is sketched in Fig. 1.1. The result are convergence zones to which water is flowing from both cross-wind directions. This leads to the accumulation of foam. Due to the continuity of the mass flow, there must be other zones where the water submerges from the depth (divergence zones). Similar structures have been observed by Langmuir (1938) on the ocean surface, where seaweed accumulated in streaks. He concluded that these structures are due to eddies beneath the water surface as shown in the lower part of the image 1.1. These are Langmuir circulations and can be observed when wind and waves interact with each other. From this example one learns that it is possible to investigate processes beneath the water surface by observing their footprint on the water surface.

There are techniques available to study the near-surface turbulence. Melville et al. (1998) put floating glass microspheres on the water surface and investigated the evolution of the footprint of Langmuir circulations on the water surface after inducing wind. Another technique to investigate the near-surface processes by observing the

water surface is thermal imagery. In the Langmuir circulation example, a distinct thermal footprint is visible, because surface water cools over time due to evaporation. Therefore, in zones where water is coming to the surface (between the foam lines in image 1.1), the temperature is higher than at the convergence zones, where the surface water has been in contact with the air for a longer time. Marmorino et al. (2004) investigated the size of Langmuir circulation at the ocean surface with this technique, while Veron and Melville (2001) conducted laboratory experiments on the evolution of the thermal footprints of Langmuir circulations. Also, other footprints of near-surface turbulence have been investigated with this technique. For example, Jessup et al. (1997b) investigated the thermal footprint of a breaking wave and related the recovery rate of a breaker with the energy dissipation, which is a measure for the near-surface turbulence. Also, microscale breaking has been investigated by thermal imaging. Zappa et al. (2001) and Zappa et al. (2004) studied the relation of gas exchange with the renewed surface of a microscale breaker. Divergence and convergence zones and the flow field on the water surface have been investigated with thermal imagery by Garbe et al. (2003). However, there are still remaining questions on the processes producing smaller streaks, which are only induced by shear stress (no waves) and hence cannot be Langmuir circulations.

The measurement techniques described above all investigate the heat exchange. None of them is able to visualize air-water gas exchange. Since the diffusion of heat is a factor of 100 faster than the diffusion of gases, it is still under discussion whether the near-surface turbulence has a similar influence on heat and gases. Studies by Asher and Litchendorf (2009) and Asher et al. (2012) demonstrate differences between the exchange of heat and gas, while a recent study by Nagel et al. (2014) shows the scalability of heat and gas and suggests that the same processes act. A technique able to simultaneously image heat as well as gas concentrations on the water surface is highly desirable to answer this question.

For imaging concentration fields laser-induced fluorescent techniques are used. They image the concentration profile near the water surface vertically, e.g. Friedl (2013), Herlina and Jirka (2008), and Münsterer (1996). For these measurements a vertical resolution far better than 10 µm is necessary, since the thin aqueous mass boundary layer has to be visualized. This is challenging for a moving water surface with wave amplitudes in the order of several centimeters. Thus, these techniques are not applicable to large wind-wave facilities. However, only in the medium wind speed regime, when waves are present, microscale wave breaking and Langmuir circulations occur. Thus, a new technique is needed, which is able to image the concentration fields also at large wind-wave facilities. The technique should be capable to visualize concentration fields horizontally to investigate the processes that occur in cross and along-wind direction. The goal of this thesis is to provide such a technique, apply it to a large wind-wave facility and investigate the footprints of gas exchange collocated and simultaneously with heat and wave imagery.

2
Theory

In this chapter, an introduction on processes controlling air-water gas exchange is given. It is structured in three main sections: description of transport mechanisms, main parameters to describe the exchange, and the turbulent processes driving the transport. Molecular diffusion is the controlling transport mechanism directly at the interface, since turbulence is inhibited. The existing turbulent processes, e.g. microscale wave breaking and Langmuir circulations, enhance the exchange of gas, heat, and momentum at the interface dramatically. A short summery on the state of knowledge on the most important processes is given.

2.1 Transport

Heat, trace gases, and momentum are transported either by random motion or by directed motion. Molecular diffusion and turbulent flow are random transport processes. Both motions aim at compensating disequilibriums. While molecular diffusion is a statistical process independent of the direction, turbulence seems to be chaotic, but has a certain inertia and is dependent on the direction. In most cases, turbulent transport is more effective than the molecular diffusion. An exception is the transport close to interfaces, which will be addressed in sec. 2.2. Advection on the other hand is a directed motion, a consequence of the mean bulk velocity of a fluid. This section gives an overview of the different transport mechanisms and the most important mathematical descriptions. For a more detailed description refer to Csanady (1973), Cussler (2009), Roedel (2000), and Schwarzenbach et al. (2003).

2.1.1 Molecular diffusion

Molecular diffusion is caused by random motion of molecules (or atoms) due to their thermal energy. Each molecule has a translation energy and moves with a Boltzmann distributed thermal velocity in a medium until it hits another molecule. After the elastic collision the molecule moves in a direction, which is uncorrelated to its previous direction. The stochastic motion is described by the random walk model (Pearson 1905). Molecules compensate gradients and move in the direction of the lower concentration. The considered volume must be larger than the mean free path, which is the distance between collisions, to describe the movement of a cloud of molecules. Fick (1855) proposed for a macroscopic description of the flux a proportionality to the concentration gradient

$$\mathbf{j}_\mathrm{c} = -D\nabla c. \tag{2.1}$$

This law is called **Fick's first law** with the diffusion coefficient D, which is a matter constant. The diffusion coefficient is defined by

$$\mathrm{D} = \frac{1}{3}ul, \tag{2.2}$$

with the mean thermal velocity u and the mean free path l. Due to the equal movement in all three directions the factor is multiplied. The mean thermal velocity and hence the diffusion increase with temperature and decrease with the weight of the molecule.

In analogy to Fick's first law eq. (2.1), which describes the flux of gases, the flux for heat is described by **Fourier's law** of thermal conduction

$$\mathbf{j}_\mathrm{h} = -\lambda\nabla T \tag{2.3}$$

with the thermal conductivity number λ and the temperature T. The flux for the momentum is described by **Newton's law** of viscosity

$$\mathbf{j}_\mathrm{m} = -\nu\nabla(\rho u) \tag{2.4}$$

with the kinematic viscosity ν, the density ρ, and the mean velocity u (Csanady 1973). In analogy to eq. (2.2), the thermal diffusivity χ ($= \lambda/\mathrm{c_p}\rho$) and the kinematic viscosity ν are described. The specific heat coefficient is $\mathrm{c_p}$. **Schmidt numbers** are defined as

$$Sc = \frac{\nu}{D} \tag{2.5}$$

to describe the differences between diffusion of momentum and gases. The **Prandtl number** is defined in analogy to the Schmidt number as

$$Pr = \frac{\nu}{\chi} \tag{2.6}$$

to describe the differences between momentum and heat. The *Sc* and *Pr* numbers for most substances in air are close to one. For water this is different. For example the Schmidt numbers for ammonia in air and water at 25 °C are 0.62 and 610, respectively (Fogg and Sangster 2003). The Prandtl numbers for heat are 0.71 (air) and 7 (water) (Schimpf 2000).

The temporal change in concentration is described by **Fick's second law** (Fick 1855). By inserting Fick's first law eq. (2.1) into the continuity equation and assuming that no concentration is produced or annihilated, one obtains with Gauss's theorem

$$\frac{\partial c}{\partial t} = D\Delta c. \tag{2.7}$$

In analogy, the diffusion equations for heat and momentum are written as

$$\frac{\partial T}{\partial t} = \chi\Delta T \tag{2.8}$$

and

$$\frac{\partial \mathbf{u}}{\partial t} = \nu\Delta \mathbf{u}. \tag{2.9}$$

2.1.2 Turbulence

Turbulent motion is described as temporally and locally instationary and its flow seems to be chaotic. It is generated by random disruptions of a flow. Eddies, which occur in a large range of scales, are a common concept to describe turbulence. Large eddies are the source for turbulent energy, e.g. due to the energy of large streams. Energy is then transferred to smaller eddies. The scale, where energy is neither produced nor annihilated, is called internal subrange (Kolmogorov 1941). The cascade continues to very small scales in the order of millimeter, where viscous dissipation is important. The turbulent energy is dissipated by molecular friction, which is converted to thermal energy.

A comparison of the mass forces and the molecular viscous forces has to be conducted, to describe the turbulence of a flow. The **Reynolds number**

$$Re = \frac{ul}{\nu} \tag{2.10}$$

is a measure for the level of turbulence, where u is the mean velocity, ν the kinematic viscosity of the medium and l is a characteristic length (Stokes 1850). For small Reynolds numbers, the flow is considered laminar and the velocity field is stationary. If the Reynolds number increases above a critical number, the flow gets immediately turbulent and the velocity field is instationary.

On small scales molecular diffusion is statistically and uncorrelated, while turbulent motion is correlated and the movement of a molecule is described by an

autocorrelation. Turbulence is less random than molecular diffusion. Molecular motion only occurs on small scales and is described macroscopically by Fick's first law (see eq. (2.1)), turbulent eddies occur on all scales and cannot be easily described macroscopically. Therefore, turbulence seems more chaotic by observing it on large scales.

Turbulent diffusion

In special cases, turbulent flow may be described in analogy to molecular diffusion, e.g. close to boundaries (see sec. 2.1.1). This is valid only for long time periods or stationary problems (Kundu 2008). The turbulent flow is mathematically described by the **Reynolds decomposition**. The concentration and the velocity are characterized by a temporal mean and fluctuations

$$c = \overline{c} + c' \tag{2.11}$$

and

$$\mathbf{u} = \overline{\mathbf{u}} + \mathbf{u}'. \tag{2.12}$$

A special case with a concentration gradient only in z-direction is considered, to simplify the following considerations. Hence, the concentrations in x- and y-direction are considered to be equally distributed and the flux is only directed in z-direction. By inserting eq. (2.11) and eq. (2.12) in the equation for the flux for concentrations

$$j_{c,z} = u_z c \tag{2.13}$$

and considering that $\overline{c'} = \overline{u'} = 0$ (in a time period long enough, the mean fluctuation has to be equal to zero), the flux is

$$j_{c,z} = \overline{cu_z} + \overline{c'u'_z}. \tag{2.14}$$

The first term describes the advection of a mean concentration with the mean flow and the second term the turbulent flux, which is interpreted as a covariance and is called eddy correlation. Not included in this equation is the diffusion term eq. (2.1), which has to be added to describe all transport mechanisms.

A **turbulent diffusion coefficient** K is defined as

$$K(z) := -\frac{\overline{c'u'_z}}{\frac{\partial \overline{c}}{\partial z}}, \tag{2.15}$$

to get an analogy with molecular diffusion. The turbulent diffusion coefficient is only valid for the cases described above and if $\frac{\partial \overline{c}}{\partial z} \neq 0$. By inserting this formulation

into the second term of eq. (2.14), one gets for the **turbulent flux**

$$j_{c,z} = -K(z)\frac{\partial \overline{c}}{\partial z}. \tag{2.16}$$

A **turbulent Schmidt number** is introduced in analogy to the Schmidt number for diffusion

$$Sc_t = \frac{K_m}{K}, \tag{2.17}$$

with the turbulent Schmidt number for momentum K_m. The following sections will show why it makes sense to construct this analogy to the diffusion.

Equivalently, a turbulent flux density (Reynolds stress) can be derived for momentum

$$\mathbf{j}_{m,turb} = \rho u_*^2 \tag{2.18}$$

with the **friction velocity**

$$u_* = \sqrt{\overline{\mathbf{u}_i' \mathbf{u}_j'}}. \tag{2.19}$$

This definition is only valid in the fully turbulent flow region. The friction velocity is a measure for the shear stress. It is an important parameter to describe the exchange of gases, as will be shown in sec. 2.2.

2.2 Exchange between air and water

In this section, the transport of trace gases between air and water is discussed. In the beginning of this section the main transport mechanisms, which are dominant for the exchange at the air-water interface, are addressed and the mass boundary layer is defined. In the following part, the main parameters describing the transport are introduced and the partitioning between air and water is discussed. At the end of this section, different theoretical models describing the relation between the gas exchange rate and the turbulence are discussed.

2.2.1 Boundary layers

Boundaries are surfaces or regions, in which a property of the system changes tremendously. If the boundary has a certain spacial extension it is called transition zone and if there is a discontinuity at the boundary it is called interface. An interface is for example the water surface, where the density of two media, air and water, changes extensively. In the following, the transfer at the air-water interface is discussed in more detail.

Trace gases, heat, and momentum are transported by molecular diffusion and turbulence as described in sec. 2.1. The effectiveness of transport is depicted by the molecular and turbulent diffusion coefficients, see eq. (2.2) and eq. (2.15). It was already noted that transport by turbulence is usually much more effective than

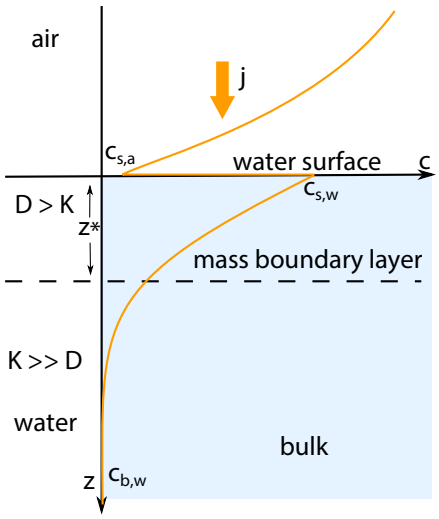

Figure 2.1
Typical concentration profile for the invasion of a gas with solubility $\alpha > 1$. The concentration is on the x-axis, the depth on the y-axis. The mass boundary layer depth in water is marked by the dotted line.

transport by molecular diffusion (K ≫ D). An important exception are boundary layers, which form at the air-water interface. Turbulent eddies cannot penetrate through the surface, due to the large differences between the densities of water and air ($\rho_w/\rho_a \approx 780$). Eddies get smaller with decreasing distance to an interface (Prandtl 1957) ($K(0) = 0$). Close to the water surface, in the boundary layer, the turbulent transport is not as efficient as molecular diffusion, due to the small eddy sizes ($K < D$). Since random motion is much slower than turbulence, the resistance to the flux lies in the boundary layer, which is the bottleneck of the exchange.

Summing up the effect of diffusion and turbulence, eq. (2.1) and eq. (2.16), the flux in z-direction is

$$j_c = -(K(z) + D)\frac{\partial c}{\partial z}. \tag{2.20}$$

The flux is constant over depth for a stationary concentration profile, due to mass conservation. Since the size of the eddies increases with increasing distance from the water surface, the turbulent diffusion coefficient increases as well. The molecular diffusion coefficient is independent of the distance. Therefore, the concentration gradient is the largest close to the water surface, where almost all change in concentration is happening. A typical depth profile of the concentration is shown in Fig. 2.1. In the depth, at which the molecular and turbulent diffusion coefficients are in the same order, lies the so called **boundary layer thickness** z_*. It has typical thicknesses in water in the order of 100 µm (Jähne et al. 1987). The boundary layer thickness is discussed in more detail in the following.

2.2.2 Parameters

It is intuitive to describe the effectiveness of the transport of trace gases with a resistance. The **transfer resistance** is derived by eq. (2.20) in analogy to the resistance in electrical circuits as

$$R_{1,2} = \frac{c(z_2) - c(z_1)}{j} = -\int_{z_1}^{z_2} \frac{1}{(K(z) + D)} \mathrm{d}z. \tag{2.21}$$

It has the unit time per distance and describes the time a gas needs to be transported from z_2 to z_1. The inverse of the resistance is called **transfer velocity** k and is a measure for the mean velocity with which trace gases are transported through a layer with the depth $\Delta z\,(=\ z_2 - z_1)$.

The boundary layer thickness z_* is defined as the intercept of the tangent to the concentration profile at the surface and the bulk

$$z_* = \frac{\Delta c}{\frac{\partial c}{\partial z}\big|_{z=0}}. \tag{2.22}$$

By using this definition, the transfer resistance is rewritten as

$$R = \frac{z_*}{D}. \tag{2.23}$$

Another parameter to describe the transfer process is the time, which is needed to cross the boundary layer. This **time constant** is given by

$$\tau = DR^2. \tag{2.24}$$

It is important that the parameters defined here are independent of model considerations. The only assumption made is that the turbulence is zero at the interface.

A transfer resistance for momentum is derived in analogy to eq. (2.21)

$$R_\mathrm{m} = \frac{\Delta(\rho u)}{j_\mathrm{m}}. \tag{2.25}$$

With the friction velocity in eq. (2.18) one gets for the dimensionless transfer resistance in the turbulent flow regime

$$\beta_\mathrm{t} = \frac{\Delta u}{u_*}, \tag{2.26}$$

with $\beta_\mathrm{t} = R_\mathrm{m,turb} u_*$.

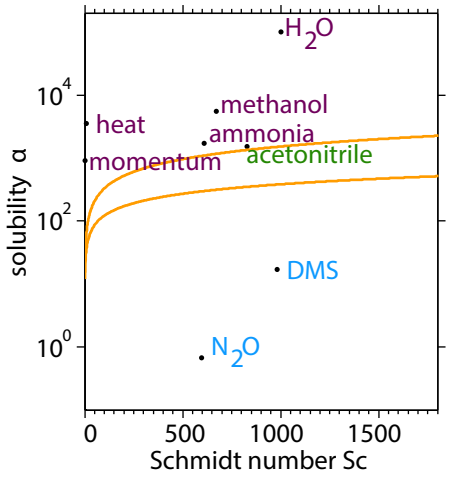

Figure 2.2
Parameter space showing the solubility and the water-side Schmidt number of different gases. Gases marked in blue are mainly controlled by the water phase, the green gas is controlled equally by both phases, and the purple gases are mainly controlled by the air side. Orange lines mark the transition zone, where the gases are controlled equally by the air and water phase ($R_a = R_w$). The lines are a result of equalizing eq. (2.37) and eq. (2.38) for a Schmidt number exponent $n = 1/2$ and $n = 2/3$. The air-side transfer resistance has to be multiplied with the solubility to change its perspective to the water side (Kräuter 2011).

2.2.3 Partitioning of the transfer resistance between air and water

The considerations described above are valid for air as well as for water. One difference between air and water is the magnitude of the diffusion coefficients (water: $D_w \approx 10^{-5}\,\mathrm{cm/s^2}$, air: $D_a \approx 0.1\,\mathrm{cm/s^2}$ (Yaws 1999)). Hence, the air-side boundary layer is larger than the water-side boundary (see eq. (2.23)). Another difference is the magnitude of the friction velocities (see eq. (2.19)). The relation of the friction velocity in water with the air-side friction velocity is

$$u_{*w} = \sqrt{\frac{\rho_a}{\rho_w}}\, u_{*a}, \tag{2.27}$$

because $j_{m,air} = j_{m,water}$. The water-side friction velocity is much smaller than the one in the air, due to the difference in the densities ($(\rho_a/\rho_w)^{1/2} \approx 0.035$ at $T = 20\,^\circ\mathrm{C}$). At the air-water interface the concentrations are in equilibrium described by Henry's law

$$\alpha = \frac{c_w}{c_a}, \tag{2.28}$$

where c_a is the concentration in air and c_w in water. The **solubility** α is dimensionless and is responsible for the jump in concentration at the water surface shown in Fig. 2.1.

As in electrical circuits it is possible to add resistances from different layers

$$R_{1,3} = R_{1,2} + R_{2,3}. \tag{2.29}$$

The resistances in air and water can be added to calculate the total transfer resistance

$$R_{tot} = \alpha R_a + R_w, \tag{2.30}$$

with the air-side R_a and the water-side R_w resistances (Liss and Slater 1974, Whitman 1923). The solubility has to be considered due to the concentration jump at the

interface. For a high solubility the resistance is mostly located in the air phase and for a low solubility in the water (Duce et al. 1991). Heat, ammonia and water vapor have a high solubility in contrast to most gases, which have a low solubility, e.g. CO_2, O_2, and N_2O. Whether a gas is controlled by the air or water phase depends on its solubility. The dependence of the controlling phase on solubility and Schmidt number/diffusion coefficient is shown in Fig. 2.2. Gases marked in blue/purple are controlled by the water/air side. Gases marked in green are in the transition zone (between orange lines) and are controlled equally by both phases. The orange lines come from semi-empirical models, which are describing the transfer resistance in dependence of the Schmidt number. These will be discussed in sec. 2.2.4. The dependence on the friction velocity/level of turbulence is shown in Kräuter (2011).

Some gases have high effective solubilities due to chemical reactions, e.g. ammonia, CO_2, and SO_2. The water-side resistance is reduced significantly, due to their reaction with hydrogen or hydroxide. An **effective solubility** is defined for ammonia as

$$\alpha_{\text{eff}} = \alpha\left(1 + 10^{-\text{pH}+\text{pK}_a}\right) = \frac{[\text{NH}_3]_w + [\text{NH}_4^+]_w}{[\text{NH}_3]_a}, \tag{2.31}$$

with the pH value and the acid dissociation constant pK_a to describe this enhancement (Fogg and Sangster 2003, Wiberg 2007). SO_2 and CO_2 have an additional term in eq. (2.31) due to their dissociation in two forms, e.g. HSO_3^- and SO_3^{2-}.

2.2.4 Conceptual Models

This section shows different theoretical/semi-empirical considerations to describe simplified the turbulence in the boundary layer. Two different cases are considered: a rigid and a free water surface. The differences are the different boundary conditions, which are described in more detail in Lamont and Scott (1970). Due to the complicated intermittent nature of gas exchange at higher wind speeds different models describing the turbulence are discussed. The conceptual models are shown schematically in Fig. 2.3.

Two-film model

The simplest model is the so called two-film model by Whitman (1923). It assumes a well mixed turbulent layer and a molecular diffusive layer. The boundary between theses layers is assumed to be sharp at $z = z_*$ (see Fig. 2.3). Even Whitman (1923) states that no such sharp change exists, since the diffusion coefficient is much smaller than the kinematic viscosity. Hence, even small eddies influence the transport much more than it is influenced by the diffusion. The model predicts a linear relationship of the transfer resistance with diffusion

$$R \propto Sc \tag{2.32}$$

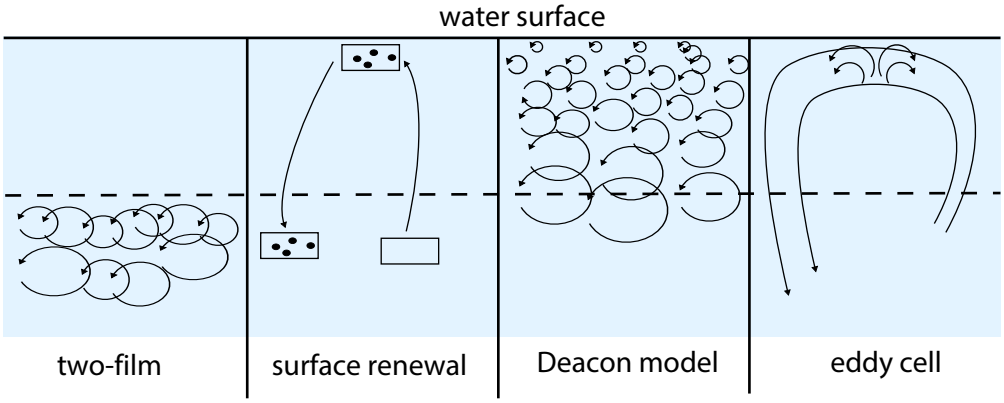

Figure 2.3.
Sketches of the turbulence structure in the two-film, surface renewal, Deacon model, and eddy cell model are schematically shown. The top solid line is the water surface and the dotted line is the boundary layer thickness.

and a linear concentration profile in the mass boundary layer. Due to its simplicity, the model is still used for estimations. The film model overestimates the transfer resistance because the exponent of the Schmidt number is usually smaller than one (Jähne 1980).

Surface renewal model

The two-film model is only applicable as an estimate for aerodynamic rigid surfaces. Higbie (1935) and Danckwerts (1951) developed a model, which is valid for aerodynamically free surfaces and it was extended by Jähne et al. (1989) for a rigid surface. The surface is continuously ruptured and new surfaces areas are formed (see Fig. 2.3). Close to the surface after a renewal event the transport is still controlled by diffusion. The renewal events (which occur randomly) are described by a statistical lifetime τ that is proportional to the depth with the power of p (Jähne 1985)

$$\tau \propto z^p. \tag{2.33}$$

Higbie (1935) and Danckwerts (1951) assumed $p = 0$ and solved the averaged transport equation

$$\frac{\partial^2 c}{\partial z^2} - \frac{c}{D\tau} = 0 \tag{2.34}$$

leading to an exponential concentration profile

$$c(z) = (c_s - c_b) \exp\left(-\frac{z}{\sqrt{D\tau}}\right) + c_b. \tag{2.35}$$

This equation is true for a free surface. Jähne et al. (1989) solved the equation for a rigid and free surface and finds for the transfer resistance

$$R \propto \frac{1}{u_*} Sc^{\frac{p+1}{p+2}}. \tag{2.36}$$

The cases for a free and rigid surface are displayed by $p = 0$ and $p = 1$, respectively. Thus, the transfer resistance is proportional to a Schmidt number with an exponent of 1/2 for a free and 2/3 for a rigid water surface.

Deacon model

A different approach was realized by Deacon (1977). He replaced the step-like drop from the two-film model in turbulence by a continuous function. The thickness of the transition zone, where the turbulence decreases gradually, depends on the viscosity of the fluid and the intensity of the turbulent kinetic energy.

This is realized by a parametrization of the turbulent diffusion coefficient (eq. (2.16)), which changes with the distance from the interface. Deacon (1977) used a semi-empirical formulation for K, based on the formulation of a velocity profile in turbulent flows at a wall given by Reichardt (1951). For first considerations, the turbulent Schmidt number (see eq. (2.17)) is assumed to be one. With the assumption, the equations is solved numerically and the resistance is given by

$$R_\mathrm{a} = \frac{15.2}{u_*} Sc^{0.61} \qquad 0.6 < Sc < 10 \tag{2.37}$$

and

$$R_\mathrm{w} = \frac{12.1}{u_*} Sc^{2/3} + \log_{10}(Sc) + 2.9 \qquad Sc > 10. \tag{2.38}$$

Equation (2.37) describes the resistance for substances with a low Schmidt number/low diffusion coefficients. This is true for the air-side diffusion coefficient and hence it is used to describe the air-side resistance. On the other hand eq. (2.38) describes the transfer for high diffusion coefficients and therefore the water-side resistance. If the turbulent Schmidt number is not set to one, eq. (2.37) has to be multiplied with $Sc_\mathrm{t}^{0.39}$ and eq. (2.38) with $Sc_\mathrm{t}^{1/3}$. By using a turbulent Schmidt number of 0.7, which is a good approximation as shown by Yaglom and Kader (1974), the transfer resistance is 10 % smaller (Deacon 1977). Comparing these equations with experiments, a good agreement is found for low wind speeds. For higher wind speeds the measured values exceed the theoretically calculated ones (Deacon 1977). This makes sense, since the formulation by Reichardt (1951) is only valid for boundary conditions at a rigid interface. At low wind speed, the boundary conditions at the water surface are more similar to the boundary conditions at a wall than for higher wind speeds when the surface is modulated by waves and disrupted by breaking waves, droplets, and bubbles.

Eddy cell model

The concept of surface renewal by Danckwerts (1951) assumes instantaneous renewal of a surface patch right at the surface with bulk water (see Fig. 2.3). If a bulk patch is transported to the surface, it is not realistic to assume that it is not exchanging concentration with the surrounding fluid. Therefore, the eddy cell model was proposed by Fortescue and Pearson (1967), where an upwelling reaches the surface. It flows along the surface, accumulates, and is then plunged back to the bulk. On its way back, it exchanges concentration with the surrounding fluid. This model only allows large energy containing eddies. Lamont and Scott (1970) extended this model and allowed a wide range of eddy sizes. They assume smaller eddies, which are superimposed on larger eddies (see Fig. 2.3). Two extreme surface types are considered: solid and free. For a solid surface they obtain

$$R \propto \frac{1}{(\epsilon\nu)^{1/4}} Sc^{2/3}, \tag{2.39}$$

with the **kinetic energy dissipation rate** ϵ and for a free surface

$$R \propto \frac{1}{(\epsilon\nu)^{1/4}} Sc^{1/2}. \tag{2.40}$$

The result shows the known Schmidt number dependencies as for the surface renewal and the Deacon model. The model is able to predict the transfer resistances within a factor of 2 (Lamont and Scott 1970). The main advantage is that it provides a unified theory to cover different types of interfaces. A disadvantage is the fact, that it is experimentally very difficult to measure the kinetic energy dissipation.

Schmidt number dependence

Independent of the models described above, a unique relationship between the transfer resistance and the Schmidt number has been found

$$R \propto \frac{\beta}{u_*} Sc^n, \tag{2.41}$$

with the Schmidt number exponent n. This generalization of the Schmidt number dependency has been proposed by Jähne (1985). Deacon (1977) found for high Schmidt numbers a Schmidt number exponent of 2/3. The same dependency on the Schmidt number has been identified by Lamont and Scott (1970) and Jähne et al. (1989) for a solid surface. A Schmidt number exponent of 1/2 has been shown by Lamont and Scott (1970) and Higbie (1935) for a free surface. Jähne et al. (1984) measured a gradual transition of the Schmidt number exponent from 2/3 to 1/2. This transition has been further investigated by Krall (2013) and Nielsen (2004).

Facet model

This models tries to merge the findings described above (Jähne et al. 2007). It accounts for the intermittent nature of the exchange process by assuming a part of the water surface to be **smooth** and having the boundary conditions of a rigid surface. The **rough** parts of the water surface have the boundary condition of a free water surface. These parts are described by eq. (2.41). The fractional area of the surface that can be described as rough is denoted by a_w. Differences between these two equations are the **Schmidt number exponent** n and the dimensionless momentum resistance β. The total transfer velocity is

$$k = (1 - a_w)\frac{u_*}{\beta_s}Sc^{-2/3} + a_w\frac{u_*}{\beta_w}Sc^{-1/2}, \tag{2.42}$$

with the smooth and wavy dimensionless transfer resistance β_s and β_w. Richter and Jähne (2011) parameterized the fraction of the wavy surface in dependence on the mean square slope σ_s^2 as

$$a_w(\sigma_s^2) = \frac{(\sigma_s^2)^\gamma}{\delta^\gamma + (\sigma_s^2)^\gamma}. \tag{2.43}$$

This describes the gradual transition from a smooth to a wavy surface or in other words the transition of the Schmidt number exponent. The parameters δ and γ are interpreted as the midpoint and the steepness of the transition. A similar model has been proposed by Zappa et al. (2001) and Zappa et al. (2004). They part the surface in areas with and without microscale breaking (see sec. 2.3.4).

Experimentally, the facet model was tested by measuring the Schmidt number exponent dependency on the mean square slope. Measurements were conducted by Krall (2013), Degreif (2006), and Nielsen (2004). They measured different values for the parameters. These variations have been linked to experimental difficulties, different geometries of the wind-wave facilities and uncertainties in the diffusion coefficients.

2.3 Turbulent processes

Exchange at the air-water interface is controlled by the near-surface turbulence that dissipates its energy close to the water surface. One parameter, which might be able to describe the near-surface turbulence is the turbulent energy dissipation ϵ. Theoretical models predict a direct relationship between ϵ and the transfer velocity (Kitaigorodskii 1984, Lamont and Scott 1970, McKenna and McGillis 2004). Experimentally, this relationship was shown by Zappa et al. (2007) and Zappa et al. (2008). However, it is very difficult to measure the turbulent kinetic energy dissipation. Hence, it would be favorable to describe the near-surface turbulence by the producing mechanisms. The remaining questions are which mechanisms produce

the near-surface turbulence and how is the energy input by the wind distributed.

Wind enhances indirectly the transfer across the interface. The shear stress due to the wind produces a current (tangential stress) and waves (form drag) (Banner and Peirson 1998). The interaction of the shear current and the waves produce eddies, which are perpendicular to the wind direction. These eddies are called Langmuir circulation (LC). They were found to enhance the exchange (Veron and Melville 2001). At higher wind speeds, wave start to break. First without bubble entrainment on small scales, microscale breaking, and for higher wind speeds large wave breaking with bubble entrainment occurs and mixes the trace gas effectively into the bulk. In the following, the different mechanisms will be described in more detail.

2.3.1 Shear stress

Wind, which blows over a water surface transports momentum across the interface (see sec. 2.1). Shear stress is the force F per area A that acts coplanar to the surface

$$\tau = \frac{F}{A}. \tag{2.44}$$

Two types of shear flow are distinguished: free and wall-bounded shear flow. The water surface is regarded as a wall bounded shear flow and will be discussed in the following. The wall free case is described in detail in Kundu (2008).

The main difference between the two types is that the wall bounded shear is affected by the viscosity of the medium with the higher viscosity (wall). At the surface, the Reynolds stress vanishes and the flow is laminar, see eq. (2.4). In the viscous sublayer, which is the boundary layer of momentum, the velocity profile is linear. Compared to the mass boundary layer the viscous boundary layer is much larger. In the fully-turbulent flow region, the shear stress is described by eq. (2.18) and the velocity profile has a logarithmic form. The velocity profile is described by the **law of the wall**. In the wake part or outer layer, no theory exists to describe the velocity profile. However, experimental results show self-similarities of wind profiles in this region (Hinze 1975, Troitskaya et al. 2012). Experimental and theoretical results show that the wind stress is the main mechanism for the production of small-scale turbulence and indirectly controls the air-water exchange (Peirson 1997, Tsai et al. 2005). If the wind starts blowing, the shear stress at the surface is transformed to a shear current and a viscous layer forms at the surface. If waves are formed a part of the shear stress goes into the form drag of the waves. At higher wind speeds, the fraction of the drag is growing while the shear current input is only slightly increasing (Peirson 1997). The exact partitioning for different wind speeds is not yet known and remains subject to ongoing research.

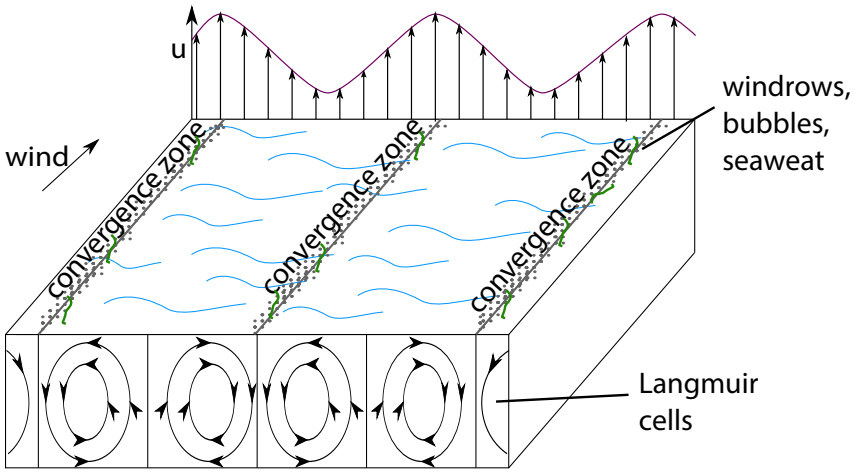

Figure 2.4.
Sketch of idealized Langmuir circulations. The surface velocity *u* is shown in the upper part of the image. (Modified from Thorpe (2004))

2.3.2 Langmuir circulation

Langmuir (1938) was the first one who reported on Langmuir cells. He observed numerous streaks of seaweed nearly parallel to the wind direction (see Fig. 2.4). Langmuir circulation (LC) are described as an array of counter-rotating vortices at the water surface that have horizontal axes aligned with the wind. Regions of convergence and divergence are found, due to the alternating signs of two vortices. In the convergence zones, algae, bubbles, and foam accumulate into narrow bands. These bands are called windrows, and they are found at ocean, lake and river surfaces. They are not as linear and regularly spaced as shown in Fig. 2.4. Mostly they are twisted and merged into each other. It was observed that the surface velocity at the windrows and beneath is larger than in between the windrows (Thorpe 2004).

There have been many ideas to describe the formation of Langmuir circulations. Craik and Leibovich (1976) and Garrett and Smith (1976) were the first who proposed as a driving force the shear-wave interaction. The stokes drift of a wave is the movement of a water package with the wave and flow. Due to the two movements, up and down by the wave and forward by the current, the package moves in spirals. The vorticity describes the spinning motion of a water package at a certain point. It is defined as the vector product of the operator ∇ and a velocity field $\mathbf{u}$. Leibovich (1983) states that by the stokes drift of a wave the vorticity of the flow field near the surface is stretched and tilted. The additionally produced vorticity is balanced by the downwards directed turbulent diffusion (see sec. 2.1.2) and Langmuir circulations start to form. These circulations enhance the transport of momentum, trace gases, and heat from the surface to the bulk (Veron and Melville 2001).

The Craik-Leibovich theory has been verified by many experimental observations, e.g. Caulliez (1998), Gemmrich and Hasse (1992), Marmorino et al. (2004), Melville

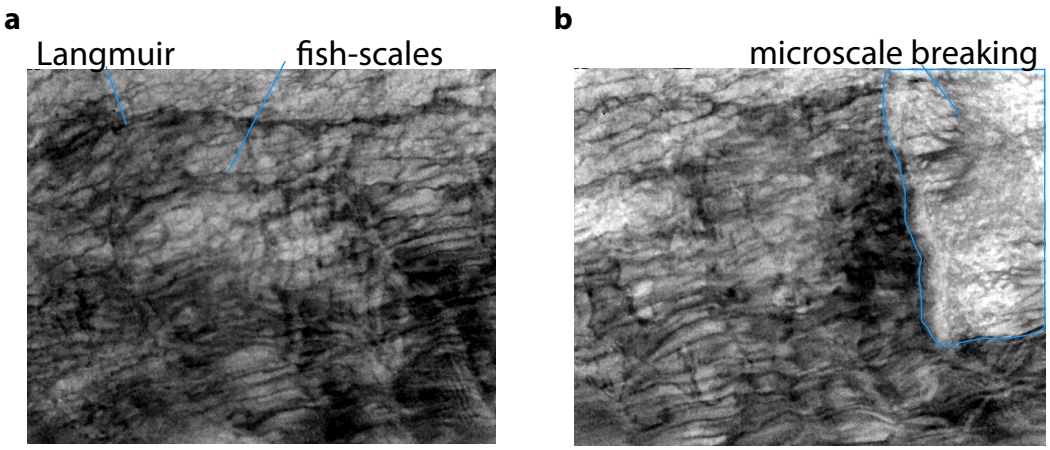

Figure 2.5.
Typical infrared images taken at the *Aeolotron* in June 2014 at a wind speed of 4.0 m/s showing **a** the thermal footprints of Langmuir circulations and fish-scale streaks and **b** the thermal footprint of a microscale breaking wave. The wind is blowing from right to left.

et al. (1998), and Veron and Melville (2001). One method to investigate LC is thermal imaging. Not only particles and bubbles are pushed together in convergence zones by the Langmuir circulations also heat accumulates in a streaky pattern. By differences in air and water temperatures heat is exchanged. The water surfaces cools due to evaporation, while the bulk water is warmer. At the divergence zones, warm water from the bulk is transported upwards and heats the surface, while the cold surface water is pushed together and the convergence zones. The convergence surface areas appear as dark streaks in the images. Typical thermal footprints of Langmuir circulations are for example shown in Fig. 2.5(a). Different authors have investigated these thermal streaks in laboratory and field experiments, e.g. Handler et al. (2012), Melville et al. (1998), Schnieders et al. (2013), Smith et al. (2007), and Veron and Melville (2001). While most authors measured heat transport by evasion, Smith et al. (2007) also investigated the structures of an invasion measurement. They found that this stable case structures are at low wind speed similar to the unstable case (evasion) structures. The exchange is symmetric as expected. The results of the invasion experiments are better comparable to the fluorescent imaging shown later in this thesis. Also, simulations for gases with small Schmidt numbers have been made for example by Tsai et al. (2005) and Handler et al. (2001). They found lines of high concentrations aligned with the wind and underlying circulations.

Two types of streaks have been found: stable ones with larger scales and smaller ones (Faller 1978, Handler et al. 2012, Langmuir 1938, Veron and Melville 2001). The larger ones have a streak spacing of meters to kilometers (Hunter 1980, Marmorino et al. 2004). The smaller streaks, which have a spacing of 2 - 10 cm between each other (Thorpe 2004), have only been observed in laboratory measurements. Veron and Melville (2001) suggest that smaller ones might not be resolved in field measurements. Melville et al. (1998) made the first observation that these small streaks are associated

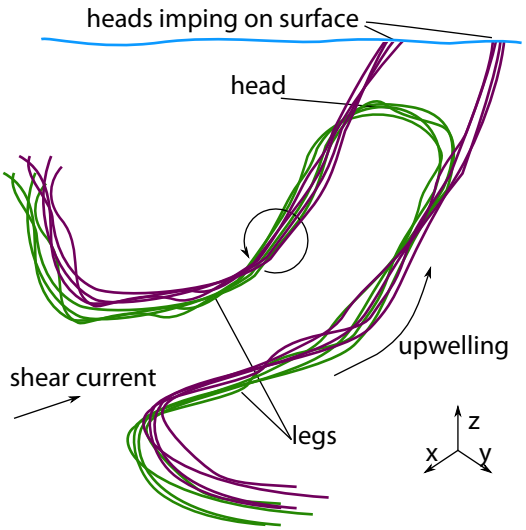

Figure 2.6
Sketch of a horse-shoe vortex. In green a bundle of vortex lines is shown moving upwards to the surface. As the vortex impinges upon the water surface, the head breaks and two pairs of vortex lines remain (purple). Image is modified after Tsai (1998).

with the longitudinal counter-rotating vorticity. He conducted particle imaging velocity (PIV) measurements close to the water surface. It has been concluded that these smaller streaks are due to the same mechanisms as the large scale LC and hence these streaks are also called LC. Marmorino et al. (2004) state that LCs play a major factor in vertical mixing and have therefore a great influence on exchange processes. Veron and Melville (2001) found that the heat and gas transfer velocities are increased by a factor of 1.7 to 2 at the onset of Langmuir circulation. They occur before wave breaking and may be the dominant source of turbulence at low wind speeds. Langmuir circulations are one of the main factors in controlling air-water exchange processes at lower wind speeds (Veron and Melville 2001).

2.3.3 Fish-scales

In the thermal images, described in sec. 2.3.2, smaller streaks have been found, located between the larger Langmuir circulation streaks (Handler et al. 2001). The smaller streaks are not as well defined as the larger LC streaks. They appear shortly after the onset of wind and during guest (short kinetic forcing by wind) and disappear quickly when the wind is turned off, while the LC remain longer. These streaks were observed, while no waves have been present and are hence only shear-induced (Schnieders et al. 2013). Handler et al. (2001) called these streaks fish-scales. They are marked in Fig. 2.5(a).

Handler et al. (2001), Rashidi and Banerjee (1990), and Tsai et al. (2005) made simulations to identify their exact nature. They found that wind stress alone can lead to the formation of streaks. This is in contradiction to the Langmuir circulations, where waves have to be present. It has been shown that these coherent turbulent structures have a very similar pattern to streaks near no-slip walls as shown by Nakawaga and Nezu (1981) and Smith and Paxson (1983). The exact nature of these

streaks is not yet clear, but different theories exist. Tsai et al. (2005) suggests the burst of horse-shoe vortices at the surface. A schematic view of a horse-shoe vortex is shown in Fig. 2.6. Horse-shoe vortices form in turbulent shear layers, due to the turning and stretching of vortices. The vortices are stretched by the flow. While the legs of the horse-shoe vortex stay at the bottom, an upward motion stretches the head further until it reaches the water surface. This is shown in green in Fig. 2.6. Close to the surface, the head bursts into two parts and impinges upon the water surface, as shown in purple in Fig. 2.6. They transport fresh water from the bulk upwards to the surface and cause an upwelling of bulk water. This mechanism is the same as on no-slip walls where the same streaky pattern has been observed (Kline 1967). Other theoretical suggestions are for example by Soloviev and Schlüssel (1994), who propose that convective cells could be elongated by shear stress. This would happen at the transition from a free to a forced convection. The producing mechanisms are still in open discussion.

Streak spacing

One of the main parameters associated with streaks is their spacing. Lam et al. (1992) found that streaks are generally quite regular and have a persistent non-dimensionless **streak spacing** of

$$l^+ = \frac{l u_*}{\nu}, \tag{2.45}$$

with the average streak spacing l. They also made numerical simulations on the spacing for different Reynold numbers. They found that the non-dimensionless streak spacing l^+ is 100 after a critical Reynold numbers of 26. Grassl (1976) estimated that the streak spacing corresponds to the thickness of the thermal boundary layer and is supposed to decrease with the friction velocity (Scott et al. 2008). Different methods have been used to compute the spacing between the streaks from manual counting (Tsai et al. 2005) over Fourier analysis (Handler et al. 2001; 2012), wavelet analysis (Scott et al. 2008) to image processing/machine learning methods (Schnieders et al. 2013). Schnieders et al. (2013) found a critical friction velocity at which the streak spacing stays constant. They concluded that the reason might be that mostly all shear stress is converted into the form drag of the waves.

2.3.4 Waves

A fraction of the wind energy is stored in the waves. If the surface stress reaches a critical level, waves get instable and break. The acceleration of the wave crest exceeds the gravitational acceleration (Phillips 1958). In other words, a portion of the fluid at the wave crest overtakes the form of the wave. It becomes turbulent as it spills down and the turbulence is decaying in the wave. Breaking waves are classified in breaking waves with and without bubble entrainment. Breaking waves play a significant role for the enhancement of gas, heat, and momentum exchange. Large breaking waves mix the trace gases effectively into the bulk. Also bubbles and droplets are produced, which additionally enhance the exchange (Mischler 2014, Woolf and Monahan 1993). At lower wind speeds, small-scale wave breaking occurs. This process is called microscale wave breaking (Banner and Phillips 1974). These waves break without bubble entrainment, but effectively mix the gas from the surface into the depth. They generate near-surface turbulence and enhance the exchange tremendously in the medium wind speed range before large scale breaking waves occur. Two types of waves are identified: **gravity waves** and **capillary waves**. Gravity waves are surface displacements, which are restored by gravity. Their wavelength is larger than the phase velocity and they have wavelengths in the range of centimeters to hundreds of meters. Capillary waves have much smaller wavelengths, but high curvatures and their restoring force is the surface tension.

Breaking waves

Breaking waves that break with bubble entrainment are divided into two groups (Handler et al. 2012): plunging and spilling breaker. A plunging breaker has a distinct overturning crest. The crest forms a jet lunging on the front phase of the wave. A spilling breaker is weaker and is described by a gradual free surface collapse. There is no distinct plunging jet. An easy way to measure the occurrence of breaking waves with bubble entrainment is by measuring the rate of white capping (Callaghan et al. 2008, Marmorino and Smith 2005, Woolf 2005). Jessup et al. (1997a) detected breaking waves with thermal imaging. They found that the recovery rate of a breaker is correlated to the energy dissipation rate and that the phase speed of the wave crest is correlated with the recovery rate. Further investigations on breaking waves have been conducted by Banner et al. (2000), Longuet-Higgins (1983), and Melville (1996).

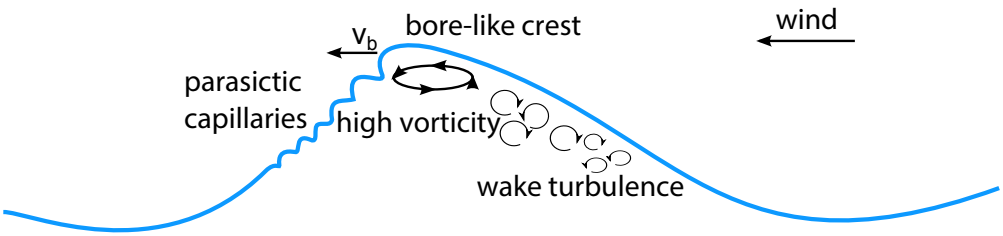

Figure 2.7.
Sketch of a microscale breaking wave. The velocity of the bore-like crest is v_b. Parasitic capillary waves form on the downwind face of the wave. Directly under the crest is a high vorticity region, which is decaying into wake turbulence after breaking. (Modified from Jessup et al. (1997b).)

Microscale breaking

Microscale breaking waves are very short gravity waves (wavelength ≈ 0.1 - 1 cm) that break without bubble entrainment (Jessup et al. 1997b). They were first mentioned by Banner and Phillips (1974). A typical microscale breaker is shown schematically in Fig. 2.7. It has a bore-like crest that moves with the speed v_b. In front of the crest are parasitic capillary waves. A region of high vorticity is beneath the wave crest (Ebuchi et al. 1987, Okuda 1982). If the wave breaks, wake turbulence is created in the back of the wave and the energy is dissipated. The interest in theses waves has grown due to the importance for gas exchange in moderate wind speeds (Melville 1996). Csanady (1990) model the influence of microscale breaking and found that the gas exchange is enhanced at moderate wind speeds. Microscale breaking is mostly investigated by thermal imaging, e.g. Jessup et al. (1997b). Figure 2.5(b) shows a typical thermal footprint of a microscale breaker. The wind blows from right to the left. The water surface is normally distributed by streaks. If a microscale breaking wave is moving through the image, it creates a lot of turbulence in its back and the water surface is renewed. The microscale breaking crest is located at the left boarder of the marked blue area. Behind the crest, the warm water from the bulk is transported upwards and the water surface is warm (white).

Zappa et al. (2001) compared the renewed area by a microscale breaker to the gas exchange and found a linear relationship for each measured gas. Siddiqui et al. (2001b) detected microscale breaking waves with infrared imagery and measured simultaneously the two-dimensional velocity fields with particle image velocimetry (PIV) beneath the wave. They found a correlation between the near-surface vorticity and the fractional area coverage of microscale breaking and local heat transfer.

2.3.5 Surfactants

Surfactants, surface active materials, consist of a hydrophilic and a hydrophobic part. They preferably accumulate at the water surface, due to their hydrophobic part. If a critical concentration is reached and the whole surface is covered by a mono-molecular surface film, the molecules start to form Micells. In Micells a couple of molecules stick their hydrophobic tails together and the hydrophilic heads are forming a ball. Surface active materials with the mentioned properties are called **slicks**. Oil films, which do not consist of a hydrophobic and hydrophilic part are called **spills**. They do not form mono-molecular surface films but rather thick films on the water surface (Hühnerfuss 2006).

Both types of films have an effect on the exchange process between air and water. In contrast to the other processes discussed above, they reduce the transfer velocity. They have mostly an indirect effect on the processes discussed above than directly on the exchange. **Indirect/dynamic** effects are the damping of waves and a change in viscoelasticity (Frew et al. 2004, Hühnerfuss et al. 1987, Kiefhaber 2014, Soloviev and Lukas 2010). The gas exchange is reduced if the waves are damped by the surfactant, since waves enhance the gas exchange. Surface films have a large indirect effect on water-side controlled gases (Broecker et al. 1978, Jähne 1985). It was found that there is no significant effect for air-side controlled gases (Liss 1983). A **direct/static effect** is an additional phase resistance in eq. (2.30). Only thick oil films of 2 - 10 µm have an additional liquid phase resistance (Garrett 1971, Jarvis 1962, Liss 1983, Liss and Martinelli 1978, Springer and Pigford 1970).

Triton X-100

Triton X-100 has been used in this study to investigate the effect of a surfactant on gas exchange and especially on the processes enhancing the gas exchange. Triton X-100 is a typical slick used for gas exchange measurements and often used as a reference substance (Frew et al. 1995, Mesarchaki et al. 2014, Wurl et al. 2011). Its molecular formula is $C_{14}H_{22}O(C_2H_4O)_n$. It consists of a hydrophobic group (aromatic hydrocarbon) and a hydrophilic group (polyethylene oxide). It is a soluble nonionic material. The maximum concentration of Triton (0.26 µmol/L) used in this thesis has no influence on the surface tension (personal communication K. Krall).

3
Methods

In this chapter a novel method to visualize the exchange of a gas at a wavy air-water interface is presented. Commonly used methods able to visualize the aqueous mass boundary layer are laser-induced fluorescence (LIF) techniques, which measure a vertical concentration profile by observing fluorescence from the side (Herlina and Jirka 2008, Münsterer and Jähne 1998). Gas concentrations are transformed into fluorescence intensity either by using acid-base reactions and pH sensitive dyes (e.g. Herzog (2010)), or by using dyes whose fluorescence is quenched by a trace gas (e.g. oxygen, see Friedl (2013)). Since the water-side mass boundary layer is in the order of 20 - 200 µm (see sec. 2.2.1), a high spatial resolution far better than 10 µm is necessary to resolve the concentration gradient at the surface. Also, high temporal resolutions are needed to detect the water surface (Friedl 2013). Thus, it is not feasible to use these techniques with high wave amplitudes. From averaged concentration depth profiles, the local transfer velocity can be determined. However, interpretation of the time resolved signal of such a profile is tricky, as no information about the horizontal direction of the observed motion is available.

Due to the spatial and temporal variability of the exchange between air and water and in order to resolve processes enhancing the exchange, e.g. microscale wave breaking, Langmuir circulation, and wave breaking (see sec. 2.3), it is desirable to image the near-surface processes horizontally at the water surface. Such a technique already exists for the investigation of heat exchange. The thermal footprint of the water surface can be visualized with infrared cameras. Since gases have a much larger water-side Schmidt number than heat (see sec. 2.1.1), it is not clear if gas and heat are influenced similar by the different processes.

Therefore, a novel two-dimensional technique to visualize gas concentrations in the water-side mass boundary layer is developed (Kräuter et al. 2014). The measure-

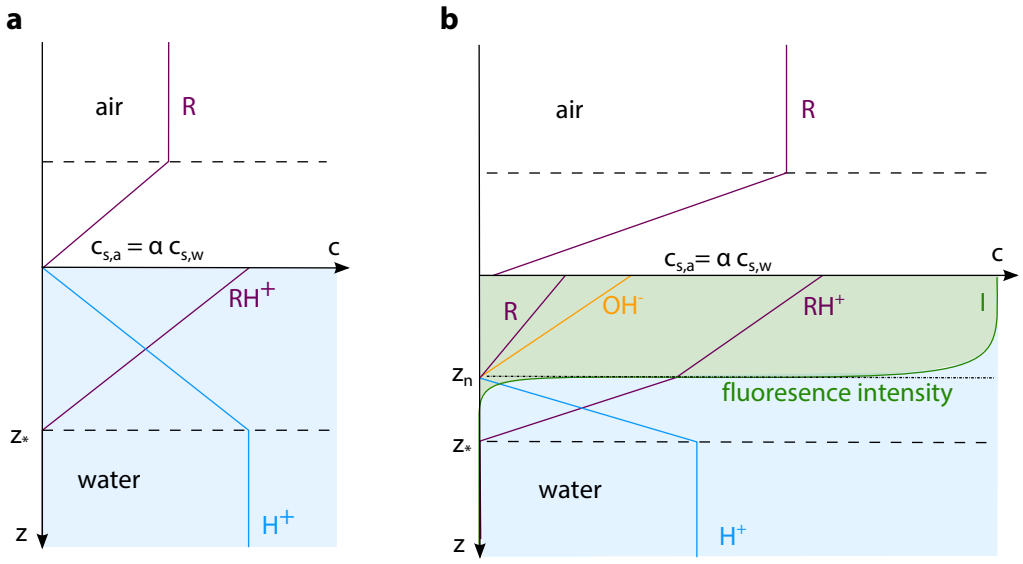

Figure 3.1.
a Schematic concentration depth profile for the invasion of an alkaline gas [R] (purple) into acid water with the boundary layer thicknesses (z_*) in air and water respectively. Also shown is the water-side concentration profile of the reaction product of the alkaline gas [RH^+]. At the surface the pH value is 7 and the concentration of [R] is close to zero. **b** For a higher concentrations of the alkaline gas [R] (purple) in the air. An alkaline layer with a neutral layer thickness (z_n) is formed in which pH > 7. Also shown is the intensity profile over depth (green line) for a pH dependent fluorescent indicator I, and concentrations of hydrogen ions (blue), hydroxide (orange) and the alkaline gas (purple). In the neutral layer the [H^+] concentration decreases due to autoprotolysis. (Modified after Kräuter et al. (2014))

ment principle of the method is based on an idea by Hiby et al. (1967) to investigate gas absorption in falling films. It was used by Braun et al. (1971), Fahlenkamp (1979), and Wolff et al. (1991) for the same purpose. A change in concentration of an alkaline gas in water is visualized by a fluorescent pH indicator. The application of a similar method for studying gas exchange at larger laboratory facilities was already proposed by Jähne (1985). However, it has never been successfully implemented before, mostly due to a lack of suitable light sources for fluorescence excitation and sensitive cameras for fluorescence detection.

In the following sections, the novel measurement technique that is based on the ideas by Jähne (1985) is presented. The chemical components, which are crucial for the technique are described. Simulations to verify the technique and to show some possibilities are presented. Additionally, a method to obtain the ratio of the air to water-side transfer velocity is proposed and the method to compute integrated transfer velocities is described.

3.1 Basic measurement principles

The main idea of the method is to transform the concentration gradient of a dissolved gas into a step function of pH, which is visualized by a pH indicator.

Chemical reactions

If an alkaline reacting gas [R] is dissolved in water, it forms a protonated ion

$$[R] + [H_2O] \longrightarrow [RH^+] + [OH^-]. \tag{3.1}$$

In an acid solution, the proton is transferred from one of the abundant $[H_3O^+]$ ions to the alkaline gas

$$[R] + [H_3O^+] \longrightarrow [RH^+] + [H_2O]. \tag{3.2}$$

A measure for the strength of the reaction with an acid solution is the acid dissociation constant

$$pK_a = -\log_{10}\left(\frac{[H_3O^+][R]}{[RH^+]}\right), \tag{3.3}$$

with the acid component $[RH^+]$ and the conjugate base [R]. The larger the difference between pK_a and the pH value

$$pH = -\log_{10}([H_3O^+]), \tag{3.4}$$

the more rapidly the base [R] is protonated.

For the boundary layer visualization (BLV) method, gases with $pK_a > 9$ are chosen. As a consequence, molecules [R] entering an acid solution immediately react to $[RH^+]$ and the concentration of [R] in water remains virtually zero. Thus, as long as the solution is sufficiently acid, water-side transport processes do not have an influence on the gas flux, the transfer is air-side controlled (see sec. 2.2.3). This is shown schematically in Fig. 3.1(a), where a concentration gradient forms in the air-side mass boundary layer. Protonated gas ions $[RH^+]$ accumulate at the water surface, while the concentration of the hydrogen ions decreases. As the surface becomes less acid, processes in the water do matter, as almost all hydrogen ions ($[H^+] < 10^{-7}$) are "eaten up" by the reaction and the supply is limited by transport from the bulk water.

The alkaline/neutral layer

If the influx of ammonia from the air is faster than this transport in the water, the reaction (3.2) is replaced by reaction (3.1) at the water surface and the pH increases above 7. This situation is shown in Fig. 3.1(b), where hydroxide ($[OH^-]$) is created in the upper layer (orange line). As the pH approaches the pK_a, the equilibrium in eq. (3.1) is shifted more and more to the left side and significant amounts of [R] are physically solved and do not react to $[RH^+]$ (purple lines). The top part of the boundary layer is now alkaline (green area). At the surface, the total water-side concentration of $c_{s,w} = [R] + [RH^+]$ has to be equal to the product of the air-side concentration $c_{s,a}$ and the solubility α (see eq. (2.28)). The depth at which pH = 7 is called neutral layer thickness z_n in the following.

Near the neutral layer, a strong pH gradient exists. This is due its logarithmic definition (see eq. (3.4)). The pH increases only by one unit, when the $[H^+]$ concentration has decreased to 10 % of the bulk concentration, by two units for a decrease to 1 % of the bulk. At this point, a small absolute decrease has a large effect on pH and the pH gradient becomes very steep as the $[H^+]$ concentration decreases to nearly zero approaching the neutral layer. In the alkaline layer above, the pH gradient is much smaller, since the pH value is closer to the pK_a value of the gas and more and more of the alkaline gas [R] is physically solved (see Fig. 3.1(b)).

Visualization of the alkaline/neutral layer

A pH dependent dye with a pK_a value close to seven is added to the water to visualize the alkaline layer. The dye has two forms, which are in a pH dependent equilibrium

$$[IH] + [OH^-] \longleftrightarrow [I^-] + [H_2O], \tag{3.5}$$

where [IH]/[I–] are the protonated/deprotonated forms of the dye. At low pH values, where many $[H^+]$ to protonate the dye are present, the equilibrium is shifted to the right, at higher pH values it is shifted to the left. Both forms can be excited to fluorescence, but have different absorption spectra. Thus, by exciting the dye with the right wavelength, it starts to emit light only for pH values larger than its pK_a value. Hence, the alkaline layer (pH > 7) is made visible. Due to the fast change in pH at the neutral layer depth, it is visible with a well defined boundary, while the bulk is non fluorescent. Since the fluorescence has an almost binary behavior with a nearly constant intensity over the alkaline layer, the depth-integrated fluorescence is linearly related to the depth of the neutral layer z_n. This allows the measurement of the neutral layer thickness by measuring fluorescence intensity.

The neutral layer thickness depends on the concentration of the alkaline gas in the air. The higher the air-side concentration, the more hydroxide is produced at the surface. The increased flux of hydroxide increases the thickness of the layer in which they are more abundant than $[H^+]$ and thus the pH > 7. Given a certain surface

concentration of ([R] + [RH^+]), the neutral layer scales with the mass boundary layer thickness. This is clear from Fig. 3.1(b). Given a fixed concentration of ([R] + [RH^+]) at the water surface and of [H^+] in the bulk, increasing the boundary layer also increases the neutral layer. However, the water surface concentration of ([R] + [RH^+]) does not necessarily scale linearly with the air-side concentration. This will be discussed in detail in app. A.1.

Possible investigations

The considerations made in this section are idealized and only true for mean concentration profiles. Time-resolving measurements as for example by Friedl (2013) and Herzog (2010) show that gases are transported randomly by eddies from the surface to the bulk. Only by averaging over many vertical concentration distributions the discussed behavior can be observed.

The concentration of the alkaline gas has to be high enough to achieve pH values larger than seven to visualize concentrations close to the water surface. For larger accumulations, the integrated intensity over the depth is higher. Due to the processes described in sec. 2.3, eddies beneath the water surface form divergence and convergence zones. In the divergence zones fresh acid water is transported to the surface and pushes the surface water aside. The surface water, which is enriched with the alkaline gas is pushed together in the convergence zones. This leads to high ammonia concentrations and high pH values and hence to fluorescence in the convergence zones. The divergence zones are acid and non fluorescent. Hence, by observing the water surface horizontally, similar structures as seen with the thermal imaging are visible (see sec. 2.3). The near-surface turbulent processes creating the concentration distributions in the mass boundary layer are visualized. This enables for example the investigation of Langmuir circulations, fish-scales and microscale breaking.

Another possibility with the new technique is to investigate the turbulent structures in different depths. This is achieved by increasing the air-side concentration of the alkaline gas, since the neutral layer depth increases and deeper turbulences are visualized.

3.2 Chemical components

A careful selection of the components is crucial to realize the method described above. Therefore, the properties of the different chemicals will be addressed in this section in more detail. Additionally, a short introduction to fluorescence is given.

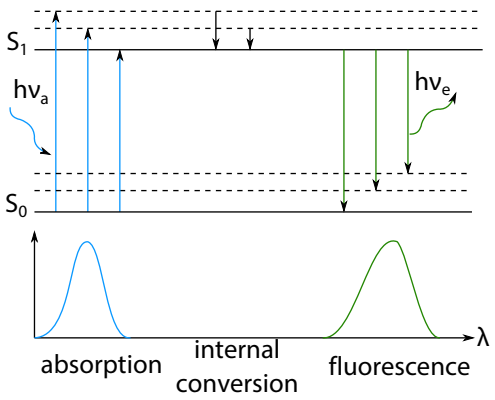

Figure 3.2
Jablonsky diagram of a simplified atomic system with two states: ground state S_o and exited state S_1. The absorption of photons is shown in blue, the emission in green. Absorption and emission spectra are shown schematically. Transitions between different vibrational and rotational states are also possible by internal conversion without photon emission (center).

3.2.1 Fluorescence basics

Fluorescence is the spontaneous emission of a photon induced by a transition from a short-lived excited electronic state to a state with lower energy. A simplified Jablonsky diagram is shown in Fig. 3.2. It shows a 2-level atomic system with the ground state S_0 and the excited state S_1. A photon with the energy $h\nu_a$ excites an electron to the excited state. The electron in the excited state dissipates some of its energy by internal conversion between the vibrational and rotational states and it then emits a photon to get back to the ground state. Emitted photons have a lower energy than the absorbed photons and hence higher wavelengths. The difference between the absorption and emission wavelengths/frequencies is called Stokes shift. Due to the additional energy levels, different transitions are possible and the absorption and emission spectra are broad. The lifetime of the excited state is on the of nanoseconds.

3.2.2 Indicators

Fluorescent indicators were already introduced in sec. 3.1. Depending on the pH value, either the protonated form [IH] or the deprotonated form [I^-] is dominant. If used in low concentrations, they do not have a significant influence on the pH value. However, the concentration of the dye must be much smaller than the [H^+] concentration. If the pH value of the water is the same as the dissociation constant pK_a of the dye, both forms exist in the same concentration ([IH] = [I^-]). This point is called equivalence point or acid-base equivalence point. Figure 3.3 shows the absorption at different wavelengths and varying pH values. The wavelength at which the absorption is constant at all pH values is called isosbestic wavelength. Close to this point the intensity changes faster. For further reading it is referred to Lakowicz (2006).

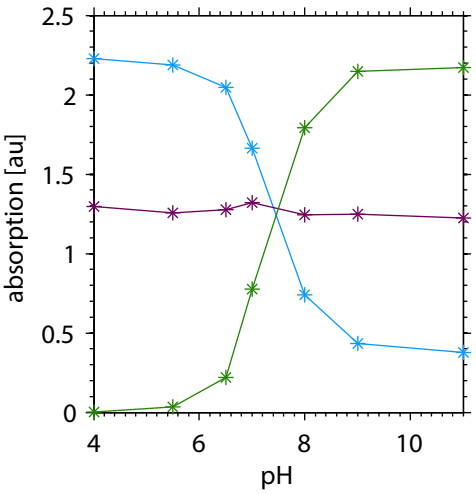

Figure 3.3
Measured absorption spectra of Pyranine at different wavelengths and pH values. At $\lambda = 370$ nm (blue line) the absorption is higher for low pH values while at $\lambda = 470$ nm (green line) the absorption is largest at higher pH values. At the isosbestic point $\lambda = 415.8$ nm (purple line) the absorption is independent of the pH value.

Fluorescent indicator

In sec. 3.1, it is pointed out that the equivalence point should be close to seven to get a sharply defined neutral layer depth. This is fulfilled for the pH dependent fluorescent indicator Pyranine, shown in Fig. 3.3. **Pyranine**, which is also called HPTS (8-hydroxypyrene-1,3,6- trisulfonic acid) has the chemical formula $C_{16}H_2Na_3O_{10}S_3$. Its molar mass is 524.4 g/mol. The protonation time of Pyranine is approx. 5.6 ns. Avnir and Barenholz (2005) report a pK_a value of approximately 7.3. The pK_a value varies in the range of 7.3 - 8.04 depending on the concentration of additional salts/ions in the solution. Measurements on this dependency have been conducted by Förster (1950), Goldberg et al. (1992), Pines and Huppert (1986), and Herzog (2010). Pyranine has been used before to measure the concentration of ammonia by Wolfbeis and Posch (1986).

The [IH] and [I^-] components are excited at different wavelengths, but they have the same emission spectra. The absorption and emission spectra of Pyranine are shown in Fig. 3.4 for different pH values. Light with wavelengths larger than 415 nm is absorbed by alkaline solutions. The alkaline absorption peaks at $\lambda = 455$ nm. At lower wavelengths the absorption is larger for acid solutions. At $\lambda = 415.9$ nm the absorption is independent of the pH value (see also Fig. 3.3). This is the so called isosbestic point. This wavelength is used to calculate the total concentration of Pyranine in water (Avnir and Barenholz 2005).

Pyranine has many advantages compared to other fluorescent indicators. Wolfbeis et al. (1983) studied 20 different pH indicators to find that Pyranine is the most suitable one for pH measurements in water. They point out the large Stokes shift of 61 nm, which makes the excitation light better distinguishable from the emission light. This facilitates the use of broad band light sources, which are used in this study (see sec. 4.1). The emission peaks at $\lambda = 511$ nm (Avnir and Barenholz 2005) shown in Fig. 3.4(b) for an excitation at $\lambda = 455$ nm. Another benefit of Pyranine is its high

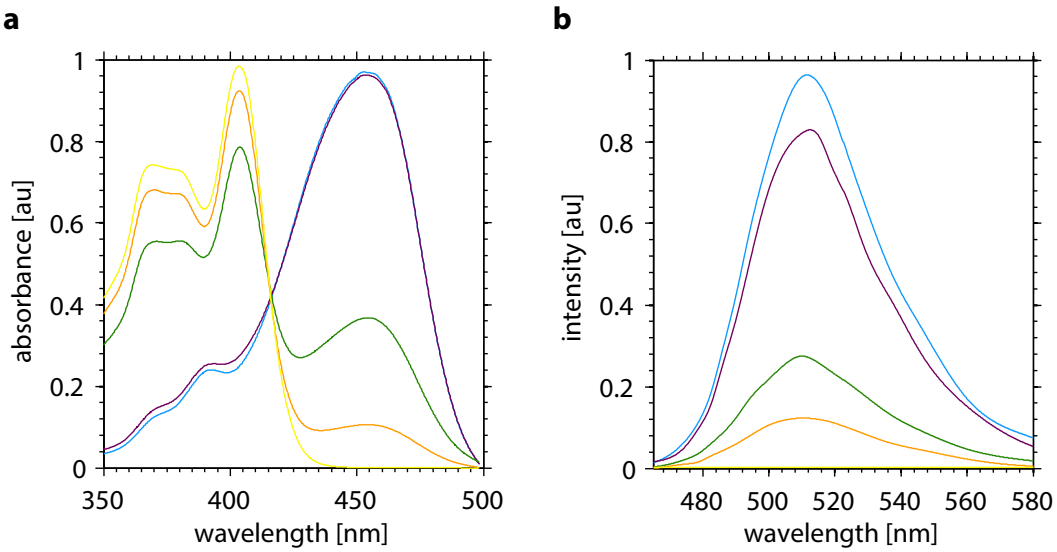

Figure 3.4.
a Absorption spectra of Pyranine for different pH values: pH = 11 (blue line), pH = 9 (purple line), pH = 7 (green line), pH = 6.5 (orange line), and pH = 4 (yellow line). **b** Emission spectra of Pyranine at an excitation wavelength of $\lambda = 455$ nm (Wolfbeis et al. 1983) for the same pH values as in (a).

quantum efficiency of 0.986 (Wolfbeis et al. 1983). Nearly all absorbed light is emitted. Many other properties make Pyranine to a well suited dye for the method described in sec. 3.1, e.g. the insensitiveness for photo bleaching, temperature, and quenching with oxygen (Wolfbeis et al. 1983). It has a low surface activity avoiding surface contamination by the dye itself (Avnir and Barenholz 2005). Barnadas-Rodríguez and Estelrich (2009) investigated the effect of Triton X-100, the surfactant used in this thesis, on the fluorescence of Pyranine. There is no effect on the intensity for the concentrations of Triton used in this study. Table 3.1 summarizes the most important properties of Pyranine.

Table 3.1.
Short summery of the properties of Pyranine and Tartrazine. The molar masses are taken from NIST (National Institute of Standards and Technology). The other properties of Pyrainine can be found in Avnir and Barenholz (2005) and Wolfbeis et al. (1983) and of Tartrazine in Perez-Urquiza and Beltran (2001).

compound	formula	M [g/mol]	pK_a	$\lambda_{max,abs}$ [nm]	$\lambda_{max,emi}$ [nm]
Pyranine	$C_{16}H_2Na_3O_{10}S_3$	524.4	7.3	455	511
Tartrazine	$C_{16}H_9N_4Na_3O_9S_2$	534.4	4.57	426	-

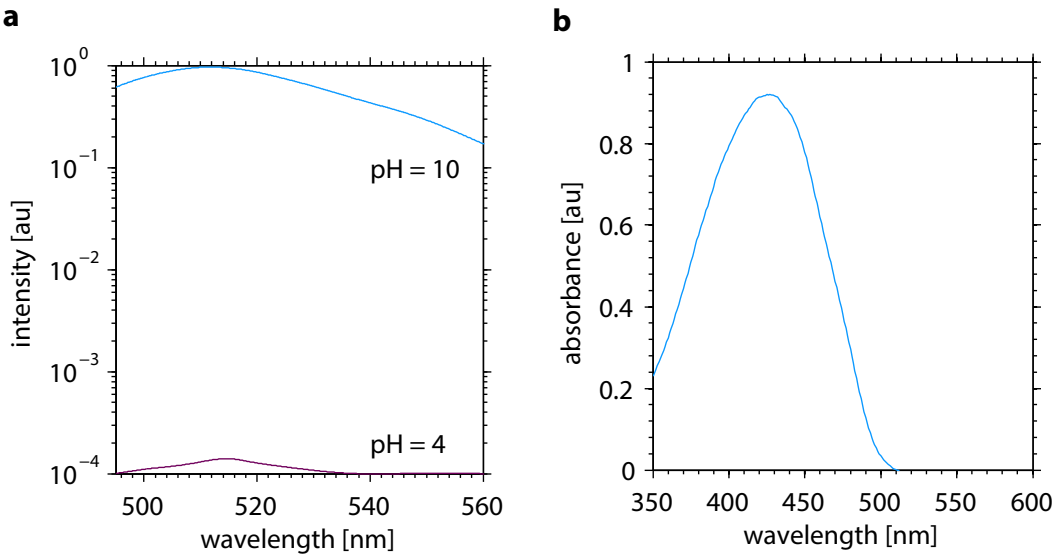

Figure 3.5.
a Emission spectra of Pyranine in the wavelength range from $\lambda = 495$ nm to $\lambda = 560$ nm in a logarithmic scale. The blue line shows the emission at pH = 10 and the purple line at pH = 4. **b** Absorbance of Tartrazine in a concentration of 5×10^{-6} mol/L in a 10 cm cell.

Absorbing dye

Figure 3.5(a) shows the emission spectra of Pyranine in a logarithmic scale for a high (blue line) and a low (purple line) pH value for an excitation at $\lambda = 455$ nm. Even at low pH values there is some fluorescence from the acid bulk. It is necessary to suppress the shown fluorescence from the acid water bulk to achieve the binary behavior of the neutral layer, meaning that no fluorescence is coming from the layer beneath the neutral layer. Additionally, the wave crests of larger waves would be brighter due to the larger underlying water body and the troughs would be darker. This would lead to a miss interpretation of the neutral layer thickness.

As shown in Fig. 3.5(a), the intensity ratio between high and low pH values is approximately 10^{-4}. Thus, an alkaline layer of 100 µm is as fluorescent as 100 cm of the acid bulk. This causes a problem for larger water columns as have been used in this study. However, if a second dye, which absorbs the excitation light (and does not emit fluorescent light) is mixed in the water, fluorescence from the bulk is suppressed.

One possible absorbing dye is **Tartrazine** (Food Yellow 4). The absorption spectrum is shown in Fig. 3.5(b). Tartrazine absorbs in the blue wavelength range, which corresponds to the excitation light for Pyranine and is therefore suitable.

Tartrazine is a synthetic azo dye, which is used in the food industry as a colorant (yellow). The IUPAC name is Trisodium (4E)-5-oxo-1-(4-sulfonatophenyl)-4-[(4-sulfonatophenyl)hydrazono]-3-pyrazolecarboxylate and its molecular formula is $C_{16}H_9N_4Na_3O_9S_2$. It has a molar mass of 534.4 g/mol and is soluble in water. Tar-

trazine stays colorfast also in acid media and under high irradiation and temperatures. Perez-Urquiza and Beltran (2001) report a pK_a value of 4.57. In Tab. 3.1 the main properties of Tartrazine are summarized.

Figure 3.5(b) shows the absorption of Tartrazine in water at a concentration of 5×10^{-6} mol/L in a 10 cm cell. This leads to a decrease of to 1/e in the intensity of the excitation light in 10 cm for the used light sources in the experiments (see sec. 4.1.4). The same concentration was used in the experiments conducted in this study. Since the neutral layer is in the order of some millimeters, the decrease of the incident light within this layer can be neglected.

3.2.3 Alkaline gas

Table 3.2.
Short summary of the properties of ammonia, methylamine, and dimethylamine. The molar masses are taken from NIST (National Institute of Standards and Technology), the solubilities from Sander (1999), and the diffusion constants from Yaws (1999). The star marks the solubility used for the calculations in this study.

compound	formula	M [g/mol]	α	pK_a	D_w [cm^2/s]	D_a [cm^2/s]
ammonia	NH_3	17.03	800-2256 (1713*)	9.25	1.64×10^{-5}	0.23
methylamine	CH_3NH_2	31.06	880-2202	10.60	1.61×10^{-5}	0.15
dimethylamine	$(CH_3)_2NH$	45.08	758-1394	10.71	1.25×10^{-5}	0.12

Amines are good candidates as alkaline gases due to their high pK_a values and high solubilities, see Tab. 3.2. Since **ammonia** is the least toxic and a lot of absorption reference data for ammonia are available (Bouwmeester 1981, Edner 1993, Mellqvist 1995, Tannenbaum et al. 1953), it was selected for the measurements presented in this thesis. The absorption reference data is important to monitor the air-side concentration with a spectroscopic technique.

Ammonia consists of one nitrogen and three hydrogen atoms (NH_3), its IUPAC name is azane. It is a colorless diamagnetic gas with a characteristic pungent smell. In connection with water ammonia acts as a base, takes up a proton

$$[NH_3] + [H_2O] \rightleftharpoons [NH_4^+] + [OH^-] \tag{3.6}$$

and reacts to ammonium (NH_4^+) and hydroxide (OH^-). Clegg and Brimblecombe (1989) measured a dissociation constant pK_a for the reaction at 25 °C of 9.25 and report a temperature dependence of

$$pK_a = 14 - \log_{10}(16.9732 - \frac{4411.025}{T} - 0.0440T). \tag{3.7}$$

Another important attribute of ammonia to be a well suited alkaline gas is its high

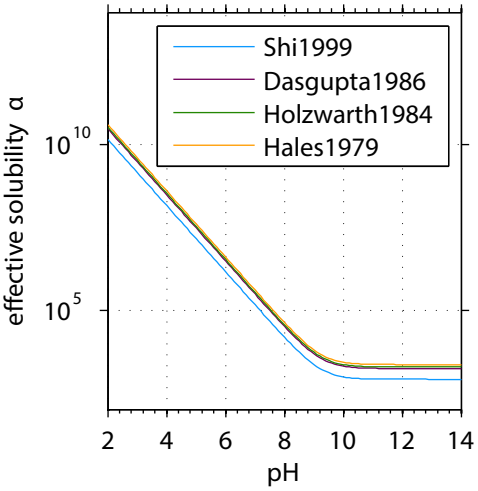

Figure 3.6
The effective dimensionless solubility α of ammonia for different pH values. Physical solubilities are taken from Shi et al. (1999), Dasgupta and Dong (1986), Holzwarth et al. (1984), and Hales and Drewes (1979) at 20 °C.

solubility in water. A high solubility leads to high accumulation rates in the waterside boundary layer (see sec. 2.2.2). For ammonia, different physical solubilities are reported in the literature. The values vary from a dimensionless physical solubility of $\alpha = 812$ (Shi et al. 1999) to $\alpha = 2256$ (Hales and Drewes 1979). In Fig. 3.6 the effective dimensionless solubility α is shown for different pH values. For the figure, the physical solubilities of the four authors are taken and the dependence of the effective solubility on the pH is calculated by eq. (2.31).

Dasgupta and Dong (1986), Hales and Drewes (1979), Shi et al. (1999), and Holzwarth et al. (1984) argue about the true value and point out different error sources in the measurements. For example Shi et al. (1999) measured at very high pH values and argues that other authors do not measure at high enough pH values. They state that at high pH values, ammonium and hydroxide are forming a surface complex, which lowers the uptake capacity of ammonia at the surface and hence the physical solubility. Other authors measure at low or high concentrations of ammonia and propose this may be an effect explaining the different results (Hales and Drewes 1979). In the following the solubility measured by Dasgupta and Dong (1986) will be used, since they collected their data at a high pH value and at concentrations in the low parts per million range, which resembles the measurement conditions in this study. The temperature dependence of the solubility is given by

$$\ln k_H = \frac{4092}{T} - 9.7 \tag{3.8}$$

with the Henry solubility k_H in mol/(m^3 Pa). The given error is less than 5 % (Dasgupta and Dong 1986). The diffusivity of ammonia is shown in Tab. 3.2. Additionally, one should consider the diffusivity of ammonium and hydroxide. The diffusivity of hydroxide is 5.28×10^{-5} cm^2/s and hence much higher than the diffusivity of

ammonium ($D = 1.96 \times 10^{-5}\,\mathrm{cm^2/s}$). The coupled diffusion coefficient is

$$D_{\mathrm{NH_4OH}} = \frac{2}{1/D_{\mathrm{NH_4^+}} + 1/D_{\mathrm{OH^-}}} = 2.9 \times 10^{-5}\mathrm{cm^2/s} \tag{3.9}$$

as shown by Cussler (2009). Amines, e.g. methylamine and dimethylamine are also good candidates as an alkaline reacting gas, due to their high solubility and large pK_a values. They are combinations of ammonia with alkyl or aryl groups and are organic compounds. In comparison to ammonia they have larger pK_a values. This would lead to higher pH values at the surface and within the neutral layer. Table 3.2 gives a short summary on the main properties of ammonia and two amines.

3.3 Simulations

For the method explained above it is assumed that the neutral layer has a binary behavior with a steep cutoff. By increasing the air-side concentration or if the mass boundary layer gets thicker it was argued that the neutral layer is increasing as well. To check the assumptions, find the most suitable concentrations of the used chemicals and to find a relationship between the fluorescent intensity/neutral layer thickness and the ammonia concentration, the chemical system is simulated (Kräuter et al. 2014). The concentration and intensity profiles in the water are calculated. For simplification, only averaged profiles are computed.

To calculate the averaged profiles of the intensity, ammonia, ammonium, and hydrogen concentrations, the equations describing the chemical system must be solved. Autoprotolysis of water

$$[\mathrm{OH^-}] \cdot [\mathrm{H^+}] = 10^{-14}\mathrm{mol^2/L^2}, \tag{3.10}$$

mass conservation of ammonia

$$[\mathrm{NH}_x]_\mathrm{w} = [\mathrm{NH_3}]_\mathrm{w} + [\mathrm{NH_4^+}], \tag{3.11}$$

mass conservation of Pyranine

$$[\mathrm{I}]_\mathrm{tot} = [\mathrm{IH}] + [\mathrm{I^-}] = \mathrm{const.}, \tag{3.12}$$

charge conservation

$$[\mathrm{H^+}] + [\mathrm{NH_4^+}] = [\mathrm{OH^-}] + [\mathrm{I^-}] + [\mathrm{Cl^-}], \tag{3.13}$$

the acid-base equilibrium of the indicator, the ammonia hydrogen reaction (eq. (3.5), and eq. (3.6)) are considered. $[\mathrm{NH}_x]_\mathrm{w}$ is the total water-side ammonia concentration, including ammonia and ammonium. Its surface concentration $[\mathrm{NH}_x]_\mathrm{s,w}$ is scaled to the air-side concentration by Henry's law eq. (2.28). The air-side concentration

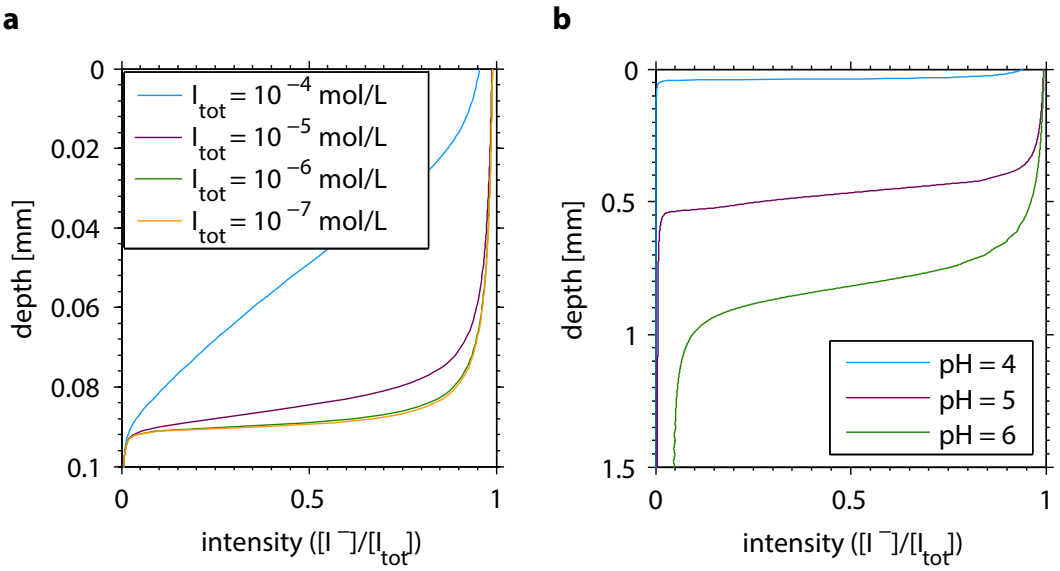

Figure 3.7.
a Averaged and normalized intensity profiles over the depth for different concentrations of Pyranine. The boundary layer thickness in the simulations is set to 200 µm, the surface concentration of $[NH_x]_s$ is 2.5×10^{-4} mol/L and the pH value is 4. For the simulation, the surface renewal model is used. **b** Normalized intensity depth profiles for different pH values at the start of a measurement. The Pyranine concentration in water is 10^{-6} mol/L and the surface concentration is $[NH_x]_s$ is 2.5×10^{-4} mol/L. (Modified after Kräuter et al. (2014))

$[NH_3]_a$ is controlled by the injection rate and therefore $[NH_x]_{s,w}$ can be controlled. $[I]_{tot}$ is the concentration of Pyranine, which is mixed into the water, which partly dissolves to its deprotonated form (see sec. 3.2). $[Cl^-]$ is the chloride concentration in water. Hydroxide chloride is added prior to an experiment to change the pH value of the water. $[I]_{tot}$, $[NH_x]_{s,w}$ and $[Cl^-]$ are controllable parameters. The other chemicals are variables, which must be calculated numerically. The problem consists of six equations (eq. (3.5), (3.6), (3.10), (3.11), (3.12), and (3.13)) and six variables ($[H^+]$, $[NH_4^+]$, $[OH^-]$, $[I^-]$,$[NH_3]_w$, $[NH_x]_w$) and can therefore be solved.

Two models describing the concentration profile are used to compute a depth profile: the small eddy model (SEM) and the surface renewal model (SRM) (see sec. 2.2.4). In every simulation two of the three controllable components ($[I]_{tot}$, $[NH_x]_{s,w}$, and $[H^+]$ (pH)) are kept constant while the other one is varied. In the simulations shown and explained in the following section, the boundary layer depth is set to 200 µm. If the bulk pH value is not varied it is four ($[H^+] = 10^{-4}$ mol/L), the $[NH_x]_s$ concentration (surface concentration consisting of ammonia and ammonium) is 2.5×10^{-4} mol/L and the Pyranine concentration is $[I]_{tot} = 10^{-6}$ mol/L. The shown simulations use the surface renewal model to describe the gas exchange, but nearly the same results are achieved for the small eddy model (Coantic 1986), which will be shown at the end of this section.

Pyranine

Figure 3.7(a) shows the normalized intensity profiles ($[I^-]/[I]_{tot}$) over the depth for different Pyranine concentrations. $[I^-]$ is the component of Pyranine that is excited to fluorescence and abundant in alkaline water. The lower the concentration is, the steeper the intensity profile over the depth gets. At high concentrations (blue line) the intensity decreases slowly towards the depth. Pyranine reacts with the hydrogen molecules (see eq. (3.5)) and therefore the pH change is buffered. A higher pyranine concentration leads to higher absolute intensities. A concentration of $[I]_{tot} = 10^{-6}$ mol/L (green line) seems to be the best compromise between a high intensity and a steep profile.

Hydroxide chloride/pH

At the beginning of each measurement a certain amount of hydroxide chloride is added to the water to adjust the pH value. The used concentration is crucial, since it influences the steepness of the neutral layer (binary behavior) and the amount of ammonia needed to start the fluorescence. For lower pH values more ammonia is needed to neutralize the pH value and hence start the fluorescence.

In Fig. 3.7(b) the normalized intensity over the depth for different hydroxide chloride concentrations (pH) is shown. For higher pH values (green line) the normalized intensity profile decreases slower than for higher values (blue line). Therefore, a low pH value is most suitable to get a steep change in intensity, but at lower pH values higher ammonia concentrations are needed. A pH of approximately 4 was found to be most suitable.

Surface concentration

In Fig. 3.8(a), the normalized intensity profiles for different $[NH_x]_s$ surface concentrations are shown. This shows the behavior discussed in sec. 3.1 that for higher ammonia concentrations in the air the neutral layer thickness increases. If the ammonia concentration in the air increases, the flux to the water increases and more ammonia accumulates at the water surface. As shown in the figure, higher surface concentrations lead to larger neutral layer depths.

Overall, the simulations demonstrate the importance of choosing the most suitable concentrations of the chemical components and provide an effective tool to do so. Otherwise, the desired sharp increase of intensity at the neutral layer depth is not realized and the assumption that the intensity is proportional to the neutral layer depth is not valid.

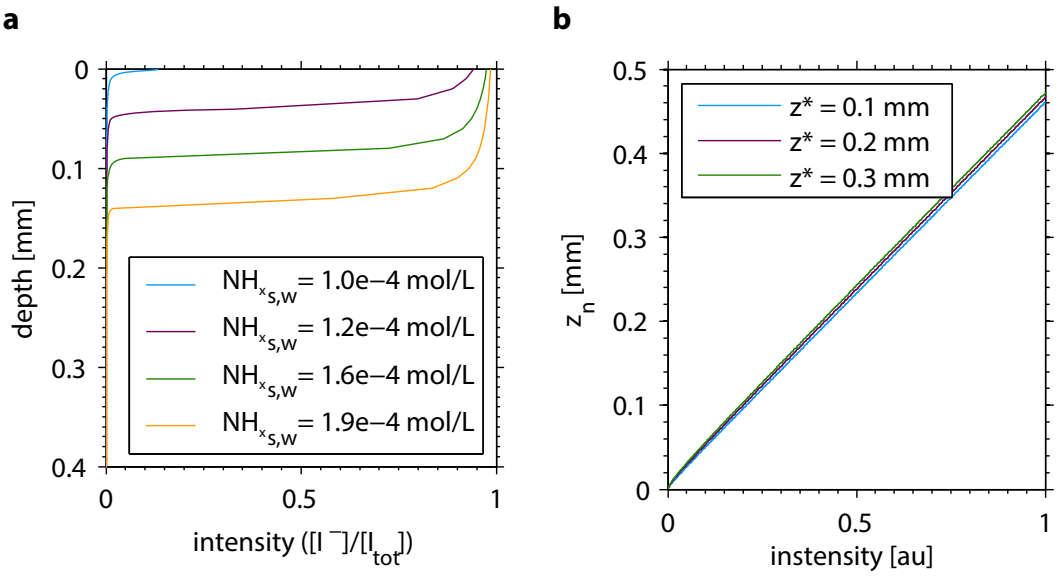

Figure 3.8.
a Normalized intensity depth profiles for different [NH_x] surface concentrations (air-side ammonia concentrations). The boundary layer thickness is 200 µm, the pH value is 4 and the Pyranine concentration is 10^{-6} mol/L. **b** Relation between the neutral layer depth and the integrated and normalized intensity for different boundary layer depths. (Modified after Kräuter et al. (2014))

Relations of neutral layer depth

The simulations above can also be used to show the relationship between different measurable and not measurable values. The neutral layer thickness for example is a value that cannot be directly measured. However, the intensity should be proportional to the thickness as explained before. The neutral layer thickness is calculated in the simulations, by determining the maximum of the intensity gradient. In Fig. 3.8(b), the neutral layer thickness is shown in dependence of the intensity for different boundary layer thicknesses. As can be seen, the neutral layer thickness is linearly related to the absolute intensity for different boundary layer thicknesses. By a calibration of the optical system before a measurement, the absolute neutral layer thickness is determined (see sec. 4.2).

In Fig. 3.9(a), the neutral layer thickness normalized by the boundary layer thickness is shown versus the total ammonia concentration at the surface for different theoretical concentration profiles. Shown are the surface renewal model in blue (SRM) (Danckwerts 1951, Higbie 1935) and the small eddy model in purple (SEM) (Coantic 1986). By measuring the neutral layer thickness and the increasing water-side surface [NH_x] concentration, different models could be tested and the boundary layer thickness could be estimated. Since the water-side surface concentration of [NH_x] cannot be measured directly, the air-side concentration of ammonia has to be used. Since the solubility at the surface changes during the experiments, it is not possible to get the $[NH_x]_{s,w}$ concentration or even get a linear relationship between

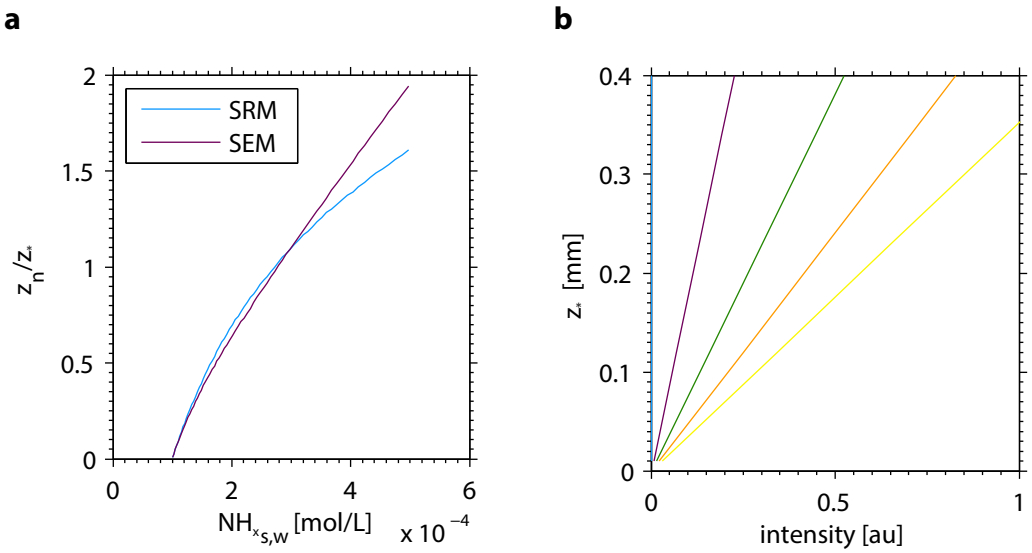

Figure 3.9.
a Relationship between the normalized neutral layer depth and the surface concentration for the surface renewal model (blue) and the small eddy model (purple). **b** For different ammonia surface concentrations the relation between the boundary layer depth and the intensity is shown (blue = 10^{-4} mol/L; purple =1.2 × 10^{-4} mol/L; green = 1.6 × 10^{-4} mol/L; orange = 1.9 × 10^{-4} mol/L; yellow = 2.5 × 10^{-4} mol/L).

the two concentrations. The limitations are discussed in detail in app. A.1.

Figure 3.9(b) shows the boundary layer thickness versus the intensity for different ammonia concentrations. The blue line on the y-axis has the smallest concentration (10^{-4} mol/L). The concentrations increase until the yellow line (2.5 × 10^{-4} mol/L). It is concluded that for averaged mean profiles at a certain water-side surface concentration, there is a linear relation between intensity and the boundary layer thickness and hence inverse to the transfer velocity (see eq. (2.23))

$$k([\mathrm{NH_x}]_{s,w}) \propto \frac{1}{I}. \tag{3.14}$$

3.4 Ratio of the air and water-side transfer velocity

In this section, a method to measure the ratio of the air to the water-side transfer velocity is proposed. The proposed method is only valid for air-side controlled gases as for example ammonia. The flux of ammonia in the air is described by eq. (2.21) as

$$j_a = k_a([\mathrm{NH_3}]_{b,a} - [\mathrm{NH_3}]_{s,a}), \tag{3.15}$$

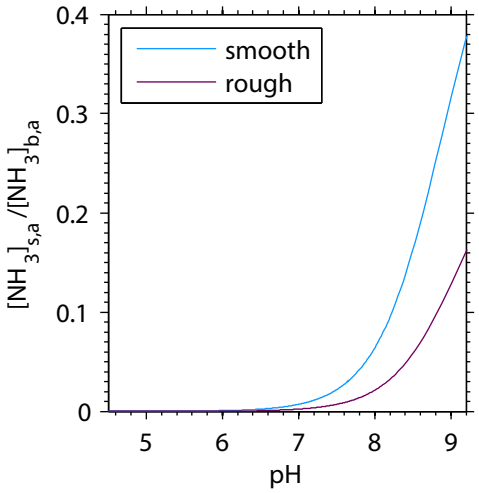

Figure 3.10
The ratio of the air-side surface to bulk concentration of ammonia is shown in dependence of the pH value/solubility (see Fig. 3.6(a)). The ratio depends on the Schmidt number exponent. The two curves are the limiting cases of a smooth surface ($n = 2/3$, blue) and a rough surface ($n = 1/2$, purple).

with the air-side transfer velocity k_a, the ammonia concentration in the air bulk $[NH_3]_{b,a}$, and at the surface $[NH_3]_{s,a}$. It follows for the flux in the water

$$j_w = k_w([NH_x]_{s,w} - [NH_x]_{b,w}), \tag{3.16}$$

with the water-side transfer velocity k_w, the water-side concentration of ammonia and ammonium at the surface $[NH_x]_{s,w}$, and in the bulk $[NH_x]_{b,w}$. Due to mass conservation the fluxes ($j_a = j_w$) are equal and it follows

$$\frac{k_a}{k_w} = \frac{([NH_x]_{s,w} - [NH_x]_{b,w})}{([NH_3]_{b,a} - [NH_3]_{s,a})}. \tag{3.17}$$

If all concentrations could be measured, it would be possible determine the fraction of the air to water-side transfer velocity. However, the concentrations at the interface are difficult to measure due to the high vertical resolution needed to resolve them. One can apply four approximations to solve this problem.

Approximations

Neglect ammonia surface concentration

As long as the exchange of ammonia is air-side controlled, the surface concentration is much small than the bulk air concentration

$$[NH_3]_{b,a} \gg [NH_3]_{s,a}. \tag{3.18}$$

Figure 3.10 shows the dependence of the ratio of these two concentrations on the pH value of water. The lines in the figure show this relationship for two different ratios of the air to water-side transfer velocity k_a/k_w. The ratio of transfer velocities

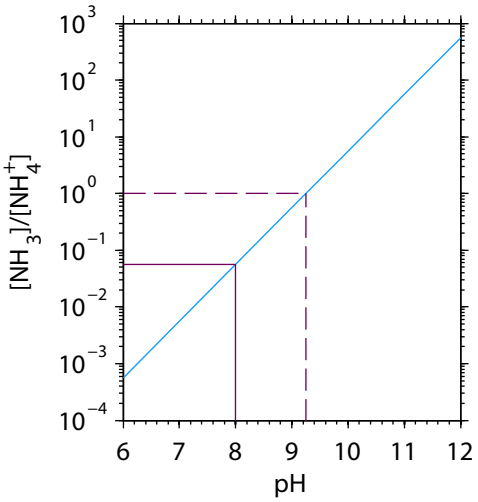

Figure 3.11
The blue line shows the ratio of the ammonia and ammonium concentration for different pH values calculated by eq. (3.3). The dashed purple line indicates a ratio of one.

is approximated by dividing eq. (2.41) for different Schmidt number exponents and dimensionless momentum transfer resistances β (see eq. (2.2.4)). The ratio changes from approximately 2000 for a solid (smooth) to 700 for a free (wavy) surface. This is used for the two lines in Fig. 3.10. At pH values smaller than 8, the surface concentration can be neglected with a maximum error for ($[NH_3]_{b,a}$ - $[NH_3]_{s,a}$) of less than 5 % . If the pH value reaches the pK_a value of ammonia (pH = 9.25) the surface concentration cannot be neglected due to an error up to 40 %. To summarize: it is possible to neglect the surface concentration for pH ≤ 8 with a maximum error of 5 %, thus in this case:

$$\frac{k_a}{k_w} = \frac{([NH_x]_{s,w} - [NH_x]_{b,w})}{[NH_3]_{s,a}}. \tag{3.19}$$

Neglect ammonia in the water

The total $[NH_x]_w$ concentration in eq. (3.17) is the sum of ammonia and ammonium solved in the water. One approximation is to neglect the ammonia concentration, since for pH < 8 it is much smaller than the ammonium concentration in water

$$[NH_3]_w \ll [NH_4^+]. \tag{3.20}$$

In Fig. 3.11, the dependence of the ammonia/ammonium ratio on the pH value is shown. At low pH value, all ammonia that is solved as $[NH_3]$ in water rapidly reacts with the hydrogen molecules to ammonium. At a pH value of 9.25 (equals pK_a) the concentration of ammonia and ammonium are equal (dashed purple line). Hence, not all ammonia molecules, which are diffusing into the water, are reacting with the hydrogen molecules. Some ammonia gets solved in water. At pH values lower than 8 the ratio $[NH_3]_w/[NH_4^+]$ is less than 5×10^{-2}. By neglecting $[NH_3]_w$ at pH

values smaller than 8 the estimated error is less than 5 % and the ratio of the transfer velocities is

$$\frac{k_a}{k_w} = \frac{([NH_4^+]_{s,w} - [NH_4^+]_{b,w})}{[NH_3]_{s,a}}. \tag{3.21}$$

Equal fluxes

Due to charge conservation the fluxes of ammonium and hydrogen in the water must be opposite and equal

$$j_{NH_4^+} = -j_{H^+}. \tag{3.22}$$

The ammonium concentration $[NH_4^+]$ is replaced by the negative concentration of hydrogen. This is an advantage, since hydrogen in the bulk can easily be measured with a commercial pH sensor and for the ratio follows

$$\frac{k_a}{k_w} = \frac{([H^+]_{b,w} - [H^+]_{s,w})}{[NH_3]_{s,a}}. \tag{3.23}$$

Neglect hydrogen at the surface

Still, the problem of measuring the surface concentration of hydrogen remains. Since the bulk pH value is small ($pH \leq 4$) and Pyranine starts to emit light at $pH \approx 7$, it is possible to neglect the surface concentration of hydrogen.

$$[H^+]_s \ll [H^+]_b \tag{3.24}$$

In the case of a pH value of 7, the error would be 0.1 % and at higher surface pH values even less.

By including the approximations explained above in eq. (3.17) one gets

$$\frac{k_a}{k_w} = \frac{[H^+]_{b,w}}{[NH_3]_{b,a}}. \tag{3.25}$$

The quantities in the equation can all be measured. It is possible to determine the ratio of the transfer velocities for pH values larger than 7 with an error of maximum 5.2 % (estimated by error propagation). At larger pH values the error increases in the approximations eq. (3.18), eq. (3.20), and eq. (3.22), since the pH value change is rapid due to its logarithmic definition. Because the surface pH value cannot be measured directly, the ratio of the transfer velocities can only be measured if the surface starts to be fluorescent ($pH_{surf} \approx 7$).

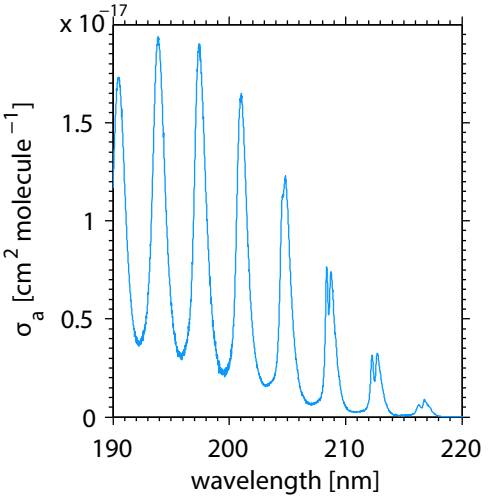

Figure 3.12
The UV absorption cross section of ammonia at 300 K from λ = (190 - 220) nm (Liang et al. 2007).

3.5 Differential optical absorption spectroscopy

The air-side ammonia concentration is measured by UV spectroscopy. The differential optical absorption spectroscopy (DOAS) method (Platt et al. 1979) is used to obtain absolute concentrations. A very brief presentation of the method is given in the following section.

Basics

Each atom/molecule has different discrete energetic states. Photons transport energy depending on their wavelength. If the energy of a photon matches the energy of a band gap of a molecule/atom it is absorbed. The absorption and scattering of light in a medium is described by the **Beer-Lambert Law**

$$I(\lambda, L) = I_0(\lambda) \cdot \exp(-\sigma(\lambda) c L), \tag{3.26}$$

where I is the measured intensity, I_0 is the light spectra without any gas, σ is the absorption cross section, c is the concentration of the gas, and L is the path length. The absorption cross section is a characteristic parameter for a molecule. For ammonia it is shown in Fig. 3.6. It consists of several peaks which correspond to energy differences between electronic states.

If only one gas would be present in the air volume, the lamp spectra without gas could be measured easily ,and there were no scattering processes in addition to absorption, the concentration of a gas could be calculated with eq. (3.26). However, the air has more than one constituent. Gases like nitrogen and oxygen are present. The UV light used to measure the absorption of ammonia produces ozone, which

has characteristic lines in the same wavelength range as ammonia.

$$3\,O_2 \longrightarrow 2\,O_3 \quad (\lambda < 242\,\mathrm{nm}) \tag{3.27}$$

Due to the fixed installation of the spectrometer in the wind-wave facilities, the lamp intensity changes due to the movement of the facility caused by the moving water. This leads to a broad band change of the measured lamp spectra. The Beer-Lambert Law eq. (3.26) cannot be easily used due to these two effects.

DOAS

Platt et al. (1979) invented a technique for the simultaneous measurement of different trace gases in the atmosphere. This technique is used for the determination of the ammonia concentration. The main idea is to split the absorption cross section in two components: broad-band $\sigma_b(\lambda)$ and narrow-band $\sigma'(\lambda)$ structures

$$\sigma(\lambda) = \sigma_b(\lambda) + \sigma'(\lambda). \tag{3.28}$$

The broad-band part includes for example changes of the illumination and scattering effects. In the narrow-band part the absorption peaks of different trace gases are covered. In essence, the spectrum is high pass filtered to remove the broad-band structures and a reference absorption cross section is fitted to the residual narrow-band structures. A detailed description of the technique can be found in Platt and Stutz (2008).

DOASIS

The evaluation of the measured spectra is conducted with the software *DOASIS* by Kraus (2006). The spectrometer data processing routine was developed in co-operation with J. Zielcke and P. Lübcke of the Platt group. The spectrometer has a finite optical and spectral resolution, while the reference cross spectra is measured with a higher resolution. A convolution of a point spread function (PSF) with the reference spectra is conducted to obtain the same spectral resolution. The PSF of the spectrometer is retrieved by measuring the line of a mercury lamp with the used spectrometer. The mercury line is very narrow (a few pm) and the measured peak is, due to the lower resolution of the spectrometer a delta function. An offset is added to the signal to prevent negative intensities. Thermally excited electrons generate an additional signal, which is dependent on the integration time. A spectrum is recorded with a closed entrance slit and the same integration time as during the measurements to correct for these two effects. Since the dark current is temperature dependence a dark spectrum is measured before each measurement. This signal is subtracted from each measured spectrum.

DOASIS corrects for the broad-band effects in the intensity, which differ from

the background spectra I_0, by fitting a 3rd order polynomial to the signal. The fitted polynomial is subtracted from the measured spectra and only the narrow-band structures are present. These bands are fitted with a standard least-square fit to the convoluted reference absorption cross section and the concentration is obtained with eq. (3.26).

3.6 Transfer velocity

In the section above, the computation of the ammonia concentration in air is explained. This section addresses the evaluation of transfer velocity from the concentration measurements for the highly soluble gas ammonia. A more detailed description is found in Kräuter (2011) and Mesarchaki et al. (2014).

A two box model, with the air and water space as the two closed compartments is assumed. The gas is exchanged between these two compartments by gas exchange through the water surface. Ammonia is injected into the sealed air space with a constant flux during the measurement. Without considering gas exchange the concentration in the air space would increase linearly. However, due to the high solubility, ammonia accumulates in the water. The mass balance in air is

$$V_\mathrm{a}\dot{c}_\mathrm{a} = -Ak\left(c_\mathrm{a} - \frac{c_\mathrm{w}}{\alpha}\right) + \dot{V}c_\mathrm{i} - \dot{V}_\mathrm{a}c_\mathrm{a}, \tag{3.29}$$

where V_a is the air volume, A the water surface, α the dimensionless solubility, $\dot{V}$ the input rate, $\dot{V}_\mathrm{a}$ is the leaking volume flux, c_i the input concentration, and c_a and c_w the air and water-side ammonia concentrations, respectively. The last term on the right side of eq. (3.29) describes the fact that the air space is not completely air tight but has small leaks.

If the air-side concentration is much larger than the water-side concentration divided by the solubility ($\frac{c_\mathrm{w}}{\alpha} \ll c_\mathrm{a}$), eq. (3.29) simplifies to

$$0 = \dot{c}_\mathrm{a} + \frac{Akc_\mathrm{a}}{V_\mathrm{a}} - \frac{\dot{V}}{V_\mathrm{a}}c_\mathrm{i} + \frac{\dot{V}_\mathrm{a}}{V_\mathrm{a}}c_\mathrm{a}. \tag{3.30}$$

This assumption is usually fulfilled for highly soluble gases. The water-side concentration is monitored in this experiment by the pH value of the water. Equation (3.30) is solved and for the air-side concentration one gets

$$c_\mathrm{a}(t) = \frac{\dot{V}c_\mathrm{i}}{Ak}(1 - \exp(-\lambda t)), \tag{3.31}$$

with $\lambda = \frac{Ak}{V_\mathrm{a}} + \frac{\dot{V}_\mathrm{a}}{V_\mathrm{a}}$. By fitting this equation to the air-side concentration profile, λ is

determined and hence the transfer velocity

$$k = (\lambda - \lambda_f) h_a, \tag{3.32}$$

with the leak rate $\lambda_f = \frac{\dot{V}_a}{V_a}$ and the height of the air space h_a. The leak rate is measured by measuring the air-side concentration of a non soluble gas. The difference in input and measured concentration is only due to leaks in the air (Mesarchaki et al. 2014).

4
Setup and calibration

This chapter describes the experimental realization of the boundary layer visualization, which was described in sec. 3.1. A short overview of the facilities, at which measurements have been conducted, is given as well as their instrumentation. For a successful realization of the visualization method, a number of crucial optical components have to be carefully selected. For example, to resolve the finest structures on the water surface, a high resolution camera is needed (see sec. 2.3). Also, high power light sources, which are matched to the absorption spectrum of Pyranine (see Fig. 3.4), are necessary to excite fluorescence. The calibration of the camera and light source system for optical defects and the measurement of the fluorescent layer thicknesses is shown at the end of this chapter.

4.1 Setup

Experiments have been performed at two different wind-wave facilities. The setups and the used components are described in detail in this section. Preliminary experiments were conducted at the small linear wind-wave tank (*Benjamin*), the main experiment at the large annular wind-wave facility (*Aeolotron*).

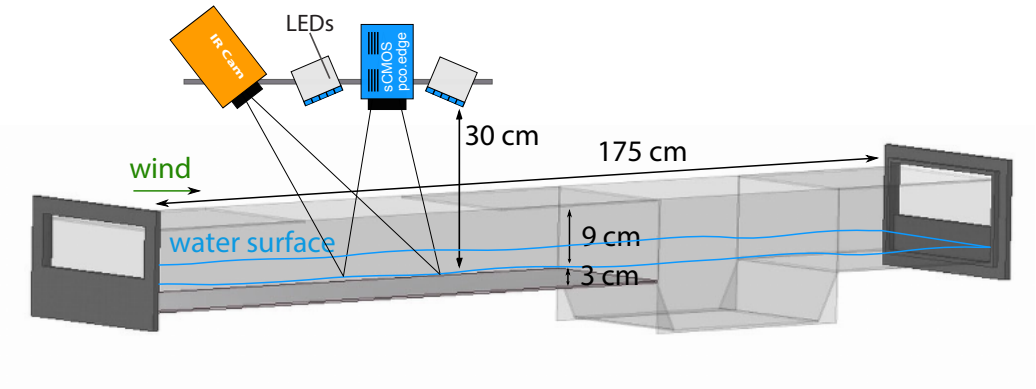

Figure 4.1.
Sketch of the linear wind-wave tank and the setup for the boundary layer visualization. Image modified after Warken (2010).

4.1.1 Linear wind-wave tank

In Fig. 4.1 a sketch of the small linear test facility (*Benjamin*) at the Institute of Environmental Physics in Heidelberg is shown. The tank is described in detail by Krah (2014), Warken (2010), and Winter (2011). Here, only the main aspects important for this thesis are discussed. With a filling height of 3 cm, the water volume of the tank is 22 L and the air volume is 220 L (including the air tubing). A fan generates wind, ranging from 1.5 m/s to 7 m/s and blows the air from left to right. After leaving the area shown in Fig. 4.1, the air is circulated through a tubing system in the back of the facility (Warken 2010). The walls, bottom, and the ceiling are made of Schott Borofloat®glass. This allows optical access from all sides. The materials used have a high chemical resistance to enable the measurements of reactive and corrosive chemicals, e.g. ammonia and hydroxide chloride. On the ceiling, there are two cover plates which can be opened. By changing the cover plates the UV spectrometer can be easily installed at the facility (Winter 2011).

For the visualization of the neutral layer thickness, an illumination and an optical sensor are necessary. The components, a camera (blue) and light sources (LED arrays), are shown in Fig. 4.1. From now on, this setup, consisting of a camera and the light source, is called BLV setup (boundary layer visualization). The BLV setup is mounted 30 cm above the water surface, 50 cm downwind of the beginning of the water channel. The distance over which the wind blows is called fetch. Collocated and simultaneous images with the BLV setup and an infrared camera have been recorded. The infrared camera (orange) has been mounted next to the BLV setup as shown in Fig. 4.1. Because the infrared camera is unable to see through glass, the cover plate was removed and the measurements were conducted with an open air space. Since the spectrometer is installed in the two cover plates, no concentration measurements have been possible during the comparison measurements.

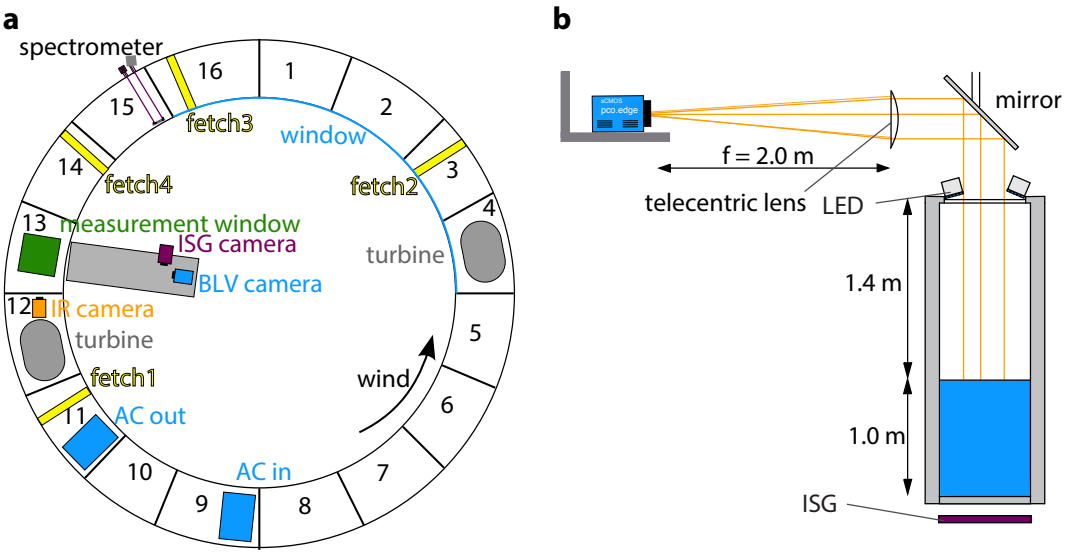

Figure 4.2.
a Sketch of the large annular wind-wave facility, *Aeolotron*, at the Institute of Environmental Physics in Heidelberg. The facility is viewed from the top and the 16 segments are shown (Modified after Krall (2013)). **b** Boundary layer visualization setup at the large wind-wave facility *Aeolotron* viewed from the side. BLV camera and light sources, as well as the ISG light source are shown. (modified after Kräuter et al. (2014)).

4.1.2 Large annular wind-wave tank

The majority of experiments in this study were conducted at the *Aeolotron*, the large annular wind-wave facility at the Institute of Environmental Physics. A sketch of the tank viewed from the top is shown in Fig. 4.2(a). The tank is annular, with an inner diameter of 9 m and a water channel width of 0.6 m. At a mean water depth of 1 m, the water volume is approx. 18000 L. The air volume is approx. 25000 L. The *Aeolotron* is parted into 16 segments as shown in Fig. 4.2(a). Two turbines shown in gray in segments 4 and 12 are producing wind with a maximum reference wind speed of 12 m/s. The channel itself is built to be chemically resistant to corrosive gases and fluids. It is thermally isolated and air tight with very low leakage rates ($\mathcal{O}(0.1)$ 1/h) (Krall 2013). The air tightness of the facility has an unwanted consequence for thermal imaging: The air quickly saturates with water vapor and evaporation (with the associated heat flux) at the water surface stops. Thus, to allow IR imaging of heat fluxes, the air is actively dehumidified with a newly installed air-conditioning system (AC) using a high efficiency heat pump. The air inlet of the AC is installed at segment 9 (see Fig. 4.2(a)). The flushed air is first cooled by condensation and then heated before it is blown out at segment 11. Furthermore, it reduces the reference wind speed by approx. 1.2 m/s at each condition due to its directed flow.

Unlike linear wind-wave facilities, annular facilities do not have a beginning, at which the wind starts to interact with the water, they have unlimited fetch. This also helps to interpret measurements that are integrated over the whole facility, e.g. gas

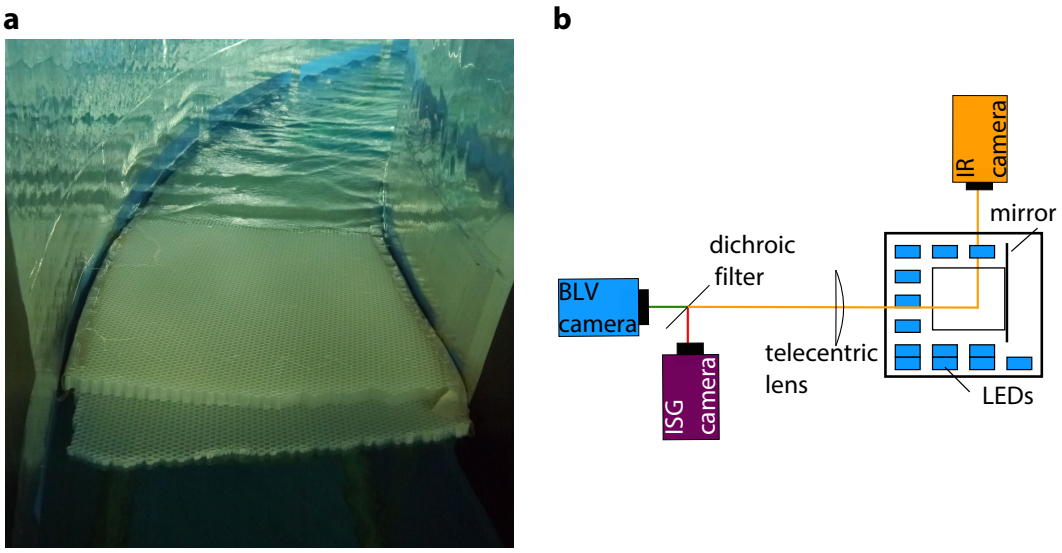

Figure 4.3.
a The wave absorber installed at fetch 4. The waves in the back of the image are clearly visible. After the wave absorber no waves are present. **b** Sketch of the camera setup at the large annular wind-wave facility viewed from above. A dichroic filter reflects the red light of the ISG and transmits the green pyranine fluorescence.

exchange by mass balance. Flow conditions (wind speed, currents, waves) should be the same everywhere along the circumference of the facility. This is not completely true, since the wind is generated locally with two turbines. Due to this and the fact that the annular shape also causes secondary flows, the wind speed and water current vary slightly along the facility (Bopp 2014).

While unlimited fetch is a key advantage of an annular facility, it is also possible to study the initial generation waves and shear currents and the associated flow patterns and turbulence generation. A wave absorber can be installed inside the facility to reduce the fetch to a fraction of the circumference (0 - 27 m). A picture of the wave absorber is shown in Fig. 4.3(a). Behind the absorber, waves and surface currents need to rebuild. Four different positions of the wave absorber have been used in this study, they are marked in yellow in Fig. 4.2(a). The distances between the end of the wave absorber and the center of the measurement window are 23.4 m, 10.2 m, 4.5 m, and 2.0 m for fetch 1, fetch 2, fetch 3, and fetch 4, respectively.

The boundary layer visualization (BLV) setup is installed at segment 13. The setup is shown in Fig. 4.3(b) viewed from the top and in Fig. 4.2(b) viewed from the side. The camera is mounted in the focal point of a large planoconvex BK7 lens (diameter d = 0.32 m, focal length f = 2 m). This lens and the 135 mm standard camera lens form an object-space telecentric lens. This ensures a constant magnification factor even at changing water height due to waves. Over a mirror inclined at 45°, the camera is able to observe a (25 cm × 21) cm^2 patch of the water surface. The light sources are mounted directly above the glass window that is installed in the ceiling

of the wind-wave tank at a height of 1.40 m. The light sources are focused on the measurement spot to enable the highest intensities.

Additional instrumentation is installed at the *Aeolotron*. An infrared camera Velox 327k M by IRcam is mounted in segment 12 in an inclined position and observes the same surface patch as the visible-range camera, which is observing the fluorescence. An imaging slope gauge (ISG) is installed in segment 13 to measure the wave slope at the *Aeolotron* (Kiefhaber et al. 2014). The light source of the ISG is mounted underneath the wind-wave tank as shown in Fig. 4.2(b). They illuminate the water surface with red light at the same measurement spot as the boundary layer visualization setup. The high-speed camera is mounted next to the camera of the BLV setup. This is shown in Fig. 4.3(b). Also installed (and used in the experiments) are Pt-100 temperature sensors (Greisinger, *GMH 5530*) in the air and water, humidity sensors, a conductivity sensor (Greisinger, *GLF 100 RW*), a pH sensor (Greisinger, *GMH 5530 pH/mV* with an electrode *GE106*), an anemometer (Greisinger, *STS020*), and a pitot tube in the air and an acoustic Doppler anemometer (Nobska, *MAVS-3*) in the water.

4.1.3 Camera

For the visualization of the fluorescence signal a *PCO.edge* camera by PCO AG has been used. The scientific CMOS camera was selected because of its high-speed, high-resolution and low-noise. The maximum frame rate is 100 Hz at a full resolution of 5.5 mega pixels (2160 × 2560), the pixel size is 6.5 × 6.5 µm. The major technical challenge in realizing the BLV method is achieving a sufficient signal-to-noise ratio in the fluorescence measurement. The fluorescent layers in the water are very thin (typically well below 1 mm), so only a small fraction of the incident light is actually absorbed. To give an estimate, in an alkaline solution with the Pyranine concentration that was used during the measurements ($c = 5 \times 10^{-6}$ mol/L), a layer with 1 mm thickness has an absorbance of approx. 8.8×10^{-3}. Thus, only 2 % of the incident light contribute to the fluorescence signal (see app. A.2). Furthermore, fluorescence is radiated isotropically and only 2.8×10^{-5} % are captured by the camera (see app. A.2) (Kräuter et al. 2014). Therefore, a very sensitive and low-noise camera is crucial to achieve a sufficient signal to noise ratio.

The *PCO.edge* has a wide dynamic range of 16 bit (65536 gray values). As will be shown later, this is important since the dynamic range of structures on the water surface is also large. Data volume is always an issue with high resolution imaging techniques. In the *PCO.edge*, a compression scheme is implemented, which allows for an online compression of 16 bit data into an 8 bit format, which is nearly lossless. A detailed description of the matter is given by Jähne (2013). It is based on the fact that in high end cameras, the dominant source of noise is photon noise, which increases with the square of the gray value (Poisson distribution). Thus, at higher gray values, a lower resolution is required, since noise is much higher. The result of the nonlinear gray value transformation has approximately equal noise at all the

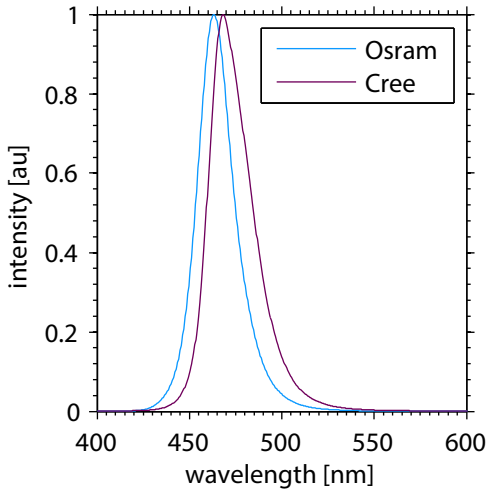

Figure 4.4
Intensity spectra for the used Cree and Osram high power LEDs.

new gray levels. The transformation is given by

$$g(x, y) = \sqrt{(n(x, y) - \text{offset}) \times \text{gain}}, \tag{4.1}$$

where $g(x, y)$ is the saved image, $n(x, y)$ is the original image, and gain and offset are user selectable values to make use of the full 8 bit scale in the output image $g(x, y)$.

Table 4.1.
Camera settings for the different experiments at the small and large facility. The integration time t_{int} is duration, for which the LEDs are flashed, f is the frame rate and x is the resolution.

experiment	sensor size [px^2]	image size [cm^2]	f [Hz]	t_{int}[ms]	Δx [mm/px]
Aeolotron	1600 × 1370	25 × 21	100	1.0	0.156
Benjamin	2560 × 2160	11 × 9.3	15	2.0	0.4

The bottleneck for continuous recording of high frame rate, high resolution images is the speed at which data can be written to the hard disks. In the BLV experiments at the *Aeolotron*, the image size was set to the maximum value, at which data could be recorded continuously. In the preliminary experiments, only shorter sequences with lower frame rates were recorded that could be stored in computer memory, so there was no restriction in image size. The image sizes used in the different experiments are given in Tab. 4.1.

4.1.4 Light sources

A light source, which emits wavelengths around the absorption maximum of 455 nm, is required to excite fluorescence in Pyranine in an alkaline medium (sec. 3.2.2). Since monochromatic light is not required and a large patch on the water surface

needs to be illuminated, it is advantageous to use LEDs instead of a Laser. With the recent progress in blue LED technology (Nakamura 1998), sufficient intensities are achieved with high power LED light sources.

Normalized spectra of the used blue high power LEDs are shown in Fig. 4.4. The LEDs by Cree (*XLamp XP-E*, blue), which have been used at the small linear wind-wave tank, are shown in purple and emit in the wavelength range of approximately 430 - 540 nm. The maximum intensity of the LED lies at a wavelength of $\lambda = 468$ nm and the maximum forward current is 1 A.

Due to the larger distances of the LEDs and the camera from the water surface at the *Aeolotron* (see Fig. 4.2(b)), significantly more light output is required there. The Cree light sources turned out to be insufficient, so another set of light sources was built. These are based on newer Osram *OSLON SSL* LEDs (type LB CPDP-GZHX-1). Their spectral peak is at $\lambda = 463$ nm, thus the spectrum has better overlap with the pyranine absorption spectrum (see Figs. 4.4(b) and 3.4(a)). The maximum LED current is 2 A in pulsed operation (for duty cycles less than 50 %). The format of the new light sources was optimized for operation at the *Aeolotron* (see Fig. 4.3(b)), to maximize the number of LEDs that can be placed above the measurement window. In the setup used in the main experiment, 26 light sources with 18 LEDs each were used (468 LEDs total, compared to 200 LEDs in the original light sources). In high power LED applications, good thermal management is essential to avoid overheating the LEDs. The light sources have large aluminum blocks with a high heat capacity and the LEDs are flashed with a duty cycle of 10 % (1 ms integration time at 100 Hz).

Customized LED drivers are used, which are able to control the current and trigger the LED flashes. To focus the LED light and reduce the illumination angle of approx. 120° (Cree) and 150° (Osram), lenses (Carclo, type 10412) were mounted on each LED. The combination of the Cree LEDs and the lenses produce 9.3 cd/lm at 17° FWHM and the Osram LEDs with lenses give 12 cd/lm at 15° FWHM. The LEDs without the lenses can be described as a Lambertian emitter, which emits the radiant intensity $1/\pi$ cd/lm perpendicular to the surface. Thus, due to the lenses the intensity is enhanced by a factor of $12\,\pi$, or approximately 38.

4.1.5 Optical filters

A disadvantage of LEDs compared to lasers is their broad emission spectrum. In the BLV method, the spectrum needs to be restricted for two reasons: a) the camera should only observe fluorescence light and not LED light and b) fluorescence should only be excited Pyranine in an alkaline medium (at the water surface), not in the acid bulk water. Due to the small thickness of the surface layer (compared to the thickness of the bulk of 1 m), the suppression of bulk fluorescence must be better than 10^{-6}. Filters were used in front of the LEDs, as well as in front of the camera.

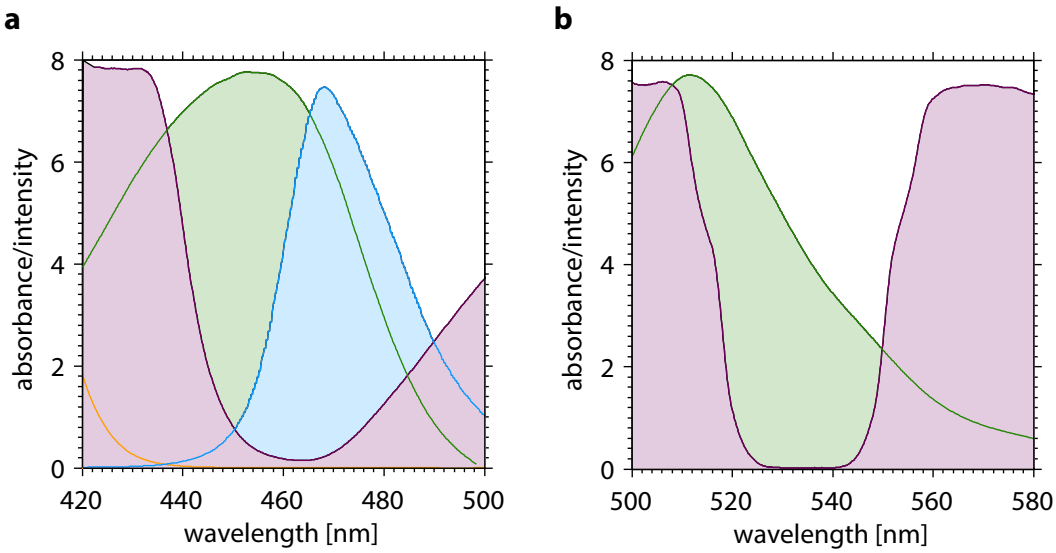

Figure 4.5.
a Spectral separation of excitation and fluorescence light: **a** Filters (2×DT-Blue and GG 445, purple) restrict the LED emission spectrum (blue) to match the absorption of Pyranine for high pH (green) but not for low pH (orange). **b** A band-pass filter (BP (543 × 20 nm), purple) is placed in front of the camera to suppress reflections of the LEDs, but also cuts into the emission spectrum of pyranine (green). (Modified after Kräuter et al. (2014))

Small linear facility

The filter set used for the measurements at the small linear facility is shown in Fig. 4.5. The blue curve is the emission spectrum of the Cree LEDs. In front of the LEDs, two short-pass filters (Optic Balzers *DT-Blue*) and a long-pass filter (Schneider Kreuznach *GG 455*) filter the high and low end of the spectrum, the filter absorbance is shown in purple. The high wavelength end suppression is required to avoid seeing the light sources directly in the camera images, e.g. through reflections from the water surface or from the floor of the water channel. At the lower end of the emission spectrum, the LED spectrum overlaps with the absorption of the acid form of Pyranine (orange curve). Suppression of this end of the spectrum is necessary to suppress bulk fluorescence.

In Fig. 4.5(b) the spectral window of the camera is shown. It is restricted by a green band pass filter (BP(534 × 20 nm), Edmund Optics). The absorption spectra of the filter is shown in the figure as the purple area. Lower wavelengths are filtered to avoid reflections of the blue light source. The green area in Fig. 4.5(b) shows the emission spectra of Pyranine for high pH values, which lies in the optical range of the camera spectral window. However, more than 50 % of the fluorescence light need to be filtered to cut out the LED light.

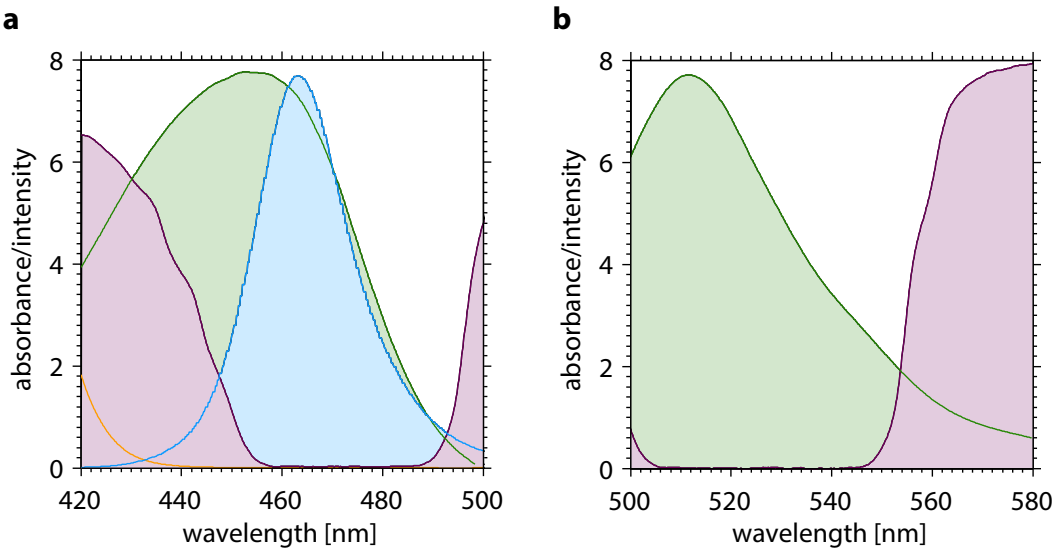

Figure 4.6.
a Improved spectral separation of excitation and fluorescence light at the *Aeolotron*. **a** A custom band-pass filter(Delta (BP (470 × 35 nm)), purple) still suppresses excitation of Pyranine in low pH (orange) by the LEDs (Osram, blue), but has higher transmission in the spectral band of the high pH pyranine absorption (green). **b** Due to the improved LED spectrum and filter, LED emission above 500 nm is negligible and the camera spectral window (band-pass filter by Edmund Optics (BP (525 × 45 nm), purple) can be widened to capture more fluorescent light (green).

Aeolotron

After tests had proven the old light sources to be insufficient for measurements at the *Aeolotron* and the decision was made to build new light sources, also the filters were optimized to enable higher fluorescent intensities. Since commercially available filters were not well suited for the BLV application, new bandpass filters for the LEDs were custom made (Delta, BP (470 × 35 nm)). Absorption by the acid component of Pyranine below 440 nm, as well as blue LED light in the camera spectral window above 500 nm are significantly reduced compared to the former solution. In Fig. 4.6 the new set of filters is shown. In blue, the intensity of the OSRAM LEDs is plotted. The filter absorbance is shown in purple in Fig. 4.6(a), the green area marks the alkaline absorption of Pyranine. Compared to the old set of filters, much higher intensities are transmitted by the filter and hence more light is absorbed by the dye. The transmitted light of an individual LED is a factor of 6 higher only due to the advanced filters. In Fig. 4.6(b) the alkaline emission intensity spectrum of Pyranine (green) and the absorbance of the Edmund Optics (BP (525 × 45 nm)) bandpass filter used in front of the camera (purple) are shown. The reflections by the LED light sources are further reduced and the red light sources of the imaging slope gauge ($\lambda \approx 600$ - 660 nm) are not interfering with the measurements (Kiefhaber et al. 2014).

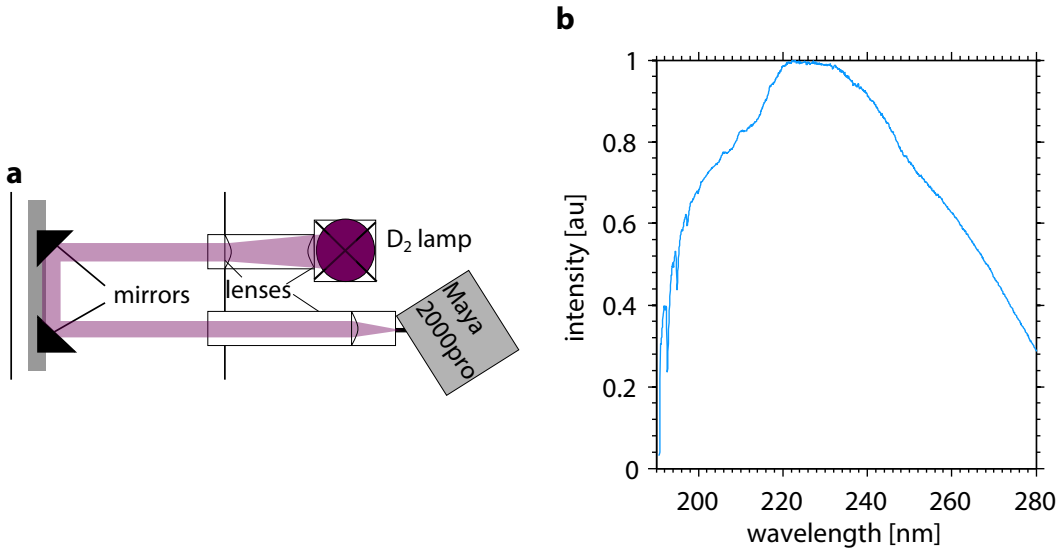

Figure 4.7.
a Sketch of the setup of the UV spectrometer installed at the *Aeolotron* consisting of an UV lamp and a spectrometer by Ocean Optics (*Maya 2000pro*). **b** Measured normalized intensity of the used deuterium lamp by Heraeus (D_2^{plus}).

4.1.6 Spectrometer setup

For the method described in sec. 3, it is necessary to monitor the ammonia concentration in the air. Concentrations were measured using differential optical absorption spectroscopy (DOAS) with a custom made UV spectrometer.

An UV spectrometer setup has been installed to measure the ammonia concentration in the air at the *Aeolotron*. A sketch of the setup is shown in Fig. 4.7(a). A deuterium light source (Heraeus, Deuterium lamp D_2^{plus}) has been used. In Fig. 4.7(b), the emission spectrum of the Deuterium lamp is shown. The light beam is bundled and parallelized by two lenses and enters through a tubing system into the air space of the *Aeolotron* in a height of approx. 2.30 m. Two mirrors reflect the light beam and it is directed to another tube. In this tube a further lens is mounted, which bundles the light into the spectrometer slit. No optical fiber has been used to avoid UV absorption in the fiber. The used spectrometer (Ocean Optics, *Maya 2000Pro*) has a spectral range of 190 - 290 nm. As described in sec. 3.5, high intensities in the range of $\lambda = 200 - 230$ nm are necessary to measure the ammonia concentration. The absorption length for this setup is 134 cm and it is installed in segment 15 (see Fig. 4.2).

4.1.7 Infrared camera

For collocated and simultaneous imaging of the thermal and fluorescent footprints, infrared cameras are mounted at the two wind-wave facilities.

Small linear facility

Comparative measurements of the BLV method with infrared imagery (camera: Thermosensorik *CMT 256*) were conducted in a set of experiments at the small facility. The setup with the thermal imaging system at the small wind-wave tank is sketched in Fig. 4.1. A similar patch on the water surface as for the BLV camera is imaged by the infrared camera. Therefore, the camera has to be inclined. The resolution of the infrared imager is (256 × 256) pixel. It is sensitive in a wavelength region of 3.4 - 5.1 µm and has a maximum full-frame rate of 885 Hz. The absorption in water in this spectral range is (10^6 - 10^4) 1/m and hence the visible depth is approx. 100 µm (Schimpf 2000). The camera was triggered with the same signal as the visible camera and the light sources with a frame rate of 15 Hz and an integration time of 2 ms. The used lens has a focal length of 50 mm. Since infrared radiation in the sensitivity range of the camera is absorbed by the glass walls of the facility, the cover plate at a fetch of approx. 50 cm was removed.

Aeolotron

Simultaneous and collocated measurements with an infrared camera (IRcam, *Velox 327k M*) have been conducted in the large facility. The infrared camera is mounted at the ceiling of segment 12 as shown in Fig. 4.2(a). By tilting the camera it was possible to measure the thermal structures at the same water patch as the camera of the BLV setup. The infrared camera has a resolution of (640 × 512) pixel. The spectral region the sensor is sensible, is 3.4 - 6 µm and as for the other camera the visible depth is approx. 100 µm. The water surface sees a thermal footprint of approx. (47 × 38) cm^2 and the used lens had a focal length of 50 mm. Since the camera itself cannot be triggered externally the trigger signal of this camera was used to trigger all the other devices, e.g. light sources, visible camera, and the ISG (see sec. 5.2). The frame rate was set to 100 Hz and an integration time of 2.5 ms has been used.

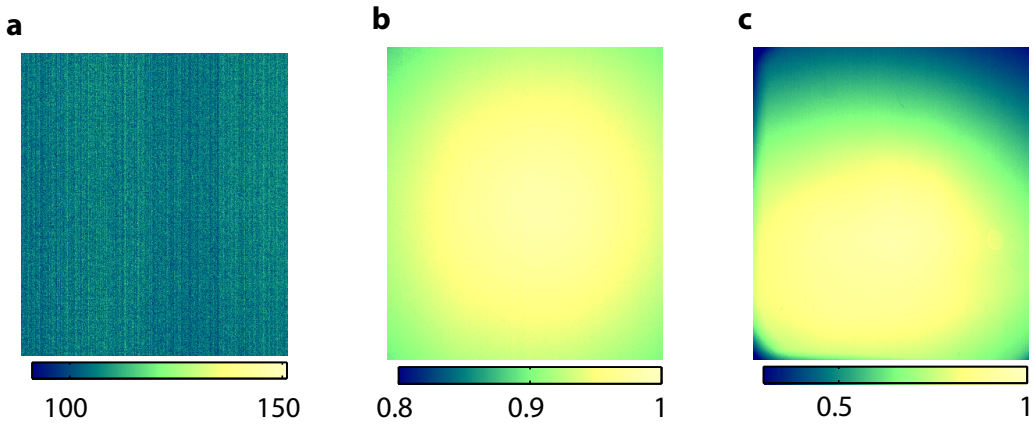

Figure 4.8.
a Mean dark image (1500 images) recorded with a closed lens and an integration time of 9.9 ms. The colormap shows raw 16 bit gray values, the nonlinear transformation described in sec. 4.1.3 was not applied. Typical fixed pattern noise is visible. **b** Flat field correction: The image shows a homogeneously illuminated surface. At the edges of the image the intensity drops due to vignetting and shading effects of camera/lens. **c** Normalized illumination distribution of the light sources on the water surface without the flat field correction measured at the *Aeolotron*. The intensity drops up to 70 % at the image corners.

4.1.8 Imaging slope gauge

With the imaging slope gauge (ISG), the two-dimensional slope of the water surface is measured. From this, statistical parameters, such as the mean square slope, can be derived. Also, it is possible to reconstruct the small-scale 3D shape of the surface. It consists of a high-speed camera *PCO.dimax* and a custom made light source with red LEDs. The light source is illuminating the measurement area from underneath the wind-wave tank as shown in Fig. 4.2(b). The setup and its capabilities are discussed in detail in Kiefhaber et al. (2014). During the measurements conducted in this thesis, the ISG camera was installed next to the BLV camera as shown in Fig. 4.2(a) and Fig. 4.3(b). A dichroic filter by Optic Balzers (*DC-Red*) is used as a beam splitter. It is mounted in front of both cameras. The filter transmits the green Pyranine fluorescence light and reflects the red ISG light.

4.2 Calibration

In this section the calibration of the BLV setup is addressed. The calibration of the ISG is discussed in detail in Kiefhaber et al. (2014), Rocholz (2008), and Reith (2014) and the calibration of the infrared camera can be found in Nagel (2014).

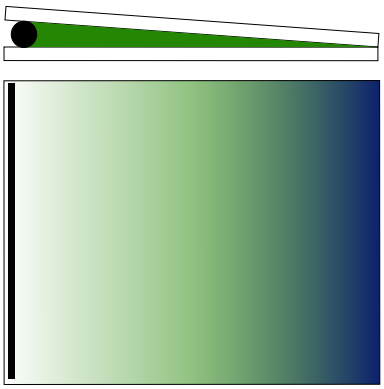

Figure 4.9
Sketch of the calibration wedge viewed from the side and from the top. The size is (25 × 21) cm². The distance between the glass plates is 2.5 mm (left) and 0 mm (right).

Camera calibration

Every camera has a pronounced and characteristic fixed pattern noise as shown in image 4.8(a). This fixed pattern noise is removed from the camera images by subtracting an averaged dark image. This image is acquired by covering the lens and taking 1500 images with the same integration time settings as during the measurement but without the nonlinear transformation described in sec. 4.1.3.

Images of a homogeneous illuminated surface (Ulbricht sphere) have been recorded to correct for shading and vignetting effects of the camera lens and the filter (see sec. 4.1.5). An example image is shown in Fig. 4.8(b) for the *Nikkor* 85 mm lens with an f-number of 2. The mean of these images is normalized to a range of [0, 1]. Recorded images are then divided by this image to correct for the shading. This correction is included in the flat field image of the LED illumination described in the following section.

Flat field correction

Since the illumination of the used light sources on the water surface is not completely homogeneous, a correction is applied to the images. After testing several possible ways to acquire calibration images for the flat field correction, the most suitable was found to simply take longer exposure images of the flat water surface. With adequate averaging, the fluorescence signal of the water bulk is still sufficiently strong to acquire the calibration images. An example is shown in Fig. 4.8(c). Every recorded image is later divided by the normalized flat field correction image, this also corrects for shading and vignetting described above.

Acid bulk correction

In sec. 4.1.5, the necessity of suppressing light coming from the acid bulk was highlighted. While the filters in front of LEDs and camera reduce the intensity of bulk fluorescence by many orders of magnitude, there is still a non-zero transmission. Thus, the BLV camera measures light coming from the acid bulk. This effect is mostly suppressed by adding the absorbing dye, Tartrazine, to the water (see sec. 3.2.2). Some measurements have been conducted without Tartrazine, therefore it is necessary to correct for the acid bulk fluorescence. This can be realized by taking an image without wind before each measurement condition. The image is then corrected by the dark and flat field images and is than subtracted from each image. This correction does not correct for the effect due to different wave heights.

Neutral layer thickness calibration

As explained in detail in sec. 3.3, the intensity in the BLV image is proportional to the neutral layer thickness. At high gray values the neutral layer is thicker. The dependence of the gray value on the fluorescent layer thickness is determined by calibration. A calibration wedge consisting of two borofloat glass plates with a linearly increasing distance as shown in Fig. 4.9 is used. On one end, a precision steel bolt with 2.5 mm diameter is used as spacer between the two glass plates, at the other end, they are placed directly onto each other. In between the plates alkaline water with the same concentration of Pyranine as used during the measurements is injected. The wedge is closed from all sides and put on a raft in the field of view of the BLV camera, where calibration images are acquired.

5 Experiments

In this chapter, the experiments conducted at the small linear and the large annular facility at the University of Heidelberg are summarized. The setup, geometry, and instrumentation at the wind-wave tanks are detailed in sec. 4.1. Here, the measurement conditions and procedure are shown in more detail.

5.1 Preliminary experiments

Preliminary experiments to optimize and verify the measurement technique have been conducted at the small linear wind-wave tank *Benjamin* (see sec. 4.1.1). A set of measurements has been recorded for a first comparison of the fluorescence structures to the patterns visible in thermal imagery. Since the IR camera cannot see through the glass walls, the facility was opened by removing one of the cover plates.

The chemicals, Pyranine and hydroxide chloride acid, were well mixed in the water before each measurement. At the start of each measurement, the wind and wave field were given time to reach equilibrium. Then ammonia was injected into the air space directly with a syringe. A slower injection was not feasible due to the open facility. It would have taken too much time to get to sufficiently high concentrations in the air. Approximately 15 ml of air saturated 100 % with ammonia was injected at the downwind end of the water channel to allow it to mix with the air in the recirculation tube. Both cameras and the LEDs were triggered externally and the cameras measured simultaneously with a frame rate of 15 Hz.

At eight different wind speed conditions the experiments were conducted. The conditions during the measurements are shown in Tab. 5.1. The camera settings are shown in Tab. 4.1.

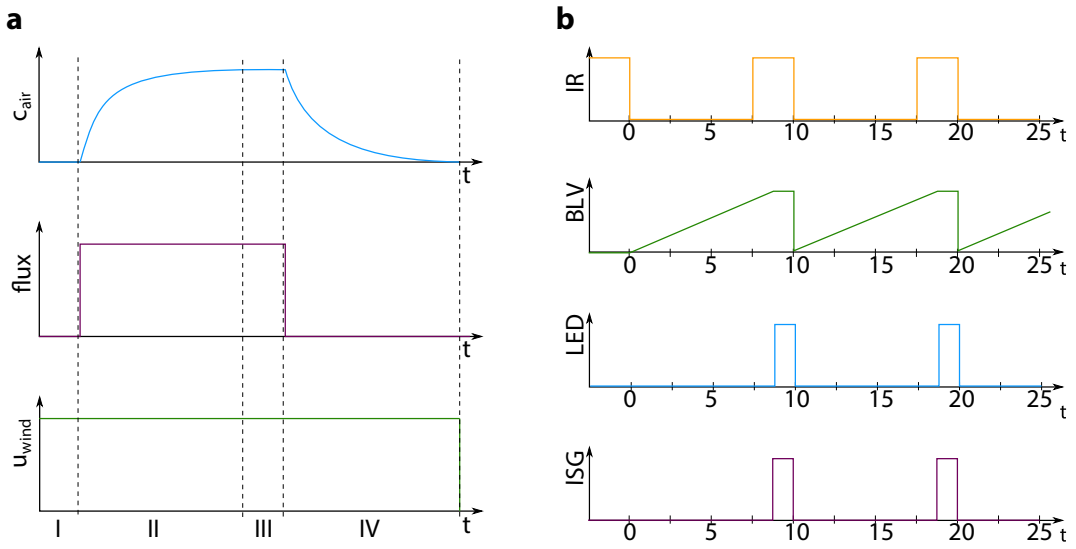

Figure 5.1.
a Description of the measurement phases for the experiments in the *Aeolotron*. In blue, the temporal evolution of the ammonia concentration in the air is shown, in purple the input of ammonia and in green the wind speed. Each measurement is parted in 4 different phases. **b** Trigger signals of the IR camera (orange), the BLV camera (green), the BLV light sources (blue) and the ISG (purple). For the BLV camera, the effect of the rolling shutter is sketched, camera lines are activated one by one, but the LEDs are flashed only while all lines are active.

5.2 Measurements at the Aeolotron

In Fig. 5.1(a) the measurement procedure at the large *Aeolotron* wind-wave facility is shown. In phase I, the wind and wave filed were given time to reach equilibrium as during the measurements in the small linear facility. In phase II, ammonia from a gas bottle is injected directly into the air space in segment 6 (see Fig. 4.2(a)) using stainless steel tubing. The ammonia flux is set by a flow controller. A spectrometer, installed in segment 15, is constantly measuring the air-side concentration of ammonia. The ammonia concentration in the air increased (phase II) until the equilibrium concentration was reached (phase III). In equilibrium, the air-water exchange rate and the input rate of ammonia were equal. After reaching the maximum concentration, the flux was turned off. The concentration of ammonia in air decreased as more and more was dissolved in water (phase IV).

Figure 5.1(b) shows the timing of the cameras and the light sources. Since the infrared camera (IR, orange line) cannot be triggered externally, all the other devices were triggered by the falling edge[1] of this camera. The infrared camera measured with a frame rate of 100 Hz and had an integration time of 2.5 ms. The *PCO.edge* camera (BLV, green curve) was run in a rolling shutter modus. Its integration time

[1] The frame grabber sends the trigger signal, if it receives the measured data from the infrared camera.

Table 5.1.
Boundary layer visualization and simultaneous infrared measurements at the small linear facility at different wind speeds. The free stream u_0 and friction velocities u_* are taken from Krah (2014). The values marked with "*" are extrapolated.

u_0 [m/s]	u_* [cm/s]	pH	Ind. [10^{-6} mol/L]	T_{water} [°C]
1.5	2.5	4.2	5	22.6
2.2	6.0	4.2	5	22.6
3.5	10.0	4.2	5	22.6
4.8	16.0	4.2	5	22.6
5.8	23.0	3.7	5	22.6
7.0	31.0	4.0	5	22.6
8.0*	39.0*	4.0	5	22.6
9.2*	47.0*	5.8	5	22.6

was set to 9.9 ms. All pixels of the sensor are active after 8.8 ms. The blue light sources (LED, blue line) were flashed for 1 ms after a delay of 8.8 ms. In the millisecond when the light sources were flashed, all camera sensor lines are active. Thus, a rolling shutter effect was avoided. This mode is run continuously during phases II and III of Fig. 5.1(a). During phase II, wave slope statistics are measured with the imaging slope gauge (ISG) (Kiefhaber et al. 2014, Rocholz 2008).

In phase III, the ISG is triggered such that it acquires a two-dimensional wave slope image synchronized with the flashes of the BLV light sources. The resulting data is used to create an overlay of the BLV, thermal imagery, and wave height reconstructed from the wave slope images. The ISG cannot operate continuously in this mode, but is limited to 80 s measurement periods, after which longer breaks for saving the data are required.

The measurements conducted at the *Aeolotron* are parted in ten conditions shown in Tab. 5.2 and Tab. 5.3. The condition "no AC clean" is a typical condition at the *Aeolotron* (Kräuter 2011, Mesarchaki et al. 2014, Nielsen 2004). Before the measurements, the water surface was cleaned with a skimmer, which removes the surface water layer, where surfactants and dirt accumulates. In contrast to all the other conditions measured during this campaign the air condition was turned off. Simultaneous thermal measurements are not available. The "clean" and the "clean/Tartrazine" case were conducted in the same way, but the air conditioning was turned on. The air condition alters the wind field in the channel and leads to different conditions from the "no AC" case at the same wind speed setting. For the "Tartrazine" measurements, the absorbing dye Tartrazine (see sec. 3.2.2) was added to the water to suppress bulk fluorescence. Three measurement runs with different amounts (0.05 µmol/L (0.6 g/18000 L) and 0.26 µmol/L (3 g /18000 L)) of the artificial surfactant Triton X-100 (see sec. 2.3.5) added to the water were conducted. During the fetch conditions, the wave absorber (see sec. 4.1.2) was installed in the facility. Cleaning of the water surface with the skimmer was attempted before the start of the measurement, but was not as efficient as without the wave absorber. Each condition consists of a set of

wind speeds. As in the experiments at the small linear facility the wind speed was controlled by setting a frequency for the axial ventilators. Table 5.2 and Tab. 5.3 show the different conditions and the used frequencies.

For all conditions, the measured environmental parameters are also shown in these tables. The reference wind speed u_{ref} was measured with a propeller anemometer. Due to interrupts or defects of the device, some values are approximations from measurements of the pitot tube. Both instruments are located next to each other in segment 15 and are influenced similarly by changes in the wind field. Thus, a linear relationship between the pitot tube and anemometer wind speed was found and used as an approximation if one device did not work. These values are marked in Tab. 5.2 with a star "*". With an ultrasonic Doppler anemometer the bulk water velocity v_w was measured. By using the momentum balance method and the bulk velocity, the friction velocity was calculated. A detailed description of the procedure is given by Bopp (2014). No values are shown for the fetch conditions, since some assumptions needed to determine the friction velocity at the fetch conditions are not fulfilled. The other parameters are the air T_a and water temperatures T_w, the pH value in the water bulk, the conductivity λ, the relative humidity in segment 13 H_{seg13}, the concentration of dissolved Pyranine (Ind.), and the ammonia flux controlled by the flow controller. In the last column, the date of the measurement run is shown. At each day of the experiment, the measurements were conducted in ascending order of the wind speeds.

Table 5.2.
Measurement conditions during the campaign at the large wind-wave facility. The values marked with "*" are approximations due to interrupts or defects of the measuring devices. They should be considered with caution and have large error bars.

condition	f	u_{ref}	v_{w}	u_*	mss	T_{w}	T_{a}	pH	λ	H_{seg13}	Ind.	NH_3	date
	[HZ]	[m/s]	[cm/s]	[cm/s]		[°C]	[°C]		[μS/cm]	[%]	[10^{-6} mol/L]	[mL/min]	
no AC clean	5	1.5	1.5	0.22	0.0054	21.0	22.1	3.9	20.2	98	6	10	09/06
	7	2.2	2.3	0.31	0.0061	21.1	22.0	4.0	19.7	100	6	30	09/06
	9	2.7	3.1	0.40	0.0149	20.9	21.8	3.9*	15.0	100	6	25	07/06
	12	3.8	4.5	0.54	0.025	21.0	21.8	3.9*	14.2	97	6	80	08/06
	16	5.1	6.5	0.75	0.0496	21.0	21.8	3.9*	12.6	100	6	80	08/06
	22	6.8	10.5	1.20	0.0822	21.0	21.8	3.9*	11.4	100	6	200	08/06
	29	8.6	15.8	1.80	x	21.0	21.9	3.9*	9.5	100	6	400	08/06
clean	5	0.4*	0.5	0.088*	x	21.4	28.6	3.7	17.1	34	6	30	10/06
	7	1.1	2.0	0.27	0.0061	22.6	28.5	4.0	17.2	37	6	25	11/06
	9	1.5	2.8	0.37	0.0131	23.3	29.5	4.0	16.2	40	6	40	11/06
	12	2.5	3.8	0.47	0.0205	23.7	28.2	4.1	15.3	47	6	60	11/06
	16	5.8*	6.0	0.69	0.0403	21.7	26.2	4.1	15.8	52	6	140	10/06
	22	7.6*	9.6	1.06	x	22.1	26.2	4.2	13.6	62	6	180	10/06
clean	5	0.4	0.5	0.088*	0.0007	21.8	28.5	3.4	26.7	34	5	15	30/06
Tartrazine	7	1.0	1.9	0.27	0.0064	22.4	26.8	3.4	25.5	36	5	30	30/06
	9	1.4	2.6	0.35	0.0124	22.7	26.9	3.5	25.0	41	5	50	30/06
	12	2.5	3.6	0.45	0.0146	22.8	27.3	3.5	24.2	46	5	70	30/06
	16	4.0	5.4	0.63	0.0315	23.1	27.6	3.5	23.2	52	5	140	30/06
	22	5.8	9.0	1.01	0.0734	23.3	27.8	3.6	21.8	60	5	180	30/06
	29	7.6	14.1	1.58	0.1127	23.5	27.6	3.6	19.5	67	5	220	30/06
0.05 µmol/L	5	0.8*	0.5*	0.088*	0.0005	21.6	28.2	3.4	29.1	33	4	20	26/06
Triton X-100	7	1.2*	1.3	0.19	0.0005	22.0	26.2	3.5	28.6	36	4	30	26/06
	9	1.3	2.3	0.31	0.0006	22.3	26.2	3.4	28.0	40	4	50	26/06
	12	2.5	3.5	0.44	0.0067	22.4	26.5	3.4	27.3	45	4	70	26/06
	16	4.1	4.8	0.57	0.0108	22.6	26.9	3.4	26.5	50	4	140	26/06
	22	6.0	8.4	0.94	0.0616	22.8	27.2	3.5	24.6	59	4	180	26/06
	29	7.8	13.8	1.54	0.1056	23.1	27.1	3.6	22.5	66	4	220	26/06
0.26 µmol/L	5	0.8	0.5	0.091*	0.0005	22.4	28.9	3.7	21.0	34	4	15	27/06
Triton X-100	7	1.2	1.2	0.18	0.0005	23.0	27.4	3.7	20.0	35	4	25	27/06
	9	1.5	2.2	0.30	0.0006	23.3	27.4	3.7	19.9	39	4	40	27/06
	12	2.5	3.4	0.43	0.0018	23.5	27.7	3.7	19.0	44	4	60	27/06
	16	4.2	4.4	0.53	0.0047	23.7	28.2	3.8	18.8	48	4	100	27/06
	22	6.1	7.3	0.82	0.0269	24.0	28.7	3.8	17.5	56	4	140	27/06
	29	7.9	12.9	1.46	x	24.3	28.6	3.9	16.2	65	4	200	27/06

Table 5.3.
Measurement conditions during the campaign at the large wind-wave facility. The values marked with "*" are approximations due to interrupts or defects of the measuring devices. The values with an exclamation mark "!" for the fetch conditions symbolizes that theses values should be considered carefully, since the method to determine them is not valid with a wave absorber in the facility.

condition	f	u_{ref}	v_{w}	u_*	mss	T_{w}	T_{a}	pH	λ	H_{seg13}	Ind.	NH_3	date
	[Hz]	[m/s]	[cm/s]	[cm/s]		[°C]	[°C]		[µS/cm]	[%]	[10^{-6} mol/L]	[mL/min]	
0.26 µmol/L	5	0.8	0.5*	0.088*	0.0006	23.8	30.3	4.1	18.0	34	4	15	28/06
Triton X-100	7	1.2	1.2	0.19	0.0006	24.2	28.8	4.2	17.6	36	4	25	28/06
Tartrazine	9	1.4	2.5	0.33	0.0006	24.5	28.9	4.2	17.0	39	4	40	28/06
	12	2.5	3.4	0.42	0.0028	24.6	29.1	4.2	16.9	44	4	60	28/06
	16	4.2	4.3	0.52	0.005	24.8	29.6	4.3	16.1	48	4	100	28/06
	22	6.1	7.3	0.82	0.0297	25.0	29.8	4.5	15.6	56	4	140	28/06
fetch 1	7	1.1	0.2	x	0.001	22.3	26.6	4.0	24.8	37	3	30	17/06
23.4 m	9	1.4	0.6	x	0.0176	22.9	27.6	4.2	23.9	40	3	50	17/06
	12	2.3	1.4	x	0.023	23.1	27.7	4.2	22.9	47	3	70	17/06
	16	2.3*	1.4	x	x	23.1	27.7	4.2	22.9	47	3	140	18/06
	22	5.6	3.3	x	0.0757	23.0	27.4	4.0	19.7	60	3	180	18/06
	29	7.3	5.3	x	0.1161	23.4	27.6	4.3	17.0	65	3	250	18/06
fetch 2	7	1.1*	0.6*	x	0.0007	21.7	25.7	3.4*	31.5	36	1	30	16/06
10.2 m	12	2.4	2.4	x	0.0302	21.7	25.7	3.9*	30.1	46	1	70	16/06
	16	3.6	4.3	x	0.0353	21.7	25.7	3.6*	28.6	54	1	140	16/06
	22	5.5	6.9	x	0.0735	21.7	25.7	3.6*	26.6	60	1	180	16/06
fetch 3	7	1.1	0.2*	x	0.0007	23.2	27.3	3.9	21.9	37	3	30	19/06
4.5 m	9	1.4*	0.6*	x	x	23.2	27.3	3.9	20.9	41	3	50	19/06
	12	2.3	1.4	x	0.0235	23.5	27.8	4.0	19.9	47	3	70	20/06
	16	3.8	2.1	x	0.0446	23.8	28.4	4.1	18.6	52	3	140	20/06
	22	5.8	4.1	x	0.0659	24.1	28.6	4.3	17.1	59	3	180	20/06
	29	7.5	6.6	x	x	24.3	28.7	4.5	16.0	65	3	250	20/06
fetch 4	7	1.1	0.2*	x	0.0007	23.7	27.5	3.8*	23.0	38	3	30	21/06
2.0 m	9	1.3	0.2	x	0.0008	24.0	28.3	3.8*	22.3	41	3	50	21/06
	12	2.3	1.6	x	0.0136	24.2	28.6	3.8*	22.0	47	3	70	21/06
	16	3.8	2.6	x	0.0405	24.3	28.9	3.8*	21.0	53	3	140	21/06
	22	5.7	4.9	x	0.0588	24.6	29.1	3.8*	19.7	60	3	180	21/06
	29	7.4	7.7	x	0.0885	24.7	29.0	3.8*	18.4	64	3	200	21/06

6
Data processing

In the following chapter, the algorithms to process the recorded fluorescence and thermal images are presented. Corrections and calibrations are applied to the BLV images to convert the gray values into neutral layer thicknesses. The IR images are processed and registered on the BLV images. With the preprocessed images further evaluations have been conducted, e.g. comparison of thermal and fluorescent structures, a computation of the lifetime, and the surface velocity of streaks. From the measured air-side concentrations of ammonia, transfer velocities (integrated over the whole facility) are computed with a box model. Also, the computation of the ratio of the air to water-side transfer velocities is described.

6.1 Preprocessing

In the following, the steps to preprocess all fluorescence and infrared images are discussed. These steps have been conducted before the images have been further processed to gain additional parameters.

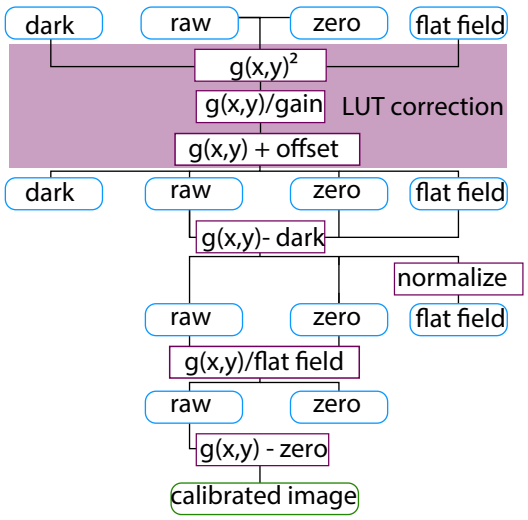

Figure 6.1
Preprocessing routine for the BLV images, correcting for fixed pattern noise ("dark"), acid bulk fluorescence ("zero") and the inhomogeneities of the illumination ("flat field").

6.1.1 Correction of the fluorescence images

A 16 to 8-Bit data reduction has been conducted by using a look up table (LUT) (see sec. 4.1.3) based on the idea that photon noise (increasing with the square root of the intensity) is the dominant contribution to the total noise. This has been conducted to reduce the amount of data recorded by the *PCO.edge*. Due to this, gray values are no longer linearly related to the recorded intensities. Equation (4.1) is solved for $n(x, y)$ to get an image with linear gray values

$$n(x, y) = \frac{g(x, y)^2}{\text{gain}} + \text{offset} \tag{6.1}$$

where $n(x, y)$ is the corrected image, $g(x, y)$ is the measured image, the gain is the factor by which the images have been multiplied to enhance the intensity, and the offset is the minimum dark current.

The LUT correction has to be applied to all images (dark, flat field, zero, raw). This is shown in Fig. 6.1 in the purple box. As a reminder, the dark image is the fixed pattern noise image of the camera sensor (see Fig. 4.8(a)), the zero image is an image of the water surface recorded before each wind condition to correct for the changing pH value in the water bulk (acid fluorescence) and the flat field image corrects for the inhomogeneous illumination of the light sources (see sec. 4.2).

Figure 6.1 gives an overview of the complete correction procedure for the raw images. After the LUT correction, the dark image is subtracted from the raw, zero, and flat field images. In the following, the flat field image is normalized. Both the raw and zero images are then divided by the normalized flat field image. In the last step, the zero image is subtracted from the raw image. The result is a calibrated image, which is used for further processing of the data.

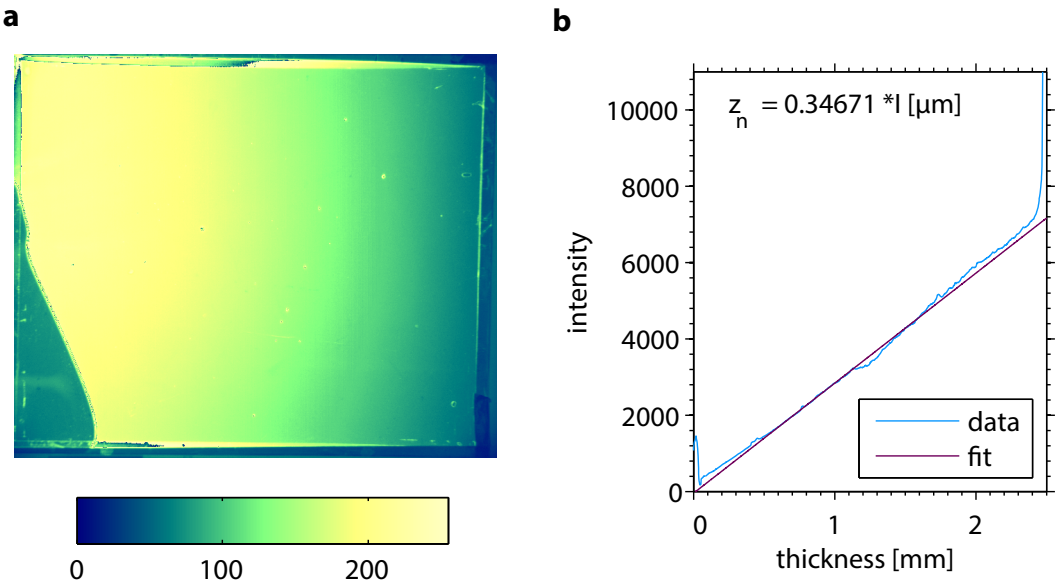

Figure 6.2.
a Image of the calibration wedge filled with alkaline water viewed from the top. Bright spots are air bubbles between the glass plates and on the left corner of the wedge is air. **b** Fluorescent intensity calibration: The blue line shows the intensity over the depth of the wedge at one line in the left image. In purple a linear fit from z = (0.2-2.2) mm is shown. The result of the fit is shown in the top of the image, where I is the intensity and z_n is the neutral layer thickness.

6.1.2 Neutral layer thickness calibration

As described in sec. 4.2, calibration images of a wedge filled with alkaline water with the same concentrations of Pyranine and Tartrazine as used during the measurements are recorded. The calibration procedure was repeated each time the concentration of the dyes changed (e.g. because fresh water was used or the water was filtered). An example image is shown in Fig. 6.2(a). The color code shows the uncalibrated gray values. First, the images are preprocessed as described in sec. 6.1.1. After this correction, a mean image is computed from a series of 1500 images to reduce noise. In Fig. 6.2(a) bright spots are visible. These are air bubbles, which are produced by the injection of the alkaline water between the glass plates with a syringe. The dark patch at the injection spot in the lower left corner in Fig. 6.2(a) could not be avoided, when filling water between the glass plates. Each image is corrected using a Matlab® script, to correct for these distortions in the images. First, the wedge image is rotated to align the sides of the wedge with the image edges. A 15 × 15 median filter (*medfilt2*) is used, to filter the bubbles. An intensity profile along the gradient of the wedge (from a thickness of 0 to 2.5 mm) is shown in blue in Fig. 6.2(b). From a linear fit to this profile (purple), the relation between corrected image intensities and thickness of the fluorescence layer is obtained. The resulting relation converting corrected gray values to neutral layer depths is given at the top of the figure.

The intensity measured with the wedge has to be corrected for reflections of the

glass plates and the acrylic float, which the wedge is placed upon for the measurements (see Fig. 4.9). Therefore, the indices of refraction of the different media must be considered. The glass plates (borofloat glass) have a refraction index of 1.47, water has an index of 1.33 and the float (Plexiglas) has an index of 1.49. By inserting these equations into Fresnel's equation the percentage of reflection is calculated between two media by

$$R = \left(\frac{n_1 - n_2}{n_1 + n_2} \right)^2, \tag{6.2}$$

where R is the reflection and n_1 and n_2 are the refractive indices of the two media. At (Plexi)glass/water interfaces, only about 0.25 % of light are reflected, which can be neglected. Also, all secondary reflection intensities (being the product of two small reflection coefficients) are small. The only relevant contributions to the total fluorescence intensity are the transitions from air to glass at the top (3.6 %) and from glass to air at the bottom of the wedge (3.6 %), as well as the transition from air to Plexiglas at the top of the float (3.9 %). While the first transition reduces the intensity of light available to excite fluorescence in the wedge, the latter two increase the intensity by reflecting back the transmitted light. Accounting for all relevant processes, the total intensity is by 3.5 % enhanced. This effect is considered in the intensity shown in Fig. 6.2(b).

6.1.3 Correction of the infrared images

The gray values of the recorded infrared images are converted to absolute temperatures online during the measurement. The necessary calibration coefficients have been measured before with a black body, as described in detail by Schimpf (2000) and Nagel (2014). For the purposes of this study, knowledge of absolute temperatures is not required, only temperature differences are important. Thus, a mean image without thermal structure is subtracted from each image. This reduces some anisotropies encountered in the IR images even after the online calibration.

Additional filtering is applied, to remove hot (broken) pixels. Broken pixels have a) constant values or b) deviate significantly from their neighbor pixels. Thus, a pixel is identified as broken if a) it has a value of zero after subtracting the mean image or b) the difference between the local median value (computed from its 5×5 neighbors) and its value is larger than 300 mK. For this temperature difference threshold, different values have been tested. After the broken pixels have been identified, their intensity values are interpolated based on the intensities of their neighbors. The interpolated image $n(x, y)$ is computed from the original image $g(x, y)$ by

$$n(x, y) = \frac{(1 - m(x, y))\, \mathcal{B}(g(x, y)\, m(x, y))}{\mathcal{B}(m(x, y))} + m(x, y) g(x, y), \tag{6.3}$$

where $m(x, y)$ is one for good pixels and zero for broken pixels and $\mathcal{B}$ represents a

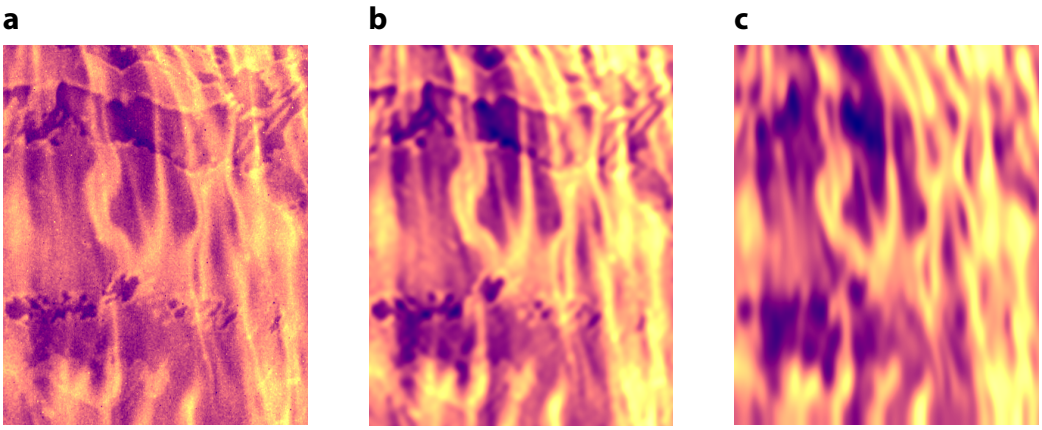

Figure 6.3.
a Unfiltered infrared image at a wind speed of approx. 1 m/s for a clean water surface. **b** Same image filtered with a Butterworth filter to reduce noise. **c** Additional Butterworth filter in wind direction to reduce the reflections in the infrared images.

Gaussian smoothing filter (5×5 filter, $\sigma = 1$). Good pixels are not affected by this transformation, only the values of bad pixels are replaced by a weighted mean value of the surrounding area.

Reduction of noise and reflections

In Fig. 6.3(a), an example infrared image is shown after the removal of the hot pixels. It has been measured at approx. 1 m/s wind speed at the large annular wind-wave facility, the wind is coming from the bottom. In Fig. 6.3(a), in addition to the physical temperature signal from the water surface, two sources of error are visible. The image is noisy and reflections from the water surface are visible. The latter is clearly identified in image sequences, here they appear as elongated structures from left to right.

Different types of filter have been tested to reduce the noise. The most effective was found to be a forth order Butterworth filter (see, e.g. Oppenheim and Schafer (2010)) (Matlab® function *butter*) with a (normalized) cutoff frequency of 0.1 ($k_{\max} = 1/20$ px^{-}1). The filter is applied separately in the x- and y- directions and forward and backward to prevent phase lags (Matlab® function *filtfilt*). The noise is reduced, but also the thermal streaks are smoothed and the thin structures are not as clearly visible as before.

After this smoothing, the reflections are still visible in the image. A second Butterworth filter is applied, but only in the along-wind direction to further reduce them. This strongly affects the reflections (with their stronger cross-wind gradients), but not as much the physical streaks visible on the surface, which are mostly oriented in the along-wind direction. A fourth order Butterworth filter with a cutoff frequency of 0.03 (wavenumber = 3/200 px^{-1}) is used. The result is shown in Fig. 6.3(c). Clearly,

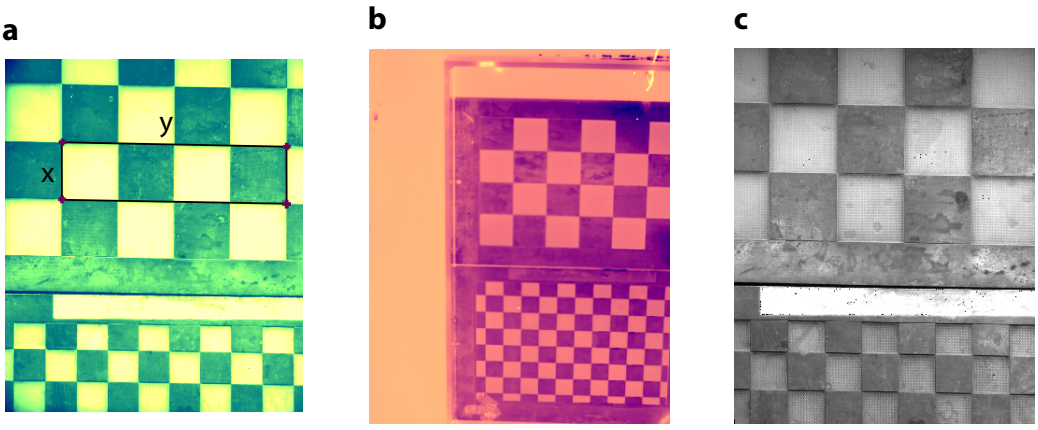

Figure 6.4.
a Chessboard calibration images at the *Aeolotron* with **a** the BLV camera and an image size of (25 × 21) cm², **b** the infrared camera and an image size of (47 × 38) cm² and **c** the ISG camera and an image size of (22 × 18) cm².

the reflections are reduced.

6.1.4 Image registration

Simultaneous and collocated measurements with the BLV setup, the ISG, and the infrared camera have been conducted. The surface patches are overlapping, but not identical. Images with a chessboard have been recorded with each camera to correct for these differences. The images are shown in Fig. 6.4. As seen in the images, the areas of the water surface seen by the cameras are different. The IR camera has a large footprint (47 × 38) cm², while those of the BLV and ISG cameras are more similar ((25 × 21) cm² and (22 × 18) cm².). Also, while the BLV and ISG cameras are looking down vertically, the IR camera is inclined. For this registration, changes in the distance between the cameras and the water surface (due to waves) are not accounted for. This leads to errors particularly at higher wind speeds. For the detection of the chessboard corner points, the algorithm included in the camera calibration toolbox for Matlab® is used (Bouguet 2008). The coordinates of the corners are extracted in all three images. Then, the perspective projection that is necessary to map the points in the different images is computed (Matlab® function *fitgeotrans*). The infrared image is mapped on the BLV image and the BLV image is mapped on the ISG image (Matlab® function *imwarp*). Before mapping the IR image to the BLV image, the resolution of the BLV image is reduced (Matlab® function *resize*, 1600 × 1370 to 640 × 512 pixel). This limits the amount of up sampling necessary on the IR image, which has a much lower resolution. The coefficients of the transformations are saved and are later used for all images.

6.2 Structure analysis

In the following section, the procedure to compare the thermal and fluorescence images and the computation of the surface velocity and the lifetime of the streaks by a cross correlation are described.

6.2.1 Comparison of fluorescent and thermal structures

In this section, the data processing to compare fluorescent and thermal structures is described. The BLV and IR images are decomposed into different wavenumber ranges by a Laplacian pyramid and the correlation coefficient between the images is computed. As described in sec. 6.1, the BLV and IR images are preprocessed and registered.

Laplacian pyramid

In a Laplacian pyramid, an image is decomposed into a sequence of bandpass filtered images with different wavenumber ranges (Burt and Adelson 1983). According to the uncertainty principle, gaining frequency or wavenumber information is possible only at the cost of losing spatial information. In the Laplacian pyramid decomposition, the wavenumber resolution is rather coarse (one octave per step), leaving good local information. The Laplacian pyramid is derived directly from a Gaussian pyramid decomposition. A smoothing filter is applied to level i and the resolution is reduced by a factor of two (i.e. every second pixel of the filtered image is dropped) to compute level $i+1$ of a Gaussian pyramid. The smoothing filter has to suppress all information contained in wavenumbers above half the Nyquist wavenumber of step i to fulfill the sampling theorem for step $i+1$. The last level of the Gaussian pyramid is a 1×1 pixel image, its gray value corresponds to the mean gray value of the original image. The decomposition is expressed as

$$g(x,y)^{(0)} = g(x,y), \qquad g(x,y)^{(i+1)} = \mathcal{B}_{\downarrow 2} g(x,y)^{(i)}, \tag{6.4}$$

with the image $g(x,y)$ and the low-pass filter $\mathcal{B}_{\downarrow 2}$ with the sampling rate two. The Laplacian pyramid is constructed from the Gaussian pyramid by taking the difference of successive levels. Level i of the Laplacian pyramid is computed as

$$l(x,y)^{(i)} = g(x,y)^{(i)} - \uparrow_2 g(x,y)^{(i+1)}, \tag{6.5}$$

where $\uparrow_2$ is an up sampling operator, which expands level $i+1$ of the Gaussian pyramid by a factor of two, thus giving it the same resolution as level i. For the computation of the different levels of the Gaussian/Laplacian pyramid in Matlab® , a 5×5 Gaussian smoothing kernel with a standard deviation of one is used (Matlab® function *imfilter*). For the up- and down sampling, the function *imresize* is used. As the zeroth level

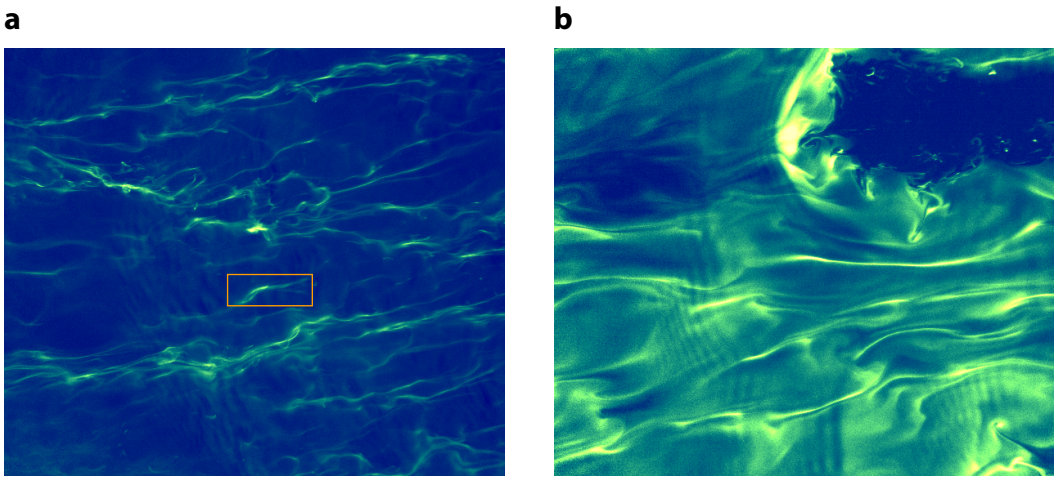

Figure 6.5.
a Streak tracking for surface velocity and lifetime computation: The orange rectangle marks a streak to be tracked. Image is taken at 2.5 m/s wind speed in clean water (no AC). **b** Example of a microscale breaker in a fluorescence image. The typical features of a microscale breaker are the bright crest and the dark area behind the crest. The wind direction is from left to right.

of the pyramid, 512 × 512 pixels are cut from the registered BLV and IR images. The pyramid thus has a total of nine levels.

Correlation coefficient

A correlation coefficient is calculated to get a measure for the similarities and differences between the IR and BLV images. This is realized with the Matlab® function *corr2*. It normalizes both images and computes the correlation coefficient between the pixels of the images

$$R = \frac{\sum_i \sum_j (g_{\mathrm{IR}}(i,j) - \overline{g_{\mathrm{IR}}(x,y)})(g_{\mathrm{BLV}}(i,j) - \overline{g_{\mathrm{BLV}}(x,y)})}{\sqrt{\sigma_{\mathrm{IR}}\sigma_{\mathrm{BLV}}}}. \tag{6.6}$$

The BLV/IR cross correlation is computed for each level of the Laplacian pyramid and averaged over 7500 images (75 s). Also, the temporal evolution of the correlation with increasing ammonia concentration is computed. For this, the calibrated images are filtered as explained in sec. 6.1.3, to reduce the effect of noise and reflections. The correlation coefficient is computed and averaged over 1500 images (15 s).

6.2.2 Surface velocity

The water surface velocity is determined by tracking the motion of a (stable) streak on the water surface (see Fig. 6.5). Since the advection of structures due to the mean current is faster than processes changing the appearance of the streaks, they

can be treated as passive "particles", which move with the fluid. The shift of a structure between two image pairs is determined by finding the maximum of the cross correlation base. The cross correlation is defined as

$$(f \cdot g)(\mathbf{r}) = \int_{-\infty}^{\infty} \int_{-\infty}^{\infty} f^*(\mathbf{x}) g(\mathbf{x} + \mathbf{r}) d\mathbf{x}. \tag{6.7}$$

It is easily computed in Fourier space, where it reduces to a complex product

$$\mathcal{F}(f \cdot g) = (\mathcal{F}(f))^* \mathcal{F}(g) \tag{6.8}$$

where $\mathcal{F}$ denotes the 2D Fourier transform. The cross correlation is then obtained by applying the inverse Fourier transform. An advantage of this procedure is that the cross-correlation is easily determined with sub-pixel accuracy. For this, the left hand side of eq. (6.8) is placed in the center of a larger array containing zeros before applying the inverse Fourier transform ("zero padding"). By this, the cross correlation is interpolated to the size of the larger array. For the velocity measurements of this study, an up sampling factor of 10 was used (0.1 pixel resolution). In the implementation of the algorithm, first, a lower resolution cross correlation matrix is computed in which the approximate position of the peak is determined, then an up sampled version of just the area around the peak is computed. The algorithm is proposed by Guizar-Sicairos et al. (2008) and described in more detail by Kiefhaber (2014). The position of the peak of the cross correlation (and thus the shift x of the streak from one image to the next) is determined and the velocity is obtained from

$$v_s = x\, f\, \Delta x, \tag{6.9}$$

with the resolution of the image Δx (see Tab. 4.1) and the frame rate f. At higher wind speeds the structures change more rapid and in some cases the assumption that the streaks are passive "particles" moving with the mean flow is not valid anymore. Many of these cases are filtered by reducing the range of allowed values of the shift. This is implemented in the cross correlation algorithm. When searching the maximum of the cross correlation, only a portion of the matrix is used, since for example large shifts in the cross-wind direction are a certain sign of a false correspondence.

6.2.3 Lifetime

The streak is tracked as described in sec. 6.2.2 to compute the lifetime of a streak. A streak, or more precisely a rectangular interrogation window containing a streak, is thus followed in a Lagrangian reference frame, moving with the mean velocity. The streak is considered "alive" as long as the correlation coefficient (see eq. (6.6)) is greater than 0.2. The lifetime is thus defined as

$$\tau = \frac{n_i}{f}, \tag{6.10}$$

where n_i is the number of images before the correlation drops below 0.2 and f is the frequency with which the BLV images are recorded. Correlation coefficients are computed by the function *corr2* (see sec. 6.2.1). The stopping criteria has been chosen by preliminary observations. For lower values it occurs that two close streaks are mismatched and the wrong streak is followed. Also at too high thresholds, short interruptions due to waves stopped the correlation, while the streak has been unchanged after the wave. Hence, 0.2 was found to be a good value to decide if a streak disappears or changes his form too much.

One difficulty that occurred for low wind speeds is that before the streak changes its structure enough or disappears it moves out of the image. Hence, the tracking of the streak stops. This is a problem particularly at low wind speeds, where streaks are very stable. Therefore, lifetimes of streaks at low wind speeds are a lower limit. Streaks would live longer, but cannot be tracked long enough.

6.2.4 Microscale wave breaking detection

In Fig. 6.5(b) an example of a microscale breaker in a fluorescence image is shown for a wind speed of 2.5 m/s at clean water conditions. A manual procedure has been used to compute the rate of microscale breaking. Therefore, the number of microscale breakers during 75 s in the images have been counted. The number of microscale breaking events n_i is divided by the elapsed time in the images to get the rate

$$\nu_{\mathrm{mb}} = \frac{n_i}{t}. \tag{6.11}$$

By counting microscale breaking at one point (rather than counting all events in the image) a better comparable value to the renewal rate of gas exchange could be achieved. The main characteristics of a microscale breaker are described in sec. 2.3.4. An example of microscale breakers in a BLV image is shown in Fig. 6.5(b). However, the challenge is to find a clear definition for a microscale breaker. Does a high intensity crest alone account for a microscale breaker? Has the surface to be renewed (dark) at that point or has the wave to break? Hence, it is simpler to count the events in one image, since the size is clear and in nearly all cases the microscale breaker breaks and renews the surface in the image.

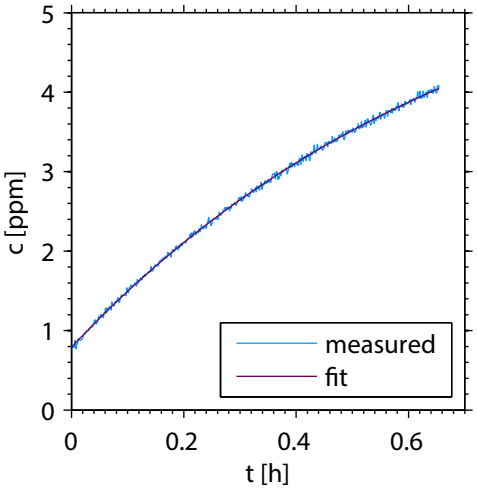

Figure 6.6
Computation of the transfer velocity: Fit of the air-side concentration of ammonia over time at a wind speed of 1.5 m/s. The blue line shows the concentration and the purple line the fit to the data (see eq. (6.12)).

6.3 Transfer velocity

In this section, the calculation of the integrated transfer velocities for ammonia by applying the box model described in sec. 3.6 and the determination of the fraction of the air to water-side transfer rate are shown (see eq. (3.17)).

6.3.1 Integrated transfer velocities

The air-side concentration of ammonia has been measured by differential optical absorption spectroscopy (DOAS) as described in sec. 3.5. The air-side concentration has to be fitted by an exponential function (see eq. (3.31)) to get integrated transfer velocities. This has been realized by a nonlinear least-square fit (Matlab® function *lsqnonlin*).

The fit interval starts a minute after the injection of ammonia into the air space. This was due to the injection at a single point. In the first minute, the ammonia is not yet homogeneously distributed in the air space. On the other hand the flux controller is working normally up to a pressure of 8 bar. Ammonia has a vapor pressure of approx. 8 bar, depending on its temperature. If the ammonia gas bottle was opened the flux controller needed seconds to control the flux of ammonia. This lead to higher fluxes at the beginning of the injection and hence in the observed ammonia concentration. Therefore, the start of the fitting has been chosen to be one minute after the start of the injection to omit the unrealistic peaks. A function in the form of

$$c(t) = x_0 + x_1(1 - \exp(-\lambda t)) \tag{6.12}$$

has been fitted to the increase of the air-side concentration (see Fig. 6.6). The free parameter x_0 has been included in the fit, due to the non zero concentration at the start of the fitting interval and λ is the fit coefficient, which is used to compute the

transfer velocity (see eq. (3.32)). The only unknown parameter is the leak rate, which influences λ. Since no leak rates have been measured during the experiments in this thesis, the measured leak rates from the *Aeolotron* experiments in February/March 2011 (Krall 2013, Kräuter 2011, Mesarchaki et al. 2014) have been used. The leak rates increase with the wind speed and range from 0.07 to 0.35 1/h. The measurement of the leak rate is explained in detail in Krall (2013).

6.3.2 Ratio of the air to water-side transfer velocity

In sec. 3.4, it was shown that for an air-side controlled gas it is possible to determine the ratio of the air to the water-side transfer velocity. By changing the formulations in eq. (3.25) one gets for the ratio

$$\frac{k_a}{k_w} = \frac{10^{-pH_b}}{c_{b,a}}. \tag{6.13}$$

Therefore, one needs to know the pH value in the water bulk pH_b and the air-side concentration of ammonia in the air bulk $c_{b,a}$. Both parameters are measured continuously during the experiments. As mentioned in sec. 3.4, eq. (6.13) is only applicable for surface pH values around 7, since three of the four approximations made are not valid for higher pH values and one is not valid for lower pH values. An error due to the approximations of 5 % has been estimated (see sec. 3.4). With the standard methods it is not possible to measure the pH value directly at the surface. However, the fluorescent indicator Pyranine starts to emit fluorescent light at a pH value around 7. Hence, if the surface starts to be fluorescent one knows that the pH value is approx. 7 and eq. (6.13) is used to compute the ratio of the transfer velocities.

From visual inspection, it is very clear at which time the fluorescence starts, the maximum error is estimated to be ± 7.5 s. This is the time of one recorded sequence, since one sequence is dark and two sequences further there is a clear signal (one sequence is 15 s long). It is necessary to convert the air-side concentration to mol/L by

$$c_a[\text{mol/L}] = \frac{c_a[\text{ppm}]}{V_{mol} \cdot 10^6}, \tag{6.14}$$

with the molar volume V_{mol} (24.4 L/mol @ 25 °C) to compute the transfer velocity ratio from the measured ammonia and $[H^+]$ concentrations at the determined time. The error for the concentration and pH value are approximated by the temporal error of ± 7.5 s of the fluorescence detection. For the pH value the error is approx. 4×10^{-3} and for the air-side concentration it depends on the wind speed. It increases from low wind speeds, where the concentration increase is slow, from approx. 3×10^{-2} ppm to 0.4 ppm for the high wind speeds, when the increase is much faster. The error for the ratio is computed by error propagation. These errors account for the uncertainty in the temporal detection of the fluorescent structures. Not included is the approximation error of 5 % and the error, which could arise from the devices itself. In the

technical data sheet of the pH sensor the absolute error is estimated with 10^{-3}. The absolute error of the concentration measurements due to the DOAS fit (see sec. 3.5) is 5×10^{-3}. Both errors are negligible compared to the error in detection time. The maximum error at the highest wind speed is 20 %.

7
Results and Discussion

Images recorded with the novel boundary layer visualization technique, imaging the surface footprints of near-surface turbulence, are analyzed in sec. 7.1. Microscale breaking and its influence on air-water gas exchange is addressed in sec. 7.2. A direct comparison of collocated infrared and fluorescence images, which were recorded simultaneously, is shown and discussed in sec. 7.3. Integrated transfer velocities of ammonia, as well as the ratio of the air to the water-side transfer velocities are given in sec. 7.4. Additional parameters, which are important for air-water exchange processes, such as the surface velocity and the dimensionless momentum transfer resistance are presented in sec. 7.6 and sec. 7.7.

7.1 Fluorescent footprints of near-surface processes

In this section the fluorescent footprints of near-surface flow processes in the boundary layer visualization (BLV) images are shown, explained, and discussed in detail. Parameters to describe the fluorescent footprints quantitatively are given and their meaning is discussed. At the beginning of this section a general description of the fluorescence images is given and then specific near-surface processes are discussed in detail. Image sequences have been recorded for all conditions described in Tab. 4.1.2 and Tab. 5.3 at the large annular wind-wave facility *Aeolotron*. Example images of the different conditions are shown. It should be noted that some aspects described in the following section are more easily observed when watching sequences of images. Example sequences are linked[1] in the caption of the following figures.

In Fig. 7.1, four snapshots are shown for different wind speeds at the condition

[1] https://www.youtube.com/channel/UCXeBh78HHowMzlLBuPJIM8Q

"clean Tartrazine". The snapshots have a size of 25 cm along and 21 cm in cross-wind direction. The resolution is 0.156 mm/pixel and the wind is always blowing from right to left. Observed intensities are calibrated by a wedge and converted to a neutral layer thickness (see sec. 6.1.2). Fluorescent light is emitted, wherever the pH is larger than seven. However, the depth from which the fluorescence is coming is not measured; the signal at each pixel is integrated over the full water column. Hence, the calibrated thickness cannot always be interpreted as the thickness of a fluorescent layer at the surface. A threshold concentration of ammonia in the air is needed to increase the pH at the surface above seven to excite fluorescence. In the first image (a) the reference wind speed is 0.4 m/s and the air-side concentration is $c_a = 1.9$ ppm, in image (b) $u_{ref} = 1.4$ m/s ($c_a = 5.2$ ppm), in image (c) $u_{ref} = 4$ m/s ($c_a = 10$ ppm), and in image (d) $u_{ref} = 5.8$ m/s ($c_a = 8$ ppm).

The images in Fig. 7.2 show snapshots of the water surface for the condition with a concentration of 0.26 µmol/L of the surfactant Triton X-100 (see sec. 2.3.5). The reference wind speed increases from image (a) to (d) from 0.8 m/s to 6.1 m/s. The air-side ammonia concentrations are (a) $c_a = 2.2$ ppm, (b) $c_a = 5$ ppm, (c) $c_a = 9.8$ ppm, and (d) $c_a = 9$ ppm. The images have wind speeds and air-side ammonia concentrations that are close to the ones in Fig. 7.1. The images are compared in the following sections and the effect of the surfactant on the fluorescent streaks is investigated.

Figure 7.3 shows two images recorded with the wave absorber ("beach") installed in the Aeolotron. The resulting fetch is 2.0 m in image (a) and 23.4 m in image (b). The reference wind speed for both conditions is 2.3 m/s and the air-side concentration is 5.4 ppm. The only difference is the fetch. These images demonstrate the effect of different wave fields: (a) very young wave field, which is still building up and (b) an older one.

In Fig. 7.4, a space-time image is shown, which allows gaining insights into the temporal evolution of the fluorescent structures. The image is created by observing the change of a single column of the BLV image (see purple lines in Figs. 7.1(b) and 7.2(b)) over time. Thus, the y-axis is the fluorescence profile in the cross-wind direction and the x-axis is time, a total of 45 s are shown here. These time series give insights into the build up and break up of a surface film (a) and shows the temporal footprints of waves, fish-scales, and Langmuir circulations (b). All of these will be discussed below.

7.1.1 Fish-scales and Langmuir circulation

Turbulent eddies in the water transport fresh (slightly acid) water to the surface and renew the surface. This fresh water pushes the "old" surface water aside. Due to mass conservation the water from the surface is transported downwards at another location. Bright convergence zones, at which the surface water that was enriched with ammonia accumulates and is down-welled and dark divergence zones, at which fresh acid water is brought to the surface, are forming. At a shear driven surface the footprints of these zones are called streaks.

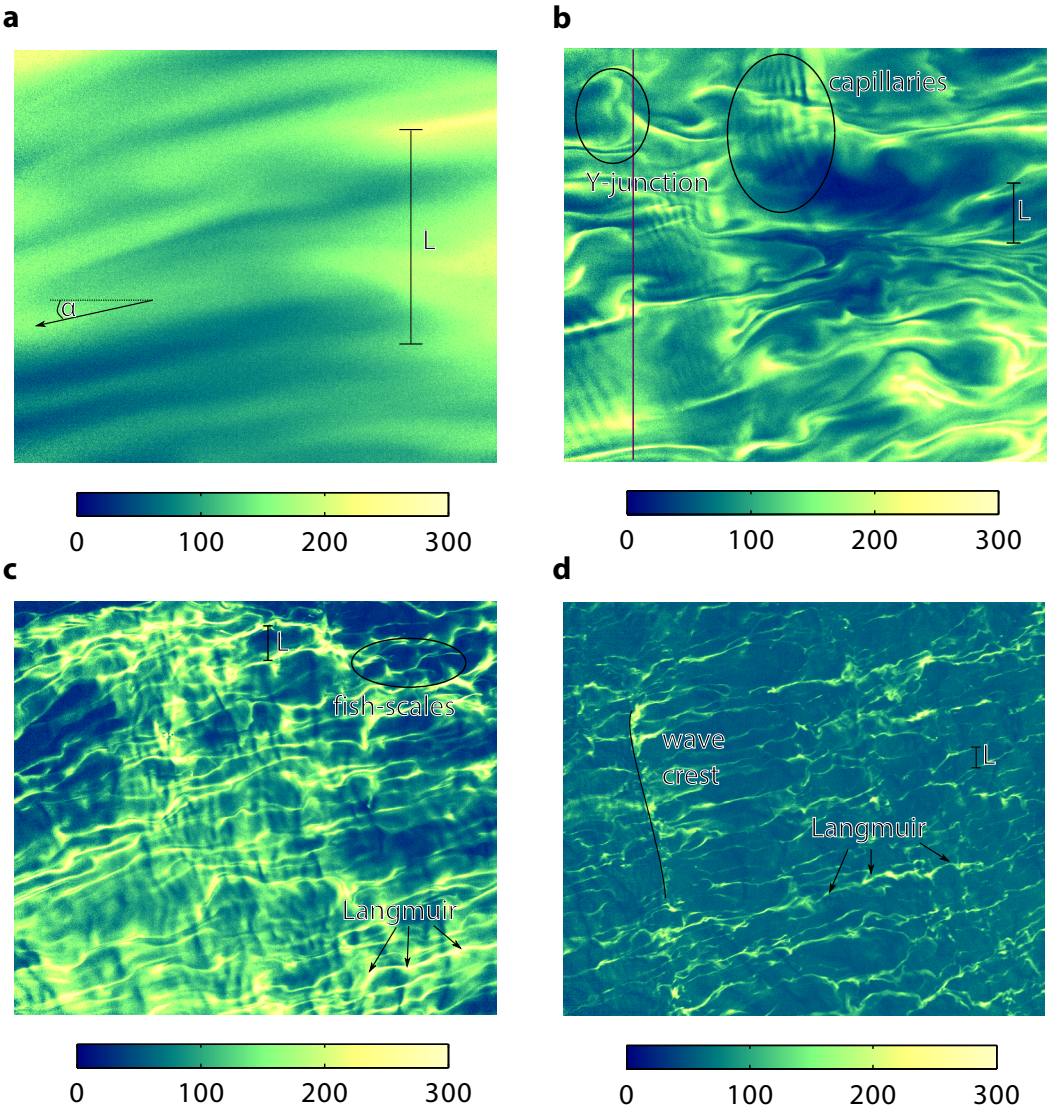

Figure 7.1.
BLV example images for a clean water surface. The image sizes are (21 × 25) cm^2. The color maps show the thickness of the alkaline layer in micrometers. Wind is blowing from right to left with reference speeds of **a** 0.4 m/s ($c_a = 1.9$ ppm) **b** 1.4 m/s ($c_a = 5.2$ ppm) **c** 4.0 m/s ($c_a = 10$ ppm), and **d** 5.8 m/s ($c_a = 8$ ppm). In each image the theoretically expected streak spacing (see eq. (2.45)) is indicated by a bar. In image (a) the angle between the wind and the streak direction is shown. Fish-scales, footprints of Langmuir circulations, Y-junctions, and waves (capillaries and a wave crest) are labeled in the images. The vertical purple line in image (b) marks the location of the temporal evolution shown in Fig. 7.15(b). Image sequences of a 3D height reconstruction with an overlay of the BLV images can be found at the following links for 1.4 m/s, 2.5 m/s, and 4.0 m/s.

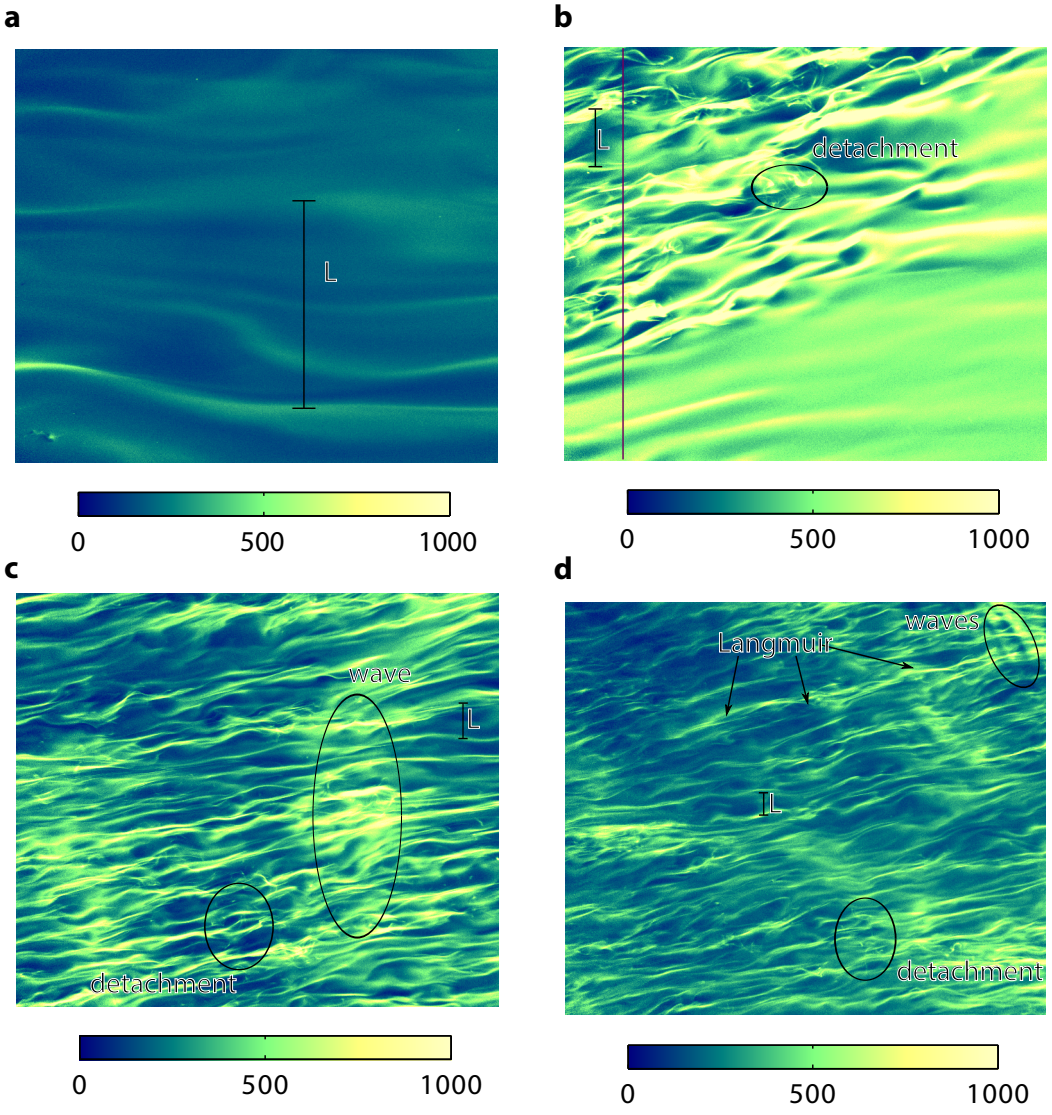

Figure 7.2.
Same as Fig. 7.1, but for surfactant-covered water (0.26 µmol/L Triton X-100 and Tartrazine). Wind speeds are **a** 0.8 m/s ($c_a = 1.7$ ppm) **b** 1.4 m/s ($c_a = 5$ ppm) **c** 4.2 m/s ($c_a = 9.8$ ppm), and **d** 6.1 m/s ($c_a = 9$ ppm). An image sequences of a 3D height reconstruction with an overlay of the BLV images can be found at the following link for 3.4 m/s.

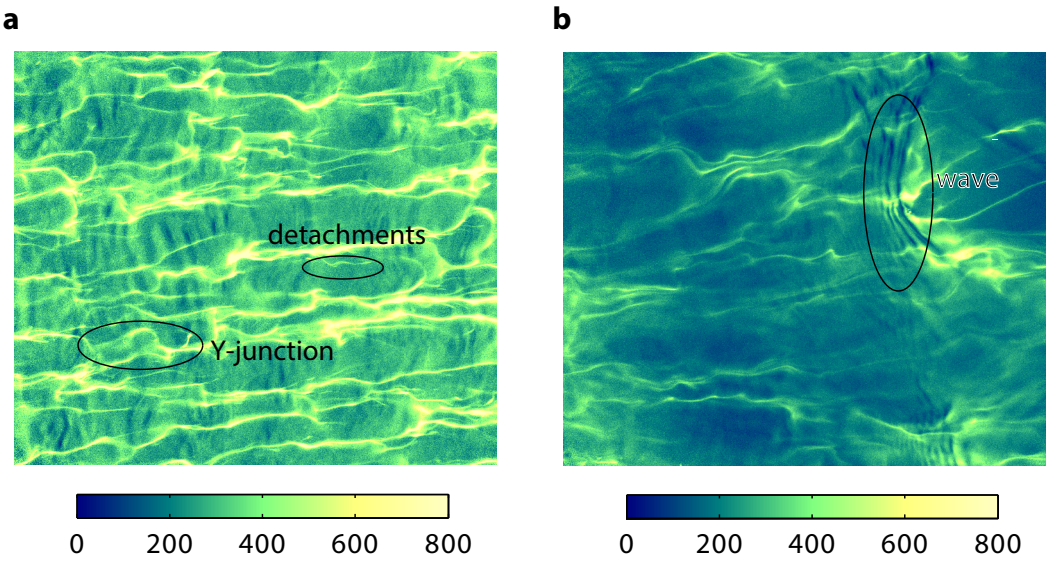

Figure 7.3.
Same as Fig. 7.1, but for clean water at two different fetches at a wind speed of 2.3 m/s. The concentration in the air is $c_a = 5.4$ ppm at both conditions. Fetches are **a** 2.0 m (fetch 4) and **b** 23.4 m (fetch 1).

From the analysis of infrared imagery, two distinct types of streaks are known: Langmuir and fish-scale (see sec. 2.3.2). The main differences between the two are their lifetime. While streaks caused by Langmuir circulation (LC) are relatively persistent the fish-scales appear only shortly. In the fluorescence images, the same types of patterns are observed as in the thermal images. Langmuir circulation streaks and fish-scales are marked in Fig. 7.1(c), (d), and in Fig. 7.2(d). In the space-time image in Fig. 7.4(b) the differences are much clearer than in a snapshot, since the lifetime of a structure at a certain point is visible. LC streaks are more prominent due to their longer lifetime. As described in sec. 2.3.3, the nature of fish-scales is shear stress alone. An interaction of waves and the shear current is required to form LC cells, as explained in sec. 2.3.2. Therefore, the streaks in Fig. 7.1(a) and Figs. 7.2(a) and (b), where the wind speed is too low to form waves, are fish-scales. Even at the lowest measured wind speed and at conditions with an additional damping of near-surface turbulence due to a surfactant, a streaky pattern is observed. The process creating fish-scales is not yet fully understood.

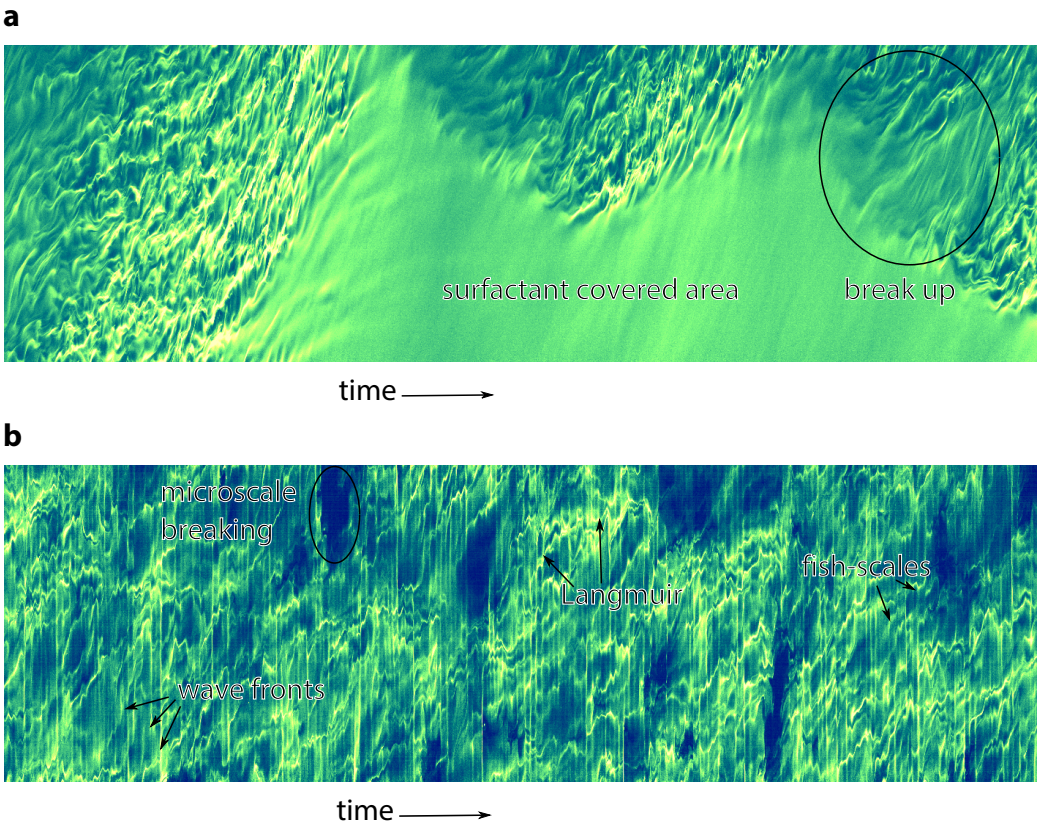

Figure 7.4.
Space-time images: Time series of neutral layer thickness of one column of a BLV image (cross-wind direction), time is increasing to the right. **a** Surfactant case: the temporal evolution of the profile in Fig. 7.2(b) is shown for 45 s. A patchy structure of the surface conditions is visible. **b** Same as before but for clean water: the profile is taken from Fig. 7.1(b). Distinct footprints of Langmuir circulation, fish scales and microscale breaking are observed.

Dependence on surface films

Comparing the images in Figs. 7.1 and 7.2, differences are most prominent at the lower wind speeds. At the lowest shown wind speed the clearest difference is the intensity. The thickness of the neutral layer in Fig. Fig. 7.2(a) is much higher than in Fig. 7.1(a) even though the air-side ammonia concentration was lower. This is expected since the near-surface turbulence is reduced and hence the boundary layer is thicker. This leads to higher accumulations of ammonia at the surface and the depth, at which the critical concentration for fluorescence is exceeded, is further down. The transfer velocity for a surfactant covered conditions is reduced by up to 70 % compared to clean water conditions (Mesarchaki et al. 2014). Hence, the boundary layer thickness is enhanced as well. This is discussed in detail in sec. 7.5.

Streaks can be observed in both images. Apart from the differences in neutral layer thickness, the images are very similar. In both cases no waves are present. The images Fig. 7.1(b) and Fig. 7.2(b) look very different. While clear structures have evolved in the condition with clean water, in the condition with the surfactant the surface is partly covered by areas with streaks and partly covered with a relatively homogeneous distribution of neutral layer thickness. The streaks are not Langmuir circulations, since waves were not present. This is shown by the very low value of mean square slope measured by the ISG. A better comparison of the two conditions is possible with the space-time images in Fig. 7.4. Both temporal evolutions show streaky patterns. In image (b) the footprints of Langmuir circulations, fish-scales, and waves (even microscale breaking) are clearly visible (waves will be discussed in the following sections). In image (a) the build and break up of the mostly homogeneous fluorescent area is shown. It is assumed that the surface patch, in which ammonia is transferred into the bulk water from the surface mostly by diffusion, is covered by an area of a high surfactant concentration. Surface divergence and convergence (i.e. flows along the water surface) are almost fully suppressed, which is a typical effect of surfactants. The surface film changes the hydrodynamic boundary conditions, since spreading the film requires a certain force (McKenna and Bock 2006). On the patches where streaks are forming, surface flows are not fully suppressed, which hints at a lower film pressure opposing the flow and thus at a lower density of the surfactant. The Eulerian view, shown in Fig. 7.4, demonstrates the behavior that at a certain point the diffusive area starts to evolve on the inner wall of the wind-wave facility and slowly covers the whole surface and suppresses the streaks. In a Lagrangian view (video sequences), one sees that a surface patch covered with the surfactant moves around the wind-wave facility and only slightly changes its shape during time. The accumulation of the surfactant at the inner wall is expected due to the secondary flows in the air at the annular wind-wave facility (Bopp 2014).

Moreover, the images imply that the surfactants are not equally distributed on the whole surface but rather accumulate in patches. The boarder of the high density surfactant area seems to be rather sharp. At the downwind end of the surfactant patch streaks are not changed by the surfactant. At the upwind edges of the surfactant

covered area (break up area) the streaks are not as distinguished as downwind. These areas seem to be covered by a surfactant but maybe not in such high concentrations as in the part where diffusion seems to be the controlling transport mechanism. This behavior is not visible at lower wind speeds. This leads to the conclusion that the surfactant is equally distributed for low wind speeds, while it is pushed into patches of high concentrations if the shear stress is sufficiently high. In the video sequences of the images 7.2(c) and (d) such areas are also not visible. It is concluded that at higher wind speeds, the soluble surfactant is mixed into the bulk by the increasing turbulence and has no time to rebuild.

By comparing the images 7.1(c) and (d) with the images 7.2(c) and (d), one sees that the shape of the streaks is different. In clean water, the streaks seem more curvy (disturbed in the direction), while the streaks in the surfactant covered case are straighter. A hypothesis for the more stretched structures might be that the near-surface turbulence is reduced by the surfactant. In the images 7.1(c) and (d) small capillary waves are present, while in the images 7.2(c) and (d) only larger waves are visible. This can also be observed in the mean square slope measurements, since the *mss* is 6.3 (c)/2.5 (d) times larger for clean water. It is suspected that smaller not visible eddies beneath the surface are as well suppressed by the surfactant as the waves.

Fetch dependence

Differences in intensity are also clearly visible in Fig. 7.3. At the same color map scaling, image (a) is much brighter than images (b) although they are recorded at the same air-side concentration and wind speed. However, the wave field is different. This has been achieved by placing a wave absorber in the facility at different positions. This breaks the radial symmetry of the water channel and leads to a position-dependent wave field. The Fig. 7.3 shows the fluorescent footprints at two different fetches, i.e. downwind distances from the wave absorber. For the long fetch of 23.4 m in Fig. 7.3(b) the streaks seem more chaotic than for the short fetch of 2.0 m in Fig. 7.3(b). There, the streaks are brighter, more aligned with the wind speed, and more persistent. Waves seem to increase the near-surface turbulence and reduce the boundary layer thickness. Therefore, the structures in Fig. 7.3(b) are more chaotic and less bright (smaller boundary layer thickness) than in Fig. 7.3(a).

Orientation

Streaks are more or less aligned with the wind direction. The angle α, shown in Fig. 7.1(a) between the mean bulk air flow and the streaks on the water surface is approx. 15°. The angle increases with wind speed to about 20°. For the short fetch condition in Fig. 7.3(b) the streaks are aligned with the mean wind direction.

The mean wind direction is not comparable to the surface wind direction. As shown by Bopp (2014), the wind close to the surface is slightly directed to the inner wall. He measured at a distance of some millimeters away from the water surface. The water flow at a distance of 10 cm is slightly directed to the outer wall (Bopp 2014). The orientation of the streaks shows that the surface velocity is directed slightly to the inner wall. Therefore, the mean flow has to change its direction between the water surface and a depth of 10 cm. Due to the wave absorber the water and wind fields are disturbed and the surface water flow is more aligned with the mean wind direction.

Y-junctions

Another footprint that is for example marked in Fig. 7.1(b)and Fig. 7.3(a) is a Y-junction. A streak splits up into two streaks. The preference of a streak to form a Y shape with the open end downwind is shown by Farmer and Li (1995) and Marmorino et al. (2004). The same is observed in this thesis. Tsai (1998) and Tsai and Liu (2003) investigate the nature of these footprints in numerical simulations. They find that the process creating these footprints is a local upwelling, which emerges from Ω-shaped horse-shoe vortices (see Fig. 2.6). At the surface they break into two parts and induce local upwelling. Hence, they disturb the streak pattern and Y-junctions are formed. This process is shear induced and hence can be seen during most conditions. At the lowest wind speed (images 7.1(a) and 7.2(a)) Y-junctions have not been observed. This might indicate that a stronger shear stress is needed to create these horse-shoe vortices.

7.1.2 Streak spacing

The spacing between streaks is an indicator for the cross-wind distance between two along-wind eddies (see sec. 2.3.3). The theoretical dimensionless streak spacing $l^+ = lu_*/\nu$ found to be 100 (see sec. 2.3.3). The average streak spacing is l, u_* is the friction velocity, and ν is the kinematic viscosity. Thus, with increasing friction velocity the spacing l between the streaks is decreasing. The expected average streak spacing l (assuming $l^+ = 100$) is indicated by the bar and the "L" in each image (see Figs. 7.1 and 7.2).

Schnieders et al. (2013) find a critical friction velocity ($u_{*,c} = 0.7$ cm/s) at which the streak spacing stagnates. The same limit has been suggested by Banner and Peirson (1998). They find that at the critical friction velocity most of the wind stress

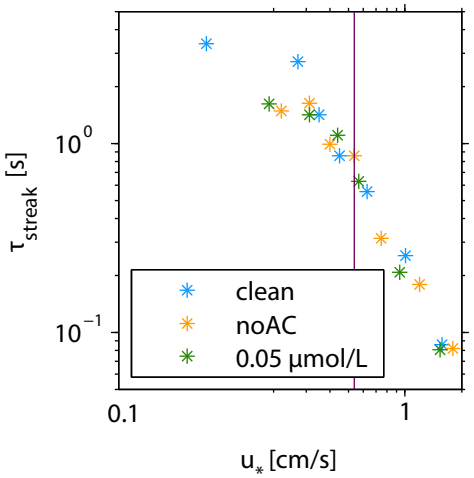

Figure 7.5
Dependence of the streak lifetime on friction velocity. Values are from clean water (blue), no AC (orange) and low surfactant concentration (green) cases. Lifetimes given at $u_* \leq 0.5$ cm/s are only lower limits (purple line), as streaks are advected out of the image before they disappear.

is transformed into form drag of the waves and a smaller part is transformed into tangential stress. Schnieders et al. (2013) propose that this stagnation starts with the onset of gravity waves. These are waves which are restored by gravity and not surface tension as capillaries (see sec. 2.3.4). Larger scale gravity waves are certainly present in images 7.1d and 7.2d. However, the visual impression is that the streak spacing still decreases. Schnieders et al. (2013) mention that the low resolution of the infrared images could be a problem for determining a correct streak spacing at higher wind speeds. This will be investigated in detail in a further study.

7.1.3 Lifetime of streaks

In Fig. 7.5 the lifetime of streaks for three different conditions is shown. In blue, the condition with clean water and the absorbing dye Tartrazine, in orange clean water without air conditioning and in green, water with a concentration of 0.05 µmol/L Triton X-100 are shown. To compute the lifetime of streaks, they are tracked in the image until the correlation between the image of the streak at the beginning and after a certain time is below a threshold of 0.2. The time elapsed between these images is the lifetime. In sec. 6.2.3, the computation of the lifetime is described in detail. There is an upper limit for the lifetime detection, for low wind speeds. This is due to the fact that the streaks live longer than they are visible in the image. Hence, the lifetimes below a friction velocity of 0.5 cm/s are only a lower limit. The limit is marked by the purple line in Fig. 7.5.

The lifetime of a streak seems to be only dependent on the friction velocity and not on the surface conditions. This confirms that at higher wind speeds the conditions are comparable (Kiefhaber 2014, Kräuter 2011). The surfactant does not play a significant role at the high wind speeds. At lower wind speeds effects would be expected, but cannot be evaluated because of the mean surface velocity. A larger image area has to be used to investigate the lifetime of streaks at lower surface velocities.

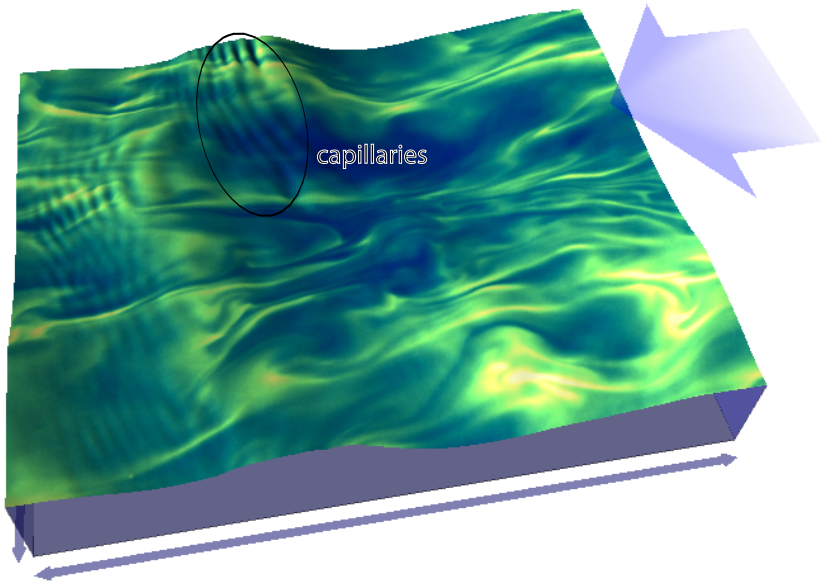

Figure 7.6.
3D rendering of the water surface with BLV image overlay (created with WaveVis, Jung (2008)). The same BLV image as in Fig. 7.1(b) is shown. The large arrow indicates the wind direction and the image size is (22 × 17) cm².

7.1.4 Non-breaking waves

Non-breaking waves are visible for example in Fig. 7.1(b). A set of capillaries is well recognizable in the upper middle part of the image. The confirmation that these structures are indeed waves can be seen in Fig. 7.6. This image shows an overlay of the boundary layer visualization and the water surface elevation reconstructed from imaging slope gauge measurements. The overlay has been realized with the WaveVis visualization tool (Jung 2008, Wanner 2010). The capillaries from Fig. 7.1(b) are clearly visible in the back of the image 7.6 and the wave crests and troughs correlate with the intensity differences.

Waves cause different footprints, e.g. in Fig. 7.1(d) a bright wave crest is marked, in Fig. 7.2(c) the wave enhances the brightness in a broad part (no capillaries) and in Figs. 7.2(d) and 7.3(b) some smaller capillary waves are visible, comparable to Fig. 7.1(b) can be seen. In the time series waves are also clearly visible. In Fig. 7.4(b) wave fronts are detectable as vertical bright lines. These are the bright wave crests, e.g. of microscale breakers.

The visibility of the waves might be due to three reasons: the wave itself accumulates ammonia at the crest, height differences due to waves change the fluorescence, and/or the wave acts as a lens. The first effect would be directly due to gas exchange and clearly interesting, but it has not been observed in this strength in the infrared images for non-breaking waves. High intensities at the crest of microscale breakers,

which will be shown and discussed in the next paragraph, are also visible in infrared images and hence are a physical aspect. The second reason might be due to additional fluorescence from the bulk (see sec. 3.2). This effect cannot be completely excluded, but should be reduced due to the absorbing dye Tartrazine in the water (see sec. 3.2) and the filters in front of the light sources (see sec. 4.1.5). This should only play a role for larger wave heights and in the conditions without Tartrazine. In the images in Fig. 7.1 and Fig. 7.2 Tartrazine is added to the water. The other optical reason might be due to a lens effect of the waves. The light is focused beneath the wave crest and defocus in the wave trough. Hence, the fluorescence at the wave crest would be higher than in the wave trough. Possibly, it is a combination of all three effects.

In Fig. 7.1(d) large gravity waves are present, which modulate the height and hence decrease the sharpness of the image due to the small depth of field. On the large gravity wave many small capillary waves can be seen.

The waves interact with the streaks. A non-breaking wave stretches the streaks and it seems that the streaks have a wider spacing behind the wave crest. After the wave passed the streaks regain their original form. The tangential stress is reduced at the wave crest (Banner and Peirson 1998, Okuda et al. 1977, Peirson 1997) and the streak spacing increases (see eq. (2.45)).

7.1.5 Detachments from the alkaline layer

With the boundary layer visualization technique it is possible to investigate turbulence in different depths. By changing the flux of ammonia into the water, the mean thickness of the fluorescent layer can be controlled (see sec. 3.1). However, especially for higher ammonia fluxes, fluorescent layers can also exist beneath the surface, outside the mass boundary layer. These fluid packets of high pH and high concentration of ammonia are transported downwards by large eddies and then diffused by mixing with the slightly acid bulk water. During the experiments, such events were observed from a side-view window. Detached fluid packets are also visible in the BLV image sequences since they are advected only with the bulk current and not with the higher surface current. The detachments are for example shown in Fig. 7.2(b) and (c) from above.

These surface renewal events appear randomly and the concentration gets randomly detached beneath the surface and small thin streaks are transported away from the surface. These detachments have also been observed by laser-induced fluorescence measurements (Friedl 2013). They are not aligned with the wind speed and seem chaotic. After a few seconds, depending on the strength of the mixing, the structures disappear by neutralization. In the experiments for this thesis, no information about the depth of these detached structures could be gained. This is the goal of another experiment (see sec. 8.2).

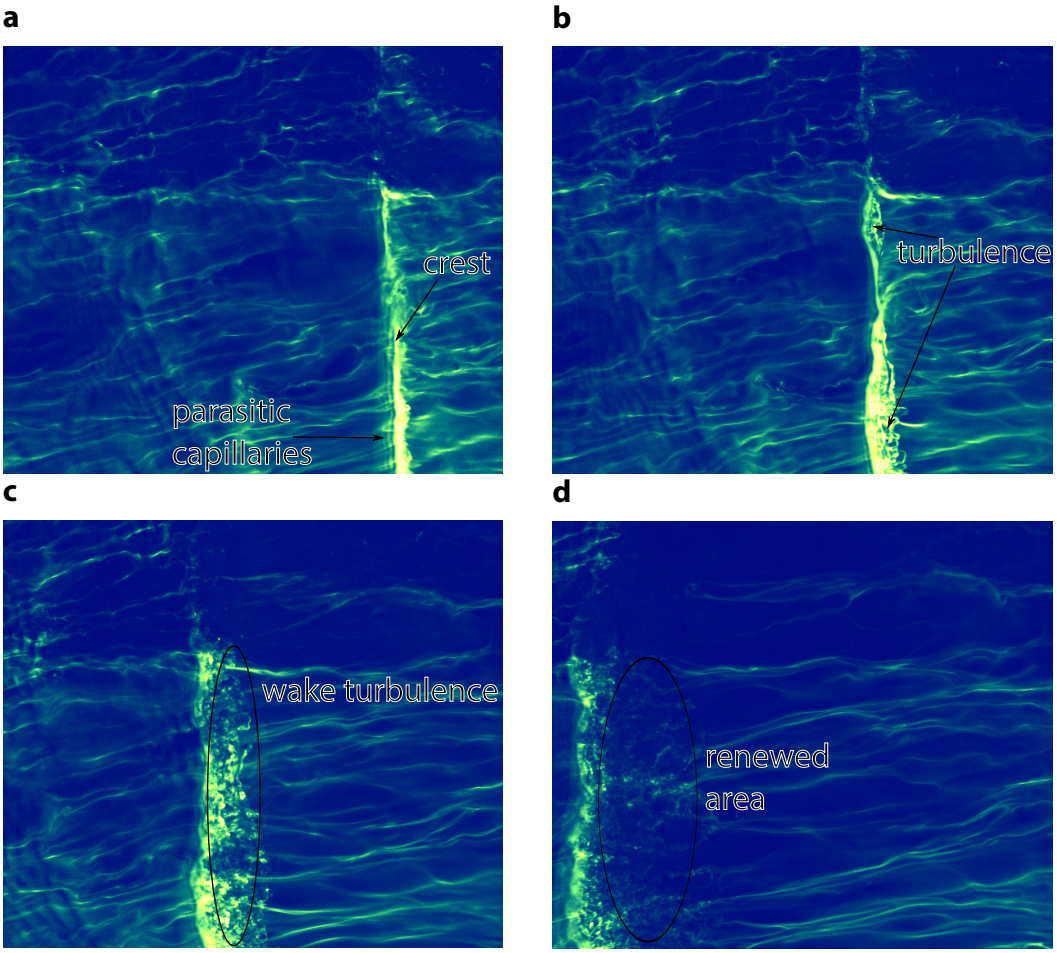

Figure 7.7.
Evolution of a microscale breaker: BLV example acquired with clean water and 4 m/s wind speed.**a** Ammonia is accumulated at the wave crest, which has parasitic capillary waves in front. **b** The wave is breaking and ammonia is effectively transported downwards. **c** The wave starts to break, ammonia is transported downwards at the back of the crest. Wake turbulence can be clearly seen, **d** The wave vanishes; its wake is still clearly turbulent. The area behind the wave is renewed (darker).

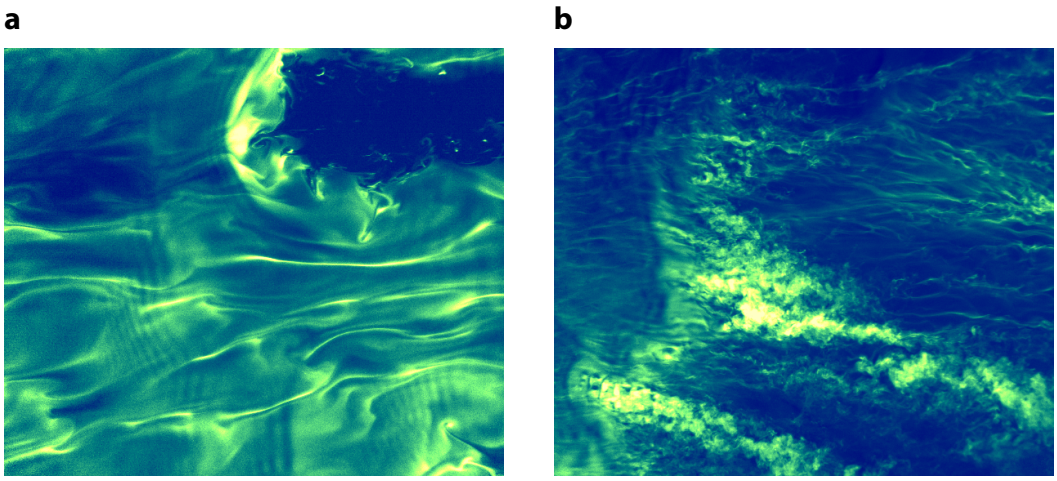

Figure 7.8.
Two further examples of microscale breakers. **a** The wind speed is 1.4 m/s, the ammonia concentration is 5.2 ppm, and the water surface is clean. **b** The water surface is covered with a concentration of 0.26 µmol/L Triton X-100, the wind speed is 6.1 m/s, and the air-side concentration is approx. 9 ppm.

7.1.6 Microscale wave breaking

Short gravity waves with typical wavelengths smaller than 1 m become unstable if the shear stress reaches a critical value. They dissipate energy without creating bubble plumes or foam at the surface. This subtle process is called microscale wave breaking (see sec. 2.3.4). Microscale breaking waves have been investigated extensively with the help of thermal imagery (Jessup et al. 1997b, Siddiqui et al. 2001a, Zappa et al. 2004). In their wake, warm bulk water replaces the surface that has cooled by evaporation (see Fig. 2.5(b)). In BLV fluorescence images, microscale breaking waves cause different footprints. An example of the evolution of a microscale breaker is shown in Fig. 7.7. At the build up of the microscale breaker, surface water that is enriched with ammonia is accumulated at the wave crest. The wave crest moves faster than the surrounding streaks. In front of the wave crest parasitic capillaries are visible, which are a typical feature of microscale breaking waves (see Fig. 2.7) (Jessup et al. 1997b). Turbulent kinetic energy is produced at the breaking crest. Since the concentration at the wave crest is high, the turbulent eddies which mix ammonia from the crest into the bulk are visible. By observing the microscale breakers from the side one can see that the fluorescent eddies are transported to the depth. They look similar as shown in Fig. 2.7. The fluorescent surface waters that are mixed into the bulk are rapidly diluted by the high turbulence levels and the acid water from the bulk is pushed upwards behind the microscale breaker. Thus, behind the breaker, the intensity of fluorescence is decreased. Before the microscale breaker moves through the image the streaks are curvy. Afterwards the lines seem to be more straight.

The shown images demonstrate a typical evolution of microscale breaker. However, they occur in different sizes, have curved and straight wave crests and move not

always aligned with the wind direction. Examples of other forms of microscale breakers are shown in Fig. 7.8. The smaller one in (a) has a curved wave crest. Figure 7.8(b) shows a microscale breaker for water which is covered with Triton X-100. The crest is already broken and only the wake turbulence can be clearly seen. It is much wider and the small eddies cannot be distinguished. It looks like an ammonia cloud. The renewed area can hardly be determined, since the concentration below the water surface interfere the observation of the renewed area. The differences between the two surface conditions might also be due different ammonia concentrations in the air. Nevertheless, it could also be an indication for a reduction in small-scale turbulence in the case of a surfactant covered surface as has been proposed in sec. 7.1.1.

The feature of imaging the turbulence behind the microscale wave breaker is a tool to investigate their different behavior. The wake turbulence, which has been measured by particle imaging velocimetry (Siddiqui et al. 2001a), can now be investigated with the same technique simultaneously. As already mentioned in sec. 7.1.5 by increasing the ammonia concentration in the air further depths can be observed and a 3D reconstruction is possible with multiple cameras.

7.2 Microscale wave breaking and gas exchange

This section describes microscale wave breaking events (MB) quantitatively. It is discussed at which conditions and wind speeds MB occurs and which parameters can be used to describe it. Additionally, its impact on gas exchange is discussed.

7.2.1 Occurrence of microscale wave breaking

In Tab. 7.1, the occurrence of microscale wave breaking (MB) is shown for all conditions and wind speeds. The wind speeds are given by the turbine frequency in Hertz, since the reference wind speeds for the different conditions vary slightly (see Tab. 5.2 and Tab. 5.3). The crosses mark that no MB has been observed, while the check marks symbolize MB. Conditions with large scale wave breaking with air entrainment ("white capping") are marked with "b". At clean water conditions MB occurs from 7/9 Hz. With higher concentrations of the surfactant, MB begins at higher wind speeds (12/16 Hz). The shorter the fetch, the more wind is needed to enable MB in the measurement area. At the shortest fetch (fetch 4), MB has not been observed at any condition. Wave breaking with bubble entrainment start at 22 or 29 Hz, depending on the condition.

Table 7.1.
Detection of microscale wave breaking for all conditions and wind speeds. The wind speed is given by the used wind generator frequency in Hz. The crosses "x" mean that no microscale breaking has been detected, the check markers symbolize microscale breaking, and "b" stands for a breaking wave with bubble entrainment. The minus symbolizes that the condition has not been measured.

condition/wind [Hz]	5	7	9	12	16	22	29
no AC clean	x	✓	✓	✓	✓	b	b
clean	x	x	✓	✓	✓	b	-
clean/Tartrazine	x	x	✓	✓	✓	b	b
0.05 µmol/L Triton	x	x	x	✓	✓	b	b
0.26 µmol/L Triton	x	x	x	x	✓	✓	-
0.26 µmol/L Triton/Tartrazine	x	x	x	x	✓	✓	-
fetch 4 (2.0 m)	-	x	x	x	x	x	x
fetch 3 (4.5 m)	-	x	x	✓	✓	✓	-
fetch 2 (10.2 m)	-	x	-	✓	✓	✓	-
fetch 1 (23.4 m)	-	x	✓	✓	✓	b	b

Discussion

Microscale wave breaking occurs if the surface shear stress is high and the waves become instable and break. Hence, a certain energy input is needed. This is not only dependent on the shear stress, but also on the water surface conditions (surfactant coverage). For clean water the friction velocity has to be larger than 0.27 cm/s, for a medium concentration of Triton larger than 0.31 cm/s, and for a high concentration larger than 0.43 cm/s. The differences between the clean water conditions are due to the air conditioning which reduces the wind speed and hence the friction velocity. Air from the facility is extracted at segment 9 and travels through pipes and the air conditioner and is pushed back into the facility at segment 11, see Fig. 4.2. Since the pushed back air is directed downwards, the wind speed is slowed down by a constant factor.

For the different fetches microscale breaking starts at different wind frequencies. At all fetch conditions microscale breaking might occur at the same wind frequency of the turbine, but it is not always visible in the image area. The shorter the fetch, the less time the wave has to build up and get unstable. For shorter fetches, MB occurs at higher wind speeds. This demonstrates that the build up time of MB is shorter for higher wind speeds. At the shortest fetch of 2 m no microscale breaking is detected. Hence, 2 m is not enough to build up a microscale breaker even a reference wind speed of 7.4 m/s. For breaking waves with bubble entrainment the same conclusion can be made. A certain time/length is needed to build up waves that are steep enough to break.

For the condition with medium surfactant coverage, the waves start to break with bubble entrainment at the same wind speed as for the clean water case. Hence, the effect of the surfactant (medium concentration) is small at higher wind speeds.

At high concentrations of Triton the waves are still not breaking for the highest measured wind speed (22 Hz).

7.2.2 Frequency of microscale wave breaking

By comparison of Tab. 7.1 with the transition of the Schmidt number exponent measured by Krall (2013), a good correlation is observed. The Schmidt number exponent is approx. 2/3 in case of no microscale breaking and 1/2, if breaking with bubble entrainment occurs (see Tab. 7.2). Hence, it is suspected that the Schmidt number exponent transition can be related to a parameter describing microscale breaking. In the following section, the dependence on the frequency of microscale wave breaking is investigated. The detection of MB events is described in sec. 6.2.4.

The Schmidt number exponent has not been measured during BLV experiments. Hence following Krall (2013), the Schmidt number exponents are estimated with the facet model (see sec. 2.2.4). The Schmidt number exponent is calculated by

$$n(\sigma_s^2) = \frac{\frac{2}{3}(1 - a_w(\sigma_s^2))\frac{1}{\beta_s}Sc^{-2/3} + \frac{1}{2}a_w(\sigma_s^2)\frac{1}{\beta_w}Sc^{-1/2}}{(1 - a_w(\sigma_s^2))\frac{1}{\beta_s}Sc^{-2/3} + a_w\frac{1}{\beta_w}(\sigma_s^2)Sc^{-1/2}}, \tag{7.1}$$

with the fraction of the wavy surface $a_w(\sigma_s^2)$, which is calculated by eq. (2.43) (Krall 2013). The mean square slope has been measured with the imaging slope gauge (see sec. 4.1.8). The *mss* (σ_s^2) and the additional parameters$\delta = 0.0395$, $\gamma = 3.04$, $\beta_w = 6.7$ $\beta_s = 12.2$, and the Schmidt number Sc = 600 are used. Additional parameters are taken from Krall (2013). The results for the Schmidt number exponent n are shown in Tab. 7.2.

Figure 7.9 shows the dependence of the Schmidt number exponent, estimated by the facet model, on the frequency of microscale breaking events per square meter. The shown conditions are: clean water without air conditioning (orange), clean water with AC with, and without Tartrazine (blue), 0.05 µmol/L Triton X-100 (green), and with the surfactant concentration 0.26 µmol/L (purple) (with and without Tartrazine). With increasing frequency, the Schmidt number exponent decreases from 2/3 to 1/2. Except some outliers the relation seems linear.

Discussion

Figure 7.9 shows the dependence of the Schmidt number exponent on the frequency of microscale breaking. Krall (2013) estimated an error of max. 10 % for the Schmidt number exponent deviation from the facet model. This error would explain most outliers in Fig. 7.9. The Schmidt number exponents for the high surfactant case (purple) at a frequency of 34 Hz/m^2 might be overestimated. In the measurements of Krall (2013) at the same condition the Schmidt number exponent is approx. 0.5.

The measurements of the Schmidt number exponent are difficult. The only candi-

Table 7.2.
Schmidt number exponents for three different conditions computed by the facet model with the parameters: $\delta = 0.0395$, $\gamma = 3.04$, $\beta_w = 6.7$ $\beta_s = 12.2$, and Sc = 600 (Krall 2013). The mean square slope values have been measured during the experiment shown in this thesis (see sec. 4.1.2).

condition	wind [Hz]	u_{ref} [m/s]	*mss*	*n*
noAC	5	1.5	0.00535	0.66
	7	2.2	0.00607	0.66
	9	2.7	0.01493	0.63
	12	3.8	0.02499	0.57
	16	5.1	0.04958	0.51
	22	6.8	0.08216	0.50
AC clean	7	1.1	0.00611	0.66
	9	1.5	0.01310	0.64
	12	2.5	0.02049	0.60
	16	4.0	0.04028	0.53
AC clean /Tartrazine	5	0.4	0.00071	0.67
	7	1.0	0.00637	0.66
	9	1.4	0.01237	0.64
	12	2.5	0.01464	0.63
	16	4.0	0.03153	0.55
	22	5.8	0.07343	0.50
	29	7.6	0.11265	0.50
0.05 µmol/L Triton	5	0.8	0.00055	0.67
	7	1.2	0.00055	0.67
	9	1.3	0.00059	0.67
	12	2.5	0.00675	0.66
	16	4.1	0.01079	0.65
	22	6.0	0.06161	0.51
	29	7.8	0.10556	0.50
0.26 µmol/L Triton	5	0.8	0.00053	0.67
	7	1.2	0.00055	0.67
	9	1.5	0.00056	0.67
	12	2.5	0.00179	0.67
	16	4.2	0.00468	0.67
	22	6.1	0.02690	0.56
0.26 µmol/L Triton /Tartrazine	5	0.8	0.0006	0.67
	7	1.2	0.00062	0.67
	9	1.4	0.00064	0.67
	12	2.5	0.00278	0.67
	16	4.2	0.00496	0.67
	22	6.1	0.02965	0.55

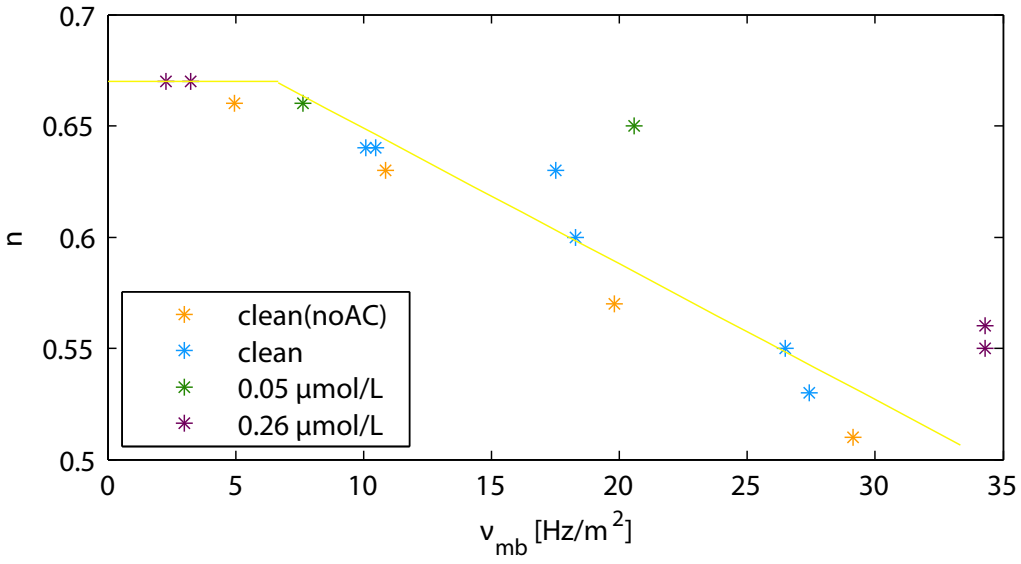

Figure 7.9.
The Schmidt number exponent is shown in dependence of the frequency of microscale breaking per square meter for different conditions. The Schmidt number exponents are estimated by the facet model (see sec. 2.2.4). The yellow line shows a linear fit to the data, except for the 0.26 µmol/L Triton data in purple (explanation in the text). The transition between 2/3 and 1/2 correlates well with the increase in microscale breaking frequency.

date to get an estimate for the Schmidt number exponent is at the moment the mean square slope. It is possible to measure the mean square slope during field campaigns Kiefhaber (2014). The detection of microscale breaking events on the other hand is easier, since it can be realized by thermal imaging (Jessup et al. 1997b, Zappa et al. 2004). In Fig. 7.9 a linear fit to the data is included in the figure

$$n = -0.0061\, \nu_{\mathrm{mb}} + 0.69. \tag{7.2}$$

For this fit the data point at the high surfactant concentration are excluded. Most data points fit well to this line even for different conditions. Hence, at least under the laboratory conditions at the Aeolotron, the frequency of microscale breaking gives a good estimate of the Schmidt number exponent.

In Fig. 7.10, the dependence of the time constant of gas exchange of a sparingly soluble gas (N_2O, taken from Krall (2013)) is shown over the period between microscale breakers. It is not compared to the ammonia exchange rate, since ammonia is mainly controlled by the air-side. The time constant of the gas exchange increases with increasing time constants for microscale breaking, but they have different sizes. The main reason for the difference between the time constants is the way the MB period was determined: Every MB event in the BLV image has been counted, regardless of its size. Thus, at any given point in the image, fewer renewal events due to MB have taken place and the MB period is larger, closer to the gas exchange time period.

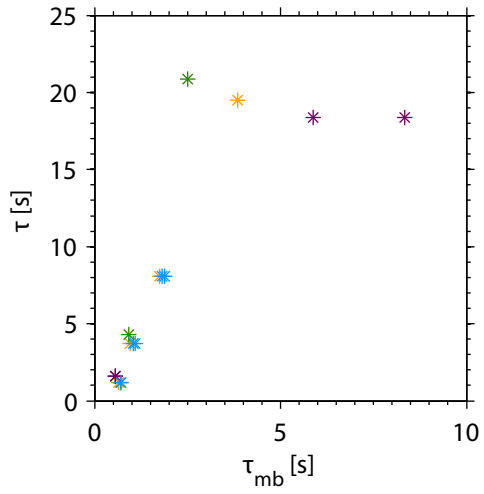

Figure 7.10
Time constant of N_2O gas exchange (low solubility) plotted over the mean period between microscale breaking events in the image.The gas exchange time constant is higher when the period between microscale breakers is higher, but the absolute values are different. The time constant of N_2O is computed from the transfer velocity measurements by Krall (2013).

The reason why this MB detection procedure achieves more reliable results than by counting at one point is described in sec. 6.2.4.

7.2.3 Recovery rate and renewed area

Jessup et al. (1997b) suggest to compute the recovery rate of microscale breaking or the area of the renewed surface and correlate these to the gas exchange rate. The recovery rate is the time the fluorescent footprints need to recover from a microscale breaker, which has renewed a certain area (renewed area). If the recovery rate of microscale breaking would be the same as the time constant for gas exchange, it would not be possible to compute it in the conducted experiments. For example, at the lowest wind speed where MB occurs, the time constant of gas exchange is approx. 20 s. This means that if a microscale breaker moves through the measurement spot and renews the surface (dark surface in the BLV images) it would take 20 s for the streaks to reform. However, the computed surface velocity, as will be shown in sec. 7.6 at that wind speed is approx. 7 cm/s. Hence, the advection of the renewed area by the mean current is much faster than the recovering of streaks by gas exchange. The same is found for the other conditions. The surface velocity must be reduced to investigate the recovery time, but that might as well reduce the exchange rate.

The renewed surface area has for example been investigated by Zappa et al. (2004) and Jessup et al. (1997b). They detected the surface area with a threshold algorithm, since the renewed area is brighter in the infrared images as the surrounding area. In the infrared images recorded during the experiments of this thesis, this is not possible, since a lot of reflections are visible and disturb the image. Also, the contrast between the renewed areas and the surrounding area is not as high as can be seen in Fig. 2.5(b). In the fluorescence images, the exact boundaries of the renewed area are in most cases unclear. The crest of the microscale breaker in Fig. 7.7 is clearly visible and also the turbulence behind the crest. However, the dark area behind the crest is

not distinguishable from the dark area between the streaks (see 7.7). In Fig. 7.8(b) the crest is clearly visible and the turbulence behind as well, but due to the turbulent structures the renewed area cannot be distinguished. Hence, even with the eye it is not possible to clearly identify the renewed area. A contrasting example is shown in Fig. 7.8(a), the renewed area is clearly visible. This example is rather an exception.

7.3 Comparison of gas and heat structures

In this section, the thermal and fluorescent surface footprints of the processes driving air-water exchange processes are compared. Therefore, simultaneous and collocated images have been recorded with the BLV setup and an infrared camera. The comparison of heat and gas exchange is an open research field. In some models describing gas exchange and the near-surface turbulence structure, the transfer velocities of different trace gases or heat scale with the diffusivity of the gas (or Schmidt number). Experimental evidence is inconclusive. While some authors find that heat exchange rates ($Sc = 7$) can be scaled to yield gas exchange rates ($Sc = \mathcal{O}(100)$), e.g. Nagel et al. (2014), others find that the scaled transfer rates are significantly overestimated, e.g. (Asher et al. 2012). It is still unclear if there is an error in one evaluation/measurement technique or why different results are achieved. This thesis concentrates on the comparison of the footprints on the water surface of gas and heat exchange and shows the differences and similarities. Due to the different diffusion coefficients (expressed in the different Schmidt numbers $Sc = \nu/D$) broader structures are expected for thermal footprints than for fluorescent footprints. Differences in the renewed area due to faster recovery might be observed. Clearly the detachments in the fluorescent signal (see sec. 7.1.5) are a difference to the thermal footprint, but this is only due to the different measurement techniques. In the infrared images, only the very surface layer is visible, while the BLV images give an integrated signal of fluorescence in the water column from all depths. For a comparison the differences in the techniques have to be considered. These measurements are the first simultaneous and collocated heat and gas exchange measurements of a surface patch (Kräuter et al. 2014). Asher et al. (2012) measured heat and gas exchange at the same location, but at different times and the gas exchange was only measured at one point with laser-induced fluorescence (LIF).

Throughout this thesis, infrared images are inverted and shown in a yellow-purple (dawn) color map (yellow is cold and purple is warm) and fluorescence images in a yellow-blue (seashore) color map to easily distinguish between images. First, a qualitative comparison is made to explain the differences and similarities by example images at different wind speeds and conditions. Secondly, a quantitative comparison at different length scales (Laplacian pyramid) is discussed and the evolution of the correlation coefficient over increasing air-side ammonia concentration is shown.

7.3.1 Qualitative comparison

The infrared images are mapped onto the fluorescence images, as described in sec. 6.1.4. All images are preprocessed as described in sec. 6.1.1, except for the reduction of the reflections as described in sec. 6.1.3. IR and BLV images taken at five different conditions are shown in Fig. 7.11. The images display an area of (21×21) cm^2. The wind blows from right to left. The images (i) and (l) are recorded at the small linear wind-wave facility and the shown area is (4×4) cm^2.

Figure 7.11(a) and (d) show the fluorescent and thermal footprints of a clean water surface at a wind speed of 1 m/s. The main structures are visible in both images. However, in the infrared images reflections are superimposed (dark areas in cross-wind direction). A streak, which is superimposed by a reflection is not or only partly visible. Since only the infrared images are affected by reflections, these corrupt the direct comparison. By filtering as described in sec. 6.1.3, the reflections can be partly removed.

Another example for a reflection can be seen in Fig. 7.11(e) at the left corner. The wave is much larger in this case and the reflection has no thin structures and the streaks can be distinguished underneath the reflection. In this image another difference is shown. The detachments of ammonia into the depth (see sec. 7.1.5) in Fig. 7.11(b) are not visible in the thermal image. Due to the strong absorption of IR radiation between 3 and 5 µm by water, only temperature fluctuations in the top 100 µm are visible.

Except for the detachments the footprints in images Fig. 7.11(b) and (e) are similar. However, in some occasions, streaks that are very close to each other in the BLV image cannot be resolved in the IR image (see large circles in image (b) and (e)). Additionally, the fluorescent streaks are thinner than the thermal streaks, due to the already mentioned difference in their diffusion coefficients (see sec. 2.1.1). The diffusion coefficient of heat is a factor of 100 larger than the diffusion coefficient of gases in water. Heat on the water surface spreads much faster than gases and two streaks can merge due to this. Another effect is the different resolution of the two cameras (see sec. 4.1.3 and sec. 4.1.7). Since the resolution of the infrared camera (640 × 512 pixels), of which only about a half is shown the BLV footprint, is much smaller than the visible camera (1600 ×1370 pixels), thin streaks might not be distinguishable in the infrared images.

The images in Fig. 7.11(c) and (f) are taken at a wind speed of 7.6 m/s, the highest recorded wind speed. The water has been cleaned before the experiment, hence these images show the roughest measured surface condition. In these images clear differences are visible. Clear streaks and structures can be seen in the fluorescence image. In the infrared image no streaks are visible. This is most probable due to the lower resolution of the infrared camera, since the streaks are much thinner than at lower wind speeds. The very bright structures in the fluorescence image can be vaguely discerned in the thermal images, as marked in the figures. These images show a further advantage of the fluorescence imaging; higher resolutions can be

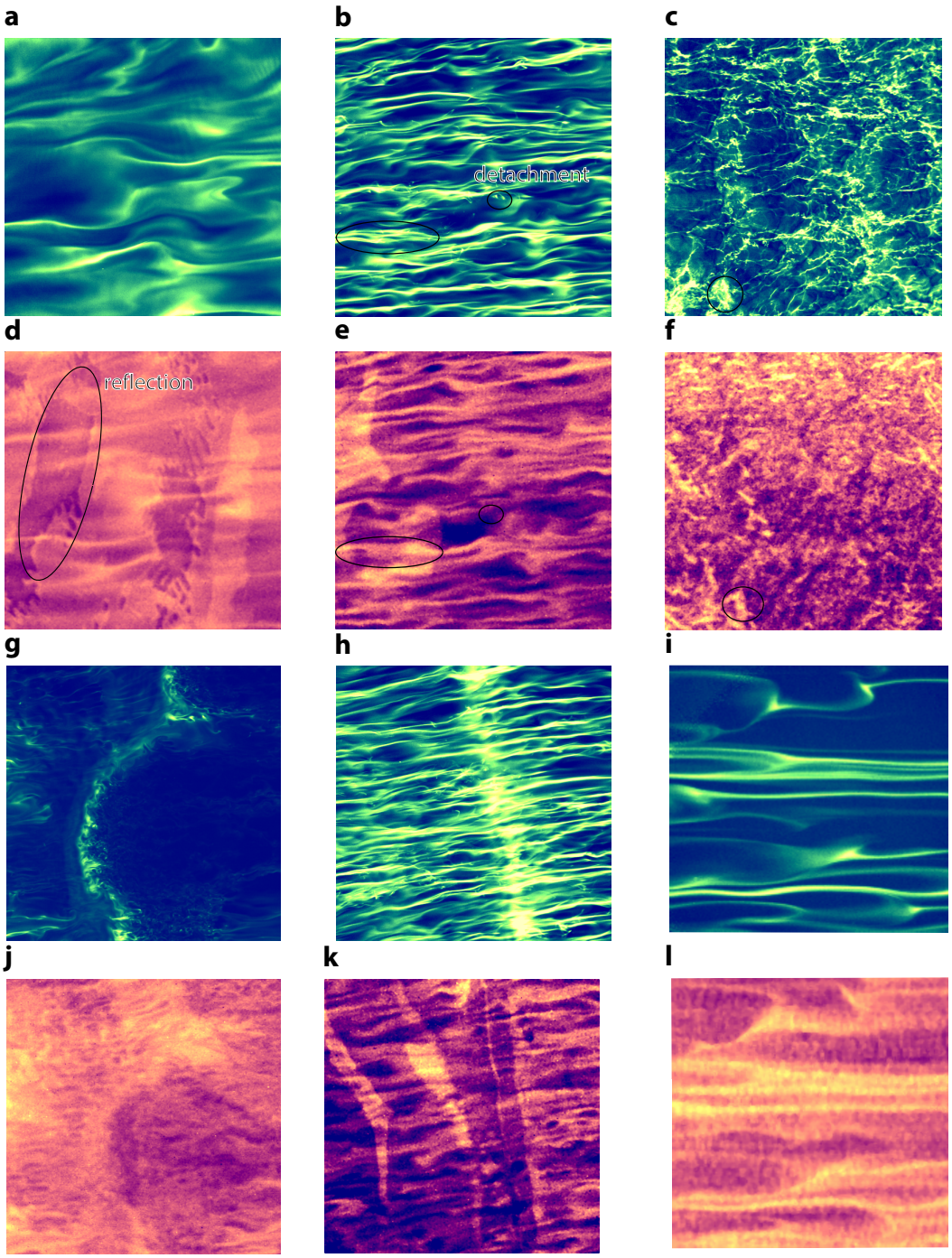

Figure 7.11.
Pairs of BLV (blue-green) and IR (purple-yellow) images. The footprint is (21 × 21) cm², the IR image is mapped onto the BLV image. Bright/yellow is lower temperature, dark/purple higher temperature water. Wind speeds and conditions are **a** 1 m/s (clean water), **b** 2.5 m/s (0.26 µmol/L Triton X-100), **c** 7.6 m/s (clean water), **j** 4.0 m/s (clean water), and **k** 4.2 m/s (0.26 µmol/L Triton X-100). The images **i** and **l** show measurements conducted at the small linear wind-wave facility. The image area is (4 × 4) cm².

more easily achieved. The streak spacing (see sec. 7.1.2) can be computed for the fluorescence images, but only hardly for the thermal images at these high wind speeds. This might explain why a stagnation of the streak spacing for higher wind speeds has been computed in other studies using IR imagery (Schnieders et al. 2013).

Figure 7.11(g) and (i) show the thermal and fluorescent footprints of a microscale wave breaker. In the fluorescence image the wave crest is clearly visible. Behind the wave crests the surface is renewed and is darker in both images. The differences are the footprints behind the wave crest. In the thermal images in the renewed area some structures are still or again visible while in the fluorescence image it is completely renewed. The difference might again be due to the faster diffusion of heat. Therefore, the heat structures recover after a shorter time while gases need longer to rebuild structures at the surface. Directly behind the wave crest the turbulent wake part of the microscale breaker is only visible in the fluorescence images. This allows drawing the conclusion that these structures are located beneath the layer that is visible for the IR camera.

A further difference is shown in Fig. 7.11(h) and (k). Non-breaking waves cause high intensity signals in the fluorescence images as shown in (h), while they lead to broad dark reflections in the thermal images. Hence, the images differ a lot at these conditions. This is shown in the following section.

In the images recorded at the small linear facility shown in Fig. 7.11(i) and (l), no reflections are visible. These images demonstrate the high resemblances of the structures. Furthermore, the same differences as in the other images are visible. Two close streaks, which are distinguishable in the BLV image, appear as one thick streak in the IR image.

7.3.2 Quantitative comparison

Multi-scale analysis/ Laplacian pyramid

For a quantitative comparison of the heat and gas structures, the IR and BLV images are decomposed in several band-pass filtered images. The so-called Laplacian pyramid is computed as described in sec. 6.2.1. The uncertainty relation dictates that good resolution in wavenumber space can only be bought at the cost of spatial resolution (Jähne 2005). Laplacian pyramid only yields low wavenumber resolution thus keeping relatively high spatial resolution, making it ideal for the comparison of the structures. From Fig. 7.12(a) and (d) to Figs. 7.12(i) and (l), increasing structure sizes are contained in the shown levels of the pyramid. The center wavenumber and structure size of each pyramid level are shown in Tab. 7.3.

Observing the images in Fig. 7.12, the differences between the thermal and fluorescent footprints described in sec. 7.3.1 are observable. By comparing for example image (c) and (f) the reflections in the infrared image are clearly visible, while none are visible in the fluorescence image. On the other hand in images (b) and (c) the capillaries in the fluorescence images are visible, while the same structures cannot

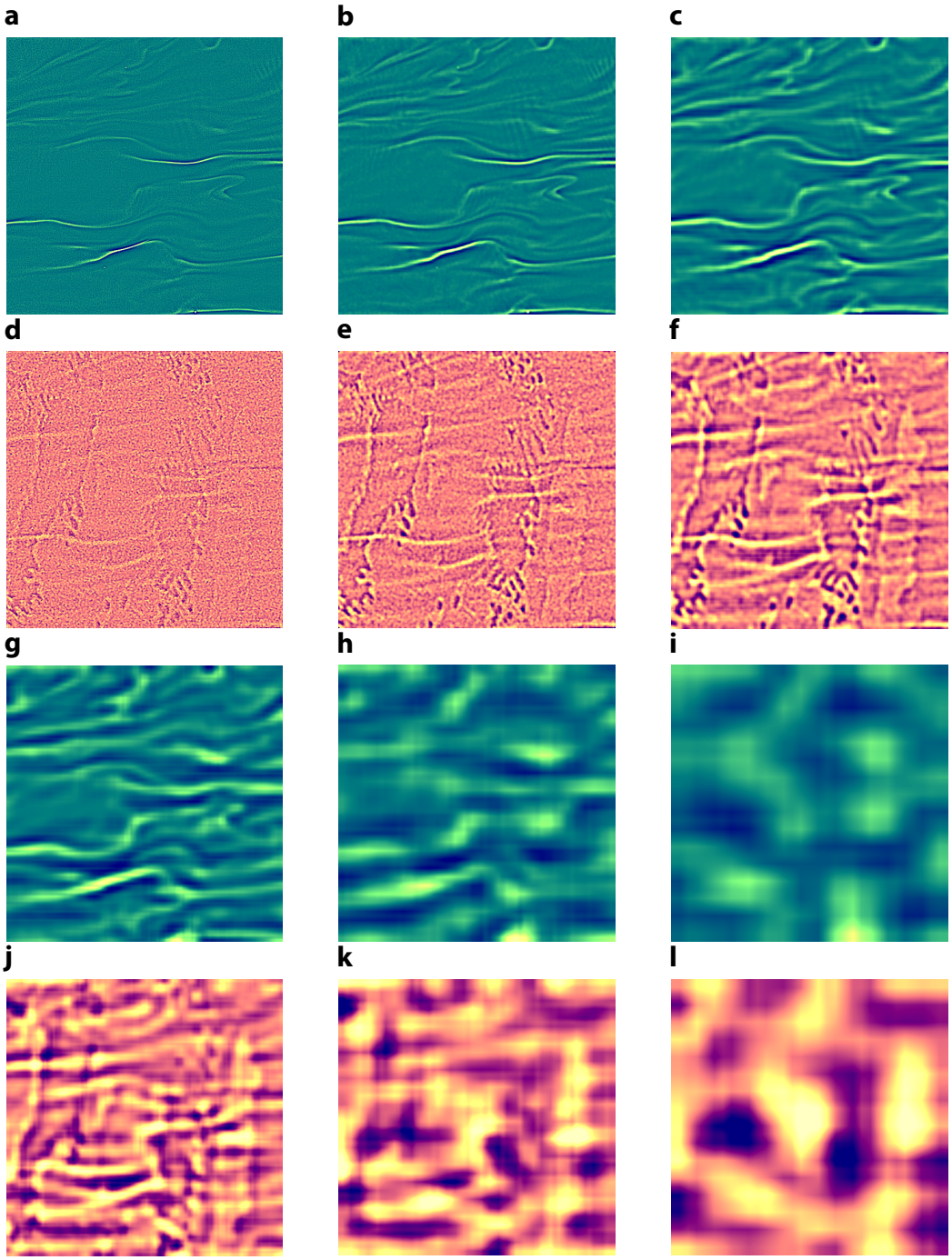

Figure 7.12.
Laplacian pyramid band-pass decomposition for different levels (level 1 to 6) at a wind speed of 2.5 m/s. The level gets lower from (a) to (l) and the thermal images with the same level as the fluorescence images are shown bellow the fluorescence images.

Table 7.3.
Level of the Laplacian pyramid and their center wavenumber and structure size.

pyramid level	center wavenumber [rad/cm]	structure size [mm]
1	105	0.4 - 0.8
2	52	0.8 - 1.6
3	26	1.6 - 3.2
4	13	3.2 - 6.4
5	7	6.4 - 12.8
6	3	12.8 - 25.6
7	2	25.6 - 51.2
8	0.7	51.2 - 102.4
9	0.4	102.4 - 204.8

be seen in the corresponding infrared images (e) and (f).

The correlation coefficient between the thermal and fluorescence images is obtained as described in sec. 6.2.1. The results are shown in Fig. 7.13. The correlation coefficient is shown in dependence of the level of the Laplacian pyramid. The first six levels are shown in Fig. 7.12 and the other three are shown in Fig. A.4. The correlation coefficient at level 10 is the coefficient between the original (not filtered) images. The correlation is shown for different wind speeds for the clean water condition with Tartrazine in (a) and with a concentration of 0.26 µmol/L Triton X-100 with Tartrazine in (b). The turbine frequencies are 5 Hz (blue), 7 Hz (purple), 9 Hz (green), 12 Hz (orange), 16 Hz (dotted blue), 22 Hz (dotted purple), and 29 Hz (dotted green). The corresponding wind speeds are shown in Tab. 5.2 and Tab. 5.3. The correlation coefficient increases with increasing level and is lower for higher wind speeds. In the condition with the surface active material on the surface the correlations are higher compared to the clean case.

Temporal evolution

The images shown above have been recorded at the end of each measurement condition, phase III in Fig. 5.1, in which the influx of ammonia into the *Aeolotron* balances the flux from air to water and the concentration in the air remains constant. As described in sec. 3.3 the higher the air-side ammonia concentration is, the thicker is the neutral layer. Hence, turbulence structures further away from the water surface are visualized. The development of the correlation between the thermal and fluorescent structures over time/increasing ammonia concentration are investigated. While the thermal imaging is independent of time, the fluorescence images change tremendously over time as shown in Fig. 7.14. At the beginning of each measurement no fluorescence is visible (a) and the higher the concentration gets the brighter the structures become and more structures are visualized. At low concentrations only the zones were ammonia converges are visible (larger streaks). These zones expand and it seems as if the streaks get broader. At the high concentrations all areas

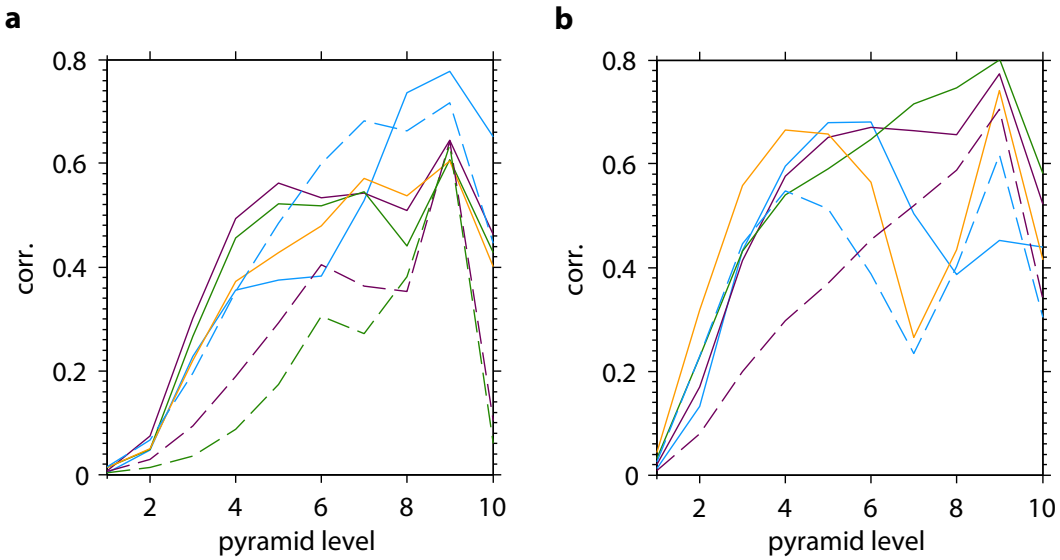

Figure 7.13.
Mean correlations ($t = 75$ s) between the fluorescent and thermal images for increasing pyramid levels of the Laplacian pyramid and different wind speeds and **a** clean water, **b** 0.26 µmol/L Triton/Tartrazine. The turbine frequencies are 5 Hz (blue), 7 Hz (purple), 9 Hz (green), 12 Hz (orange), 16 Hz (dotted blue), 22 Hz (dotted purple), and 29 Hz (dotted green). Structure scale increases from level 1 to 9. The correlation of the original images is shown as level 10 for reference. The correlation is better for higher levels, as the impact of noise, reflections and differences in the diffusion coefficients decreases.

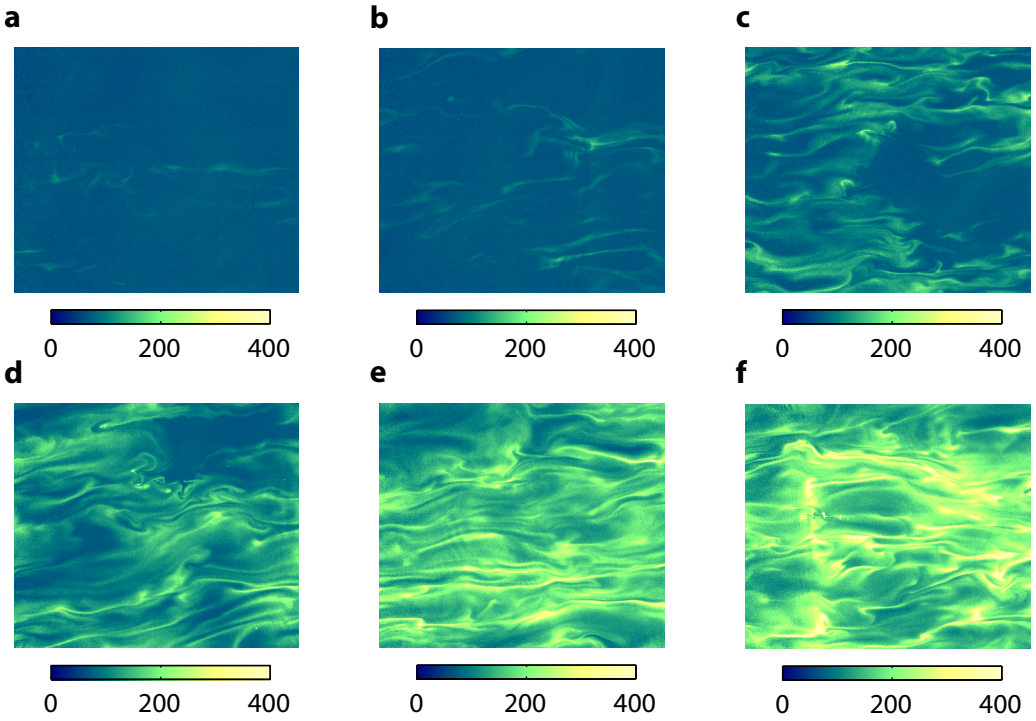

Figure 7.14.
Fluorescence structures at different air-side ammonia concentrations. Wind speed is 1.4 m/s in clean water conditions. Concentrations are **a** 2.6 ppm, **b** c = 3 ppm, **c** c = 3.3 ppm, **d** c = 3.7 ppm, **e** c = 4.8 ppm, and **f** c = 5.3 ppm.

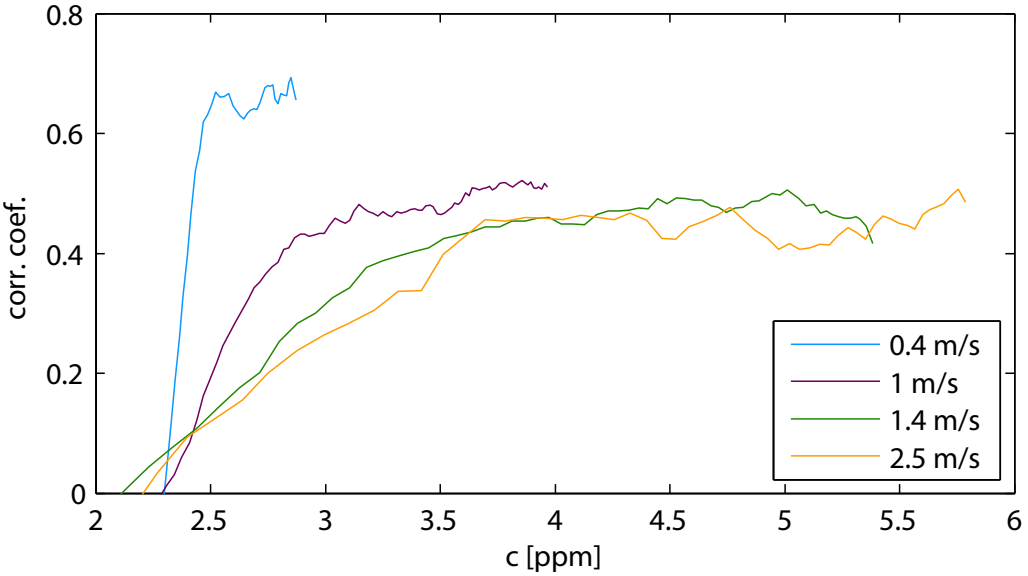

Figure 7.15.
Temporal evolution of the correlation coefficient between the thermal and fluorescence images is shown in dependence of the air-side ammonia concentration for different wind speeds at clean water conditions with Tartrazine.

are fluorescent and the different footprints are only distinguishable due to higher intensities at the convergence zones (see Fig. 7.14(f)). At high concentrations more structures are visible.

In Fig. 7.15, the temporal evolution of the correlation coefficient is shown in dependence of the air-side ammonia concentration for different wind speeds. The condition shown is clean water with Tartrazine. The reference wind speeds are 0.4 m/s (blue), 1.0 m/s (purple), 1.4 m/s (green), and 2.5 m/s (orange). The correlation coefficient is calculated as described in sec. 6.2.1. At a certain concentration the correlation increases for all wind speeds. The higher the wind speed the slower the increase is. At a second concentration the curves reach an equilibrium and only fluctuate a bit. For higher wind speeds the concentration at which the equilibrium is reached is larger. Except for the lowest wind speed, the asymptotic value is only about 0.4. However, as mentioned before, the absolute correlation coefficients should not be over-interpreted due the contamination of the images by reflections and wave effects. These are mainly due to optics.

Discussion

Laplacian pyramid The cross correlation of the BLV and IR images increases for increasing levels of the Laplacian pyramid (see Fig. 7.13). This is expected, since the defects of the images described above (waves, reflections) are filtered out at higher levels. On the first levels the reflections are a major reason for low correlation coefficients. As described in sec. 7.3.1 the footprints of the gas exchange are thinner than thermal structures due to the lower diffusion coefficients. This also causes differences, since two close thin streaks cannot be distinguished in the thermal images.

The correlation decreases for higher wind speeds. One reason is that the reflections are more prominent for higher wind speeds, they increase significantly from 0.4 m/s to 1 m/s due to smaller and more often occurring waves. For higher wind speeds as for example shown in Fig. 7.11(c) and (f) the structures look very different and the correlation is low, except for level 9. The correlation for the original images is most of the time the same as for a pyramid level of 4 to 5. The most relevant structures lie in this wavenumber range.

The correlations between thermal and fluorescence images are higher for the condition with a surfactant than for clean water as shown in Fig. 7.13. This is due to the suppression of smaller reflections as shown in Fig. 7.11(b) and (e). The waves are damped by the surfactant (see sec. 2.3.5) and the small waves (capillaries) are suppressed. The larger reflections do not disturb the streaks as much as the smaller reflections.

The dip in correlation at level seven for 12 Hz and 16 Hz are likely due to the appearance of broad waves. These waves enhance the intensity in the fluorescence image locally, while a large dark reflection appears in the infrared image as shown in Fig. 7.11(h) and (j). These broad structures have a large influence in level seven of the Laplacian pyramid.

It is concluded that the broader structures/lower wavenumber ranges of the thermal and fluorescence images correlate the most. This is not unexpected due to the differences caused by diffusion and resolution. The reflections in the infrared images cause the main differences and lower the correlation coefficient. Higher correlations are expected, if the reflections are reduced. Hence, the absolute correlation coefficients should not be considered as the real correlation between heat and gas exchange. From visual inspection of the images ignoring the reflections, the correlation of heat and gas footprints is expected to be higher. For further measurements of comparing heat and gas exchange structures one should try to avoid the reflections.

Comparison with the preliminary experiments Preliminary measurements have been conducted at the small linear wind-wave facility (see sec. 4.1.1). The use of this tank for investigations of exchange processes is limited, but it has easy optical access. Preliminary experiments have been conducted there to test the setup (see sec. 5.1). Some results of these experiments have been published (Kräuter et al. 2014). Additional results are presented here to demonstrate that streaks are also present

in the small facility and the transport mechanism is not only diffusive. Two corresponding fluorescent and thermal images are shown in Fig. 7.11(i) and (j). The shown image area is (4×4) cm^2. The wind blows from right to left. In the presented images no reflections are present in the thermal images. The correlation coefficient of the shown (non decomposed) images is 0.74 and hence higher than at the measurements at the *Aeolotron* shown above. The recorded sequences demonstrate as well that similar structures are present at the small test wind-wave facility.

Temporal evolution The correlation increases as the concentration of ammonia in the air increases. An increase in ammonia concentration causes an increase in the mean neutral layer thickness. Hence, for low concentrations, the neutral layer is thin. The higher the concentration gets the thicker the mean neutral layer is and the closer the neutral layer thickness gets to the depth into which the infrared camera is able to see (approx. 100 µm due to its sensitive spectral range of 3.4 - 6 µm). The concentrations at which the correlation stagnates are found to lie between 70 - 100 µm (see mean neutral layer thicknesses in sec. 7.5). Fluctuations that can still be seen are due to the effects discussed above e.g. waves, reflections, and ammonia detachments. The difference in the concentration at which the equilibrium is reached is due to the fact, that higher concentrations/fluxes are needed to image similar thickness, since the boundary layer thickness decreases for higher wind speeds. Therefore, higher air-side bulk concentrations are needed to get to the same air-side surface concentration and to the same neutral layer. It is expected that for even higher concentrations the correlation would decrease due to the more often occurring detachments of ammonia (see sec. 7.1.5).

7.4 Transfer velocities

In the following section the transfer velocity for ammonia in dependence of different parameters and conditions is shown. Also, the ratios of the air to the water-side transfer velocity, which have been computed by the method proposed in sec. 3.4, are shown. The results are discussed in detail.

7.4.1 Integrated transfer velocities

In Fig. 7.16, the calculated transfer velocities for different conditions and in dependence of different parameters are shown. The transfer velocities have been determined from a global mass balance, as detailed in sec. 3.6 and sec. 6.3.1.

Figure 7.16(a) shows the transfer rates for clean water. In orange, the case without air conditioning (AC) is shown and in blue with air conditioning. The orange circles are reference transfer velocities of acetonitrile without AC. These values have been measured in another campaign at the *Aeolotron* in February/March 2011 (Kräuter 2011, Mesarchaki et al. 2014) under comparable conditions. Acetonitrile is used as a reference gas, since it has a solubility of 1536 (Snider and Dawson 1985) close

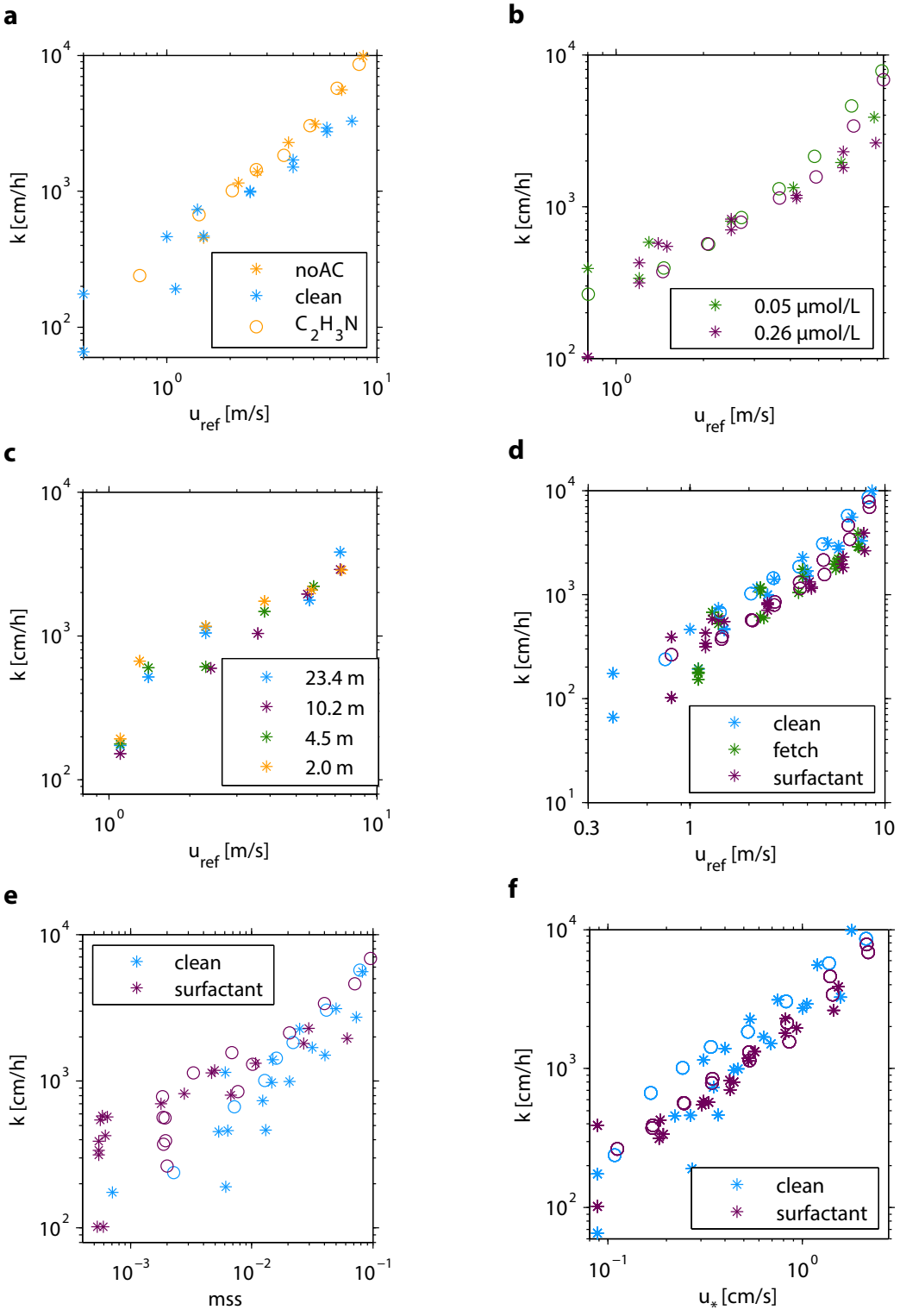

Figure 7.16.
Transfer velocities of ammonia (stars) and acetonitrile (circles) versus the reference wind speed, the mean square slope and the friction velocity for different conditions. The transfer rates of acetonitrile have measured without the air conditioning (noAC) at the *Aeolotron* in February/March 2011 (Kräuter 2011, Mesarchaki et al. 2014).

to the solubility of ammonia ($\alpha \approx 1713$). In the double logarithmic representation, the transfer velocities almost fall on a straight line. The transfer velocities with air condition are generally smaller than the values without AC. The transfer rates of acetonitrile are similar to the ammonia rates, measured without the AC.

All transfer velocities of ammonia (stars) shown in Fig. 7.16(b) are measured with air conditioning and the ones for acetonitrile (circles) without. This figure shows the transfer velocity for different concentrations of the surfactant Triton X-100 (sec. 2.3.5). The green markers show the values for 0.05 µmol/L and the purple ones are measured at a concentration of 0.26 µmol/L. The values for the lower concentration of Triton are slightly larger than the ones with the higher concentration. The rates for acetonitrile lie in-between the ammonia rates, only at higher wind speeds they are larger.

In Fig. 7.16(c) the transfer velocity is shown for different fetches (with AC) (see sec. 4.1.2). Fetch 2 has the lowest transfer velocities and fetch 4 has the highest transfer velocities, an exception is the highest wind speed.

Figure 7.16(d) summarizes the results from the Fig. 7.16(a) to (c). Blue markers correspond to a clean surface, purple markers to a surfactant covered surface, including the medium and high concentration, and all green markers the fetch conditions, including the four fetches. In the double logarithmic representation, the transfer velocities in dependence of the reference wind speed almost fall on a straight line. Only the fetch and surfactant covered conditions have some deviations at the low wind speeds. At comparable wind speeds, the transfer velocities for the clean conditions are the largest.

Figure 7.16(e) shows the same values as in Fig. 7.16(d) but in dependence of the mean square slope (*mss*). The values scatter a lot and no clear trend can be observed.

Figure 7.16(f) shows the dependence of the transfer velocities with the water-side friction velocity. The data scatter a bit for the lowest friction velocity.

Discussion

The values in Fig. 7.16(a) are measured at the same wind generator frequency, but there is a clear trend, the transfer velocities without air conditioning are larger. The reason for this is probably the directed flow of the AC, which reduces the wind speed (see sec. 4.1.2). However, if the only effect of the AC were a global reduction of the wind speed, the data measured with the AC should still align with the data measured without the AC when plotted against the wind speed (see Fig. 7.16(a)). Since this is not the case, it is obvious that the AC significantly alters the air-side flow field in the *Aeolotron*. Additionally, the mean square slope and the friction velocity are reduced at the same wind generator frequency. In Fig. 7.17(a) the mean square slope is plotted over the reference wind speed. At the same wind speed the mean square slope is enhanced for the condition with AC compared to the case without AC. Since the air conditioning blows the air towards the water surface, additional waves are created. The measurement area of the ISG is only a few meters apart and hence the wave slope is enhanced. At higher wind speeds this effect does not play a role anymore,

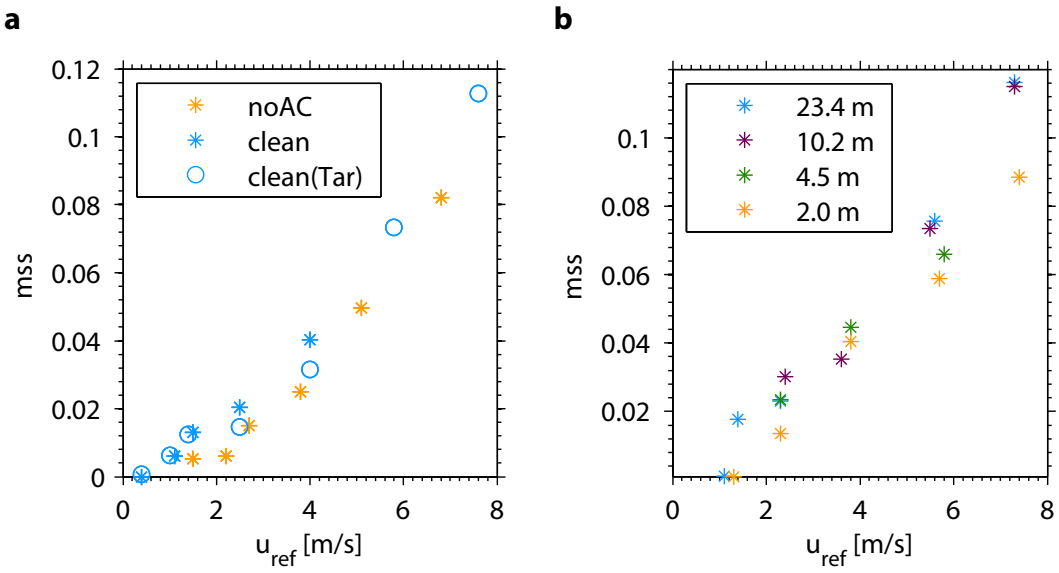

Figure 7.17.
a Comparision of the mean square slope (*mss*) for the case with and without air conditioning in dependence of the reference wind speed. The blue circles display the clean case with the additional dye Tartrazine. **b** Mean square slope for different fetches in dependence of the wind speed.

since the kinetic forcing by the wind is stronger than the air conditioning.

The transfer velocities of acetonitrile (no AC) from the experiment in 2011 fit well with the data without the air conditioning. This is expected, since acetonitrile has a solubility of 1536, which is quite similar to the solubility of ammonia and both are mainly controlled by the air side. It also demonstrates the reproducibility of experimental conditions in the *Aeolotron*. The good agreement with acetonitrile shows that the measured transfer rates with the new spectrometer setup, as shown in Fig. 4.7 and the method described in sec. 3.5 can be trusted. This is also shown in Fig. 7.16(b) by comparing the transfer velocities with surfactant covered water.

Figure 7.16(b) shows the expected behavior that the transfer velocities at larger concentrations of the soluble surfactant Triton X-100 are smaller (Liss and Martinelli 1978, Mesarchaki et al. 2014). The effect is much smaller than for gases with low solubilities, which are controlled by the water side. As described in sec. 2.3.5, surfactants mostly damp the waves and have an indirect effect on the gas transfer. Since the air-side boundary layer is not much effected by the waves (wind speed is much larger than phase velocity of waves), gases that are controlled by the air side are not influenced by the indirect effect. The small difference may be due to the fact, that ammonia is not only controlled by the air phase, but has a water-side contribution to the total transfer resistance (Kräuter 2011).

Figure 7.16(c) shows integrated transfer velocities for different fetch conditions. The wave absorber considerably changes the wave field directly behind as can be seen in Fig. 7.17 and thus leads to spatially inhomogeneous conditions. However, the

exact position of the wave absorber should not have an impact on integrated transfer velocities if there was a true radial symmetry in the facility. Still, for the shortest fetch, the transfer velocities are largest, except for the high wind speeds. This may be due to the fact that the wind field is not homogeneous and there is no true radial symmetry (it is broken, for example, by the two wind generators). The wave field is very sensitive to the wind conditions particularly at the onset of wave development at very low fetches. If the flow is more turbulent here and initial wavelets are created earlier, this may have a significant effect on the integral conditions. The variations are not large and might be additionally due to surface contaminations, especially at lower wind speeds. The skimmer could not be used as supposed and the water surfaced could still be covered by a surfactant. These are just suggestions, for a clear answer more data for different fetch conditions have to be measured. Since gas exchange measurements with the wave absorber have never been conducted before in the *Aeolotron*, no data for comparison are available at the moment.

Figure 7.16(d) to (f) show the transfer velocity in dependence of different parameters: the reference wind speed, mean square slope, and friction velocity. The mean square slope data scatter the most. This is not surprising, since *mss* is a wave parameter and as mentioned before, ammonia is air-side controlled. The good correlation between gas transfer velocities and *mss* reported in other studies (Frew et al. 2004, Jähne 1985) is valid for water-side controlled gases only. These gases are controlled by processes related to the wave field and the reduction of their transfer rates due to surfactants correlates well with the reduction of *mss* (Kiefhaber 2014, Kräuter 2011).

In the double logarithmic representation, the transfer velocities shown in Fig. 7.16(d) and (f) in dependence of the reference wind speed and the friction velocity almost fall on a straight line. This dependence has been shown in different laboratory and field experiments of highly soluble gases (Liss 1973, Mesarchaki et al. 2014, Münnich et al. 1978, Sverdrup et al. 1942). The main parameter describing the turbulence in the air is the shear stress. Hence, a good correlation between this parameter and the transfer velocity is expected. The fetch conditions should be interpreted with caution, since the determination of the friction velocity with the method described by Bopp (2014) is not valid in these conditions. The wave absorber influences the bulk water velocity and strongly affects the momentum balance used by the method.

Overall, the global gas transfer rates shown in Fig. 7.15 are consistent with the behavior expected from other experiments. The acetonitrile transfer velocities have been compared with field and laboratory measurements and theoretical models (Kräuter 2011, Mesarchaki et al. 2014) and fitted well. Therefore, it can be concluded that the measured ammonia transfer rates and the concentration measurements with the new setup and evaluation are trustworthy.

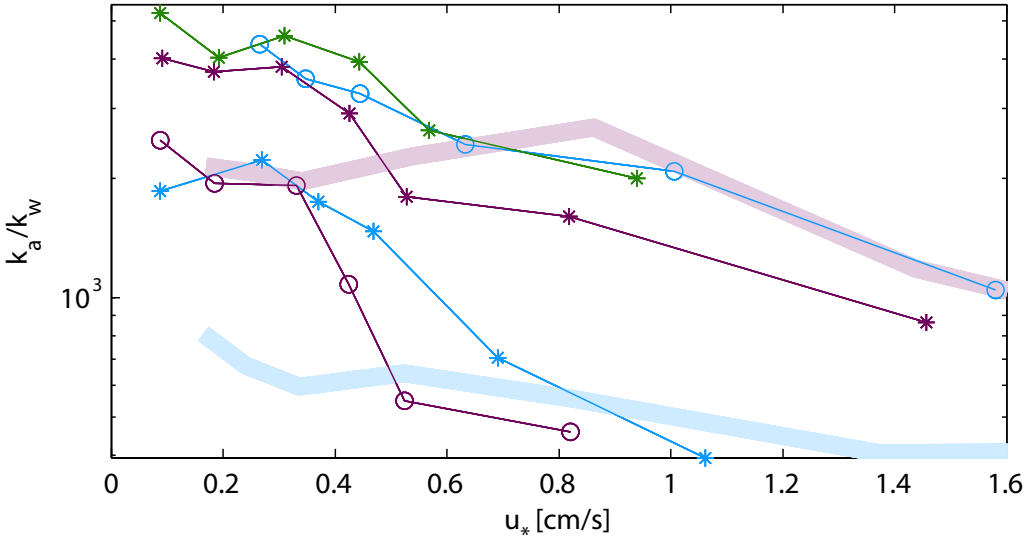

Figure 7.18.
Ratio of the air to the water-side transfer velocity for different conditions in dependence of the water-side friction velocity. The blue markers represent the clean condition, the green markers the condition with the medium concentration of Triton X-100, and the purple markers show the high surfactant concentration. The circles are the conditions with the absorbing dye Tartrazine. The pale blue and red lines are model expectations including experimental parameter.

7.4.2 Ratio of the air to water-side transfer velocity

Gases with intermediate solubilities like ammonia have non-negligible transfer resistances both in the air and water-side boundary layer. Following the Liss and Slater (1974) formalism, this is described by their air-side and water-side transfer velocities. In sec. 3.4, it was derived that the ratio of the transfer velocities k_a/k_w can be derived from the BLV data. As described in sec. 6.3.2, the ratio of the transfer velocities can be computed by

$$\frac{k_a}{k_w} = \frac{[H^+]}{c_a}, \tag{7.3}$$

with the air-side concentration c_a and the concentration of the hydrogen ions. The results of the evaluation are shown in Fig. 7.18 and Tab. A.1. There, the ratio of the transfer velocities is shown in dependence of the friction velocity. The blue lines show the results for clean water with AC. The stars display the measurements without the absorbing dye Tartrazin and the circles with Tartrazine. In green, the data measured with a concentration of 0.05 µmol/L Triton X-100 are shown and in purple with 0.26 µmol/L (see sec. 2.3.5). Due to a malfunction of the pH sensor, not all measurements could be evaluated. The data points are clustered into two regimes. A lower one for clean (without Tartrazine) and 0.26 µmol/L (with Tartrazine) covered water and a higher one for all other conditions. All curves show the same trend - they decrease towards higher friction velocities.

The thick pale blue and red lines show theoretical approximations. For this, models (see sec. 2.2.4), describing the gas exchange, are used. In the air, the Schmidt number for ammonia is approximately one. Equation (2.37) describes the dependence of the transfer velocity/resistance for Schmidt numbers close to one. For the dimensionless momentum resistance in eq. (2.37), a value of $\beta = 15.2$ is used (see sec. 2.2.4). The water-side transfer velocity can be estimated by eq. (2.41), where the dimensionless momentum resistance β and the Schmidt number exponent n are experimental parameters. For an approximation of β, values measured by Krall (2013) for clean and surfactant covered water are used. The Schmidt number exponents are determined by the facet model as described in detail in sec. 7.2.1. The approximation of the ratio can then be calculated by dividing eq. (2.37) by eq. (2.41), which leads to

$$\frac{k_a}{k_w} = \frac{\beta_w Sc_w^n}{15.2 Sc_a^{0.61} \sqrt{\frac{\rho_a}{\rho_w}}}, \tag{7.4}$$

with the densities in water and air ρ, respectively. The densities are needed to transform the air-side friction velocity to the water side (see eq. (2.27)).

The pale blue curve is the model result for the clean case and the pale purple line is valid the case for water covered by Triton X-100 with a concentration of 0.25 µmol/L. The pale lines start at higher friction velocities than the measured lines. This is due to the air conditioning that was turned on for the measurements conducted during this thesis and not during the measurements of Krall (2013) in 2011. The air conditioning reduces the wind speed and friction velocity. In the following, these pale lines will be called theoretical lines, although they are only based on theoretical models, but also on experimental parameters. The theoretical line for clean water does not agree with the measured data at low friction velocities. For the higher wind speeds the pale purple curve seems to fit rather well. However, the data already show a discrepancy to the theoretical predictions, since the surfactant cases due not always fit to the theoretical surfactant line and the clean conditions do not fit to the clean theoretical line.

Discussion

The overall trend in Fig. 7.18 is clearly that the ratio of the transfer velocities decreases towards higher friction velocities. This is the expected behavior. It is found by a number of studies that the air-side transfer velocity increases linearly with the wind speed (Liss 1973, Mackay and Yeun 1983, Mesarchaki et al. 2014, Münnich et al. 1978, Sverdrup et al. 1942), while the water-side transfer velocity exhibits quadratic growth with increasing wind speed (Ho et al. 2006). Highly soluble gases such as water vapor are normally used to measure the air-side transfer velocity, since all their resistance lies in the air phase (Liss and Slater 1974). CO_2 and other gases with low solubility are used to measure the water-side transfer velocity due to their major resistance

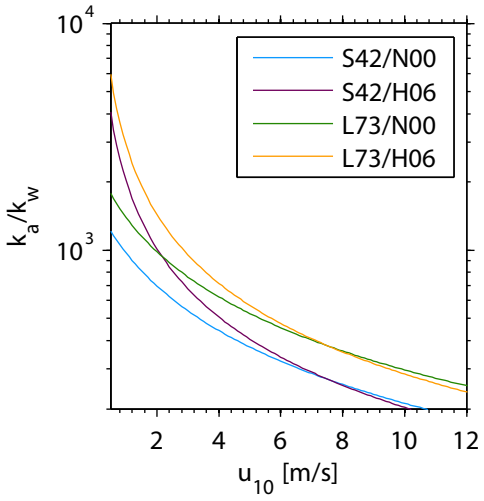

Figure 7.19
Ratio of the water vapor transfer velocity k_a to the CO_2 transfer velocity k_w in dependence of the wind speed in 10 m height. The ratios are calculated from different parameterizations for H_2O and CO_2 by Sverdrup et al. (1942) (S42), Nightingale et al. (2000) (N00), Liss (1973) (L73), and Ho et al. (2006) (H06).

in water. The ratio of the transfer velocities for water vapor and CO_2 over the wind speed in 10 m height, using different combinations of parameterizations from the literature (references are given in the caption), is shown in Fig. 7.19. The wind speeds in ten meters height, shown in the figure, are comparable to the friction velocities shown in Fig. 7.18. Transfer velocity ratios from the semi empirical parameterizations show a similar behavior as those in Fig. 7.18. They decrease with increasing friction velocity. The same behavior with the friction velocity is also seen in the theoretical approximations (pale thick lines). The magnitude of the computed (thin lines), parameterized (see Fig. 7.19), and theoretical lines (pale broad lines) are similar.

However, there are clearly two different regimes in Fig. 7.18 and no obvious reason has been found for this. According to the theoretical lines, the purple and green lines should lie in the higher regimes and the blue ones in the lower regime. In the following the different error sources are discussed in detail:

Surfactant From the theoretical prediction, it is expected that the ratio is smaller for clean water than for surfactant covered water, since the film strongly suppresses the water-side transfer velocity, but has little effect on the air-side transfer (see sec. 2.3.5). However, as can be seen in Fig. 7.18, the regimes are not separated according to surfactant concentration but seem arbitrary. One of the clean conditions and one of the surfactant conditions have significantly lower values than the others.

Tartrazine An effect by the absorbing dye Tartrazine, which was only used in two conditions (marked by circles) can also be excluded, as one of the Tartrazine conditions is in the lower regime and one in the higher regime.

Errors in the concentration measurements The errors of the experimental values for k_a/k_w, estimated in sec. 6.3.2, range from approx. 2 % for the low friction velocities up to approx. 22 % for the highest. These errors cannot explain the differences between the regimes. In sec. 7.4.1, it is shown that the transfer velocities derived from the rate of change of the concentrations is consistent with earlier experiments. Still, this does not guarantee that the absolute values are correct. Large errors

in the absolute concentrations are excluded by comparing the influx of ammonia at the beginning of the injection into the air space with the rise in concentration measured by DOAS. Assuming that gas exchange is negligible at the very beginning, the expected concentration is compared to the actual concentration (see app. A.2). The measured and approximated values deviate by 5 %. This small error cannot explain the differences between the two regimes in Fig. 7.18. The pH sensor has not been working properly during all experiments as has been mentioned before. In some instances, pH values are clearly too low or too high and not consistent with measured conductivities or the ammonia input into the water. Therefore, some measurements are excluded in this section. A reason for the malfunction might be air bubbles that have attached to the sensor in the water. The sensor was mounted in a non-transparent pipe and could not be visually observed during the experiment. However, during the most experiments the sensor seemed to work properly. It shows the expected increase with the ammonia/ammonium input to the water and in other experiments with known pH values it showed the expected values. Still, the pH sensor could be part of the problem, but there is no clear evidence.

7.5 Mean intensities

In Fig. 7.14, the evolution of the neutral layer depth with increasing flux is shown. The mean neutral layer thickness was computed from the calibrated mean intensities (see sec. 6.1.2). Results of the computation are shown in Fig. 7.20 for the condition with clean water and Tartrazine and in Fig. 7.21 for the case with a concentration of 0.26 µmol/L Triton X-100 and Tartrazine. The neutral layer thickness in micrometers is shown in dependence of the flux into the water. The calculation of the flux is described in sec. A.2. At a certain flux, the pH at the surface reaches 7 and the surface starts to fluoresce. At this point, the neutral layer thickness is zero. With increasing flux, the neutral layer depth increases, the increase is steeper for lower wind speeds.

Discussion

Compared to the thicknesses shown in the images in sec. 7.1 , the mean values presented here are smaller. The neutral layer thicknesses shown here resemble much more the mean boundary layer thicknesses measured with laser-induced fluorescent techniques, e.g. Friedl (2013). As described in sec. 3, the mean neutral layer thickness can be related to a fraction of the aqueous mass boundary layer thickness. The higher the flux, the higher the neutral layer thickness is and the larger the fraction of the mass boundary layer that is imaged.

Figure 7.20 and Fig. 7.21 illustrate the increase of the neutral layer. At a certain flux rate the water surface becomes neutral ($z_n = 0$), because all available hydrogen ions have reacted with ammonia. The critical rate needed for fluorescence is higher for

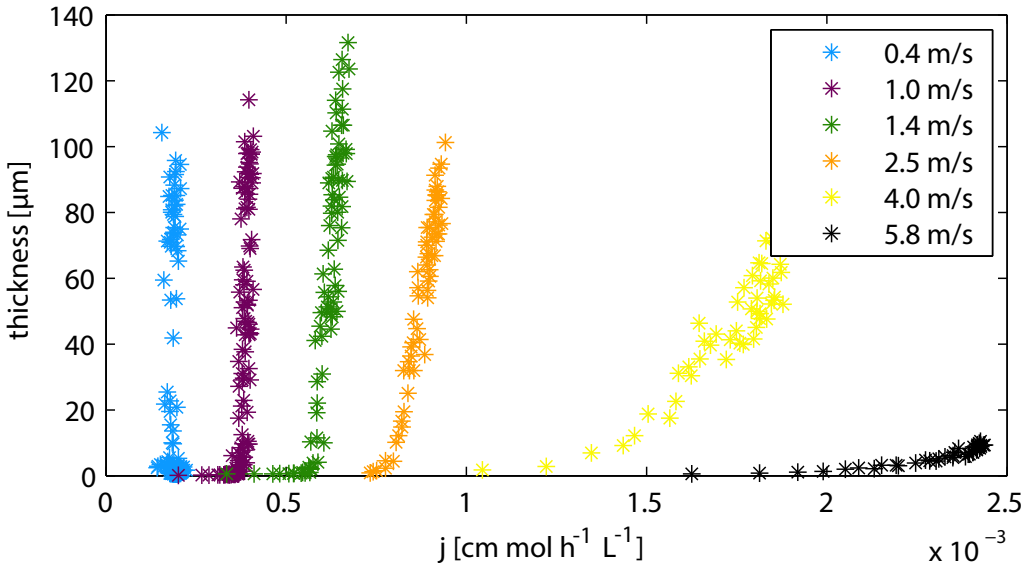

Figure 7.20.
Mean neutral layer thickness (intensity) over the flux of ammonia into the water for different wind speeds at clean water surface conditions with Tartrazine. The flux has been approximated as described in app. A.2.

increasing wind speeds. This is expected since higher fluxes are needed to achieve sufficiently high concentrations of ammonia at the water surface. If the near-surface turbulence is increases, ammonia is transported faster to the bulk and hence higher fluxes are needed to achieve high enough concentrations at the surface to change the pH to seven. In Fig. 7.20 and Fig. 7.21 this can be observed. Lower fluxes are needed for the surfactant covered cases, since the near-surface turbulence is reduced (see sec. 7.1.6).

Additionally, by comparing those figures it is observed that the neutral layer thicknesses are much larger in the condition with the surfactant. This is due to the reduced turbulence, which leads to a larger boundary layer thickness and hence to a larger neutral layer thickness. Since the boundary layer thickness is inversely proportional to the transfer rate, one can conclude that the transfer velocity is reduced. The observations in this section are only valid for the water-side transfer velocity (water-side boundary layer thickness). In sec. 7.4, it was shown that the total transfer velocity of ammonia is not influenced that strongly by the surfactant, since ammonia is mostly air-side controlled.

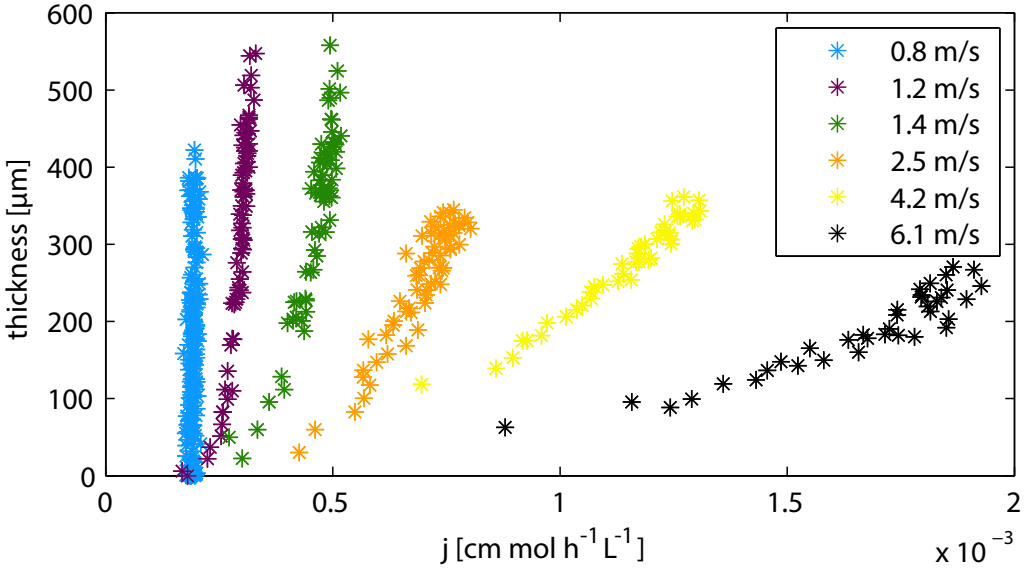

Figure 7.21.
Mean neutral layer thickness (intensity) over the flux of ammonia into the water for different wind speeds at the condition with 0.26 µmol/L Triton X-100 and Tartrazine. The flux has been approximated as described in app. A.2.

7.6 Surface velocity

Measurements of the surface velocity allow insights into the momentum transfer into the shear current. Measurements of the mean surface current are not easy to obtain in standard experiments for measuring water flow using particle imaging velocimetry or particle tracking velocimetry. Both methods typically require a certain minimum distance to the water surface to obtain reliable values. In the BLV images, it is possible to track the motion of the fluorescent structures, which are known to be attached to the surface flow. The procedure is somewhat similar to the experiments by Gutsche (2014), who placed thermal markers onto the water surface using an infrared laser and followed their motion. The velocities are computed by a cross correlation of two consecutive images of a fluorescent footprint on the water surface (see sec. 6.2.2).

In the following, the computed velocity v_s will be called surface velocity. However, one should keep in mind that the velocity of the streaks (i.e. the down welling zones of the cross-wind flow) was computed and this might be different from the mean surface velocity (Thorpe 2004). Figure 7.22(a) shows how the surface velocities increase almost linearly with reference wind speed. In blue the results of the BLV technique and in orange the results by Gutsche (2014) are shown. The water surface has been cleaned before the experiments and the air conditioning has been turned off. At similar conditions Gutsche (2014) measured surface velocities by the active infrared technique in the *Aeolotron*. The results by Gutsche (2014) fit well with the surface velocities computed in this thesis. In Tab. 7.4 the surface velocities computed

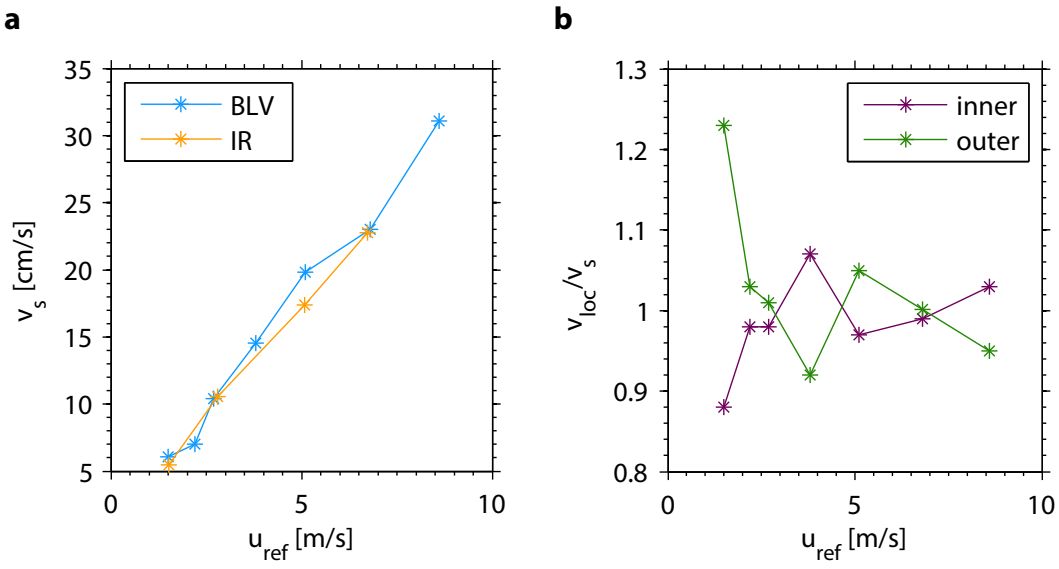

Figure 7.22.
a Dependence of measured surface velocity the surface velocity on the reference wind speed. Results from streak tracking (blue) and active thermography (orange, taken from Gutsche (2014)). Both have been measured at clean conditions without the air conditioning. **b** Radial differences in measured surface velocity (normalized to the overall mean velocity at each wind speed). Velocities measured in the outer half of the image are higher on average than those measured in the inner half.

by the streak tracking are shown.

Figure 7.22(b) shows the dependence of the surface velocity on the location in the image (closer to the inner and outer wall). The local surface velocities v_{loc} are divided by the mean surface velocity v_s. The recorded images are parted in two equally sized parts in wind direction (each $(10.5 \times 25)\,cm^2$). Green markers show the velocities, determined at points closer to the outer wall of the wind-wave facility. The purple data points are closer to the inner wall. Overall, outside velocities tend to be higher than inside velocities, although the presence of a notable exception (the fourth value) calls for caution in interpreting these results. There certainly is a large effect at the lowest wind speed and less difference at higher wind speeds. The value for the highest wind speed should be considered with caution due to bad statistics. In the following, it is assumed that the distribution of velocities can be neglected and the mean velocity is representative of the overall surface conditions.

In Fig. 7.23, the surface velocity distributions are shown for different wind speeds for clean water without air conditioning. From left to right the wind speed increases from 1.5 m/s to 6.8 m/s as displayed in the figure. In purple, the mean surface velocity is shown, which can be found in Tab. 7.4. The sample sizes for the different wind speeds is decreasing with increasing wind speed. This is due to the short lifetimes of the streaks at the high wind speeds. Most of the streaks changed dramatically or disappeared between two images and could not be tracked. In fact, the number of

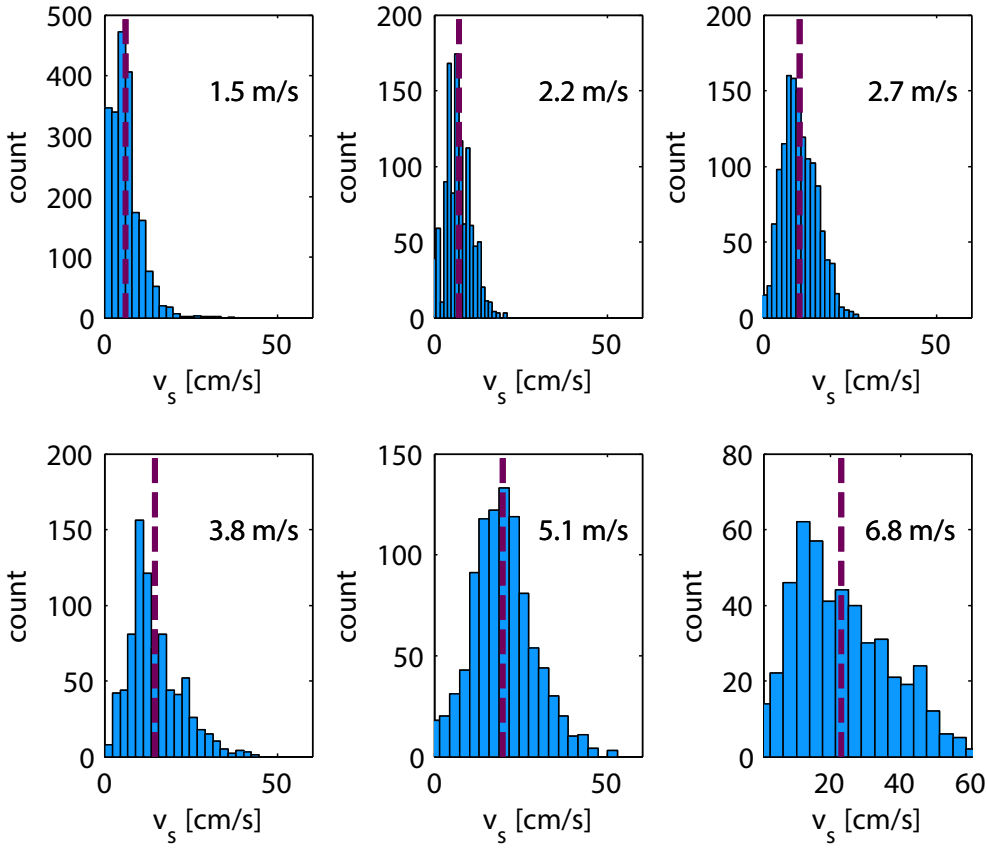

Figure 7.23.
Distribution of the surface velocity for different wind speeds for clean water without air conditioning. The numbers in the figures display the reference wind speeds and the purple lines the mean surface velocity shown in Tab. 7.4.

Table 7.4.
Conditions during the experiments with clean water and without the air conditioning. The surface velocity v_s computed by tracking of the streaks is shown and the dimensionless momentum transfer resistance computed by the difference of the surface and bulk velocity (see eq. (2.26)). The error of the surface velocity is the error of the mean value ($\sigma_{v_s}/\sqrt{n}$).

u_{ref} [m/s]	u_* [cm/s]	v_w [cm/s]	v_s [cm/s]	Δv_s [cm/s]	σ_{v_s}	β_t
1.5	0.22	1.5	6	1	44	23
2.2	0.31	2.3	7	1	37	16
2.7	0.40	3.1	10	1	48	19
3.8	0.54	4.5	15	3	75	21
5.1	0.75	6.5	20	3	90	19
6.8	1.20	10.5	23	6	140	11
8.6	1.80	15.8	31	6	173	9

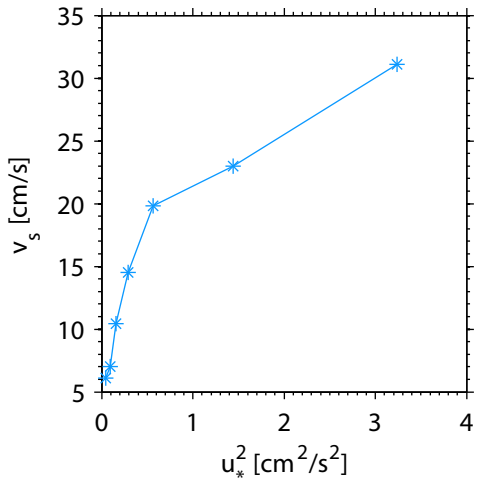

Figure 7.24
Surface velocity in dependence of the squared water-side friction velocity, which is proportional to the momentum flux from air to water (see eq. (2.18)). At higher momentum fluxes (higher wind speeds), the increase in surface velocity is much lower. This is likely due to the transfer of momentum directly into the waves by form drag.

data decreases from approx. 2000 at 1.5 m/s to 450 values at 6.8 m/s. It is shown that the velocity distributions get broader for higher wind speeds. This can be explained by the waves which modulate the wind speed. The same behavior is shown by the standard deviation σ_{v_s} in Tab. 7.4.

Discussion

The velocities shown in the previous figures are computed by tracking streaks on the water surface. Surface water packages at the location of the streaks were found to be faster as the surrounding water if they are due to Langmuir circulations (Thorpe 2004). Thus, it is expected that the computed velocities are higher than the mean velocity. As shown in Fig. 7.22(a) by a comparison with an independent infrared technique, the computed velocities are comparable to the mean surface velocity (Gutsche 2014). As discussed in sec. 7.1.1 some streaks are fish-scales, which are not due to Langmuir circulation. How the velocity of these streaks behaves has not been investigated. However, as shown by Fig. 7.22(a) the technique used in this thesis seems to be able to measure surface velocities.

Bopp (2014) presents water velocity profiles from acoustic Doppler velocimetry in the *Aeolotron*. Results are reported for depths of 100 - 700 mm below the water surface. A velocity profile at a reference wind speed of approx. 5.7 m/s in the measurement area of the BLV was investigated. These results are compared with the results shown in Fig. 7.22(b). Both measurements show that the velocity at the inner wall is slower than at the outer wall. Additionally, the velocities of Bopp (2014) are measured 100 mm beneath the water surface. The direction of the flow in this lower layer is slightly directed to the outer wall, while the streaks are slightly directed to the inner wall (see sec. 7.1.1). This indicates that the flow field changes tremendously in the layer between the surface and 100 mm beneath the water surface and even changes its cross-wind direction.

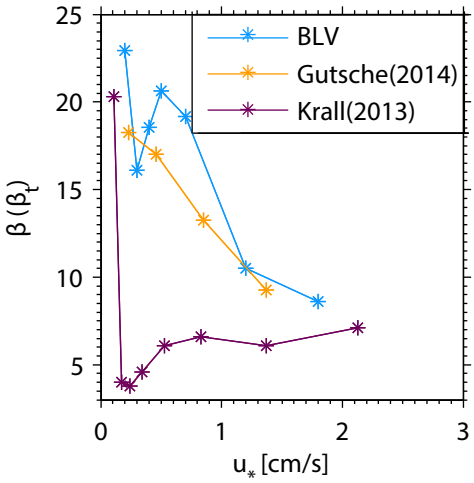

Figure 7.25
Dimensionless momentum resistance in dependence of the friction velocity determined by the surface velocity measurements (see sec. 7.6) conducted in this thesis (blue), IR surface velocity measurements (Gutsche 2014) (orange), and integrated gas exchange measurements by Krall (2013) (purple). Resistances determined from surface velocity measurements are significantly higher than those from gas exchange.

The friction velocity is proportional to the square root of the shear stress/momentum flux (see eq. (2.18)). The shear stress is the sum of the tangential stress τ_t on the water surface and the form drag τ_f ,which transfers momentum directly into waves

$$\tau = \tau_t + \tau_f = \rho u_*^2. \tag{7.5}$$

Tangential stress is related to the surface velocity. As shown in Fig. 7.24 with increasing momentum input by the wind the surface velocity increases fast and then more slowly. This is consistent with the observations of Peirson (1997) that at higher wind speeds a significant portion of the total momentum input is transferred directly into the wave field via form drag. The change in gradient is linked to the occurrence of breaking waves with bubble entrainment (see sec. 7.2.2). The reason is that the surface flow is constantly disrupted by the breaking waves.

7.7 Dimensionless momentum transfer resistance

The dimensionless transfer resistance of momentum β is a parameter, which is a measure for the exchange of momentum between air and water (see sec. 2.2.2). It can be computed by measuring the surface, bulk, and friction velocities in the water

$$\beta_t = \frac{v_s - v_b}{u_*}. \tag{7.6}$$

The results of this computation are shown in Fig. 7.25 by the blue points and in Tab. 7.4. With active thermal imaging, Gutsche (2014) measured surface velocities and computed the dimensionless momentum transfer resistance by eq. (7.6) (orange). Another method to estimate β is by measuring the gas exchange velocity and the Schmidt number exponent. By inserting these values and the friction velocity in

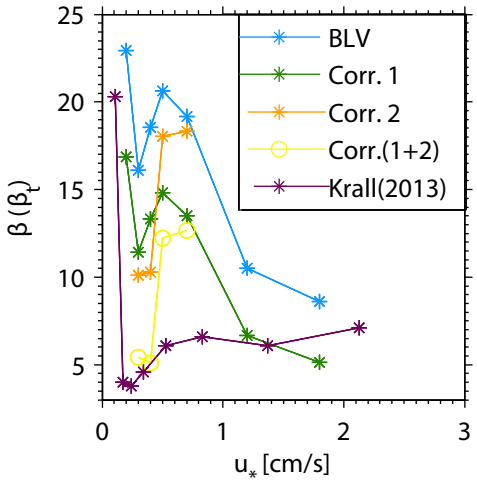

Figure 7.26
Dimensionless momentum resistance from BLV (blue) and gas exchange measurements (purple). The discrepancies are reduced if corrections are applied for the enhancement of the local surface velocity in the measurement section (green) and the turbulent resistance in the bulk (orange). The combined effect of both corrections is shown in yellow.

eq. (2.41), β can be computed. This has been realized in the *Aeolotron* by Krall (2013) shown in purple. The values computed by the surface velocity are more than three times larger at the low wind speeds than the values by Krall (2013). At higher friction velocities the computed β agree better.

Discussion

As can be seen in Fig. 7.25, the two methods of determining the dimensionless transfer resistances lead to a large discrepancies between the results. In general, the values determined from surface velocities are much higher than those from gas exchange measurements. Only at the highest wind speed, the two data sets converge. Two differences between these measurements are identified and explain the discrepancies. The first obvious difference is that the BLV and IR computations of the surface velocities are local measurements while the gas measurements are integrated over the whole facility. As discussed in sec. 4.1.2, the conditions in the *Aeolotron* are not fully homogeneous. Measurements of the wind field by Bopp (2014) show an enhanced wind speed close to the water surface in the measurement region of the BLV and IR imagery. Bopp (2014) estimated an enhancement of the surface velocity of up to 20 % compared to the mean surface velocity. This would lead to a decrease of β as shown by the green points in Fig. 7.26.

The second reason, which leads to a drastic decrease in β, is that the momentum transfer determined by eq. (7.6) includes the turbulent resistance of momentum. This is not included by the gas exchange measurement, since the turbulent exchange is neglected in eq. (2.41). The turbulent momentum resistance can be discarded by replacing the bulk current velocity in eq. (7.6) with the flow velocity just outside the viscous boundary layer. For the lowest four wind speeds, velocity profiles are available from particle tracking measurements in a recent study by Scherr (2014). The velocity is taken from the non dimensionless depth $z^+ = 30$ ($z^+ = zu_*/\nu$, with

the kinematic viscosity ν), which is the depth at which the logarithmic layer starts (Kundu 2008). In Fig. 7.26, the corrected β values are shown in orange.

By combing this effect and the reduced surface velocity of 20 % (yellow), the values agree with those from gas exchange measurements for the low wind speeds. The discrepancies that still remain for the two medium wind speeds, might be due to the low resolution in the profiles measured by Scherr (2014) at these conditions and the associated large measurement errors.

The corrected dimensionless momentum resistances at higher friction velocities are lower than the values from gas exchange measurements. As already discussed in sec. 7.6, the surface velocity does not describe the complete momentum transfer. At higher wind speed some momentum is used to form waves. This means that the momentum resistance is inhibited in the gas exchange β (purple), but not in the surface velocity β (blue and orange). Therefore, the calculated β by the surface velocity is too low.

8

Conclusions and Outlook

8.1 Conclusions

Novel boundary layer visualization technique

A novel two-dimensional visualization technique has been developed, which is able to image the horizontal footprints of near-surface turbulence at a wavy air-water interface. The approach is very different from commonly used laser-induced fluorescence methods, which typically visualize gas concentrations along a depth profile at a single point. Due to the high resolution requirements involved in those techniques, it is nearly impossible to apply them at large wind-wave facilities. The new technique is observing the water surface from above, allowing it to study processes driving air-water gas exchange even at large wave amplitudes, which are present at the large annular wind-wave facility *Aeolotron* in Heidelberg.

The basic idea of the method is to transform a concentration gradient into a sharp gradient in pH and to visualize the pH value with a fluorescent dye (Pyranine). The invasion of the alkaline reacting gas ammonia into slightly acid water is exploited for this. Hydrogen ions at the surface are rapidly depleted by the reaction with ammonia, which leads to an increase of pH. Driven by the concentration gradient between surface and bulk water, ammonium is transported to the bulk, while hydrogen ions are transported to the surface. Thus, depending on the surface concentration of ammonia, a smaller or larger fraction of the aqueous mass boundary layer is made alkaline. By exciting the deprotonated form of Pyranine, fluorescence is only emitted from this alkaline layer. The average thickness of the alkaline layer can be controlled by the flux of ammonia into the water, which allows to study processes in different depths (see sec. 3.1).

Measurement setup optimization

The selection of certain chemical and optical properties is crucial to the success of the method at larger wind-wave facilities. Therefore, the dependence of the behavior of the chemical system in the water on the concentrations of the constituents (ammonia, hydrogen chloride, and Pyranine) has been analyzed in simulations to find optimum values (see sec. 3.3). While the basic idea of the method has already been applied almost 50 years ago by Hiby et al. (1967) for falling films, and proposed by Jähne (1985) to be used for the study of air-sea gas exchange, it has never before been successfully applied to wind-wave facilities. From a technical point of view, the biggest challenge is to create a high power, narrow-band area light source to excite fluorescence only in deprotonated pyranine molecules, which are abundant in the alkaline layer at the water surface and not in the protonated molecules in the many orders of magnitude larger acid bulk. This was only possible with state-of-the-art high power LEDs (see sec. 4.1.4) and custom band-pass filters (see sec. 4.1.5). In addition, a very low noise camera (*PCO.edge*) was used to acquire the weak fluorescence signal (see sec. 4.1.3). The camera is observing a (21×25) cm^2 water surface patch with a spatial resolution of 150 µm, the high temporal resolution of 100 fps allows the detailed study of all stages even of rapid processes such as wave breaking.

Systematic laboratory experiments

The setup for the boundary layer visualization technique (BLV) was installed at the large annular wind-wave facility *Aeolotron* in Heidelberg (see sec. 4.1.2). Extensive experiments covering a large range of environmental conditions were conducted combining the BLV technique with measurements of wave slope (imaging slope gauge) and passive thermography at the same footprint. Seven different wind speeds ranging from 0.4 m/s to 8.6 m/s were used and measurements were performed with clean water as well as after adding two different concentrations of Triton X-100. Also, for the first time, systematic measurements with fetch limited waves were conducted in the *Aeolotron* (see sec. 5). For this, a wave absorber was installed at four different locations. Thanks to the collocated BLV, IR and wave measurements, a direct comparison of the surface footprints of heat and gas exchange was possible for the first time. Also, the effect of waves (e.g. microscale breakers) on gas exchange was investigated.

Fluorescence footprints of flow processes

A detailed analysis of the fluorescent structures in the BLV images is given and the footprints of the different processes known to contribute to gas exchange were identified. These include fish-scales, Langmuir circulations, microscale breaking, as well as waves breaking with bubble entrainment (see sec. 7.1). During all measurement conditions including the lowest wind speeds and the cases with a surfactant where no waves have been present, streaks on the water are observed. Even at very low levels of near-surface turbulence, a process able to form streaks must be present (see sec. 7.1.1).

However, in the measurements in which the soluble surfactant Triton X-100 has been added to the water, areas where diffusion seems to be the dominant process and areas characterized by a streaky structure are observed simultaneously (see sec. 7.1.1). It is concluded that the distribution of the surfactant on the water surface is not homogeneous. This result highlights the large local differences of the transfer process, particularly at the annular *Aeolotron*, where surfactants tend to accumulate in patches at the inner wall. Especially in the interpretation of integrated transfer velocities which are averaged over the whole water surface, this has to be accounted for.

Microscale breaking and Schmidt number exponent

If the ammonia concentration at the surface is high enough, surface water, which is transported into the depth by a larger scale motion (e.g. during wave breaking), is still fluorescent in the bulk, before it is neutralized by the surrounding hydrogen ions. Thus, at higher air-side ammonia concentrations, eddies transporting ammonia into the depth can be investigated (see sec. 7.1.5). This enables the study of the evolution of microscale breakers including the visualization of the wake turbulence in the depth. It is shown that a microscale breaker accumulates surface water with high ammonia concentration at its crest and transports it from the breaking crest effectively into the bulk, where it is dissipated by small eddies. Behind the microscale breaker the surface is completely renewed (see sec. 7.2).

It is known that the Schmidt number exponent, which allows scaling of transfer velocities of different gases, has a gradual transition from 2/3 to 1/2 with increasing wind speed and surface roughness. From the analysis of the BLV data, the transition is shown to correlate with the frequency of microscale breaking (see sec. 7.2.2). On the other hand, it is unaffected by Langmuir circulations, which are also known to enhance the gas exchange. When no microscale breaking occurs, the Schmidt number exponent is 2/3 and when waves start to break with bubble entrainment, the exponent is 1/2. Surface films significantly reduce the occurrence of microscale breaking and delay the transition from smooth to rough, which then happens in a smaller wind speed range.

Comparison with thermal images, surface velocities and transfer rates

A direct comparison of the BLV images with IR images shows a very high resemblance of the dominant visible structures (see sec. 7.3.1). In a more detailed multi-scale analysis, it is found that the correlation of the structures is higher for smaller wavenumbers. At higher wavenumbers, the correlation decreases due to the very different diffusion coefficients of heat and gas (see sec. 7.3.2).

The water surface velocity is determined by tracking the advection of the fluorescent streaks (see sec. 7.6). From this, the dimensionless momentum transfer resistance β is derived. The values are found to agree with Krall (2013) after applying a number of corrections to the methodology used by Gutsche (2014) to infer β from surface velocity measurements. The lack of these corrections in his data set also explains the large discrepancy between his results and those obtained by Krall (2013) (see sec. 7.7).

Additionally, the integrated transfer rates of ammonia, an air-side controlled gas, were computed and their relation to parameters linked to the gas exchange was investigated. The exchange rates were comparable to previously measured air-side transfer velocities (Mesarchaki et al. 2014) and demonstrated the small influence of surface films on air-side controlled gases. It was found that the friction velocity is the most favorable parameter to describe the transfer velocity of ammonia (see sec. 7.4).

8.2 Outlook

With the novel BLV technique, a powerful tool for studying the processes that enhance air-water gas exchange is now available. The found correlation of the Schmidt number exponent with the rate of microscale breaking demonstrates that important insights into the mechanisms of gas exchange can only be gained by studying individual processes rather than averaged quantities. However, the focus of this dissertation was the development of the visualization technique and a more detailed analysis of the BLV data is beyond its scope. A more detailed quantitative analysis of the spatio-temporal structures may yield many more insights into the mechanisms of air-water gas exchange. The measurement of local water-sided transfer velocities that were originally intended for this technique by Jähne (1985) are complicated by the variations in surface pH. If the pH could be measured or estimated from modeling the processes, local transfer velocities would become available.

In the experiments it was observed that the fluorescence does not always come from a layer at the water surface. In the wake of a microscale breaker for example, the ammonia-rich layer clearly detaches from the surface and is dissipated below by turbulence. Thus, information on the depth from which the fluorescence is coming will help to investigate the three dimensional structure of the near-surface turbulence. If the presented method is combined with a multi-camera setup, this

depth information can be obtained. First measurements with such a setup using three cameras were conducted by Darya Trofimova in October 2014, the analysis of the data set is in progress.

The experimental data can be compared to direct numerical simulations of air-water gas exchange (Hung et al. 2011, Tsai et al. 2013). This will help to validate the simulations and lead to a better understanding of the processes creating the observed surface patterns. In practice, numerical simulations are still limited to small Schmidt numbers. For higher Schmidt numbers, the grid needs to be much finer to resolve the small mass boundary layer, which is too costly in terms of computational effort. Thus, by comparing the model results with the experimental data, it is also possible to study the Schmidt number scalability.

Bibliography

Asher, W. and Litchendorf, T.: Visualizing near-surface concentration fluctuations using laser-induced fluorescence, Exp. Fluids, 46, 243–253, doi: http://dx.doi.org/10.1007/s00348-008-0554-9, 2009.

Asher, W. et al.: Statistics of surface divergence and their relation to air-water gas transfer velocity, J. Geophys. Res., 117, C05 035, doi: http://dx.doi.org/10.1029/2011JC007390, 2012.

Avnir, Y. and Barenholz, Y.: pH determination by pyranine: medium-related artifacts and their correction, Anal. Biochem., 347, 34–41, doi: http://dx.doi.org/10.1016/j.ab.2005.09.026, 2005.

Banner, M. L. and Peirson, W. L.: Tangential stress beneath wind-driven air-water interfaces, J. Fluid Mech., 364, 115–145, doi: http://dx.doi.org/10.1017/S0022112098001128, 1998.

Banner, M. L. and Phillips, O. M.: On the incipient breaking of small-scale waves, J. Fluid Mech., 65, 647–656, doi: http://dx.doi.org/10.1017/S0022112074001583, 1974.

Banner, M. L., Babanin, A. V., and Young, I. R.: Breaking probability for dominant waves on the sea surface, J. Phys. Oceanogr., 30, 3145–3160, doi: http://dx.doi.org/10.1175/1520-0485(2000)030<3145:BPFDWO>2.0.CO;2, 2000.

Barnadas-Rodríguez, R. and Estelrich, J.: Photophysical changes of pyranine induced by surfactants: evidence of premicellar aggregates, J. Phys. Chem. B, 113, 1972–1982, doi: http://dx.doi.org/10.1021/jp806808u, 2009.

Bopp, M.: Luft- und wasserseitige Strömungsverhältnisse im ringförmigen Heidelberger Wind-Wellen-Kanal (Aeolotron), Masterarbeit, Institut für Umweltphysik, Univ. Heidelberg, URL http://www.ub.uni-heidelberg.de/archiv/17151, 2014.

Bouguet, J.-Y.: Camera Calibration Toolbox for Matlab, URL http://www.vision.caltech.edu/bouguetj/calib_doc/, 2008.

Bouwmeester, R. J. B. Vlek, P. L. G.: Rate controll of ammonia volatilization from rice paddies, Atmos. Environ., 15, 131–140, doi: http://dx.doi.org/10.1016/0004-6981(81)90004-4, 1981.

Braun, D., Eckstein, H., and Hiby, J. W.: Messung der Oberflächengeschwindigkeit von Rieselfilmen, Chem. Ing. Tech., 43, 324–320, doi: http://dx.doi.org/10.1002/cite.330430603, 1971.

Broecker, H. C., Siems, W., and Petermann, J.: The influence of wind on CO_2-exchange in an wind-wave tunnel, including effect of monolayers, J. Mar. Res., 36, 595–610, doi: http://dx.doi.org/10.1111/j.2153-3490.1974.tb01948.x, 1978.

Burt, P. J. and Adelson, E. H.: The Laplacian pyramid as a compact image code, IEEE Trans COMM, 31, 532–540, doi: http://dx.doi.org/10.1109/TCOM.1983.1095851, 1983.

Callaghan, A., De Leeuw, G., Cohen, L., and O'Dowd, C. D.: Relationship of oceanic whitecap coverage to wind speed and wind history, Geophys. Res. Lett., 35, L2360, doi: http://dx.doi.org/10.1029/2008GL036165, 2008.

Carpenter, L. J., Archer, S. D., and Beale, R.: Ocean-atmosphere trace gas exchange, Chem. Soc. Rev., 41, 6273–6506, doi: http://dx.doi.org/10.1039/C2CS35121H, 2012.

Caulliez, G.: The generation of the first visible wind waves, Phys. Fluids, 10, 757–759, doi: http://dx.doi.org/10.1063/1.869600, 1998.

Clegg, S. L. and Brimblecombe, P.: Solubility of ammonia in pure aqueous and multicomponent solutions, J. Phys. Chem, pp. 7237—-7248, doi: http://dx.doi.org/10.1021/j100357a041, 1989.

Coantic, M.: A model of gas transfer across air–water interfaces with capillary waves, J. Geophys. Res., 91, 3925–3943, doi: http://dx.doi.org/10.1029/JC091iC03p03925, 1986.

Craik, A. D. D. and Leibovich, S.: A rational model for Langmuir circulations, J. Fluid Mech., 73, 401–426, doi: http://dx.doi.org/10.1017/S0022112076001420, 1976.

Csanady, G. T.: Turbulent diffusion in the environment, D. Reidel Publishing Company, 1973.

Csanady, G. T.: The role of breaking wavelets in air-sea gas transfer, J. Geophys. Res., 95, 749–759, doi: http://dx.doi.org/10.1029/JC095iC01p00749, 1990.

Cussler, E. L.: Diffusion - Mass transfer in fluid systems, Cambridge University Press, Cambridge, 3 edn., 2009.

Danckwerts, P. V.: Significance of liquid-film coefficients in gas absorption, Ind. Eng. Chem., 43, 1460–1467, doi: http://dx.doi.org/10.1021/ie50498a055, 1951.

Dasgupta, P. K. and Dong, S.: Solubility of ammonia in liquid water and generation of trace levels of standard gaseous ammonia, Atmos. Environ., pp. 565—-570, doi: http://dx.doi.org/10.1016/0004-6981(86)90099-5, 1986.

Deacon, E. L.: Gas transfer to and across an air-water interface, Tellus, 29, 363–374, doi: http://dx.doi.org/10.1111/j.2153-3490.1977.tb00746.x, 1977.

Degreif, K.: Untersuchungen zum Gasaustausch - Entwicklung und Applikation eines zeitlich aufgelösten Massenbilanzverfahrens, Dissertation, Institut für Umweltphysik, Univ. Heidelberg, URL http://www.ub.uni-heidelberg.de/archiv/6120, 2006.

Doney, S. C., Fabry, V. J., Feely, R. A., and Kleypas, J. A.: Ocean acidification: the other CO2 problem, Ann. Rev. Mar. Sci., 1, 169–192, doi: http://dx.doi.org/10.1146/annurev.marine.010908.163834, 2009.

Donnelly, J. P., Cleary, P., Newby, P., and Ettinger, R.: Coupling instrumental and geological records of sea-level change: evidence from southern New England of an increase in the rate of sea-level rise in the late 19th century, Geophys. Res. Lett., 31, L0520, doi: http://dx.doi.org/10.1029/2003gl018933, 2004.

Duce, R. A. et al.: The atmospheric input of trace species to the world ocean, Global Biogeochem. Cycles, 5, 193–25, doi: http://dx.doi.org/10.1029/91GB01778, 1991.

Ebuchi, N., Kawamura, H., and Toba, Y.: Fine structure of laboratory wind-wave surfaces using an optical method, Boundary Layer Meteorol., 39, 133–151, doi: http://dx.doi.org/10.1007/BF00121871, 1987.

Edner, H.: Differential optical absorption spectroscopy (DOAS) system for urban atmospheric pollution monitoring, Appl. Opt., 32, 327–333, doi: http://dx.doi.org/10.1364/AO.32.000327, 1993.

Fahlenkamp, H.: Zum Mechanismus des Stofftransports im laminar-welligen Rieselfilm, Dissertation, Technical University of Achen, 1979.

Faller, A.: Experiments with controlled Langmuir circulations, Science, 201, 618–620, doi: http://dx.doi.org/10.1126/science.201.4356.618, 1978.

Farmer, D. and Li, M.: Patterns of bubble clouds organized by Langmuir circulation, J. Phys. Oceanogr., 25, 1426–1440, doi: http://dx.doi.org/10.1175/1520-0485(1995)025<1426:POBCOB>2.0.CO;2, 1995.

Fick, A.: Über Diffusion, Ann. Phys., 170, 59–86, doi: http://dx.doi.org/10.1002/andp.18551700105, 1855.

Fogg, P. G. T. and Sangster, J.: Chemicals in the atmosphere: solubility, sources, and reactivity, Wiley, Chichester, doi: http://dx.doi.org/10.1515/ci.2003.25.4.31b, 2003.

Fortescue, G. E. and Pearson, J. R. A.: On gas absorption into a turbulent liquid, Chem. Eng. Sci., 22, 1163–1176, doi: http://dx.doi.org/10.1016/0009-2509(67)80183-0, 1967.

Frew, N. M. et al.: Variation of air–water gas transfer with wind stress and surface viscoelasticity, in: Air-water Gas Transfer, Selected Papers from the Third International Symposium on Air-Water Gas Transfer, edited by Jähne, B. and Monahan, E. C., pp. 529–541, AEON, Hanau, doi: http://dx.doi.org/10.5281/zenodo.10405, 1995.

Frew, N. M. et al.: Air-sea gas transfer: Its dependence on wind stress, small-scale roughness, and surface films, J. Geophys. Res., 109, C08S17, doi: http://dx.doi.org/10.1029/2003JC002131, 2004.

Friedl, F.: Investigating the transfer of oxygen at the wavy air-water interface under wind-induced turbulence, Dissertation, Institut für Umweltphysik, Univ. Heidelberg, URL http://www.ub.uni-heidelberg.de/archiv/14582, 2013.

Förster, T.: Die pH-Abhängigkeit der Fluoreszenz von Naphthalinderivaten, Zeitschrift für Elektrochemie, 54, 531–535, 1950.

Garbe, C. S., Spies, H., and Jähne, B.: Estimation of surface flow and net heat flux from infrared image sequences, J. Math. Imaging Vision, 19, 159–174, doi: http://dx.doi.org/10.1023/A:1026233919766, 2003.

Garrett, C. and Smith, J.: On the interaction between long and short surface waves, J. Phys. Oceanogr., 6, 925–930, doi: http://dx.doi.org/10.1175/1520-0485(1976)006<0925:OTIBLA>2.0.CO;2, 1976.

Garrett, W.: A novel approach to evaporation control with monomolecular films, J. Geophys. Res., 76, 5122–5123, doi: http://dx.doi.org/10.1029/JC076i021p05122, 1971.

Gemmrich, J. and Hasse, L.: Small-scale surface streaming under natural conditions as effective in air-sea gas exchange, Tellus B, 44, 150–159, doi: http://dx.doi.org/10.1034/j.1600-0889.1992.t01-1-00006.x, 1992.

Goldberg, S. Y., Pines, E., and Huppert, D.: Proton scavenging in photoacid geminate recombination processes, Chem. Phys. Lett., 192, 77–81, doi: http://dx.doi.org/10.1016/0009-2614(92)85431-9, 1992.

Grassl, H.: The dependence of the measured cool skin of the ocean on wind stress and total heat flux, Boundary Layer Meteorol., 10, 465–474, doi: http://dx.doi.org/10.1007/BF00225865, 1976.

Guizar-Sicairos, M., Thurman, S., and Fienup, J.: Efficient subpixel image registration algorithms, Opt. Lett., 33, 156–158, doi: http://dx.doi.org/10.1364/OL.33.000156, 2008.

Gutsche, M.: Surface velocity measurements at the Aeolotron by means of active thermography, Masterarbeit, Institut für Umweltphysik, , Univ. Heidelberg, URL http://www.ub.uni-heidelberg.de/archiv/17431, 2014.

Hales, J. M. and Drewes, D. R.: Solubility of ammiona in water at low concentrations, Atmos. Environ., 13, 1133–1147, doi: http://dx.doi.org/10.1016/0004-6981(79)90037-4, 1979.

Handler, R. A., Smith, G. B., and Leighton, R. I.: The thermal structure of an air–water interface at low wind speeds, Tellus A, 53, 233–244, doi: http://dx.doi.org/10.1034/j.1600-0870.2001.00158.x, 2001.

Handler, R. A., Savelyev, I., and Lindsey, M.: Infrared imagery of streak formation in a breaking wave, Phys. Fluids, 24, doi: http://dx.doi.org/10.1063/1.4769459, 2012.

Herlina, I. and Jirka, G. H.: Experiments on gas transfer at the air–water interface induced by oscillating grid turbulence, J. Fluid. Mech., 594, 183–208, doi: http://dx.doi.org/10.1017/S0022112007008968, 2008.

Herzog, A.: Imaging of water-sided gas-concentration fields at a wind-driven, wavy air-water interface, Dissertation, Institut für Umweltphysik, Univ. Heidelberg, URL http://www.ub.uni-heidelberg.de/archiv/11220, 2010.

Hühnerfuss, H.: Basic physicochemical principles of monomolecular sea slicks and crude oil spills, in: Marine Surface Films, edited by Gade, M., Hühnerfuss, H., and Korenowski, G. M., pp. 21–35, Springer, doi: http://dx.doi.org/10.1007/3-540-33271-5_4, 2006.

Hühnerfuss, H., Walter, W., Lange, P., and Alpers, W.: Attenuation of wind waves by monomolecular sea slicks and the Marangoni effect, J. Geophys. Res., 92, 3961–3963, doi: http://dx.doi.org/10.1029/JC092iC04p03961, 1987.

Hiby, J. W., Braun, D., and Eickel, K. H.: Eine Fluoreszenzmethode zur Untersuchung des Stoffübergangs bei der Gasabsorption im Rieselfilm, Chemie-Ing.-Techn., 39, 297–301, doi: http://dx.doi.org/10.1002/cite.330390517, 1967.

Higbie, R.: The rate of absorption of a pure gas into a still liquid during short periods of exposure, Trans. Am. Inst. Chem. Eng., 31, 365–389, 1935.

Hinze, J. O.: Turbulence, McGraw-Hill series in mechanical engineering, McGraw-Hill, New York, 2nd edn., 1975.

Ho, D. T., Law, C. S., Smith, M. J., Schlosser, P., Harville, M., and Hill, P.: Measurements of air-sea gas exchange at high wind speeds in the Southern Ocean: Implications for global parameterizations, Geophys. Res. Lett., 33, 16 611–16 616, doi: http://dx.doi.org/10.1029/2006GL026817, 2006.

Ho, D. T., Wanninkhof, R., Schlosser, P., Ullman, D. S., Hebert, D., and Sullivan, K. F.: Toward a universal relationship between wind speed and gas exchange: Gas transfer velocities measured with 3He/SF6 during the Southern Ocean Gas Exchange Experiment, J. Geophys. Res., 116, C00F04, doi: http://dx.doi.org/10.1029/2010JC006854, 2011.

Holzwarth, G., Balmer, R. G., and Soni, L.: The fate of chlorine and chloramines in cooling towers, Water Res., 18, 1429—-1435, doi: http://dx.doi.org/10.1016/0043-1354(84)90013-7, 1984.

Hung, L.-P., Garbe, C. S., and Tsai, W.-T.: Validation of eddy-renewal model by numerical simulation, in: Gas Transfer at Water Surfaces 2010, edited by Komori, S., McGillis, W., and Krose, R., pp. 165–176, Kyoto Univ. Press, URL http://hdl.handle.net/2433/156156, 2011.

Hunter, K.: Processes affecting particulate trace metals in the sea surface, Mar. Chem., 9, 49–70, doi: http://dx.doi.org/10.1016/0304-4203(80)90006-7, 1980.

Jacobs, C., Friis Kjeld, J., Nightingale, P., Upstill-Goddard, R., Larsen, S., and Oost, W.: Possible errors in CO_2 air-sea transfer velocity from deliberate tracer releases and eddy covariance measurements due to near-surface concentration gradients, J. Geophys. Res., 107, 3128–3153, doi: http://dx.doi.org/10.1029/2001JC000983, 2002.

Jarvis, N.: The effect of monomolecular films on surface temperature and convective motion at the water/air interface, J. Colloid Interface Sci., 17, 512–522, doi: http://dx.doi.org/10.1016/0095-8522(62)90019-3, 1962.

Jessup, A. T., Zappa, C. J., Loewen, M. R., and Hesany, V.: Infrared remote sensing of breaking waves, Nature, 385, 52–55, doi: http://dx.doi.org/10.1038/385052a0, 1997a.

Jessup, A. T., Zappa, C. J., and Yeh, H. H.: Defining and quantifying microscale wave breaking with infrared imagery, J. Geophys. Res., 102, 23 145–23 153, doi: http://dx.doi.org/10.1029/97JC01449, 1997b.

Jähne, B.: Zur Parametrisierung des Gasaustauschs mit Hilfe von Laborexperimenten, Dissertation, Institut für Umweltphysik, Univ. Heidelberg, doi: http://dx.doi.org/10.5281/zenodo.10443, 1980.

Jähne, B.: Messung des Gasaustausches und der Turbulenz an der Oberfläche durch Sichtbarmachung der Grenzschicht, Tech. rep., Institut für Umweltphysik, Universität Heidelberg, doi: http://dx.doi.org/10.5281/zenodo.12201, 1983.

Jähne, B.: Transfer processes across the free water surface, Habilitation thesis, Institut für Umweltphysik, Fakultät für Physik und Astronomie, Univ. Heidelberg, doi: http://dx.doi.org/10.5281/zenodo.12202, iUP D-200, 1985.

Jähne, B.: Digital Image Processing, Springer, Berlin, 6 edn., doi: http://dx.doi.org/10.1007/3-540-27563-0, 2005.

Jähne, B.: Compression by noise equalization, Tech. rep., Heidelberg Collaboratory for Image Processing (HCI), Heidelberg University, doi: http://dx.doi.org/10.5072/zenodo.12761, 2013.

Jähne, B., Huber, W., Dutzi, A., Wais, T., and Ilmberger, J.: Wind/wave-tunnel experiment on the Schmidt number and wave field dependence of air/water gas exchange, in: Gas transfer at water surfaces, edited by Brutsaert, W. and Jirka, G. H., pp. 303–309, Reidel, Hingham, MA, doi: http://dx.doi.org/10.1007/978-94-017-1660-4_28, 1984.

Jähne, B., Münnich, K. O., Bösinger, R., Dutzi, A., Huber, W., and Libner, P.: On the parameters influencing air-water gas exchange, J. Geophys. Res., 92, 1937–1950, doi: http://dx.doi.org/10.1029/JC092iC02p01937, 1987.

Jähne, B., Libner, P., Fischer, R., Billen, T., and Plate, E. J.: Investigating the transfer process across the free aqueous boundary layer by the controlled flux method, Tellus, 41B, 177–195, doi: http://dx.doi.org/10.1111/j.1600-0889.1989.tb00135.x, 1989.

Jähne, B., Popp, C., Schimpf, U., and Garbe, C.: The influence of intermittency on air-water gas transfer measurements, in: Transport at the Air Sea Interface — Measurements, Models and Parameterizations, edited by Garbe, C. S., Handler, R. A., and Jähne, B., Springer-Verlag, doi: http://dx.doi.org/10.1007/978-3-540-36906-6_18, 2007.

Johnson, M., Hughes, C., Bell, T., and Liss, P.: A Rumsfeldian analysis of uncertainty in air-sea gas exchange, in: Gas Transfer at Water Surface 2010, pp. 464–484, Kyoto University Press, Kyoto, URL https://ueaeprints.uea.ac.uk/id/eprint/33094, 2011.

Jung, M.: Miniforschungsbericht - Entwicklung einer Visualisierung von Messdaten mittels OpenGL - WaveVis, Tech. rep., Institut für Wissenschaftliches Rechnen, Univ. Heidelberg, 2008.

Kiefhaber, D.: Optical measurement of short wind waves — from the laboratory to the field, Dissertation, Institut für Umweltphysik, Univ. Heidelberg, URL http://www.ub.uni-heidelberg.de/archiv/16304, 2014.

Kiefhaber, D., Reith, S., Rocholz, R., and Jähne, B.: High-speed imaging of short wind waves by shape from refraction, J. Eur. Opt. Soc., 9, 14 015, doi: http://dx.doi.org/10.2971/jeos.2014.14015, 2014.

Kitaigorodskii, S.: On the fluid dynamical theory of turbulent gas transfer across an air-sea interface in the presence of breaking wind waves, J. Phys. Oceanogr., 14, 960–972, doi: http://dx.doi.org/10.1175/1520-0485(1984)014<0960:OTFDTO>2.0.CO;2, 1984.

Kline, S. J.: The structure of turbulent boundary layers, J. Fluid Mech., 30, 741–773, doi: http://dx.doi.org/10.1017/S0022112067001740, 1967.

Kock, A., Schafstall, J., Dengler, M., Brandt, P., and Bange, H. W.: Sea-to-air and diapycnal nitrous oxide fluxes in the eastern tropical North Atlantic Ocean, Biogeosci., 9, 957–964, doi: http://dx.doi.org/10.5194/bg-9-957-2012, 2012.

Kolmogorov, A. N.: The local structure of turbulence in compressible turbulence for very large Reynolds numbers, Compt. Rend. Akad. Nauk SSSR, 30, 1941.

Krah, N.: Visualization of air and water-sided concentration profiles in laboratory gas exchange experiments, Dissertation, Institut für Umweltphysik, Univ. Heidelberg, URL http://www.ub.uni-heidelberg.de/archiv/16895, 2014.

Krall, K. E.: Laboratory investigations of air-sea gas transfer under a wide range of water surface conditions, Dissertation, Institut für Umweltphysik, Univ. Heidelberg, URL http://www.ub.uni-heidelberg.de/archiv/14392, 2013.

Kraus, S.: DOASIS a framework design for DOAS, Dissertation, Technische Informatik, Univ. Mannheim, 2006.

Kräuter, C.: Aufteilung des Transferwiderstands zwischen Luft und Wasser beim Austausch flüchtiger Substanzen mittlerer Löslichkeit zwischen Ozean und Atmosphäre, Diplomarbeit, Institut für Umweltphysik, Univ. Heidelberg, URL http://www.ub.uni-heidelberg.de/archiv/13010, 2011.

Kräuter, C., Trofimova, D., Kiefhaber, D., Krah, N., and Jähne, B.: High resolution 2-D fluorescence imaging of the mass boundary layer thickness at free water surfaces, J. Eur. Opt. Soc., 9, 14 016, doi: http://dx.doi.org/10.2971/jeos.2014.14016, 2014.

Kundu, P. K.: Fluid Mechanics, Academic Press, Elsevier, San Diego, CA, 4 edn., 2008.

Lakowicz, J. R.: Principles of fluorescence spectroscopy, Springer, 3 edn., doi: http://dx.doi.org/10.1007/978-0-387-46312-4, 2006.

Lam, L., Lee, S. W., and Suen, C. Y.: Thinning methodologies - A comprehensive survey, IEEE Trans. Pattern Anal. Mach. Intell., 9, 869–885, doi: http://dx.doi.org/10.1109/34.161346, 1992.

Lamont, J. C. and Scott, J. C.: An eddy cell model of mass transfer into the surface of a turbulent liquid, AlChE J., 16, 513–519, doi: http://dx.doi.org/10.1002/aic.690160403, 1970.

Langmuir, I.: Surface motion of water induced by wind, Science, 87, 119–124, doi: http://dx.doi.org/10.1126/science.87.2250.119, 1938.

Leibovich, S.: The form and dynamics of Langmuir circulations, Annu. Rev. Fluid Mech., 15, 391–427, doi: http://dx.doi.org/10.1146/annurev.fl.15.010183.002135, 1983.

Liang, M., Cheng, B., Lu, H., Chen, H., Alam, M., Lee, Y., and Yung, Y.: Isotopic fractionation of nitrogen in ammonia in the troposphere of Jupiter, Astrophys. J., 657, L117—-L120, doi: http://dx.doi.org/10.1086/513192, 2007.

Liss, P.: Gas transfer: Experiments and geochemical implications, vol. 108, Springer Netherlands, doi: http://dx.doi.org/10.1007/978-94-009-7169-1_5, 1983.

Liss, P. S.: Processes of gas exchange across an air–water interface, Deep-Sea Res., 20, 221–238, doi: http://dx.doi.org/10.1016/0011-7471(73)90013-2, 1973.

Liss, P. S. and Martinelli, F. N.: The effect of oil films on the transfer of oxygen and water vapour across an air-water interface, Thalass Jugosl, 14, 215–220, 1978.

Liss, P. S. and Slater, P. G.: Flux of gases across the air-sea interface, Nature, 247, 181–184, doi: http://dx.doi.org/10.1038/247181a0, 1974.

Longuet-Higgins, M. S.: Bubbles, breaking waves and hyperbolic jets at a free surface, J. Fluid Mech., 127, 103–121, doi: http://dx.doi.org/10.1017/S0022112083002645, 1983.

Mackay, D. and Yeun, A. T. K.: Mass transfer coefficient correlations for volatilization of organic solutes from water, Environ. Sci. Technol., 17, 211–217, doi: http://dx.doi.org/10.1021/es00110a006, 1983.

Marmorino, G. O. and Smith, G. B.: Bright and dark ocean whitecaps observed in the infrared, Geophys. Res. Lett., 32, ,L1160, doi: http://dx.doi.org/10.1029/2005GL023176, 2005.

Marmorino, G. O., Smith, G. B., and Lindemann, G. J.: Infrared imagery of large-aspect-ratio Lanmuir circulation, Cont. Shelf Res., 25, 1–6, doi: http://dx.doi.org/10.1016/j.csr.2004.08.002, 2004.

McKenna, S. P. and Bock, E. J.: Physicochemical effects of the marine microlayer on air-sea gas transport, in: Marine Surface Films: Chemical Characteristics, Influence on Air-Sea Interactions, and Remote Sensing, edited by Gade, M., Hühnerfuss, H., and Korenowski, G. M., pp. 77–91, Springer Berlin Heidelberg, doi: http://dx.doi.org/10.1007/3-540-33271-5_9, 2006.

McKenna, S. P. and McGillis, W. R.: The role of free-surface turbulence and surfactants in air-water gas transfer, Int. J. Heat Mass Transfer, 47, 539–553, doi: http://dx.doi.org/10.1016/j.ijheatmasstransfer.2003.06.001, 2004.

Mellqvist, J.: DOAS for flue gas monitoring-I. Temperature effects in the UV/visible absorption spectra of NO, NO2, SO2 and NH, J. Quanr. Specrrosc. Radior. Transfer, 56, 187–208, doi: http://dx.doi.org/10.1016/0022-4073(96)00042-8, 1995.

Melville, W. K.: The role of surface-wave breaking in air-sea interaction, Annu. Rev. Fluid Mech., 28, 279–321, doi: http://dx.doi.org/10.1146/annurev.fl.28.010196.001431, 1996.

Melville, W. K., Shear, R., and Veron, F.: Laboratory measurements of the generation and evolution of Langmuir circulations, J. Fluid Mech., 364, 31–58, doi: http://dx.doi.org/10.1017/S0022112098001098, 1998.

Mesarchaki, E., Kräuter, C., Krall, K. E., Bopp, M., Helleis, F., Williams, J., and Jähne, B.: Measuring air-sea gas exchange velocities in a large scale annular wind-wave tank, Ocean Sci. Discuss., 11, 1643–1689, doi: http://dx.doi.org/10.5194/osd-11-1643-2014, 2014.

Mischler, W.: Systematic measurements of bubble induced gas exchange for trace gases with low solubilities, Dissertation, Institut für Umweltphysik, Univ. Heidelberg, URL http://www.ub.uni-heidelberg.de/archiv/17720, 2014.

Münnich, K. O. et al.: Gas exchange and evaporation studies in a circular wind tunnel, continuous radon-222 measurements at sea and tritium/helium-3 measurments in a lake, in: Turbulent fluxes through the sea surface, wave dynamics and prediction, edited by Favre, A. and Hasselmann, K., pp. 151–166, Plenum, doi: http://dx.doi.org/10.1007/978-1-4612-9806-9_11, 1978.

Münsterer, T.: LIF Investigation of the Mechanisms Controlling Air–Water Mass Transfer at a Free Interface, Dissertation, Institut für Umweltphysik, Fakultät für Physik und Astronomie, Univ. Heidelberg, 1996.

Münsterer, T. and Jähne, B.: LIF measurements of concentration profiles in the aqueous mass boundary layer, Exp. Fluids, 25, 190–196, doi: http://dx.doi.org/10.1007/s003480050223, 1998.

Myhre, G. et al.: Anthropogenic and natural radiative forcing, in: Climate Change 2013: The Physical Science Basis. Contribution of Working Group I to the Fifth Assessment Report of the Intergovernmental Panel on Climate Change, Cambridge University Press, Cambridge, United Kingdom and New York, NY, USA, URL www.ipcc.ch/pdf/assessment-report/ar5/wg1/WG1AR5_Chapter08_FINAL.pdf, 2013.

Nagel, L.: Active thermography to investigate small-scale air-water transport processes in the laboratory and the field, Dissertation, Institut für Umweltphysik, Univ. Heidelberg, URL http://www.ub.uni-heidelberg.de/archiv/16831, 2014.

Nagel, L., Krall, K. E., and Jähne, B.: Comparative heat and gas exchange measurements in the Heidelberg Aeolotron, a large annular wind-wave tank, Ocean Sci. Discuss., 11, 1691–1718, doi: http://dx.doi.org/10.5194/osd-11-1691-2014, 2014.

Nakamura, S.: The roles of structural imperfections in InGaN-based blue light-emitting diodes and laser diodes, Science, 281, 956–961, doi: http://dx.doi.org/10.1126/science.281.5379.956, 1998.

Nakawaga, H. and Nezu, I.: Structure of space-time correlations of bursting phenomena in an open-channel flow, J. Fluid Mech., 104, 1–43, doi: http://dx.doi.org/10.1017/S0022112081002796, 1981.

Nielsen, R.: Gasaustausch - Entwicklung und Ergebnis eines schnellen Massenbilanzverfahrens zur Messung der Austauschparameter, Dissertation, Institut für Umweltphysik, Univ. Heidelberg, URL http://www.ub.uni-heidelberg.de/archiv/5032, 2004.

Nightingale, P. D. et al.: In situ evaluation of air-sea gas exchange parameterization using novel conservation and volatile tracers, Global Biogeochem. Cycles, 14, 373–387, doi: http://dx.doi.org/10.1029/1999GB900091, 2000.

Okuda, K.: The internal structure of short wind waves. Part I: On the internal vorticity structure, J. Oceanogr. Soc. Jpn., 38, 28–42, doi: http://dx.doi.org/10.1007/BF02113819, 1982.

Okuda, K., Kawai, S., and Toba, Y.: Measurement of skin friction distribution along the surface of wind waves, Journal of Oceanography, 33, 190–198, doi: http://dx.doi.org/10.1007/BF02109691, 1977.

Oppenheim, A. V. and Schafer, R. W.: Discrete-time signal processing, Pearson, Upper Saddle River, NJ, 3 edn., URL http://www1.tecnun.es/biblioteca/2010/mat1/libmat22.pdf, 2010.

Pearson, K.: The problem of the random walk, Nature, 72, URL http://www.nature.com/physics/looking-back/pearson/index.html, 1905.

Peirson, W. L.: Measurement of surface velocities and shears at a wavy air-water interface using particle image velocimetry., Exp. Fluids, 23, 427–437, doi: http://dx.doi.org/10.1007/s003480050131, 1997.

Perez-Urquiza, M. and Beltran, J. L.: Determination of the dissociation constants of sulfonated azo dyes by capillary zone electrophoresis and spectrophotometry methods, J. Chromatogr. A, 917, 331–336, doi: http://dx.doi.org/10.1016/S0021-9673(01)00707-5, 2001.

Phillips, O. M.: The equilibrium range in the spectrum of wind-generated waves, J. Fluid Mech., 156, 426–434, doi: http://dx.doi.org/10.1007/s003480050131, 1958.

Pines, E. and Huppert, D.: Geminate recombination proton-transfer reactions, Chem. Phys. Lett., 126, 88–91, doi: http://dx.doi.org/10.1016/0009-2614(86)85121-1, 1986.

Platt, U. and Stutz, J.: Differential optical absorption spectroscopy, principles and applications, Physics of Earth and Space Environments, Springer, doi: http://dx.doi.org/10.1007/978-3-540-75776-4, 2008.

Platt, U., Perner, D., and Pätz, H. W.: Simultaneous measurement of atmospheric CH_2O, O_3 and N_2O by differential optical absorption, J. Geophys. Res., 84, 6329–6335, doi: http://dx.doi.org/10.1029/JC085iC12p07453, 1979.

Prandtl, L.: Strömungslehre, Vieweg, 1957.

Quack, B., Atlas, E., Petrick, G., Stroud, V., Schauffler, S., and Wallace, D. W. R.: Oceanic bromoform sources for the tropical atmosphere, Geophys. Res. Lett., 31, L23S0, doi: http://dx.doi.org/10.1029/2004GL020597, 2004.

Rashidi, M. and Banerjee, S.: The effect of boundary conditions and shear rate on streak formation and breakdown in turbulent channel flows, Phys. Fluids, 2, 1827–1838, doi: http://dx.doi.org/10.1063/1.857656, 1990.

Reichardt, H.: Vollständige Darstellung der turbulenten Geschwindigkeitsverteilung in glatten Leitungen, Z. Angew. Math. Mech, 31, 208–219, 1951.

Reith, S.: Spatio-temporal slope measurement of short wind waves under the influence of surface films at the Heidelberg Aeolotron, Master's thesis, Institut für Umweltphysik, Univ. Heidelberg, 2014.

Richmond, R. H. and Wolanski, E.: Coral research: Past efforts and future horizons, Springer Netherlands, doi: http://dx.doi.org/10.1007/978-94-007-0114-4_1, 2011.

Richter, K. and Jähne, B.: A laboratory study of the Schmidt number dependency of air-water gas transfer, in: Gas Transfer at Water Surfaces 2010, edited by Komori, S., McGillis, W., and Kurose, R., pp. 322–332, URL http://hdl.handle.net/2433/156156, 2011.

Rocholz, R.: Spatiotemporal measurement of short wind-driven water waves, Dissertation, Institut für Umweltphysik, Univ. Heidelberg, URL http://www.ub.uni-heidelberg.de/archiv/8897, 2008.

Roedel, W.: Physik unserer Umwelt: die Atmosphäre, Springer-Verlag, 3 edn., 2000.

Sander, R.: Compilation of Henry's law constants for inorganic and organic species of potential importance in environmental chemistry, URL http://www.henrys-law.org., 1999.

Scherr, T. S.: Particle Tracking Velocimetry mit Gasbläschen nahe der Wasseroberfläche im Heidelberger Aeolotron, Master's thesis, Institut für Umweltphysik, Univ. Heidelberg, 2014.

Schimpf, U.: Untersuchung des Gasaustausches und der Mikroturbulenz an der Meeresoberfläche mittels Thermographie, Dissertation, Institut für Umweltphysik, Univ. Heidelberg, Heidelberg, Germany, URL http://www.ub.uni-heidelberg.de/archiv/545, 2000.

Schnieders, J., Garbe, C., Peirson, W., Smith, G., and Zappa, C.: Analyzing the footprints of near surface aqueous turbulence - an image processing based approach, J. Geophys. Res., 118, 1272–1286, doi: http://dx.doi.org/10.1002/jgrc.20102, 2013.

Schwarzenbach, R. P., Gschwend, P. M., and M., I. D.: Environmental organic chemistry, Wiley-Interscience, 2 edn., 2003.

Scott, N. V., Handler, R. A., and Smith, G. B.: Wavelet analysis of the surface temperature field at an air–water interface subject to moderate wind stress, Int. J. Heat Fluid Flow, 29, 1103–1112, doi: http://dx.doi.org/10.1016/j.ijheatfluidflow.2007.11.002, 2008.

Shi, Q., Davidovits, P., Jayne, J. T., Worsnop, D. R., and Kolb, C. E.: Uptake of gas-phase ammonia. 1. Uptake by aqueous surfaces as a function of pH, J. Phys. Chem. A, 103, 8812–8823, doi: http://dx.doi.org/10.1021/jp991696p, 1999.

Siddiqui, M. H. K., Loewen, M. R., Jessup, A. T., and Asher, W. E.: Infrared remote sensing of microscale breaking waves and near-surface flow fields, in: Geoscience and Remote Sensing Symposium, 2001. IGARSS 01. IEEE 2001 International, vol. 2, pp. 969 – 971, doi: http://dx.doi.org/10.1109/IGARSS.2001.976697, 2001a.

Siddiqui, M. H. K., Loewen, M. R., Richardson, C., Asher, W. E., and Jessup, A. T.: Simultaneous particle image velocimetry and infrared imagery of microscale breaking waves, Phys.Fluids, 13, 1891–1903, doi: http://dx.doi.org/10.1063/1.1375144, 2001b.

Smith, C. R. and Paxson, R. D.: A technique for evaluation of three-dimensional behavior in turbulent boundary layers using computer augmented hydrogen bubble-wire flow visualization, Exp. Fluids, 1, 43–49, doi: http://dx.doi.org/10.1007/BF00282266, 1983.

Smith, G. B., Handler, R. A., and Scott, N.: Observations of the structure of the surface temperature field at an air-water interface for stable and unstable cases, in: Transport at the Air Sea Interface — Measurements, Models and Parameterizations, edited by Garbe, C. S., Handler, R. A., and Jähne, B., Springer-Verlag, doi: http://dx.doi.org/10.1007/978-3-540-36906-6_15, 2007.

Snider, J. R. and Dawson, G. A.: Tropospheric light alcohols, carbonyls, and acetonitrile: Concentrations in the southwestern United States and Henry's law data, J. Geophys. Res., 90, 3797–3805, doi: http://dx.doi.org/10.1029/JD090iD02p03797, 1985.

Soloviev, A. and Lukas, R.: Effects of bubbles and sea spray on air-sea exchange in hurricane conditions, Boundary Layer Meteorol., 136, 365–376, doi: http://dx.doi.org/10.1007/s10546-010-9505-0, 2010.

Soloviev, A. V. and Schlüssel, P.: Parameterization of the cool skin of the ocean and the air-ocean gas transfer on the basis of modeling surface renewal, J. Phys. Oceanogr., 24, 1339–1346, URL http://journals.ametsoc.org/doi/pdf/10.1175/1520-0485%281994%29024%3C1339%3APOTCSO%3E2.0.CO%3B2, 1994.

Springer, T. and Pigford, R.: Influence of surface turbulence and surfactants on gas transport through liquid interfaces, Ind. Eng. Chem. Fundam., 9, 458–465, doi: http://dx.doi.org/10.1021/i160035a025, 1970.

Stemmler, I., Hense, I., Quack, B., and Maier-Reimer, E.: Methyl iodide production in the open ocean, Biogeosci. Discuss., 10, 17 549–17 595, doi: http://dx.doi.org/10.5194/bgd-10-17549-2013, 2013.

Stokes, G.: On the effect of the internal friction of fluids on the motion of pendulums, vol. 9, Transactions of the Cambridge Philosophical Society, URL http://www.nawcc-index.net/Articles/Stokes-InternalFriction.pdf, 1850.

Sverdrup, H. U., Johnson, M. W., and Fleming, R. H.: The Oceans, Prentice-Hall, Englewood Cliffs, NJ, URL ark.cdlib.org/ark:/13030/kt167nb66r/, 1942.

Tannenbaum, E. et al.: The far ultraviolet absorption spectra of simple alkyl amines, J. Chem. Phys., 21, 311–318, doi: http://dx.doi.org/10.1063/1.1698878, 1953.

Thorpe, S. A.: Langmuir circulation, Annu. Rev. Fluid Mech., 36, 55–79, doi: http://dx.doi.org/10.1146/annurev.fluid.36.052203.071431, 2004.

Troitskaya, Y., Sergeev, D., Kandaurov, A., Baidakov, G., Vdovin, M., and Kazakov, V.: Laboratory and theoretical modeling of air-sea momentum transfer under severe wind conditions, J. Geophys. Res., 117, C00J2, doi: http://dx.doi.org/10.1029/2011JC007778, 2012.

Tsai, W.-T.: A numerical study of the evolution and structure of a turbulent shear layer under a free surface, J. Fluid Mech., 354, 239–276, doi: http://dx.doi.org/10.1017/S0022112097007623, 1998.

Tsai, W.-T. and Liu, K.-K.: An assessment of the effect of sea surface surfactant on global atmosphere-ocean CO_2 flux, J. Geophys. Res., 108, 3127–3142, doi: http://dx.doi.org/10.1029/2000JC000740, 2003.

Tsai, W.-T., Chen, S.-M., and Moeng, C.-H.: A numerical study on the evolution and structure of a stress-driven, free-surface turbulent shear flow, J. Fluid Mech., 545, 163–192, doi: http://dx.doi.org/10.1017/S0022112005007044, 2005.

Tsai, W.-T., Chen, S.-M., Lu, G.-H., and Garbe, C. S.: Characteristics of interfacial signatures on a wind-driven gravity-capillary wave, J. Geophys. Res., 118, 1715–1735, doi: http://dx.doi.org/10.1002/jgrc.20145, 2013.

Veron, F. and Melville, W. K.: Experiments on the stability and transition of wind-driven water surfaces, J. Fluid Mech., 446, 25–65, 2001.

Wanner, S.: Interaktives Rendering von Wellendaten windgetriebener Wasseroberflächen und Ereignisklassifizierung, Diplomarbeit, Institut für Umweltphysik, Univ. Heidelberg, URL http://www.ub.uni-heidelberg.de/archiv/11904, 2010.

Wanninkhof, R.: Relationship between wind speed and gas exchange over the ocean, J. Geophys. Res., 97, 7373–7382, doi: http://dx.doi.org/10.1029/92JC00188, 1992.

Warken, P.: Hochauflösende LIF-Methode zur Messung von Sauerstoffkonzentrationsprofilen in der wasserseitigen Grenzschicht, Diplomarbeit, Institut für Umweltphysik, Univ. Heidelberg, 2010.

Whitman, W. G.: The two film theory of gas absorption, Chemical and Metallurgical Engineering, 29, 146–148, doi: http://dx.doi.org/10.1016/0017-9310(62)90032-7, 1923.

Wiberg, N.: Lehrbuch der Anorganischen Chemie, Walter de Gruyter, 102 edn., 2007.

Winter, R.: Fluorescent tracers for air-sided concentration profile measurements at the air-water interface, Dissertation, Institut für Umweltphysik, Univ. Heidelberg, URL http://www.ub.uni-heidelberg.de/archiv/12105, 2011.

Wolfbeis, O. S., Fürlinger, E., Kroneis, H., and Marsoner, H.: Fluoimetric analysis, Fresenius Z Anal Chem, 314, 119–124, doi: http://dx.doi.org/10.1007/BF00482235, 1983.

Wolfbeis, S. and Posch, E.: Fibre-optic fluorescing sensor for ammonia, Anal. Chim. Acta, 185, 321–327, doi: http://dx.doi.org/10.1016/0003-2670(86)80060-5, 1986.

Wolff, L. M., Liu, Z. C., and Hanratty, T. J.: A fluorescence technique to measure concentration gradients near an interface, in: Air-Water Mass Transfer, selected papers from the 2nd Int. Symposium on Gas Transfer at Water Surfaces, edited by Wilhelms, S. C. and Gulliver, J. S., pp. 210–218, ASCE, Minneapolis, 1991.

Woolf, D. K.: Parametrization of gas transfer velocities and sea-state-dependent wave breaking, Tellus B, 57, 87–94, doi: http://dx.doi.org/10.1111/j.1600-0889.2005.00139.x, 2005.

Woolf, D. K. and Monahan, E. C.: Bubbles and the air-sea transfer velocity of gases, Atmos. Ocean, 31, 517–540, doi: http://dx.doi.org/10.1080/07055900.1993.9649484, 1993.

Wurl, O., Wurl, E., Miller, L., Johnson, L., and Vagle, S.: Formation and global distribution of sea-surface microlayers, Biogeosci. Discuss., 8, 121–135, doi: http://dx.doi.org/10.5194/bg-8-121-2011, 2011.

Yaglom, A. M. and Kader, B. A.: Heat and mass transfer between a rough wall and turbulent fluid flow at high Reynolds and Peclet numbers, J. Fluid Mech., 62, 601–623, doi: http://dx.doi.org/10.1017/S0022112074000838, 1974.

Yaws, C. L.: Chemical Properties Handbook: physical, thermodynamic, environmental, transport, safety, and health related properties for organic and inorganic chemicals, McGraw-Hill, 1999.

Zappa, C., Banner, M., Schultz, H., Corrada-Emmanuel, A., Wolff, L., and Yalcin, J.: Retrieval of short ocean wave slope using polarimetric imaging, Meas. Sci. Technol., 19, 1–13, doi: http://dx.doi.org/10.1088/0957-0233/19/5/055503, 2008.

Zappa, C. J., Asher, W. E., and Jessup, A. T.: Microscale wave breaking and air-water gas transfer, J. Geophys. Res., 106, 9385–9391, doi: http://dx.doi.org/10.1029/2000JC000262, 2001.

Zappa, C. J., Asher, W. E., Jessup, A. T., Klinke, J., and Long, S. R.: Microbreaking and the enhancement of air-water transfer velocity, J. Geophys. Res., 109, C08S1, doi: http://dx.doi.org/10.1029/2003JC001897, 2004.

Zappa, C. J. et al.: Environmental turbulent mixing controls on the air-water gas exchange in marine and aquatic systems, Geophys. Res. Lett., 34, L1060, doi: http://dx.doi.org/10.1029/2006GL028790, 2007.

A

Appendix

A.1 Dimensionless concentration profiles

Jähne (1983; 1985) proposed a method to gain dimensionless concentration profiles by the visualization technique described in sec. 3.1. By fitting different models to these profiles even local transfer velocities could be computed. Different approximations need to be considered to enable the calculation of theses profiles with simple measurable parameters as the concentration of ammonia in the air bulk and the pH value in the water bulk. Therefore, two cases are distinguished - for high and low soluble gases. High soluble gases are mainly controlled by the air side and low soluble gases by the water side (see sec. 2.2.3). The possibilities and restrictions of these approximations suggest by Jähne (1983; 1985) will be discussed in the following in detail. The simulations presented in sec. 3.3 are used for demonstrating purposes.

A.1.1 Air-side controlled

In Jähne (1983) the dimensionless concentration profile is

$$\beta(z_{\mathrm{n}}) = \frac{R_{\mathrm{n,w}}(z_{\mathrm{n}})}{R_{\mathrm{tot,w}}} \tag{A.1}$$

where $R_{\mathrm{n,w}}$ is the water-side transfer resistance until the neutral layer depth z_{n} and $R_{\mathrm{tot,w}}$ is the total water-side transfer resistance. The dimensionless concentration profile is simulated for the small eddy and surface renewal model and the results of

the simulations are shown in Fig. A.1. The resistance until the neutral layer is

$$R_{\mathrm{n,w}}(z_{\mathrm{n}}) = \frac{[\mathrm{NH}_x]_{\mathrm{s,w}} - [\mathrm{NH}_x]_{\mathrm{n,w}}(z_{\mathrm{n}})}{j} \tag{A.2}$$

where $[\mathrm{NH}_x]_{\mathrm{n,w}}$ is the concentration of ammonia and ammonium at the neutral layer depth and the total resistance is

$$R_{\mathrm{tot,w}} = \frac{[\mathrm{NH}_x]_{\mathrm{s,w}} - [\mathrm{NH}_x]_{\mathrm{b,w}}}{j}. \tag{A.3}$$

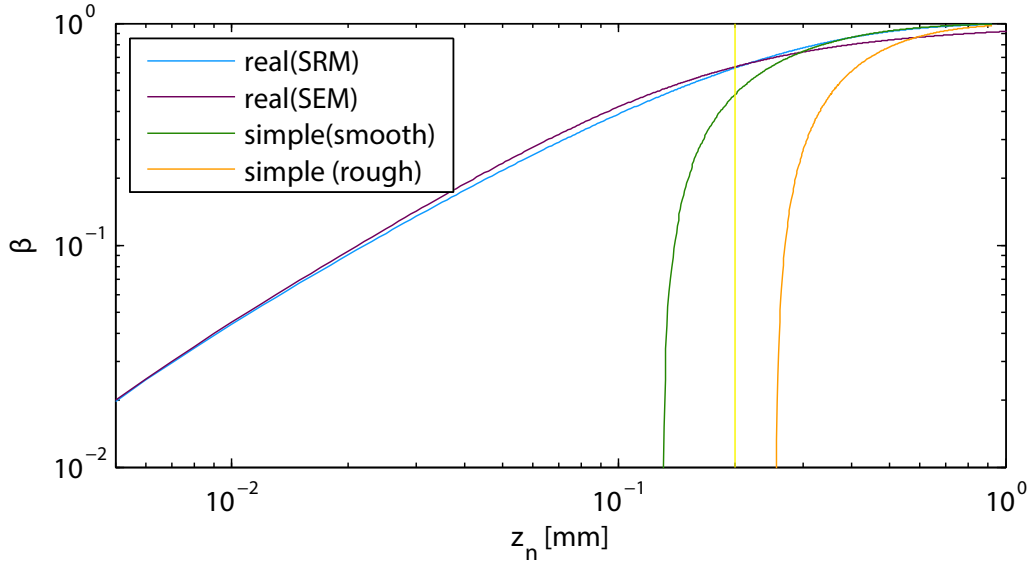

Figure A.1.
Dimensionless concentration profiles simulated by eq. (A.1) are shown for different neutral layer depths in a double logarithmic scale. The surface renewal model (SRM) is shown in blue and the small eddy model (SME) in purple. Simplified profiles computed by eq. (A.5) for a smooth surface (green) and for a rough surface (orange) are shown as well. The used boundary layer depth of 200 µm is marked by the yellow line.

By using the same approximations as shown in sec. 3.4, mass conservation, and eq. (2.21) it follows

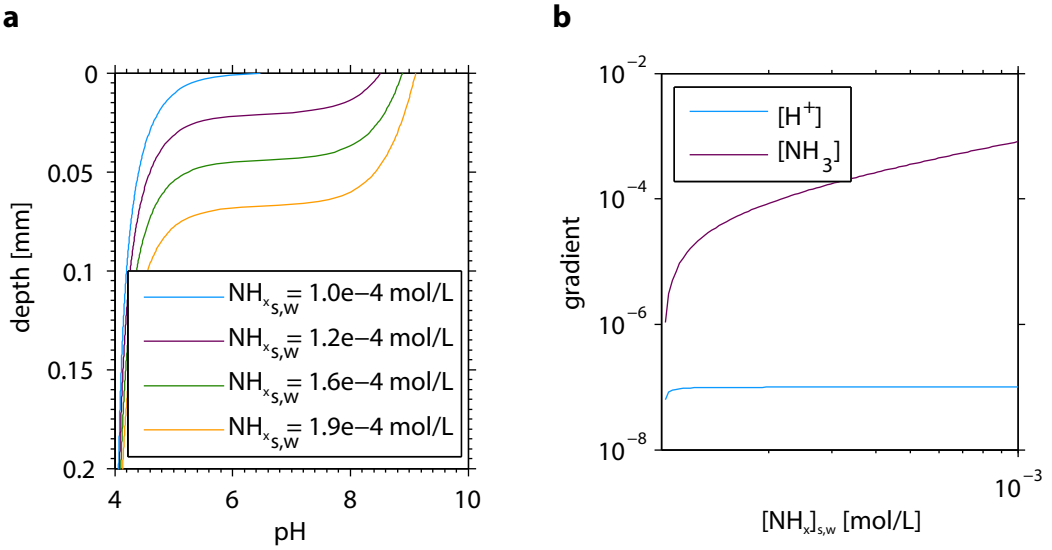

Figure A.2.
a Simulated pH depth profiles for different $[NH_x]$ (ammonia and ammonium) surface concentrations with a boundary layer depth of 200 µm. The starting pH value is 4 and the Pyranine concentration is 5×10^{-6} mol/L. **b** Simulated gradients for different $[NH_x]_{tot}$ concentrations of $[H^+]$ (blue line) and $[NH_3]_w$ (purple line). The gradient of the ammonia concentration in the water is at least one order of magnitude larger than the hydrogen gradient.

$$\begin{aligned}
\beta(z_n) = \frac{R_n(z_n)}{R_{tot}} &= \frac{[NH_x]_s - [NH_x]_n}{[NH_x]_s - [NH_x]_b} \\
&= \frac{[NH_x]_s - [NH_x]_n + [NH_x]_b - [NH_x]_b}{[NH_x]_s - [NH_x]_b} \\
&= \frac{[NH_x]_s - [NH_x]_b}{[NH_x]_s - [NH_x]_b} - \frac{[NH_x]_n - [NH_x]_b}{[NH_x]_s - [NH_x]_b} \\
&= 1 - \frac{k_w([NH_x]_n - [NH_x]_b)}{k_w([NH_x]_s - [NH_x]_b)} \\
&= 1 - \frac{k_w([NH_x]_n - [NH_x]_b)}{k_a([NH_3]_{b,a} - [NH_3]_{s,a})} \\
&= 1 - \frac{k_w([H^+]_b}{k_a[NH_3]_{b,a}}.
\end{aligned} \tag{A.4}$$

The dimensionless concentration profile is

$$\beta(z_n) = 1 - \frac{1}{\gamma}, \tag{A.5}$$

where γ is defined as

$$\gamma := \frac{k_a}{k_w} \frac{[NH_3]_{b,a}}{[H^+]_{b,w}}. \tag{A.6}$$

By varying γ (air-side ammonia concentration) different fractions of the mass boundary layer can be visualized (see eq. (A.1)). For example, by doubling the ammonia concentration, the resistance until the neutral layer depth is half of total resistance (compare eq. (A.1) and eq. (A.5)). In the last step in the derivation in eq. (A.4), the approximations mentioned in sec. 3.4 are used. Three of the approximations are not valid for pH values larger than eight. In Fig. A.2(a), the pH value for different surface $[NH_x]$ concentrations is shown. Neglecting the surface concentration of ammonia in the air leads to an error of up to 60 %. Since for higher pH values the solubility of ammonia is much smaller and the ratio of the surface to bulk concentration increases and ammonia at the air surface can no longer be neglected (see Fig. 3.10). Additionally, the fraction of the air to water-side transfer velocity changes due to a changing solubility as shown by Kräuter (2011). At a pH value over 9.25 at the water surface the solubility is not further decreasing, but at this pH value it is not possible to measure the ratio of the transfer velocities due to the other error source discussed in sec. 3.4. Hence, γ does not only change due to an increase of the ammonia concentration but due to a larger error by the made approximations. This is demonstrated in Fig. A.1. By comparing the real and simplified profiles large deviation between the real and simplified dimensionless concentration profiles are shown. Moreover, the shape of the measured profiles is tremendously different from the shape of the true concentration profiles.

A.1.2 Water-side controlled

If the pH value at the surface is larger than approx. eight the reaction shown in eq. (3.6) gets slower and ammonia is solved in water without reacting to ammonium (see Fig. 3.11). Therefore, ammonia must diffuse to the reaction partner (hydrogen) itself. Diffusion is slow and ammonia accumulates at the water surface on both sides of the interface and the air-side surface concentration cannot be neglected ($[NH_3]_{s,a} \neq 0$).

To determine a dimensionless concentration profile for the water-side controlled case Jähne (1983) proposed to describe the flux by difference of the two fluxes of the reaction partners ($j_w = j_{NH_3} - j_{H^+}$). He shows that the difference of two reactants is independent of the chemical reaction itself. He also states that if the gradient of one of the two reactions is much smaller than the other gradient the diffusion coefficients are not degenerated. Here the difference of the reactants, ammonia and hydrogen of eq. (3.6) are used. The gradients for this case are shown in Fig. A.2(b) and it is clear that the gradient of hydrogen is much smaller than the flux of ammonia. Therefore,

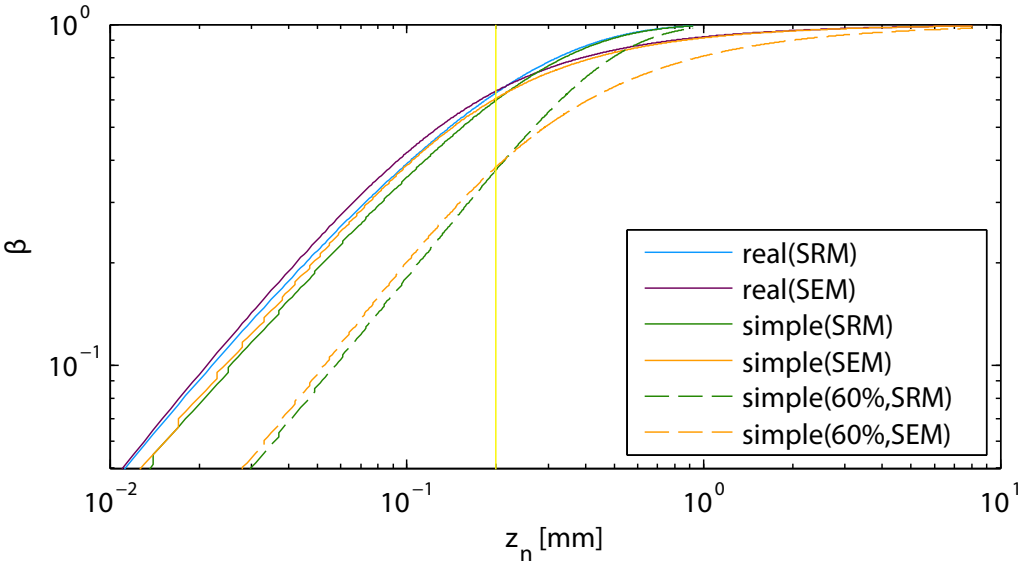

Figure A.3.
Simulated dimensionless concentration profiles for different neutral layer depths. In blue the real profile for the surface renewal and in purple for the small eddy model are shown. The green and orange solid lines show the simplified profiles calculated by eq. (A.9) with the right input value for the surface concentration. The dashed lines show the simplified profiles with a wrong surface concentration with an error of 60 %, which would be made if the air-side concentration in the bulk is used.

the flux in the water is described by

$$j_w = k_w([NH_3]_{s,w} - [NH_3]_{b,w} - [H^+]_s + [H^+]_b). \tag{A.7}$$

Since ($[H^+]_s \ll [H^+]_b$) and ($[H^+]_s \ll [NH_3]_{s,w}$) one gets for the transfer resistance

$$R_{tot,w} = \frac{([NH_3]_{s,w} + [H^+]_b)}{j}. \tag{A.8}$$

For computing the resistance until the neutral layer thickness the bulk values in eq. (A.7) are replaced by the concentrations at the neutral layer depth. By comparing the orders of the different concentrations it can be concluded that $[NH_3]_{s,w}$ is at least one magnitude larger than the other values ($[NH_3]_{s,w} \geq 10^{-5}, [NH_3]_{n,w} = 10^{-6}, [H^+]_{s,w} \leq 10^{-8}, [H^+]_{n,w} = 10^{-7}$). Inserting eq. (A.8) and the last approximation in eq. (A.1), one gets for the dimensionless concentration profile

$$\beta(z_n) = \frac{1}{1 + \frac{[H^+]_{b,w}}{[NH_3]_{s,w}}}. \tag{A.9}$$

The comparison of this simplified and the real dimensionless concentration profiles (eq. (A.1)) are simulated and shown in Fig. A.3. The profiles fit reasonably well.

However, it is not possible with the method explained in sec. 3.1 to measure the water-side surface concentration. Jähne (1983) proposed to substitute the water-side surface concentration by the air-side bulk concentration multiplied with the physical solubility. For this substitution the assumption of a well mixed air space is used. For water-side controlled gases this is true, since they have a constant concentration profile in the air. This would lead to a simplified concentration profile including only measurable parameters

$$\beta(z_{\mathrm{n}}) = \frac{1}{1 + \frac{[\mathrm{H}^+]_{\mathrm{b,w}}}{\alpha[\mathrm{NH}_3]_{\mathrm{b,a}}}}. \tag{A.10}$$

However, ammonia is controlled by the air and water phase and at its physical solubility neither part can be neglected. By using the air-side bulk value as the surface value the maximum error is 60 %. The dimensionless profiles assuming this error are shown in Fig. A.3 as the dotted lines. This would lead to errors in the determination of the boundary layer depth and hence local transfer velocity. These error would be not large, but due to an increase in ammonia at the surface and hence an increase of the pH value at the surface also the solubility changes. As shown in Fig. 3.10 the error made by neglecting the surface concentration is not constant as assumed by the simulations for the dotted lines in Fig. A.3. Hence, not the shape of the profile is also changing with increasing ammonia concentration and no fit could be conducted to the data. This is not the only challenge. As discussed in sec. 3.2 and shown in Fig. 3.6, different solubilities are reported for ammonia, which differ maximum with 50 % from the assumed solubility. To summarize the last section: At higher pH values it is possible to find a simplified dimensionless concentration profile, but due to the fact that ammonia is even for very high solubilities not water-side controlled it is not possible to measure dimensionless concentration profiles and check the models.

A.2 Estimations

Absorption by Pyranine

To estimate the absorption of blue light in a Pyranine solution with a high pH value (pH = 10) the Beer-Lambert law is used

$$I(\lambda, x) = I_0 \exp(-\epsilon c x). \tag{A.11}$$

The incident light is I_0, c is the concentration, x is the depth and ϵ is the extinction coefficient of Pyranine at a pH value of 10 ($\epsilon = 2.44 \times 10^4$ L mol^{-1}ċm^{-1} (Herzog 2010)). With a concentration of $c = 5 \times 10^{-6}$ mol/L and a depth of 1 mm, 2 % of the incoming light I_0 are absorbed.

Intensity observed by the camera

The fluorescent light of the alkaline layer is emitted isotropically. The distance from the water surface to the telecentric lens is 2 m. Thus, only a fraction of the emitted light is able to enter the lens. The diameter of the lens is 0.31 cm. Therefore, the intensity reaching the telecentric lens is

$$\frac{I}{I_0} = \frac{(\frac{0.31\,\mathrm{cm}}{2})^2\pi}{4\pi(0.02\,\mathrm{cm})^2} = 1.4\,\%. \tag{A.12}$$

After the telecentric lens the light is parallelized. Since the objective has an opening of 42.5 mm only 2 % of the 1.4 % incoming light at the telecentric lens is focused on the optical sensor.

Flux estimation

Considering the air and water spaces as two boxes one gets for the air-side

$$V_\mathrm{a}\dot{c_\mathrm{a}} = -jA + \dot{V}c_i, \tag{A.13}$$

with the volume in the air V_a ($\approx$ 25000 L), the water surface A ($\approx$ 17.9 m^2), the gas flux into the water j (see eq. (2.21)), $\dot{c_\mathrm{a}}$ is the temporal change in the air-side concentration, and the volume flux into the facility $\dot{V}c_i$. Hence, the flux of ammonia into the water is computed by

$$j = \frac{\dot{V}c_i - V_\mathrm{a}\dot{c_\mathrm{a}}}{A}. \tag{A.14}$$

The change in air-side concentration is computed by the gradient of two consecutive concentrations and the flux into the facility is the adjusted flux rate (see Tab. 5.2) multiplied with 10^6 ppm ammonia (100 % saturated air).

Test of the absolute measured air-side ammonia concentration

The ammonia concentration in the air is estimated by comparing a theoretical estimate of the concentration with the measured one. The concentration in the air one minute after the start of the injection is compared with a theoretical estimation. Therefore, in eq. (A.13) the flux into the water is neglected (assuming that the ammonia accumulates only in the air) and the concentration in the air is approximated by

$$c_\mathrm{a} = \frac{\dot{V}c_i}{V_\mathrm{a}}\Delta t. \tag{A.15}$$

The computed concentration differs by approx. 5 % from the measured one. The measured concentration is lower than the expected one. It is assumed that some ammonia is already dissolved in the water or has accumulated in the pipes.

A.3 Supplementary tables and figures

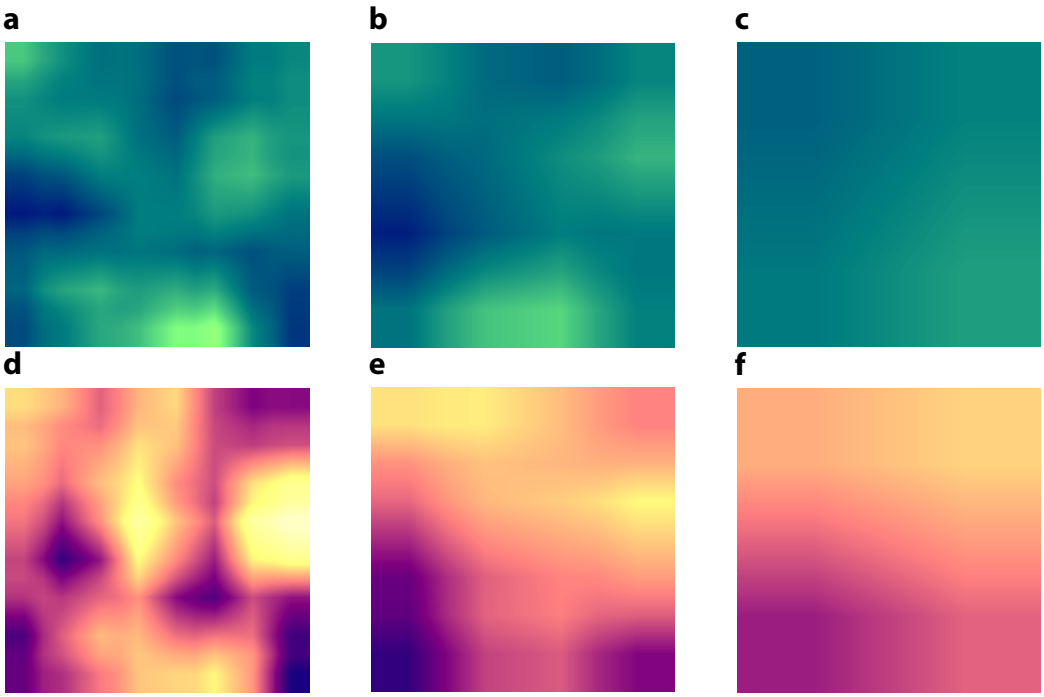

Figure A.4.
Laplace pyramid for the fluorescence and thermal image in Fig. 7.11 for different levels of the Laplacian pyramid. The levels get lower from (a) to (c) and the thermal images with the same level as the fluorescence images are bellow.

Table A.1.
Ratio of the air to water-side transfer velocities k_a/k_w for different conditions. Shown are the pH values, the air-side concentrations of ammonia c_a and the conductivity λ at the time the water surface begins to fluorescence. The error of the air side concentration is approximated by a temporal error of 7.5 s as described in sec. 6.3.

condition	f [Hz]	pH	c_a	λ [mS/m]	k_a/k_w	Δc_a	$\Delta k_a/k_w$
AC clean	5	3.96	1.44	1.71	1858	0.030	37
	7	3.98	1.15	1.72	2222	0.038	61
	9	3.97	1.50	1.62	1743	0.100	46
	12	4.13	1.23	1.53	1471	0.375	120
	16	4.05	3.08	1.58	706	0.425	86
	22	4.25	3.48	1.36	394	0.030	48
AC clean	7	3.44	2.03	2.55	4364	0.038	76
Tartrazin	9	3.46	2.37	2.5	3570	0.100	65
	12	3.48	2.47	2.42	3271	0.375	136
	16	3.50	3.17	2.32	2434	0.425	289
	22	3.54	3.38	2.18	2082	0.500	262
	29	3.59	6.00	1.95	1045	0.025	88
3 g Triton	5	3.68	1.27	2.1	4014	0.030	87
	7	3.71	1.28	2	3717	0.038	94
	9	3.73	1.19	1.99	3818	0.100	125
	12	3.73	1.56	1.9	2912	0.375	189
	16	3.75	2.41	1.8	1800	0.425	281
	22	3.82	2.31	1.75	1599	0.500	295
	29	3.88	3.72	1.62	865	0.025	116
3 g Triton	5	4.11	0.76	1.8	2492	0.030	85
Tartrazin	7	4.19	0.81	1.76	1945	0.038	74
	9	4.16	0.88	1.7	1918	0.100	84
	12	4.23	1.33	1.69	1080	0.375	82
	16	4.31	2.18	1.61	548	0.425	94
	22	4.46	1.85	1.56	457	0.025	105
0.6 g Triton	5	3.39	1.90	2.91	5232	0.030	84
	7	3.45	2.15	2.86	4027	0.038	67
	9	3.39	2.17	2.8	4581	0.100	90
	12	3.42	2.36	2.73	3931	0.375	170
	16	3.44	3.35	2.65	2645	0.425	297
	22	3.51	3.77	2.46	2000	0.030	226

Danksagung

Zunächst möchte ich erst einmal bei allen danken, die zum Gelingen dieser Arbeit in irgendeiner Weise beigetragen haben. Prof. Dr. Bernd Jähne möchte ich für die Ermöglichung und Betreuung dieser interessanten Arbeit danken. Durch ihn konnte ich mich in viele spannende und neue Fachbereiche einarbeiten und meinen Horizont erweitern. Vor allem möchte ich ihm auch danken für die finanzielle Unterstützung, um einige internationale und nationale Konferenzen zu besuchen und meine Arbeit einem breiteren Publikum vorzustellen und neue Kontakte zu knüpfen.

Herrn Prof. Dr. Werner Aeschbach-Hertig möchte ich für seine Bereitschaft zur Zweitbegutachtung dieser Arbeit in der Weihnachtszeit danken. Prof. Dr. Dirk Dubbers und Prof. Dr. Michael Doran danke ich für die Bereitschaft, Teil meines Prüfungskomitees zu sein.

Vielen Dank an die gesamte Windkanal-Gruppe, die immer für gute Stimmung und viel Unterstützung gesorgt hat. Ich bin sehr dankbar für die Hilfsbereitschaft die mir in dieser Arbeitsgruppe entgegengebracht wurde. Ich möchte Daniel Kiefhaber für das Korrekturlesen eines großen Teils meiner Arbeit und vor allem für die Gespräche über pH-Werte an der Wasseroberfläche danken. Darya Trofimova, Wolfgang Mischler und Günther Balschbach möchte ich für die vielen unterstützenden Gespräche vor allem in der Endphase danken. Ich weiß es sehr zu schätzen, dass mir immer Hilfe angeboten wurde ohne dass ich danach fragen musste. Wolfgang Mischler möchte ich insbesondere für die großartige Hilfe bei Problemen bei der Ansteuerung von Kameras danken ("Eigentlich müsste es jetzt funktionieren"). Bei Felix Friedl und Nils Krah möchte ich mich für die inspirierenden Diskussionen über Konzentrationsprofile bedanken. Max Bopp möchte ich für die schnelle Auswertung der neuen Schubspannungsgeschwindigkeiten während der Weihnachtsfeier danken und für die hilfreichen Diskussionen über Strömungsverhältnisse im Aeolotron. Bei Leila Nagel, Jana Schnieders und Jakob Kunz möchte ich mich für die Hilfe bei Fragen zur Infrarotkamera und anderen Diskussionen zum Thema Wärmeaustausch bedanken. Bei Jana Schnieders und Kerstin Krall möchte ich mich für den Aufbau der Klimaanlage bedanken, durch die die gleichzeitigen Wärmemessungen ermöglicht wurden. Ein großer Dank geht auch an mein Büro, die mich durch lustige und ernste Diskussionen auch mal von der Arbeit abgelenkt haben. Evelyn Böhm möchte ich für die Unterstützung der Arbeit durch vegane Bio Kekse danken. Johannes Zülicke und Peter Lübcke möchte ich danken für die Hilfe bei der Programmierung der DOASIS Auswertung und die Hilfestellung bei Fragen zu DOAS.

Meiner Familie und meinen Freunden gebührt ein großer Dank, da sie mich immer unterstützt haben. Ich danke dafür, dass ich trotz meiner Abwesenheit in den letzten Monaten der Endphase immer sehr viel Unterstützung bekommen habe, ob durch Gespräche, Care-Pakete oder auch einfach nur durch die Akzeptanz meiner Abwesenheit.